

Copyright
by
Ameya Umesh Borwankar
2014

The Dissertation Committee for Ameya Umesh Borwankar certifies that this is the approved version of the following dissertation:

Formation of Nanostructures and Weakening of Interactions between Proteins to Design Low Viscosity Dispersions at High Concentrations

Committee:

Keith P. Johnston, Supervisor

Thomas M. Truskett, Co-Supervisor

Jennifer A. Maynard

Venkat Ganesan

Konstantin V. Sokolov

**Formation of Nanostructures and Weakening of Interactions between
Proteins to Design Low Viscosity Dispersions at High Concentrations**

by

Ameya Umesh Borwankar, B.E.

Dissertation

Presented to the Faculty of the Graduate School of
The University of Texas at Austin
in Partial Fulfillment
of the Requirements
for the Degree of

Doctor of Philosophy

The University of Texas at Austin

December 2014

Dedication

To my family and friends, who I am indebted to for making this possible and always supporting me throughout the process. Particular mention must be made of my late uncle, Dr. Rajendra Borwankar, who inspired me to follow in his footsteps and pursue a PhD in Chemical Engineering.

Acknowledgements

This dissertation was a collaborative effort, involving a lot of teamwork on the scientific content and moral support from a large number of people without whom finishing the dissertation would have been impossible. I would first like to thank my advisor, Dr. Keith P. Johnston, for his unflagging enthusiasm for science and constant drive for fostering both personal and professional improvement. His passion for research drove me to strive for better results than I thought possible. I would also like to thank my co-advisor, Dr. Thomas Truskett for imparting his wisdom to me enabling me to gain a better grasp on the theory behind my results and his unwavering belief in and support for my ideas which helped broaden my scientific horizons. I also thank Dr. Jennifer Maynard for her willingness to participate in an effective collaboration which allowed me to evaluate and understand the biological implications of my research. Finally, I thank Dr. Venkat Ganesan and Dr. Konstantin Sokolov for their efforts in evaluating this dissertation.

I owe a great debt of gratitude to the many lab mates who have helped me grow both scientifically and personally. First, I am deeply grateful to Dr. Leo Li Ma, who introduced me to many of the techniques used in this field of research while working with Au nanoparticles during my first year as a graduate student and made my transition into graduate school easier. I am also grateful to Dr. Maria Miller for introducing me to the protein dispersion project and helping me to extend the techniques I learned for gold nanoparticles to proteins. I am indebted to Aileen Dinin, Brian Willsey, Joshua Laber, Barton Dear and Jessica Hung, who helped me collect data throughout the dissertation and spent countless hours with me trying to understand the science behind the results. In addition, I would like to thank my fellow current and former Johnston group members, including Daniel Slanac, Amro Elhag, Andrew Worthen, William Hardin, , Yunshen Chen, Robert Stover, Csaba Kotsmar, Ki Youl Yoon, Hitesh Bagaria, Ed Foster, Lynn

Foster, Jiannan Dong, Guangzhe Yue, and Zheng Xue for their encouragement, scientific discussions, and moral support. Special thanks goes to our undergraduate researchers who conducted a lot of experiments for completing this dissertation, namely, Brian Wilson, April Twu, Sai Gourisankar, Jingyan Yue and Joseph Jakubovski. I would also like to express my gratitude to the Maynard research group, especially Tarik Khan. Their willingness to conduct animal studies involving our nanoclusters helped me understand the applications of my work better. Also I would like to thank Ryan Jadrich from the Truskett research group for his help in the theoretical interpretation of experimental results. Special thanks also go to Dmytro Nykypanchuk and Oleg Gang at national institute of standards and technology (NIST) for conducting small angle x-ray scattering (SAXS) studies with our samples. I would additionally like to thank Dr. Dwight Romanovicz and Dr. Shouliang Zhang for their assistance with electron microscopy imaging of the systems including SEM and TEM.

Finally, I would like to thank the unwavering support and encouragement of my parents (Umesh and Madhuree Borwankar), my sister (Anuja Borwankar), my grandparents (Prabhakar and Padma Borwankar and Madhav and Sunila Gokhale), my aunt and uncle (Preeti and Rajendra Athavale) and my extended family in India and in the United States. Their encouragement and support kept me going through long and stressful days and nights, and they have truly played a key role in the production of this dissertation.

Formation of Nanostructures and Weakening of Interactions between Proteins to Design Low Viscosity Dispersions at High Concentrations

Ameya Umesh Borwankar, Ph. D

The University of Texas at Austin, 2014

Supervisors: Keith P. Johnston and Thomas M. Truskett

Monoclonal antibodies and other protein therapeutics are rapidly gaining popularity as a favored class of drugs for treatment of various types of diseases and disorders including rheumatoid arthritis, Crohn's disease, asthma, macular degeneration, different types of cancer. There great lot of interest in development of subcutaneous self-injection methods for administering these therapeutics to enable patient convenience which requires high concentration formulations to deliver the required dosage in the limited volume. At high concentrations, proteins have a propensity to be insoluble, aggregate, unfold, gel or denature due to strong short ranged protein-protein interactions, resulting in highly viscous solutions. Therefore, it is challenging to form highly concentrated, stable protein formulations with low viscosities. Addition of interacting co-solutes like arginine to protein formulations weakens protein-protein interactions through protein charge modification and hydrophilization of hydrophobic surface patches through binding on proteins. Weakened interactions lower the viscosity of protein formulations with 250 mg/ml protein by 5-6 times compared to conventional protein solutions in buffer not containing any co-solutes. Addition of co-solutes can also give rise to

depletion attraction between proteins which can assemble them into amorphous nanostructured domains with lowered diffusion coefficients as determined by dynamic light scattering (DLS). A free energy model was developed to explain the formation of nanostructures due to short-ranged depletion attraction and long-ranged electrostatic repulsion, whereby sizes were predicted to range from 30 to 100 nm as a function of co-solute and protein concentrations. The nanostructured domains dissociated to monomeric, active and stable protein upon dilution to about 1 mg/ml. Supplemental sizing techniques, namely, cryogenic scanning electron microscopy (cryo-SEM) and small angle x-ray scattering (SAXS) show evidence of nanostructures larger than the monomer although determining the ratio of the amount of protein in monomeric state to that in the nanostructure state is still a challenge. In order to further understand cluster formation in a simpler system, gold nanoclusters were synthesized via assembly of primary particles by reaction. The morphology of these gold nanoclusters was also controlled by favoring kinetic over thermodynamic control of growth for generating asymmetrical structures thus allowing higher extinction in the near infrared region enabling biomedical imaging.

Table of Contents

List of Tables	xvii
List of Figures	xxv
Chapter 1: Introduction	1
1.1 Origin of high viscosities and instability in protein formulations	1
1.2 Reduction of protein formulation viscosity by modifying interactions and structure.....	4
1.3 Protein cluster formation and characterization	6
1.4 Objectives	9
1.5 Dissertation outline	13
1.6 References.....	17
Chapter 2: Gold Nanoparticles with High Densities of Small Points on Nanocluster Cores with Strong NIR Extinction	24
2.1 Introduction.....	24
2.2 Materials and Methods.....	28
2.2.1 Materials	28
2.2.2 Synthesis of Au Clusters - First Iteration.....	28
2.2.3 Quenching of reactions for temporal experiments.....	29
2.2.4 Materials Characterization	30
2.2.4.1 Dynamic light scattering measurements	30
2.2.4.2 Electron Microscopy	30
2.2.4.3 Thermogravimetric analysis.....	31
2.2.4.4 Measurement of Au concentration.....	31
2.3 Results and Discussion	32
2.3.1 Formation of clusters of Au primary particles	32
2.3.2 Rapid kinetic growth generates points on primaries whereas slow growth results in equilibrium relaxation to spheres.....	33
2.3.3 Morphology of points on the nanoclusters gives rise to high NIR extinction.....	39

2.3.4 Morphology of points on the nanoclusters gives rise to high NIR40	
2.4 Conclusions.....	41
2.5 References.....	50
Chapter 3: Concentrated Dispersions of Equilibrium Protein Nanoclusters That Reversibly Dissociate into Active Monomers	56
3.1 Introduction.....	57
3.2 Methods.....	61
3.2.1 Formation of nanocluster dispersions	61
3.2.2 Characterization of the nanocluster dispersions	62
3.2.3 Characterization of the protein structure and activity.....	63
3.2.4 In vivo bioavailability in BALB/c mice.....	64
3.3 Results and Discussion	65
3.3.1 Nanocluster morphology and tunability with trehalose and dilution in buffer.....	65
3.3.2 Protein stability after dilution of the nanoclusters	68
3.3.3 Mechanism of assembly of proteins into nanoclusters	72
3.3.4 Viscosity of Nanocluster Dispersions.....	78
3.3.5 In vivo study of protein stability and pharmacokinetics in mice	79
3.4 Conclusions.....	80
3.5 References.....	91
Chapter 4: Tunable Equilibrium Nanocluster Dispersions at High Protein Concentrations	95
4.1 Introduction.....	95
4.2 Materials and Methods.....	98
4.2.1 Protein purification (FPLC)	98
4.2.2 Buffer exchange	98
4.2.3 Centrifugal filtration of protein solution to form a dispersion of nanoclusters upon concentration.....	99
4.2.4 Characterization of the protein nanocluster dispersion.....	100
4.2.4.1 Hydrodynamic diameters	100

4.2.4.2 Size exclusion chromatography	101
4.2.4.3 Enzyme linked immunosorbent assay (ELISA).....	101
4.2.4.4 Circular dichroism (CD)	102
4.2.4.5 Viscosity	102
4.2.4.6 Scanning Electron Microscopy (SEM)	102
4.3 Results and Discussion	103
4.3.1 Recap of Equilibrium free energy model.....	103
4.3.2 Nanocluster formation by the centrifugal or concentration filtration pathway	103
4.3.3 Prediction of nanocluster size based on the free energy model	107
4.3.4 Colloidal and conformational stability of proteins	110
4.4 Conclusions.....	111
4.5 References.....	117
Chapter 5: Characterization of structures in protein formulations with high co-solute concentrations by small angle x-ray scattering.....	
5.1 Introduction.....	121
5.2 Materials and methods	124
5.2.1 Materials	124
5.2.2 Preparation of dispersion samples	124
5.2.3 Characterization of the protein formulations	126
5.2.3.1 Measurement of formulation viscosity	126
5.2.3.2 Measurement of diffusion coefficient by DLS	126
5.2.3.3 Determination of protein concentration	127
5.2.3.4 Small angle x-ray scattering measurements of formulations	127
5.3 Results and discussion	128
5.3.1 Nanostructure characterization for protein concentration of 125 mg/ml	128
5.3.2 Characterization of higher protein concentration formulations	131
5.4 Conclusions.....	132

5.5 References.....	137
Chapter 6: Cryo-SEM for direct visualization of high concentration protein formulations at high and low co-solute concentration.....	140
6.1 Introduction.....	141
6.2 Materials and methods	144
6.2.1 Materials	144
6.2.2 Preparation of dispersion samples	144
6.2.3 Characterization of the protein formulations	144
6.2.3.1 Measurement of formulation viscosity	144
6.2.3.2 Measurement of diffusion coefficient by DLS	145
6.2.3.3 Determination of protein concentration	145
6.2.3.4 Cryo-SEM sample preparation and imaging.....	146
6.3 Results and discussion	147
6.3.1 High mAb concentration formulations containing 60-80 nm species	147
6.3.2 Dilution of mAb retains nanostructures	150
6.3.3 Imaging of control samples: Low co-solutes and buffer without protein	151
6.3.4 Limitations and factors affecting size measurement by cryo-SEM.....	152
6.4 Conclusions.....	153
6.5 References.....	159
Chapter 7: Reduction of mAb viscosity at 250 mg/ml by addition of high arg concentrations to modify protein-protein interactions.....	163
7.1 Introduction.....	164
7.2 Materials and Methods.....	168
7.2.1 Materials	168
7.2.2 Buffer exchange	168
7.2.3 Centrifugal concentration to >200 mg/ml.....	169
7.2.4 Characterization of the protein nanocluster dispersion.....	171
7.2.4.1 Viscosity measurement	171

7.2.4.2 DLS and diffusion interaction parameter measurements	172
7.2.4.3 Size Exclusion Chromatography	172
7.2.4.4 Protein Concentration determination in the dispersion	173
7.2.4.5 Sample storage	173
7.3 Results	173
7.3.1 Effect of co-solutes on viscosity at ~150 mg/ml mAb concentration	173
7.3.2 Effect of co-solutes on viscosity at ~250 mg/ml mAb concentration at pH ~5.5	175
7.3.3 Effect of pH on co-solutes on viscosity at ~250 mg/ml mAb concentration	178
7.3.4 Effect of a preferentially excluded co-solute trehalose on viscosity	180
7.3.5 Stability of mAb dispersion upon storage and dilution	182
7.4 Discussion	183
7.4.1 mAb dispersions without co-solute	183
7.4.2 Modification of electrostatic interactions between mAbs by arg to lower η	184
7.4.3 Modification of hydrophobic interactions between mAbs by salt and arg to lower η	185
7.5 Conclusions	186
7.6 References	200
Chapter 8: Solubilization of α -Chymotrypsinogen by interaction modification with arginine and glutamic acid	205
8.1 Introduction	205
8.2 Materials and methods	209
8.2.1 Materials	209
8.2.2 Methods	209
8.2.2.1 Dispersion preparation	209
8.2.2.2 Viscometry for the protein nanocluster dispersion	209
8.2.2.3 Measurement of diffusion coefficient by DLS	210

8.2.2.4 Protein Concentration determination in the dispersion.	210
8.2.2.5 Measurement of protein enzymatic activity and stability	211
8.3 Results.....	211
8.3.1 Protein solubilization by addition of arginine and glutamic acid	211
8.3.2 Effect of trehalose on dispersion viscosity and D/D_0	214
8.3.3 Protein stability upon dilution of dispersions	215
8.4 Discussion.....	216
8.4.1 Arginine interactions with α -CGN	216
8.4.2 Trehalose interactions with α -CGN.....	219
8.4.3 Stability of α -CGN in high concentration protein formulations with high co-solute concentrations	220
8.4.4 Origin of lowered D/D_0 high concentration protein formulations with high co-solute concentrations	221
8.5 Conclusions.....	222
8.6 References.....	232
Chapter 9: Conclusions and Recommendations	236
9.1 Conclusions.....	236
9.1.1 Modification of Protein-protein Interactions for Reducing Viscosity	236
9.1.2 Characterization of Nanostructure Formation and Dissociation by Orthogonal Techniques.....	238
9.1.3 Synthesis of Au Nanoclusters with High NIR Extinction and Controlled Morphology	240
9.2 Recommendations and Future Research.....	241
9.2.1 Improvements in the Methods of Nanostructure Size Determination and study of morphology	241
9.2.2 Further Modification of Protein-protein Interactions for Reducing Viscosity	243
9.3 References.....	244

Appendix A: Gold Nanoparticles with High Densities of Small Points on Nanocluster Cores with Strong NIR Extinction	245
A.1 Note on DLS measurements	245
A.2 Supplementary references	251
Appendix B: Concentrated Dispersions of Equilibrium Protein Nanoclusters That Reversibly Dissociate into Active Monomers	252
B.1 Note about DLS data for Chapter 3	252
B.2 Cluster Dissolution Time	253
B.3 Potential of mean force between two proteins in the presence of the surrounding media	254
B.4 Low effective dielectric constant within the clusters	256
B.5 Surface potential and zeta potential of IgG clusters.....	258
B.6 Supplementary References	269
Appendix C: Tunable Equilibrium Nanocluster Dispersions at High Protein Concentrations	272
C.1 Note on DLS data for Chapter 4.....	272
C.2. ELISA.....	275
C.3 Equilibrium model for cluster formation	275
C.4 Turbidity and additional electron microscopy of the dispersion.....	280
C.5 Dispersions with concentrations of 320 mg/ml.....	280
C.6 Room temperature storage stability.....	281
C.7 Effect of pH on cluster size	281
C.8 CD	281
C.9 Long term storage.....	282
C.10 Sterile filtration of the clusters	282
C.11 Supplementary References	303

Appendix D: Characterization of structures in protein formulations with high co-solute concentrations by small angle x-ray scattering	305
Appendix E: Cryo-SEM for direct visualization of high concentration protein formulations at high and low co-solute concentration	308
Appendix F: Reduction of mAb1 viscosity at 250 mg/ml compared to conventional solution formulations by modification of protein-protein interactions.....	314
F.1 Co-solute concentration during the filtration process in terms of Donnan equilibrium.....	314
F.2 Supplementary References	344
Appendix G: Solubilization of α -Chymotrypsinogen by interaction modification with arginine and glutamic acid	345
Bibliography	348
Vita.....	369

List of Tables

Table 2.1:	Summary of nanoparticle size, absorbance properties and zeta potential.	42
Table 3.1:	1B7 stability and activity in nanocluster dispersion samples with $c = c_E$ = 267 mg/ml diluted to 1 mg/ml in PBS prior to analysis. Error is \pm s. d.	81
Table 3.2:	Estimation of 1B7 Secondary Structure from Circular Dichroism.	82
Table 3.3:	η and D_c for mAb 1B7 and polyclonal sheep IgG mixture dispersions.	82
Table 3.4:	Pharmacokinetic parameters for curves shown in Fig. 3.6. Error is \pm s.d.	83
Table 4.1:	Hydrodynamic diameters (D_c) of protein nanoclusters for various dispersions made by the filtration concentration (C) and lyophilization dilution (LD) processes shown in Fig. 4.1b.	112
Table 5.1:	Compositions, DLS data and viscosities of samples from the current Chapter.	133
Table 6.1:	Summary of the samples contained in the current study (cit stands for citric acid).	154
Table 7.1:	Viscosity of mAb1 dispersions at ~130 mg/ml after addition of 150 mg/ml of amino acids as co-solute.....	188
Table 7.2:	Viscosity of mAb1 dispersions at ~ 150 mg/ml containing ~150 mg/ml mixtures of tre with and without amino acids as co-solutes.	189

Table 7.3:	Viscosity for mAb1 dispersions in low concentration histidine (his to his.HCl was 0.18:1 by mass in both cases) buffers at pH 5.5 run at a centrifugation speed of 5000 rcf. Rows 1 and 3 were run in Centricon centrifugal concentrator tubes with a centrifugation speed of 4500 rcf.	189
Table 7.4:	D/D_0 for dilution of mAb1 dispersions (0.5 mg/ml) with 78.6 mg/ml arg and 71.4 mg/ml glu from Fig. 7.1.	190
Table 7.5:	Viscosity of mAb1 dispersions as a function of increasing conc of arg/glu. The pH of all of the samples was 5.5 and the centrifugation speed was 5000 rcf. The uncertainty is \pm one std. dev. over multiple measurements in both concentration and viscosity.....	190
Table 7.6:	Viscosity, DLS (D/D_0) and turbidity/concentration at 350 nm of mAb1 dispersions made with the large 15 ml Centricon centrifugal concentrator tubes with a centrifugation speed of 4500 rcf and a temperature of 20 °C. The second row in each pair shown in bold is the result after sterile filtration of the row above it.	191
Table 7.7:	Viscosity of low co-solute mAb1 dispersions at various pH values all at a centrifugation speed of 5000 rcf.	192
Table 7.8:	Diffusion interaction parameter k_d values for various dilute protein solutions as measured by DLS using the CONTIN algorithm.....	192
Table 7.9:	Low viscosities for sheep IgG dispersions with high co-solute concentrations at a centrifugation speed of 10000 rcf.	192

Table 7.10:	Viscosity and D/D_0 of mAb1 dispersions with tre as the only co-solute. All samples were formulated in 50 mM phosphate buffer to set the pH. The centrifugation speed was 10000 rcf.	193
Table 7.11:	Viscosity of mAb1 dispersions with tre as the only co-solute with ammonium sulfate added to screen electrostatic interactions. All samples were formulated in 50 mM pH 8.2 phosphate buffer. The centrifugation speed was 10000 rcf.	193
Table 7.12:	Viscosity of mAb1 dispersions including tre with arg and glu at pH 7.1. The centrifugation speed was 5000 rcf.	194
Table 7.13:	SEC for diluted mAb1 dispersions compared to the monomer control.	194
Table 7.14:	SEC for mAb1 dispersions stored for 8 weeks. The values in the table are the % monomer in the sample measured by the area under the curve for the SEC. The ~250 mg/ml dispersion contained 81.4 mg/ml arg and 68.6 mg/ml glu (pH 7.1) and was 99.89% monomer pre-storage...	194
Table 8.1:	pH does not greatly affect the viscosity, but low pH dispersion are turbid and there seems to be a maximum in the size around pH 9 which is the isoelectric point.	223
Table 8.2:	Increased arginine and glutamic acid concentrations at pH 8.5 and pH 9 which is the optimized pH range for low viscosity results in increased viscosity but no change in cluster size.	224

Table 8.3:	Effect of increased trehalose concentration on viscosity and cluster size of α -CGN. Increased trehalose concentration does not significantly increase the dispersion inherent viscosity. Increased solvent viscosity causes the dispersion viscosity to increase. The cluster size increases with increased trehalose concentration.	225
Table 8.4:	Dispersion viscosities for samples from Fig. 8.3 showing very low viscosities for α -CGN dispersions. The inherent viscosity increases with the concentration of arginine and glutamic acid. For lower concentrations though, the α -CGN is in the form of very large particles as evidenced by the turbidity. Cluster size does not change greatly.	226
Table 8.5:	T_m data for the α -CGN dispersions and dilute solution controls.	226
Table A1:	Dynamic light scattering ACFs and size distributions for commercial nanourchins contrasted with particles from Chapter 2.	247
Table A2:	Summary of the NIR extinction properties and sizes of nanoclusters synthesized with dextran instead of CMD keeping all other parameters the same.	247
Table B1:	Parameters used Figs. 3.4a and 3.4c to determine the potential of mean force.	259
Table B2:	General parameters for calculating cluster diameter contours in Fig. 3.4b.....	259
Table B3:	Particular parameters for calculating cluster diameters for specific case in Fig. 3.4b.	260

Table B4:	Auto correlation functions for all of the samples analyzed by DLS in Chapter 3 with sample composition provided to relate back to the figures and tables in the paper. 200 channels were used for all the measurements.....	262
Table C1:	Model parameters for Sheep IgG. Input variables used in the model proposed by Johnston et al. ⁵ and used to generate the plots in Figs. 4.1b, 4.2b, and 4.2e are provided.....	283
Table C2:	D_c of C 220:70 nanoclusters and after subsequent sequential dilutions with buffer. The distributions for the D_c are provided in Fig. C3 and the means are in Figs. 4.2b and 4.2e. The starting solution was at a protein concentration of 70 mg/ml and was centrifuged for 35 minutes.	283
Table C3:	D_c of LD 250:100 nanoclusters and after subsequent sequential dilutions with buffer. The distributions for the D_c are provided in Fig. 4.2d.	284
Table C4:	D_c of C 250:250 nanoclusters and after subsequent sequential dilutions with buffer. The distributions for the D_c are provided in Fig. C5 and the means are in Fig. 4.2e. The starting solution was at a protein concentration of 50 mg/ml and was centrifuged for 68 minutes.	284
Table C5:	D_c , viscosity and protein % monomer after room temperature storage (C 250:100). The distributions for the D_c s are provided in Fig. C6.	284
Table C6:	Effect of pH on D_c . LD 200:80 in pH 6.9 and a dilution of LD 250:100 at pH 6.4 are contrasted to observe the effect of protein charge.....	285
Table C7:	Circular Dichroism for protein secondary structure. The fraction of protein in the different secondary structures for both LD and C samples compared to the native protein.....	285

Table C8:	D_c , viscosity and protein % monomer before and after freezing and thawing (C 220:70). The distributions for the D_c s are provided in Fig. C9. This was the same dispersion as in Fig. C1.....	285
Table C9:	D_c and viscosity of a C 220:70 nanocluster dispersion before and after sterile filtration through a 0.22 μ m polyl(vinylidene difluoride) (PVDF) filter. The distributions for the D_c s are provided in Fig C10. The starting solution at a protein concentration of 48 mg/ml was centrifuged for 27 minutes. After forming the nanoclusters, a portion was saved and a portion was filtered. Both samples were then frozen, stored for a month and thawed, and then analyzed.	286
Table C10:	Auto correlation functions for all of the samples analyzed by DLS in Chapter 4 with sample composition provided to relate back to the figures and tables in the paper. 200 channels were used for all the measurements.....	293
Table E1:	Replicate data for the samples with 240 mg/ml mAb, 40 mg/ml tre, 50 mg/ml his and 17 mg/ml citric acid.	309
Table F1:	Viscosity and D/D_0 with increasing protein concentration at 78.6 mg/ml arg and 71.4 mg/ml glu at pH 5.5. The inherent viscosity remains more or less constant. D/D_0 seems to decrease with increased protein conc. The data is shown graphically in Fig. 7.1. The centrifugation speed was 5000 rcf. The solvent viscosity in all cases was 1.5.	316

Table F2:	Viscosity and cluster size with increasing protein concentration in 20 mM pH 5.5 his buffer. The inherent viscosity increases with protein concentration while the D/D_0 seems to remain constant with increased protein conc. The data is shown graphically in Fig. 7.1. The centrifugation speed was 5000 rcf. The solvent viscosity in all cases was 1.....	317
Table F3:	DLS sizes for dilution of samples from Table 7.5 which were at pH 5.5.	318
Table F4:	Viscosity and cluster size with increasing conc of arg/glu. Replicate data for Table 7.5 at a spin speed of 5000 rcf and pH 5.5. Solvent viscosities are given in Table 7.5.....	319
Table F5:	Visc vs pH for formulations with 150 mg/ml arg. Replicate data for Fig. 7.4. Solvent viscosity for all these dispersions was 1.5 cP.	320
Table F6:	Glu lowers the viscosity compared to HCl. Same amount of interacting co-solute but glu lowers the osmolality values. The centrifugation speed for all the samples was 10000 rcf.	320
Table F7:	Viscosity and D/D_0 for the samples tested for viscosity versus shear rate in Fig. 7.5. The sample in row 2 was in 20 mM his buffer at pH 5.48.....	321
Table F8:	Viscosity and cluster size decrease with increasing conc of arg/glu/tre. Replicate data for Table 7.12. Centrifugation speed was 5000 rcf and pH was 7.1.	321
Table F9:	Auto-correlation functions for the DLS data in Table 7.1. All samples were run with 200 channels.	323

Table F10:	Auto-correlation functions for the DLS data for high co-solute (78.6 mg/ml arg and 71.4 mg/ml glu) samples in Fig. 7.1 in the paper. All samples were run with 200 channels.	327
Table F11:	Auto-correlation functions for the DLS data for low co-solute (20 mM his pH 5.5) samples in Fig. 7.1 in the paper. All samples were run with 200 channels.....	330
Table F12:	Auto-correlation functions for the DLS data for high co-solute (78.6 mg/ml arg and 71.4 mg/ml glu) samples in Table 7.6 in the paper. All samples were run with 200 channels.	333
Table F13:	Auto-correlation functions for the DLS data in Table 7.7 in the paper. All samples were run with 200 channels.	334
Table F14:	Auto-correlation functions for the DLS data in Table 7.10 in the paper. All samples were run with 200 channels.	335
Table F15:	ACFs for the data for DLS of samples from Table 7.12. All samples were run with 200 channels.	336
Table F16:	ACFs for the data for DLS of dilutions of samples from Fig. 7.1 listed in Table 7.4.	337
Table F17:	ACFs for the data for DLS of samples from Fig. 7.5 and Table 7.3 listed in Table F7.	338
Table G1:	Sample ACFs for α -CGN dispersions.	347

List of Figures

- Figure 2.1: This schematic contrasts the thermodynamically and kinetically controlled growth. At high pH (9.3), the clusters fill in or relax to form regular spherical shaped particles while at low pH (8.7), the clusters have further faceted growth on them to form flower shaped particles. At even lower pH (7.5), there is further faceted growth leading to star shaped particles.43
- Figure 2.2: Aggregation of primary particles followed by relaxation for slow thermodynamically controlled growth captured by quenching with mercapto acetic acid at different time points is shown by TEM. a, UV-visible spectra for the nanoparticles as the reaction proceeds at pH 9.3. b, quenched at 40 s. c, quenched at 45 s. d, not quenched. e. SEM image of non-quenched particles.44
- Figure 2.3: a. UV-vis-NIR spectra of final nanoparticles synthesized at 0.018 mM Au^{3+} at pH = 9.3 (dotted line), pH = 8.7(dashed line) and pH = 7.5 (solid line). All spectra are normalized to an absorbance of 1 at the peak value. b. Hydrodynamic diameter of the nanoparticles synthesized with 0.018 mM Au^{3+} at pH = 9.3 (dotted line), pH = 8.7 (dashed line) and pH = 7.5 (solid line). Histograms showing size distributions for particles from TEM image analysis synthesized at c. pH 9.3, d. pH 8.7 and e. pH 7.5. f. Picture of dispersed particles showing the difference in color between the particles from part a with the pH decreasing from 9.3 on the left to 8.7 for the middle cuvette and 7.5 for the cuvette of the right.....46

Figure 2.4: TEM images of nanoparticles synthesized with 0.018 mM Au ³⁺ at a. pH = 8.7 (TEM image also included), b. pH = 7.5.....	46
Figure 2.5: TGA profile of Au nanoparticles synthesized at 0.018 mM Au ³⁺ with a CMD coating at pH 8.7.....	47
Figure 2.6: Scheme 2. Addition of more iterations of Au precursor to the reaction mixture at pH 9.3 leads to growth of points on the spherical core. ..	47
Figure 2.7: Effect of doubling concentration of Au precursor to 0.036 mM at pH 8.7 observed by a. Low resolution TEM of nanoclusters (scale bar is 50 nm), b. Hydrodynamic diameter by DLS and c. Extinction spectra by UV-vis spectroscopy. In both cases, the solid line denotes the 0.018 mM particles while the dashed line is for the 0.036 mM particles.....	48
Figure 2.8: Low resolution TEM images of nanoparticles after different iterations synthesized with dextran (3 mM) at pH = 9.3 with a 50 nm scale bar. a, 1 iteration. b, 3 iterations. c, 7 iterations and d, 10 iterations.	49
Figure 2.9: Nanoparticles after 1-12 iterations at 0.018 mM Au ³⁺ per iteration with dextran coating at pH=9.3 characterized by (a) DLS hydrodynamic diameter and (b) UV-Vis extinction spectra.	50

Figure 3.1: Nanocluster morphology for mAb 1B7 with trehalose as extrinsic co-solute. a. Schematic of a nanocluster where in the current study green circles represent proteins, red dots, counterions and blue circles, co-solutes. Similar clusters are observed for colloids in organic solvent. b. Transparent dispersion at $c = c_E = 220$ mg/ml. c. SEM image of 3.1b indicating closely-spaced, self-crowded protein. (The “halo” on the component particles is probably an artifact of trehalose deposition during sample preparation). d. Schematic of dispersion of nanoclusters drawn to scale.84

Figure 3.2: Calculated hydrodynamic diameter by DLS for 1B7 antibody and polyclonal sheep IgG with trehalose as extrinsic co-solute. a. 1B7: serial dilutions in buffer such that $c/c_E = 1$. b. 1B7: dilution in pH 7.2 phosphate buffer with starting $c = c_E = 220$ mg/ml as in Fig. 3.2a (squares) and decreasing c_E with a constant c of 70 mg/ml with a starting c_E of 270 mg/ml (diamonds). Error bars indicate \pm s. d. in peak width. The predictions of Eq. 9 are in qualitative agreement. c. 1B7: constant c of 70 mg/ml for decreasing c_E of trehalose from 270 to 150 mg/ml as shown in legend and then a final point where c_E is raised back to 270 mg/ml, labeled as 270 mg/ml-2. d. polyclonal sheep IgG: constant c of 50 mg/ml for increasing (diamonds) followed by decreasing (squares) trehalose concentration. The reversibility suggests equilibrium cluster behavior. The theoretical predictions of the free energy model are in qualitative agreement with the data.85

Figure 3.3: BSA nanocluster size for high protein concentrations. A high concentration BSA dispersion formulated at $c = 400$ mg/ml and $c_E = 240$ mg/ml contains nanoclusters with hydrodynamic diameter of 40 nm. Dispersions formulated with lower concentrations of BSA and/or trehalose yield progressively smaller nanoclusters. Also shown is BSA monomer which is 3-4 nm in diameter.	86
Figure 3.4: Antibody conformation and activity. a. Circular dichroism spectra of a mAb 1B7 control and 267 mg/ml dispersion. All samples were diluted to 0.1 mg/ml in PBS and analyzed on a Jasco J-815 CD Spectrometer. b. Theoretical prediction of the fraction of folded protein suggesting that the native state would be favored at high $\phi_{int} = 0.6$ found in antibody nanocluster. (extended from Shen et al. 5)	88

Figure 3.5: Protein-protein, protein-cluster and cluster-cluster hierarchical interactions in nanocluster dispersions. The potential of mean force includes specific short-ranged (ssr), depletion attraction (dep) and electrostatic (el) components: $V(r) = V_{ssr}(r) + V_{dep}(r) + V_{el}(r)$. **a.** Components of $V(r)$ for protein monomers at pI and 3 pH units away from pI. **b.** Predicted cluster diameter contours. The green triangle denotes the conditions of the injected dispersion into mice at $c = 235$ mg/ml for mAb 1B7 as given in Table B3. The diagonal pathway represents dilution of the dispersion (Fig. 3.2a). **c.** $V(r)$ for two 50 nm nanoclusters based on experimental zeta potential for polyclonal IgG (Appendix B.5). *Inset*, green arc depicts range of long-ranged repulsion at the edges of two clusters and red indicates short-ranged inter-cluster attraction.90

Figure 3.6: Pharmacokinetics of concentrated 1B7 dispersion and solution controls. Time course of serum antibody concentration normalized by dose after administration of intravenous solution, subcutaneous solution or subcutaneous dispersion. Serum samples were recovered from the tail vein and the mAb 1B7 concentration determined by activity from ELISA.90

Figure 4.1: Nanocluster morphology and formation pathways. a, Schematic of a protein (green) nanocluster with trehalose molecules (co-solute, blue) and counterions of the protein (red). b, Nanocluster formation by two pathways: dilution of lyophilized powder (LD) and concentration by filtration (C). Three nanocluster diameter contours (in nm) calculated by a free energy model (Appendix C.3) are shown. Additionally, the nanocluster diameter decreases to that of a protein monomer upon dilution in buffer (shown by diagonal pathway). c, SEM image of a nanocluster from a dispersion at $c = 270$ mg/ml and $c_E = 270$ mg/ml. 114

Figure 4.2: Nanocluster hydrodynamic diameters (D_c) for filtration concentration (C) and lyophilization dilution (LD) pathways. a, D_c of the nanoclusters for C pathway at 70 mg/ml trehalose for various final c values (C 70 pathway). b, Volume average D_c and the calculated diameter from the model (Appendix C.3) for the nanoclusters from panel a (C 70) and for dilution of the C 220:70 samples with buffer. c, D_c surface for the nanoclusters interpolated from the individual experimental points. d, D_c of the nanoclusters formed by dispersing lyophilized protein powder (LD 250:100) and after subsequent sequential dilutions with buffer to 230, 120 and 60 mg/ml IgG. A similar D_c was observed for the C 250:100 dispersion. e, D_c upon dilution of both LD and C dispersions with the calculated diameters from the model corresponding to the same protein:trehalose ratios. 116

Figure 4.3: Fraction of folded protein adapted from simulations of Shen et al. ⁴³ and schematic of LD and C pathways for nanocluster synthesis in the presence (blue curve) and absence (red curve) of crowder. Small red irreversible aggregates are shown at an intermediate ϕ without crowder (here $\phi = c/1400$, where ϕ is the volume fraction of protein which has a partial molar density of 1400 mg/ml) ⁷	117
Figure 5.1: Scattering profile for a dilute protein solution at 3 mg/ml in the original formulation buffer which was used as the form factor.	134
Figure 5.2: Monomer (P1, red dots) and cluster (P2, blue dashes) samples show a very different structure at the same concentration. b. Structure factor for low co-solute monomer sample from 5.2a. c. structure factor for high co-solute cluster sample in 5.2a.	136
Figure 5.3: SAXS profiles for protein dispersions at 250 mg/ml.....	137
Figure 6.1: a, b and c. Cryo-SEM micrographs of protein clusters with 250 mg/ml mAb1, 100 mg/ml proline and 50 mg/ml his.HCl. d. Histogram of particle sizes as measured by SEM.....	155
Figure 6.2: a, b, and c. Cryo-SEM micrographs of protein clusters with 250 mg/ml mAb1, 40 mg/ml trehalose and 50 mg/ml his and 17 mg/ml citric acid. d, e and f. Cryo-SEM micrographs of a replicate of the same cluster sample. g. Histogram of particle sizes as measured by SEM for images from a, b and c. h. Histogram of particle sizes as measured by SEM for images from d, e and f.....	157

Figure 6.3:	a, b, and c. Cryo-SEM micrographs of protein clusters with 125 mg/ml mAb1, 40 mg/ml trehalose and 50 mg/ml his and 17 mg/ml citric acid. d. Histogram of particle sizes as measured by SEM.....	157
Figure 6.4:	a, b, c and d. Cryo-SEM micrographs of protein monomer at 120 mg/ml in DI water.	158
Figure 6.5:	a and b. Cryo-SEM micrographs of buffer solution with 40 mg/ml tre, 50 mg/ml his and 17 mg/ml cit at pH 6	159
Figure 7.1:	Viscosity of mAb1 dispersions as a function of the protein concentration. a. The arg glu samples had 78.6 mg/ml arg and 71.4 mg/ml glu while the histidine buffer samples were in pH 5.5 histidine buffer at 20 mM. The lines are fits with the Ross-Minton equation in terms of both $[\eta]$ and k/v . b. D/D_0 from DLS. For both a and b, the open symbols show the data for samples prepared by dilution of the highest concentration samples.....	196
Figure 7.2:	Decrease in inherent viscosity of mAb1 dispersions as the concentration of arg + glu is increased from 75 to 150 mg/ml for the data in Tables 7.4 and 7.5 at pH 5.5. The line is a guide to the eye.....	197
Figure 7.3:	Viscosity of mAb1 dispersions as a function of pH at a constant arg and glu concentration of 150 mg/ml. The ratio of arg to glu was varied to change the pH.	198
Figure 7.4:	Inherent viscosity (red diamonds) and viscosity (blue circles) for mAb 1 dispersions with 150 mg/ml arg titrated with HCl from Table F5. Centrifugation speed was 10000 rcf. The viscosity goes through a maximum near the isoelectric point, pH 9.....	199

Figure 7.5: Effect of shear rate on viscosity of mAb1 dispersions at ~228 mg/ml with 20 mM histidine and 0.05% Tween 80 (red circles) and 269 mg/ml with 78.6 mg/ml arg and 71.4 mg/ml glu (green crosses).	200
Figure 8.1: Increasing concentration of arg+glu in α -CGN dispersions leads to improved dispersibility of α -CGN. α -CGN concentration in each case was targeted to be 250 mg/ml. Arg+glu concentrations are a. 0 mg/ml, b. 25 mg/ml, c. 50 mg/ml, d. 100 mg/ml, e. 150 mg/ml and f. 200 mg/ml. As can be seen the solutions with low arg+glu are turbid while those with higher arg+glu are clear.	227
Figure 8.2: Dispersion viscosities for samples from Table 8.1 showing very low inherent viscosities for α -CGN dispersions. The inherent viscosity (blue diamonds) is lowest around pH 8-8.5 while the D/D_0 ratio (red squares) is also minimum at around pH 9.	228
Figure 8.3: Inherent viscosity has a minimum at around pH 8-8.5 and an optimum for arg+glu conc of 100 mg/ml. Space that can be explored is limited by the solubility of the excipients.	229
Figure 8.4: Sterile filtration of the clusters by centrifugal filtration does not significantly affect the D/D_0	230
Figure 8.5: a. Reaction rate of diluted α -CGN dispersions compared to dilute solution controls along with that for protein activated with trypsin. b. SDS-PAGE gel under reducing conditions and c. SDS-PAGE gel under non-reducing conditions for analysis of aggregates and degradants for α -CGN dispersions compared to dilute solution controls along with that for protein activated with trypsin.	232

Figure 8.6: Electrostatic charge map of α -CGN shows distinct charged patches. The surface is drawn where the electrostatic repulsion is ± 1 kT with red being negative charge and blue being positive charge.....	232
Figure A1: Evolution of Au nanocluster UV-vis extinction with time at 0.018 mM Au precursor and pH 8.7, with the reaction quenched by mercaptoacetic acid at each time point.	248
Figure A2: Time evolution of cluster morphology by TEM at 0.018 mM Au precursor and pH 8.7, with the reaction quenched by mercapto acetic acid at: a, 15 s. b, 30 s. c, not quenched.....	249
Figure A3: Additional STEM (a and b) TEM images (c and d) of particles synthesized at pH 8.7 at an Au precursor concentration of 0.018 mM.....	249
Figure A4: Low resolution TEM of nanoclusters synthesized with dextran as the stabilizing polymer with 0.018 mM Au precursor at a, pH = 9.3. b, pH = 8.7. c, pH = 7.5. Scale bar is 50 nm in all cases.	250
Figure A5: TGA of gold nanoclusters synthesized at 0.018 mM Au ³⁺ and a dextran coating at pH 8.7.....	250
Figure A6: Properties of nanocluster dispersions after 2 iterations of Au at pH = 9.3 (dotted line), pH = 8.7 (dashed line) and pH = 7.5 (solid line) characterized by a. Hydrodynamic diameter by DLS and b. UV- vis spectra. c. Example TEM and SEM images of particles synthesized at pH = 8.7.	251

Figure B1: SEM images of antibody nanoclusters with trehalose as co-solute. a, b, c and d, Reproducibility of multiple SEM images of 1B7 antibody nanoclusters at $c = c_E = 220\text{mg/ml}$ (identical conditions as in Fig. 3.1c). The SEM micrographs clearly show good reproducibility in the size of the $\sim 300\text{ nm}$ clusters in the dispersion for four clusters, consistent with the DLS results in Fig. 3.2a. The images were obtained from regular carbon film copper TEM grids where the nanoclusters were resting on the copper mesh. The individual protein monomers, on the order of 10 nm , appear to have a halo around them. This halo is a layer of trehalose deposited during freezing and lyophilization in sample preparation for SEM. e, Polyclonal IgG nanocluster at $c = c_E = 260\text{ mg/ml}$. The imaging was done on a lacey carbon TEM grid and the nanocluster is resting on a strand of lacey carbon.263

Figure B2: Static light scattering to determine fractal dimension. The 80 nm sheep IgG nanoclusters were formed at $c = 70\text{ mg/ml}$ IgG and $c_E = 270\text{ mg/ml}$ trehalose. The intensity which scales as the measured count rate was plotted versus the scattering vector $4\pi\sin(\theta/2)/\lambda$ at various angles from 45° to 90° . The slope of the line fit through the data multiplied by -1 , i.e., 2.6 is the fractal dimension.²⁰ In static light scattering, we assume that the structure factor is not a function of the scattering vector and therefore, the intensity is related to the scattering vector through the fractal dimension.....264

- Figure B3: Hydrodynamic diameter by DLS of polyclonal IgG nanoclusters upon dilution in buffer ($c/c_E = 1$). The protein concentrations are shown in the legend. Sequential dilution with phosphate buffer at constant c/c_E yields progressively smaller nanoclusters until monomeric protein with a hydrodynamic diameter of ~ 10 nm is observed at $c = c_E = 47$ mg/ml. The behavior and mechanism for nanocluster dissociation is similar as observed for monoclonal antibody 1B7 in Fig. 3.2a and b.265
- Figure B4: Polyclonal IgG nanocluster size at high concentration. Polyclonal sheep IgG dispersions were formulated with 300 and 350 mg/ml protein with $c/c_E = 1:0.5$ with trehalose and the resulting nanocluster hydrodynamic diameter measured by DLS.266
- Figure B5: HPLC SEC of monomer concentration after dilution of the dispersion. All samples were diluted to 1 mg/ml in PBS and analyzed with Waters Breeze HPLC with TOSOH Biosciences TSK gel G2000SW and G3000SW_{XL} columns. The mobile phase comprised 100 mM sodium phosphate and 300 mM sodium chloride buffer (pH 7.0), and the eluate was monitored by absorbance at 214 nm. a. Chromatographs are shown for (1) solution control 1B7, (2) lyophilized, reconstituted 1B7, and dispersion formulated with (3) 260 mg/ml 1B7 and 260 mg/ml trehalose. No increase was seen in aggregate concentration throughout formation of the dispersion, dilution of the clusters, and reformation of the clusters with trehalose. b. The % monomer values are given here for a wide range of indicated experiments, shown in Fig. 3.2a and 3.2b. Error indicated is \pm s. d.267

Figure B6: Absence of higher molecular weight aggregates as assessed by non-reducing SDS-PAGE. All dispersions were diluted to 1 mg/ml with PBS prior to analysis. 5 μ g of each sample was combined with non-reducing loading buffer and loaded on to a precast 4–20% SDS-PAGE gel (Bio Rad). Lane (1) molecular weight markers (Spectra BR); (2) solution control 1B7; (3) & (4) 1B7 post-lyophilization; (5) molecular weight markers (Spectra BR); (6) & (7) diluted 260 mg/ml 1B7 dispersion; (8) & (9) 260 mg/ml dispersion diluted to 75 mg/ml that was further diluted. None of the samples showed any change in molecular weight, or formation of any higher molecular weight aggregates.268

Figure B7: Viscosity calibration curve for measurements with small conical vials. The calibration curve was created using the following solution standards: DI water ($\eta_0 = 1$ cP), benzyl benzoate ($\eta_0 = 8.8$ cP), PEG200 ($\eta_0 = 50$ cP), PEG300 ($\eta_0 = 70$ cP), and PEG400 ($\eta_0 = 90$ cP). The time for the liquid level to be drawn from 0.4” to 0.1” in small conical vial (0.1 mL V-Vial, Wheaton) was measured from a video of the solution (taken with a Kodak EasyShare Z812 IS), converted using ImageJ software to a stack of images with 30 images per second. The time was measured to within 0.05 seconds at least 3 times and averaged, while maintaining the end of the plunger at the 1 ml mark. A maximum volume of 10% of the cavity in the syringe was filled with dispersion to minimize variation in the pressure drop.....269

Figure C1:	Potential of mean force between two protein monomers at the pI with trehalose concentration 70 mg/ml. V_{dep} is the force due to the depletion attraction from trehalose and V_{el} is the electrostatic repulsion. ⁵	293
Figure C2:	Turbidity of nanocluster dispersion (C 220:70) which appears transparent to the naked eye for a path length of 1 cm.	294
Figure C3:	Additional STEM (a and b) and SEM (c) images of protein nanoclusters at $c = 270$ mg/ml and $c_E = 270$ mg/ml.	295
Figure C4:	D_c of C 220:70 nanoclusters and after subsequent sequential dilutions with buffer. The legend gives the protein concentration with mean D_c s listed in Table C1 and Figs. 4.2b and 4.2e.	296
Figure C5:	D_c of C 320:70 nanoclusters at an ultra-high protein concentration. The D_c distributions for two different samples are provided with the mean D_c listed in Table 4.1.	297
Figure C6:	D_c of C 250:250 nanoclusters and after subsequent sequential dilutions with buffer. The legend gives the protein concentration with mean D_c s listed in Table C3 and Fig. 4.2e.	298
Figure C7:	D_c of C 250:100 nanoclusters upon storage of the aqueous dispersion at 23° C for up to 10 days. The mean D_c s are listed in Table C4.	299
Figure C8:	ELISA data for diluted protein samples. The raw data used for calculating the relative EC50 is shown along with the negative controls.	300
Figure C9:	D_c s of C 220:70 nanoclusters before freezing, and after either 1 or 2.5 months of frozen storage at -40°C followed by thawing. The mean D_c s are listed in Table C8.	301

Figure C10: D_c of C 220:70 nanoclusters before and after sterile filtration through a 0.22 μm filter. The mean D_c s are listed in Table C9.	302
Figure C11: Fits for the ACFs of a. cluster, b. cluster with monomer size, c. In all cases y-axis is the relaxation time in microseconds and the x-axis is the correlation function value.	302
Figure C12: Fits for the ACFs with monomer relaxation time and different second diameters. In all cases Y axis is the relaxation time in microseconds and the x-axis is the correlation function value.	303
Figure D1: Intensity profile plots for the samples in the current study that were run on the rotating anode instead of the synchrotron.	305
Figure D2: a. ACF for monomer sample from Fig. 5.1. b. ACF for cluster sample from Fig. 5.1.	306
Figure D3: a. ACF for P3, b. ACF for P4 and c. ACF for P5.	306
Figure D4: Structure factors of 250 mg/ml cluster samples from Fig. 2. a. P3, b. P4, c. P6.	307
Figure E1: Sized images and histograms for particle sizes from each individual image from Fig. 6.1a-c. a and d are Fig. 6.1a, b and e are Fig. 6.1b and c and f are Fig. 6.1c.	309
Figure E2: Sized images and histograms for particle sizes from each individual image from Fig. 6.2a-c. a and d are Fig. 6.2a, b and e are Fig. 6.2b and c and f are Fig. 6.2c.	310
Figure E3: Sized images and histograms for particle sizes from each individual image from Fig. 6.2d-f. a and d are Fig. 6.2d, b and e are Fig. 6.2e and c and f are Fig. 6.2f.	311

Figure E4:	Sized images and histograms for particle sizes from each individual image from Fig. 6.3a-c. a and d are Fig. 6.3a, b and e are Fig. 6.3b and c and f are Fig. 6.3c.	312
Figure E5:	a. ACF for DLS data from Fig. 6.1. b. ACF for DLS data from Fig. 6.2. c. ACF for DLS data from Fig. 6.3 d. ACF for DLS data from Fig. 6.4.	313
Figure F1:	Turbidity divided by concentration for the mAb1 dispersions from Table 7.6 with each pair of rows labelled in order as 1-4.	339
Figure F2:	Diffusion coefficient versus concentration data for calculating k_d for a. 30 mM his pH 5.5 and b. 78.6 mg/ml arg and 71.4 mg/ml glu.	341
Figure F3:	a. Sample SEC trace for the protein pre-processing to show the control data before cluster formation. b. Sample SEC trace for a dispersion that was ~250 mg/ml with 81.4 mg/ml arg and 68.6 mg/ml glu diluted to 1 mg/ml showing very little aggregation.	342
Figure F4:	Calibration of vial volume versus height of liquid in vial for two different vials.	343
Figure F5:	Calibration for viscosity versus flow rate based on water, N10 and N35 standards.	344

Chapter 1: Introduction

1.1 ORIGIN OF HIGH VISCOSITIES AND INSTABILITY IN PROTEIN FORMULATIONS

Proteins are the building blocks of all living things and carry out a variety of regulatory, sensory and transport functions in the body. Antibodies are a specific type of protein produced by the immune system to identify and neutralize foreign objects introduced into the body.^{1,2} Antibodies are all immunoglobulins and are roughly Y-shaped consisting of two heavy chains and two light chains each of which have a constant region and a variable region. The constant region for all antibodies for each species of organism is the same with the variable region being different for each specific antibody as it is the part of the antibody that is target specific. The variable region of the antibody contains three peptides that are called complementarity determining regions (CDRs) which are responsible for the actual binding of antibodies to their target. These parts of mAbs therefore have amino acids sequenced in a way that they have a characteristic shape and are composed of very specifically located charged and hydrophobic amino acid residues so that they complement the charges and hydrophobic regions on the target to enable binding. Therefore antibodies usually bind almost exclusively to their target which is called the antigen therefore do not affect anything except for that antigen. As a result, monoclonal antibodies (mAbs) which are antibodies produced by cell lines that consist solely of clones of a unique parent cell are greatly desired as therapeutics since they are a proverbial “magic bullet”. mAbs can be produced to target almost any entity within reason and consequently there are mAb therapeutics either currently under development or already approved by regulatory agencies in the United States or the European Union for the treatment of a very large number of diseases and disorders including rheumatoid

arthritis, Crohn's disease, asthma (from allergies), macular degeneration and many different types of cancer.³

Currently monoclonal antibodies are administered through an intravenous drip requiring medical supervision which can be time consuming and inconvenient for patients.⁴ Development of a self-administration method would be of great convenience to patients and medical professionals thus encouraging efforts into developing formulations for subcutaneous self-injection by patients. Typical dosages for monoclonal antibodies range from 50-1000 mg depending on the therapeutic in question and the body weight of the patient.^{5,6} Since intravenous drips can have a fairly large dosage volume, they allow for the use of low concentration (typically <10 mg/ml) mAb solutions which are easier to formulate. However, subcutaneous injection volume is limited to a few milliliters requiring high concentration formulations of mAbs (> 150 mg/ml) in order to maintain the required dosage. Conventional protein formulations typically contain mAbs dissolved in 20-30 mM histidine/histidine.HCl buffer at pH 5-6 with 0.05-0.1% by weight surfactant (e.g. Polysorbate 80) and sometimes a co-solute at low concentration which is usually a saccharide of some type. The buffer serves to maintain the pH while the surfactant is added to adsorb at air-water interfaces making them inaccessible to proteins since proteins tend to aggregate at these interfaces. Finally, the co-solute is sometimes present as a leftover from the lyophilization buffer or is added as a protein stabilizer for frozen solutions. At these high concentrations, mAbs have a high viscosity exceeding 20 cP at 150 mg/ml which rises even higher at more elevated concentrations.^{4,7,8} In addition to the elevated viscosity, mAbs at high concentration tend to undergo irreversible aggregation,⁹⁻¹² gelation and precipitation.^{4,13-15} The specific short ranged interactions between mAbs are responsible for these undesirable phenomena. mAbs have

hydrophobic patches on their surface formed through proximity of hydrophobic amino acid side chains which prefer to not be exposed to the aqueous environment and attract each other as a consequence.¹⁶⁻²¹ There are also cases where the FAb (functional antibody region or antibody binding region) regions of a mAb have specific interactions with each other leading to a strong attraction between them.^{22,23} The CDR regions contained in the FAb in particular are responsible for the aforementioned attraction since they are designed to bind to the same site and so have very similar structures. The interactions can be especially robust in the case of hydrophobic CDRs since they will interact very strongly with each other.²³ Charged CDRs, however, will tend to repel each other since they all have the same charge although there is a correlation between negatively charged CDRs and increased viscosity observed previously for mAbs.²⁴ Additionally, there are charged patches on other regions of mAbs apart from the CDRs due to amino acid residues. When the oppositely charged patches are aligned with each other, they can attract each other leading to intermolecular attraction between proteins although according to simulation studies, they have limited contribution to the repulsive interactions.²⁵⁻²⁹ The simulation study used spherical particles which have charged patches with variable sizes and charge magnitudes and is a fairly sophisticated model system for proteins in comparison to the hard sphere models that are used more commonly although it does not account for the complexity in protein shape.²⁵ The net charge on proteins provides for repulsion between them although the magnitude of the repulsion is a function of the pH since protein charge depends on the formulation pH.³⁰ Therefore proteins are formulated at a pH far from their isoelectric point where they have a high net charge in order to maximize the electrostatic repulsion for increased stability.⁴

To examine the effect of interactions on viscosity, a series of mAbs, with different sequences and consequently dissimilar interactions, were studied and it was seen that the viscosity was correlated with the diffusion interaction coefficient (k_d) and the osmotic second virial coefficient (B_2). As the interactions became more attractive as evidenced by more negative values of either parameter, the viscosity was seen to increase almost monotonically with the values of these parameters. Therefore, if the correlation applies to all proteins, it may be possible to reduce the viscosity of protein formulations by modifying the interactions between proteins and making them less attractive. Based on this hypothesis, several techniques have been established for reducing protein-protein interactions consequently lowering the viscosity.

1.2 REDUCTION OF PROTEIN FORMULATION VISCOSITY BY MODIFYING INTERACTIONS AND STRUCTURE

The simplest method for reducing protein-protein interactions is through modification of the protein sequence to change the location, charge and degree of hydrophobicity of patches on the protein surface.^{23,29,31-33} An easy to understand example is to increase the number of charged residues on the surface of mAbs to increase their stability through increased repulsion.³³ The sequence modification can be optimized for reducing the viscosity although the application of this technique may be limited by some detrimental effects such as reduced mAb efficacy or also decreased affinity for cellular receptors.² Since the origin of many of the aforementioned interactions is electrostatic, the screening of electrostatic interactions has the potential to reduce these interactions. Salts have been added to protein formulations to lower the viscosity through reduction of the Debye length and as a result the electrostatic interactions.^{7,17} It was observed that

chaotropic salts were more effective at reducing the viscosity than kosmotropic salts probably as a result of being more disruptive to the hydration structure at the surface of the protein which would have a greater effect on the interactions. Salts are generally not capable of affecting the hydrophobic interactions since they are generally very hydrophilic. However, a study of salts consisting of large hydrophobic organic ions showed that they can reduce the hydrophobic interactions through binding on protein patches resulting in a reduced viscosity although the effect of the salts on the protein stability remains to be studied.¹⁷

An radically different approach for reducing the viscosity of protein formulations is by making micron-sized insoluble particles of proteins. The aqueous solvent media of proteins is modified through the addition of organic co-solutes which serve to maintain these micron-sized particles of protein by preventing protein dissolution due to depressed protein solubility. The particles are hypothesized to be non-interacting except for weak van der Waals interaction.^{34,35} The internal structure of the protein particles formed may be amorphous³⁴ or even somewhat crystalline³⁵ depending on the method of sample preparation with salting out or precipitation of protein allowing for the formation of crystalline domains. The weak interactions lead to a drop in viscosity of the formulation containing micron sized particles when compared to a conventional solution at an equivalent concentration. This approach of using non-aqueous solvents to disperse micron sized protein particles was taken to the extreme by dispersing protein particles into neat ethanol.³⁶ Although the particles were observed to dissociate to monomeric protein upon dilution in some cases, the effects of the highly non-aqueous solvents *in vivo* remains to be explored and it may be preferable to entirely avoid the organic solvents.³⁴ Therefore all the approaches currently available for reducing the viscosity of

protein formulations at high concentrations have their limitations and are all also very protein specific thus limiting their applicability.

1.3 PROTEIN CLUSTER FORMATION AND CHARACTERIZATION

The aforementioned addition of salt to protein has an interesting side effect in the case of lysozyme where the addition of a high concentration of salt causes lysozyme to form small protein clusters containing up to 20 proteins per cluster.³⁷⁻⁴¹ The evidence for the previous claim is that the small angle neutron scattering (SANS) or small angle x-ray scattering (SAXS) profiles for lysozyme solutions show a secondary peak in the structure factor at a size larger than the monomer. However, these lysozyme clusters may be very short lived and the data interpretation for establishing their presence is under debate.^{42,43} Large long-lived clusters (200 nm in diameter) have been observed in lysozyme solutions at 200 mg/ml by means of dynamic light scattering (DLS) and also by Brownian microscopy (BM) where the motion of particles in the sample is observed in situ by looking at the light scattered by these entities through a microscope to locate them and then using their motion to determine diffusion rates.⁴⁴⁻⁴⁷ Both the techniques use the Stokes-Einstein model to determine size from diffusion coefficients in a concentrated solution where its applicability is questionable but they still yield a similar particle size of around 200 nm. BM is not capable of seeing protein monomers since they are too small to scatter the laser light at a high enough intensity. However based on the DLS measurements which can detect both monomer and clusters, the fraction of protein in the sample which is contained in the nanoclusters was estimated to be on the order of 10^{-6} .⁴⁴⁻⁴⁷ The very low fraction of clusters in this case and the extremely short lifetimes in the

case of the smaller lysozyme clusters mentioned earlier means that they probably do not affect the macroscopic properties of the protein formulations in a significant manner.

In contrast to the clusters in lysozyme formulations, clusters or oligomers which were observed in mAb formulations did have an impact on the macroscopic properties of the formulation.^{29,48} The viscosity of the mAb formulations increased as the size of the oligomers formed in the system became larger.⁴⁹ The oligomers were formed due to specific protein-protein interactions between mAbs where the size of the oligomer increased in direct proportion with the salt concentration used for screening the electrostatic interactions between mAbs.⁴⁹ The size of the oligomers was determined by SAXS at low mAb concentrations below 10 mg/ml while at higher concentration, static light scattering (SLS) data was fit with a model for hard sphere oligomers to indirectly arrive at the oligomer size.⁴⁹ Alternatively, neutron spin echo (NSE) measurements were conducted for the oligomers at higher protein concentrations which suggested that the size of the oligomers plateaued and did not increase above mAb concentrations of 10 mg/ml in a phenomenon similar to critical micellization behavior.⁴⁸ All mAb added above a concentration of 10 mg/ml was theorized to be contained in the oligomeric state yielding a high fraction of protein in the oligomeric state. In this case, contrary to the observations by Lilyestrom et al., the addition of salt seemed to disrupt the formation of these oligomers favoring monomeric protein.⁴⁸ Therefore the characterization of the protein oligomers is very difficult especially at high concentrations where many conventional size measurement techniques are difficult to interpret and in some cases even carry out.

To study cluster assembly with a system that is easier to quantify, the author considered the formation of gold nanoclusters through reduction of Au^{3+} . In addition to

being an excellent model system, gold nanoparticles with controlled optical and surface properties are of great interest in biomedical imaging and therapy,^{50,51} catalysis,⁵² energy,^{53,54} and plasmonic sensing.^{55,56} For biomedical imaging and therapy, the surface plasmon resonance (SPR) of Au nanoparticles needs to be tuned to be in the near infrared (NIR) region (800-1100 nm) where water, soft tissues, and blood absorb minimally.⁵⁷ Furthermore, nanoparticles of a size smaller than ~ 60 nm are of great interest for achieving desired blood residence times and cellular uptake through accumulation of nanoparticles in targeted sites including cancerous tumors and atherosclerotic plaques.⁵⁸⁻⁶³ For Au nanospheres in water, the SPR peak is at 520 nm.⁶⁴ Upon introducing asymmetry in the morphology, hybridization between dipoles and higher-order multipoles red shifts the SPR to the NIR region for various shapes of monolithic particles including Au nanorods,⁶⁵⁻⁶⁹ nanoshells,^{50,70-72} nanocages,⁷³ and nanostars (as well as related geometries, for example nanoflowers and nanourchins).⁷⁴⁻⁹⁰

In addition to studies of monolithic particles, recent efforts are underway to study shifts in the SPR from self-assembling nanoclusters composed of very closely spaced primary Au nanoparticles with either random⁹¹⁻⁹³ or controlled⁹⁴⁻⁹⁷ spacing between them. In some cases, the Au nanocluster size may be controlled by balancing long-ranged repulsion and short-ranged attraction. For example spherical 5 nm Au particles were self-assembled into reversible (biodegradable) nanoclusters with sizes ranging from 30 to 100 nm by tuning colloidal interactions to achieve strong NIR extinction even at 1024 nm.⁹¹⁻⁹³ These nanoclusters have been demonstrated to be biodegradeable and dissociate to 5 nm primary particles which can then be eliminated through the kidneys in the urine.^{91-93,98} Similarly, chains of Au particles were also formed by linking particles using a polymerase chain reaction resulting in a shift in the absorbance to the NIR.⁹⁶ Clusters

have also been formed from ~100 nm long Au nanorods⁹⁹ or ~100 nm long nanodumbbells¹⁰⁰ which shift the SPR peak to the NIR even as far as 1500 nm. Therefore, assembling Au nanoparticles into nanoclusters is an area of great interest for biomedical applications. Also the characterization of Au these nanoclusters is relatively easy when compared to that of protein oligomers with a wide range of techniques available including DLS, SAXS, transmission electron microscopy (TEM) and scanning electron microscopy (SEM). The size of Au nanoclusters is also maintained upon dilution unlike protein clusters whose properties are a function of concentration. This contributes to the comparatively facile characterization of the Au nanoclusters in contrast to protein oligomers since all the experimental techniques are easier to run and interpret at dilute conditions.

1.4 OBJECTIVES

mAb formulations for subcutaneous injection require a low viscosity at mAb concentrations greater than 200 mg/ml in order to allow for ease of processing and also to reduce the pain upon injection. mAbs also need to remain stable and active upon dilution to ensure the efficacy of the delivered therapeutic. Additionally the formation of oligomers or nanostructures in high concentration protein formulations is a matter of great interest because if these structures are not reversible, they could have a deleterious effect. The goals of this dissertation are: (1) to reduce the viscosity of protein formulations relative to those attainable by currently established technology, (2) to study the formation of nanostructures in high concentration mAb formulations by multiple complementary techniques and develop a model for describing the same (3) design Au

nanoclusters as a model system for nanostructure formation. High concentrations of a mixture of arginine and glutamic acid will be added to the mAb1 formulations for modifying the interactions between mAbs and reducing the viscosity. Trehalose at a high concentration will be added to formulations of a polyclonal sheep IgG mixture, bovine serum albumin (BSA) and mAb 1B7 leading to the formation of some nanostructures also seen in the high co-solute formulations of mAb1. These nanostructures present in the system with high co-solute concentrations will be studied by means of DLS, cryogenic scanning electron microscopy (cryo-SEM) and SAXS. Additionally the use of high co-solute concentrations will be shown to solubilize a protein (α -Chymotrypsinogen, α -CGN) which is normally insoluble at high concentration. Moreover, the retention of monomeric protein upon dilution in buffer will be demonstrated with the protein activity maintained constant. Nanoclusters will also be synthesized with Au as a model system with further growth on them to generate more asymmetric structures with a very high NIR extinction while maintaining the particle size below 60 nm for enabling a wide range of applications.

For the first goal of this dissertation, the viscosity of mAb formulations at > 200 mg/ml was reduced by about 5-6 times compared to conventional protein formulations by the addition of high concentrations of co-solutes e.g. arginine, glutamic acid and histidine although the focus will mainly be on mixtures of arginine and glutamic acid. Arginine and glutamic acid bind to proteins to reduce both the hydrophobic and electrostatic attraction between proteins which will have the effect of lowering the viscosity. The viscosity will also be studied as a function of the concentration of arginine and glutamic acid. The ratio of arginine to glutamic acid will also be varied affecting the formulation pH the impact of which on the viscosity will be studied. The importance of the interacting

co-solutes will also be examined by analyzing the protein formulations containing a non-interacting co-solute, namely trehalose, on the formulation properties. The protein specificity of the effect of co-solutes on the formulation properties will also be examined by studying 3 different proteins under similar conditions (mAb1, mAb 1B7 and a polyclonal sheep IgG mixture).

For the second goal of the dissertation, the high concentration formulations will be probed by a multitude of techniques to determine the size of entities present in the system. The diffusion coefficient as measured by DLS in the high co-solute samples is significantly lower than that for protein monomer while that for the low co-solute samples is close to the monomer value even at protein concentrations up to 230 mg/ml. The lowering of the diffusion coefficient will be theorized to be through the formation of nanoclusters. A free energy model accounting for the fractal nature of the nanoclusters will be developed to attempt to qualitatively describe the trends in measured size of nanoclusters as determined by DLS. The model will attempt to predict the nanocluster size as a function of the concentration of both protein and co-solute. The co-solute may cause assembly of these structures by giving rise to strong short-ranged depletion attraction which drives the proteins together into nanoclusters with the cumulative long-ranged electrostatic repulsion between proteins in the nanoclusters limiting the nanocluster size. The assembly therefore may be different from the assembly of the previously mentioned protein oligomers which is through specific protein interactions. Also, the extremely concentrated environment within the nanoclusters (~700 mg/ml) may provide conformational stability to proteins in the dispersion enabling dissociation to stable monomeric protein upon dilution.^{101,102} The nanostructures in similar protein formulations with trehalose, histidine and citric acid as co-solutes will be studied by

orthogonal sizing techniques, namely SAXS and cryo-SEM in addition to DLS. SAXS will be used to test for the presence of larger entities in protein formulations at 125 mg/ml mAb containing high co-solute concentrations and compare them to low co-solute formulations. Cryo-SEM will be used to visualize both the low and high co-solute formulations at high protein concentrations of 250 mg/ml. The formulations will be tested for the dissociation of any potential nanostructures upon dilution and also for retention of the activity of the protein by size exclusion chromatography (SEC), thermal melting temperature (T_m), circular dichroism (CD) and enzyme linked immunosorbent assay (ELISA).

Finally, for the third goal of this dissertation, we will synthesize ~ 60 nm Au nanoparticles exhibiting intense and broad NIR extinction from 700 to 1100 nm by reduction of HAuCl_4 with hydroxylamine in the presence of either carboxymethyl dextran (CMD) or dextran. Small nanocluster cores will initially be formed by self-assembly of closely-spaced small primary particles and then further decorated with a large number of short points. The large number of reactive sites on the ensemble of high surface area primary particles within the nanoclusters will be shown to offer the opportunity to generate a high density of points per nanocluster under kinetic control of growth at low pH values (8.7 and 7.5). For this we will adapt concepts of kinetic versus thermodynamic control of growth from monolithic particles^{73,103,104} to growth of points on self-assembled nanoclusters. At higher pH values, slower precursor reduction will be shown to result in thermodynamically controlled growth to form symmetric spherical particles with low surface energy.

1.5 DISSERTATION OUTLINE

This dissertation first introduces the concept of modifying protein-protein interactions and formation of larger nanostructures to reduce viscosity of mAbs. In Chapter 2, gold nanoparticles with a diameter of about 60 nm and a strong extinction in the NIR region at wavelengths ranging from 700 nm to 1100 nm are described. 10 nm primary Au particles come together to form ~ 30 nm Au nanoclusters. A high surface density of points is then grown on these 30 nm nanocluster cores by allowing rapid kinetically controlled growth of Au. The high NIR extinction is produced by the close proximity of the primary particles in the cores, the high surface density of points, and the high aspect ratio of the size of the points to the size of the primary particles. When the Au precursor was reduced slowly at a higher pH of 9.3, the growth was thermodynamically controlled and the nanocluster cores relaxed to spheres. In comparison to these nanocluster cores, much longer points are required for particles with spherical cores to obtain the same high NIR extinction, resulting in much larger particles being formed.

In Chapter 3, highly concentrated dispersions (up to 260 mg/ml) of monoclonal antibody (mAb) 1B7, polyclonal sheep Immunoglobulin G (IgG) and bovine serum albumin (BSA) were created having low viscosity and significantly slowed diffusion compared to the protein monomer. The slowed diffusion was speculated to be due to the formation of nanoclusters although the fraction of protein contained in the nanoclusters is unknown. Appendix B.1 describes the assumptions involved in DLS, possible limitations in the data analysis and alternate explanations for the observed trends in it. The extremely concentrated environment within the nanoclusters (~700 mg/ml) is theorized to provide conformational stability to proteins through a novel self-crowding mechanism, as shown by computer simulation. Trehalose was added as a co-solute to strengthen the short-

ranged attraction between proteins by generating depletion attraction. A semi-quantitative free energy model which includes the fractal dimension of the clusters was developed to describe the assembly of the clusters with the balance of short ranged depletion attraction arising from trehalose and long ranged electrostatic repulsion. It was theorized that the increased separation between the clusters could lead to reduced interactions which can potentially lower the dispersion viscosity in comparison to protein monomer solutions. Upon dilution of these dispersions *in vitro*, fully active protein monomers were obtained as shown with biophysical analysis (SEC, DLS, CD and sodium dodecyl sulfate polyacrylamide gel electrophoresis (SDS-PAGE)) and sensitive biological assays (ELISA). *In vivo* subcutaneous injection into mice resulted in the same amount of therapeutic being delivered in the blood as that from a dilute antibody solution injected intravenously. The data in Chapter 3 was published in ACS Nano in 2012 with Dr. Keith Johnston as the first author. The author of this dissertation contributed heavily to this work both in terms of experimentation and writing particularly with regards to development of the theoretical model and the interpretation of the data.

High concentration protein formulations (up to 330 mg/ml) were formed by the centrifugal filtration technique in Chapter 4 expanding from the lyophilization dilution method described in Chapter 3. Concentration filtration allowed for more flexibility in the composition of the formulations than the lyophilization dilution approach. The diffusion coefficient measured by DLS was lower for all of the formulations studied independent of the method of formation of the dispersion. The lowered diffusion rate was interpreted as the result of the formation of protein nanoclusters and is described in Chapter 4 by means of the nanocluster size with an alternate possible explanation and method of data interpretation of the same described in Appendix C.1. Moreover, the

stability of proteins in these formulations upon storage is established by measuring the percentage of aggregated protein upon dilution which remains unchanged as determined by SEC. Chapter 4 was published in Soft Matter as a communication.

Chapters 5 and 6 bring in techniques other than DLS, namely, SAXS and cryo-SEM, for study of the entities responsible for the reduction in the diffusion rate of entities in the high excipient samples. DLS involves assumptions that may not be valid at the high concentrations of protein considered in this dissertation and so supplemental techniques are desired. SAXS shows evidence of larger ~50 nm entities in the high co-solute samples containing 125 mg/ml protein, which were not seen in the low co-solute samples in agreement with the trends in the diffusion coefficient evident from the DLS measurements. Since cryo-SEM preserves the sample as it is present in liquid state, the clusters present in the dispersion could be observed in situ. Cryo-SEM images also displayed ~ 60 nm entities in high co-solute formulations at 250 mg/ml protein in agreement with SAXS and DLS. SAXS and cryo-SEM are based on different principles from DLS and therefore provide support to the theory that larger entities are formed in the high co-solute samples although more work needs to be done on this matter beyond this dissertation.

Chapter 7 describes the influence of high concentrations of arginine and glutamic acid on the viscosity of protein dispersions. Specifically, the viscosity of a dispersion of mAb1 in buffer is reduced from ~160 cP at 230 mg/ml mAb1 to ~40 cP at 250 mg/ml mAb1 by adding mixtures of arginine and glutamic acid as co-solutes at total concentrations ranging from 75 to 150 mg/ml. Similar behavior was observed for polyclonal sheep IgG at a concentration of ~250 mg/ml. The mixture of arginine and glutamic acid interacts with proteins blocking sites on them and reducing both the local

electrostatic attraction and hydrophobic patch interactions which may be responsible for the high protein viscosity.^{20,23,105-110} The pH of the formulations was varied to affect the charge on both the co-solutes and mAbs in order to modify binding characteristics and affect charge distributions. The co-solute concentrations were also varied to modify the depletion attraction and co-solute binding and study the effects of the same on formulation properties. Diffusion coefficients for all the formulations were measured by DLS and compared with the calculated value for mAb monomers diffusing through the same solvent as the formulation under consideration and seen to be significantly lower for the high co-solute samples. The osmotic compression arising from depletion attraction may contribute to breaking certain domains in protein networks (sometimes termed as clusters), particularly in regions where the fractal dimensions are low. Additionally, mAbs were shown to return to the monomeric state upon dilution using size exclusion chromatography (SEC) even after storage for up to 8 weeks at room temperature, in a refrigerated state or in a frozen state.

In Chapter 8, the concept from Chapter 7 of using a mixture of arginine and glutamic acid as co-solutes is extended to solubilize α -CGN at protein concentrations above 200 mg/ml and form transparent dispersions. The solubilization of α -CGN seems to need a minimum total concentration of arginine and glutamic acid of 100 mg/ml as there may be a minimum number of sites that need to be blocked by co-solutes on proteins before solubilization. Also a formulation pH above 7 was needed to achieve the aforementioned protein solubilization. Below this apparent threshold concentration of co-solutes or below the threshold pH, the protein formulations at high concentration were seen to be turbid with large chunks of protein present in them. The presence of these interacting co-solutes also yields very low viscosities of protein formulations similar to

that of mAb1 although there is no easy comparison as α -CGN is otherwise insoluble at these high concentrations. The diffusion coefficient as measured by DLS is also seen to be depressed relative to that of the protein monomer in the case of α -CGN also for the high co-solute samples. Additionally the high concentrations of arginine and glutamic acid are seen to stabilize α -CGN as determined by melting temperature and enzymatic tests.

1.6 REFERENCES

- (1) Litman, G. W.; Rast, J. P.; Shambloott, M. J.; Haire, R. N.; Hulst, M.; Roess, W.; Litman, R. T.; Hinds-Frey, K. R.; Zilch, A.; Amemiya, C. T. *Mol Biol Evol* 1993, 10, 60.
- (2) Murphy, K. *Immunobiology*; 8th ed.; Garland Science: New York, 2012.
- (3) The antibody society: Waban, MA, 2014; Vol. 2014.
- (4) Shire, S. J.; Shahrokh, Z.; Liu, J. J. *Pharm. Sci.* 2004, 93, 1390.
- (5) Bristol-Myers Squibb Company: New York, 2014; Vol. 2014.
- (6) Genentech USA, Inc.: San Francisco, 2014; Vol. 2014.
- (7) Liu, J.; Nguyen, M. D. H.; Andya, J. D.; Shire, S. J. *J Pharm Sci* 2005, 94, 1928.
- (8) Allmendinger, A.; Fischer, S.; Huwyler, J.; Mahler, H. C.; Schwarb, E.; Zarraga, I. E.; Mueller, R. *Eur J Pharm Biopharm* 2014, 87, 318.
- (9) Scherer, T. M.; Liu, J.; Shire, S. J.; Minton, A. P. *J Phys Chem B* 2010, 114, 12948.
- (10) Fields, G. B.; Alonso, D. O. V.; Stigter, D.; Dill, K. A. *Journal of Physical Chemistry* 1992, 96, 3974.
- (11) Zhou, H. X.; Rivas, G.; Minton, A. P. *Annual Review of Biophysics* 2008, 37, 375.
- (12) Young, T. M.; Roberts, C. J. *J Chem Phys* 2009, 131, 125104.
- (13) Zaccarelli, E. *J Phys: Condens. Matter* 2007, 19, 323101.
- (14) Rosenbaum, D. F.; Zamora, P. C.; Zukoski, C. F. *Phys Rev Let* 1996, 76, 150.

- (15) ten Wolde, P. R.; Frenkel, D. *Science* 1997, 277, 1975.
- (16) Andrews, J. M.; Roberts, C. J. *Biochemistry* 2007, 46, 7558.
- (17) Du, W.; Klivanov, A. M. *Biotechnol Bioeng* 2011, 108, 632.
- (18) Lee, J. C.; Timasheff, S. N. *Journal of Biological Chemistry* 1981, 256, 7193.
- (19) Liu, W.; Cellmer, T.; Keerl, D.; Prausnitz, J. M.; Blanch, H. W. *Biotechnol Bioeng* 2005, 90, 482.
- (20) Holstein, M. A.; Parimal, S.; McCallum, S. A.; Cramer, S. M. *Biotechnol Bioeng* 2012, 109, 176.
- (21) Pathak, J. A.; Sologuren, R. R.; Narwal, R. *Biophys J* 2013, 104, 913.
- (22) Kanai, S.; Liu, J.; Patapoff, T. W.; Shire, S. J. *J Pharm Sci* 2008, 97, 4219.
- (23) Connolly, B. D.; Petry, C.; Yadav, S.; Demeule, B.; Ciaccio, N.; Moore, J. M.; Shire, S. J.; Gokarn, Y. R. *Biophys J* 2012, 103, 69.
- (24) Li, L.; Kumar, S.; Buck, P. M.; Burns, C.; Lavoie, J.; Singh, S. K.; Warne, N. W.; Nichols, P.; Luksha, N.; Boardman, D. *Pharm. Res.* 2014.
- (25) Roberts, C. J.; Blanco, M. A. *J Phys Chem B* 2014.
- (26) Yadav, S.; Liu, J.; Shire, S. J.; Kalonia, D. S. *J Pharm Sci* 2010, 99, 1152.
- (27) Yadav, S.; Shire, S. J.; Kalonia, D. S. *Pharm. Res.* 2011, 28, 1973.
- (28) Yadav, S.; Shire, S. J.; Kalonia, D. S. *J Pharm Sci* 2012, 101, 998.
- (29) Zarraga, I. E.; Taing, R.; Zarzar, J.; Luoma, J.; Hsiung, J.; Patel, A.; Lim, F. J. *J Pharm Sci* 2013, 102, 2538.
- (30) Chari, R.; Jerath, K.; Badkar, A. V.; Kalonia, D. S. *Pharm. Res.* 2009, 26, 2607.
- (31) Trevino, S. R.; Scholtz, J. M.; Pace, C. N. *J Pharm Sci* 2008, 97, 4155.
- (32) Perchiacca, J. M.; Bhattacharya, M.; Tessier, P. M. *Proteins* 2011, 79, 2637.
- (33) Miklos, A. E.; Kluwe, C.; Der, B. S.; Pai, S.; Sircar, A.; Hughes, R. A.; Berrondo, M.; Xu, J.; Codrea, V.; Buckley, P. E.; Calm, A. M.; Welsh, H. S.; Warner, C. R.; Zacharko, M. A.; Carney, J. P.; Gray, J. J.; Georgiou, G.; Kuhlman, B.; Ellington, A. D. *Chem Biol* 2012, 19, 449.
- (34) Miller, M. A.; Khan, T. A.; Kaczorowski, K. J.; Wilson, B. K.; Dinin, A. K.; Borwankar, A. U.; Rodrigues, M. A.; Truskett, T. M.; Johnston, K. P.; Maynard, J. A. *J Pharm Sci* 2012, 101, 3763.

- (35) Johnson, H. R.; Lenhoff, A. M. *Mol Pharm* 2013, 10, 3582.
- (36) Srinivasan, C.; Weight, A. K.; Bussemer, T.; Klibanov, A. M. *Pharm. Res.* 2013, 30, 1749.
- (37) Cardinaux, F.; Stradner, A.; Schurtenberger, P.; Sciortino, F.; Zaccarelli, E. *Europhysics Letters (EPL)* 2007, 77, 48004.
- (38) Cardinaux, F.; Zaccarelli, E.; Stradner, A.; Bucciarelli, S.; Farago, B.; Egelhaaf, S. U.; Sciortino, F.; Schurtenberger, P. *J Phys Chem B* 2011, 115, 7227.
- (39) Falus, P.; Porcar, L.; Fratini, E.; Chen, W. R.; Faraone, A.; Hong, K.; Baglioni, P.; Liu, Y. *J Phys Condens Matter* 2012, 24, 064114.
- (40) Kowalczyk, P.; Ciach, A.; Gauden, P. A.; Terzyk, A. P. *J Colloid Interface Sci* 2011, 363, 579.
- (41) Stradner, A.; Sedgwick, H.; Cardinaux, F.; Poon, W. C. K.; Egelhaaf, S. U.; Schurtenberger, P. *Nature* 2004, 432, 492.
- (42) Shukla, A.; Mylonas, E.; Di Cola, E.; Finet, S.; Timmins, P.; Narayanan, T.; Svergun, D. I. *Proc Natl Acad Sci U S A* 2008, 105, 5075.
- (43) Godfrin, P. D.; Valadez-Perez, N. E.; Castaneda-Priego, R.; Wagner, N. J.; Liu, Y. *Soft Matter* 2014, 10, 5061.
- (44) Li, Y.; Lubchenko, V.; Vekilov, P. G. *Rev Sci Instrum* 2011, 82, 053106.
- (45) Pan, W. C.; Vekilov, P. G.; Lubchenko, V. J. *Phys. Chem. B* 2010, 114, 7620.
- (46) Vekilov, P. G. *Ann N Y Acad Sci* 2009, 1161, 377.
- (47) Vekilov, P. G. *Soft Matter* 2010, 6, 5254.
- (48) Yearley, E. J.; Godfrin, P. D.; Perevozchikova, T.; Zhang, H.; Falus, P.; Porcar, L.; Nagao, M.; Curtis, J. E.; Gawande, P.; Taing, R.; Zarraga, I. E.; Wagner, N. J.; Liu, Y. *Biophys J* 2014, 106, 1763.
- (49) Lilyestrom, W. G.; Yadav, S.; Shire, S. J.; Scherer, T. M. *J Phys Chem B* 2013, 117, 6373.
- (50) Hirsch, L. R.; Stafford, R. J.; Bankson, J. A.; Sershen, S. R.; Rivera, B.; Price, R. E.; Hazle, J. D.; Halas, N. J.; West, J. L. *Proc. Nat. Acad. Sci.* 2003, 100, 13549.
- (51) Ma, L. L.; Feldman, M. D.; Tam, J. M.; Paranjape, A. S.; Cheruku, K. K.; Larson, T. A.; Tam, J. O.; Ingram, D. R.; Paramita, V.; Villard, J. W.; Jenkins, J. T.; Wang, T.; Clarke, G. D.; Asmis, R.; Sokolov, K.; Chandrasekar, B.; Milner, T. E.; Johnston, K. P. *Acs Nano* 2009, 3, 2686.
- (52) Zhang, J.; Sasaki, K.; Sutter, E.; Adzic, R. R. *Science* 2007, 315, 220.

- (53) Ferry, V. E.; Munday, J. N.; Atwater, H. A. *Adv. Mater.* 2010, 22, 4794.
- (54) Atwater, H. A.; Polman, A. *Nat. Mater.* 2010, 9, 865.
- (55) Anker, J. N.; Hall, W. P.; Lyandres, O.; Shah, N. C.; Zhao, J.; Van Duyne, R. P. *Nat. Mater.* 2008, 7, 442.
- (56) Stewart, M. E.; Anderton, C. R.; Thompson, L. B.; Maria, J.; Gray, S. K.; Rogers, J. A.; Nuzzo, R. G. *Chem. Rev.* 2008, 108, 494.
- (57) Weissleder, R. *Nat. Biotechnol.* 2001, 19, 316.
- (58) Kooi, M. E.; Cappendijk, V. C.; Cleutjens, K.; Kessels, A. G. H.; Kitslaar, P.; Borgers, M.; Frederik, P. M.; Daemen, M.; van Engelshoven, J. M. A. *Circulation* 2003, 107, 2453.
- (59) Ma, Y.; Li, N.; Yang, C.; Yang, X. R. *Analytical and Bioanalytical Chemistry* 2005, 382, 1044.
- (60) Arruebo, M.; Fernandez-Pacheco, R.; Ibarra, M. R.; Santamaria, J. *Nano Today* 2007, 2, 22.
- (61) Betancourt, T.; Brown, B.; Brannon-Peppas, L. *Nanomedicine* 2007, 2, 219.
- (62) Schipper, M. L.; Iyer, G.; Koh, A. L.; Cheng, Z.; Ebenstein, Y.; Aharoni, A.; Keren, S.; Bentolila, L. A.; Li, J. Q.; Rao, J. H.; Chen, X. Y.; Banin, U.; Wu, A. M.; Sinclair, R.; Weiss, S.; Gambhir, S. S. *Small* 2009, 5, 126.
- (63) Davis, M. E.; Chen, Z.; Shin, D. M. *Nat. Rev. Drug Discov.* 2008, 7, 771.
- (64) Daniel, M. C.; Astruc, D. *Chem. Rev.* 2004, 104, 293.
- (65) Huang, X.; El-Sayed, I. H.; Qian, W.; El-Sayed, M. A. *Journal of the American Chemical Society* 2006, 128, 2115.
- (66) Durr, N. J.; Larson, T.; Smith, D. K.; Korgel, B. A.; Sokolov, K.; Ben-Yakar, A. *Nano Letters* 2007, 7, 941.
- (67) Pissuwan, D.; Valenzuela, S. M.; Killingsworth, M. C.; Xu, X. D.; Cortie, M. B. *J. Nanopart. Res.* 2007, 9, 1109.
- (68) Qiu, L.; Larson, T. A.; Smith, D. K.; Vitkin, E.; Zhang, S. H.; Modell, M. D.; Itzkan, I.; Hanlon, E. B.; Korgel, B. A.; Sokolov, K. V.; Perelman, L. T. *Ieee Journal of Selected Topics in Quantum Electronics* 2007, 13, 1730.
- (69) Zhu, J.; Yong, K. T.; Roy, I.; Hu, R.; Ding, H.; Zhao, L. L.; Swihart, M. T.; He, G. S.; Cui, Y. P.; Prasad, P. N. *Nanotechnology* 2010, 21.
- (70) Adler, D. C.; Huang, S. W.; Huber, R.; Fujimoto, J. G. *Opt. Express* 2008, 16, 4376.

- (71) Loo, C.; Lowery, A.; Halas, N. J.; West, J.; Drezek, R. *Nano Letters* 2005, 5, 709.
- (72) Langille, M. R.; Personick, M. L.; Zhang, J.; Mirkin, C. A. *Journal of the American Chemical Society* 2011, 133, 10414.
- (73) Skrabalak, S. E.; Chen, J.; Au, L.; Lu, X.; Li, X.; Xia, Y. *Adv. Mater.* 2007, 19, 3177.
- (74) Barbosa, S.; Agrawal, A.; Rodriguez-Lorenzo, L.; Pastoriza-Santos, I.; Alvarez-Puebla, R. A.; Kornowski, A.; Weller, H.; Liz-Marzan, L. M. *Langmuir* 2010, 26, 14943.
- (75) Nehl, C. L.; Liao, H. W.; Hafner, J. H. *Nano Letters* 2006, 6, 683.
- (76) Senapati, D.; Singh, A. K.; Ray, P. C. *Chemical Physics Letters* 2010, 487, 88.
- (77) Mueller, M.; Tebbe, M.; Andreeva, D. V.; Karg, M.; Alvarez Puebla, R. A.; Pazos Perez, N.; Fery, A. *Langmuir* 2012, 28, 9168.
- (78) Grzelczak, M.; Liz-Marzán, L. M. *Langmuir* 2013, 29, 4652.
- (79) Casu, A.; Cabrini, E.; Donà, A.; Falqui, A.; Diaz-Fernandez, Y.; Milanese, C.; Taglietti, A.; Pallavicini, P. *Chemistry - A European Journal* 2012, 18, 9381.
- (80) Kedia, A.; Kumar, P. S. *Journal of Materials Chemistry C* 2013, 1, 4540.
- (81) Pallavicini, P.; Donà, A.; Casu, A.; Chirico, G.; Collini, M.; Dacarro, G.; Falqui, A.; Milanese, C.; Sironi, L.; Taglietti, A. *Chemical Communications* 2013, 49, 6265.
- (82) Su, Q.; Ma, X.; Dong, J.; Jiang, C.; Qian, W. *ACS Applied Materials & Interfaces* 2011, 3, 1873.
- (83) Wang, Z. D.; Zhang, J. Q.; Ekman, J. M.; Kenis, P. J. A.; Lu, Y. *Nano Letters* 2010, 10, 1886.
- (84) Nhung, T. T.; Bu, Y.; Lee, S.-W. *Journal of Crystal Growth* 2013, 373, 132.
- (85) Yi, S.; Sun, L.; Lenaghan, S. C.; Wang, Y.; Chong, X.; Zhang, Z.; Zhang, M. *RSC Advances* 2013, 3, 10139.
- (86) Lu, L. H.; Ai, K.; Ozaki, Y. *Langmuir* 2008, 24, 1058.
- (87) Yuan, H.; Ma, W.; Chen, C.; Zhao, J.; Liu, J.; Zhu, H.; Gao, X. *Chem. Mat.* 2007, 19, 1592.
- (88) Kuo, C. H.; Huang, M. H. *Langmuir* 2005, 21, 2012.
- (89) Zou, X. Q.; Ying, E. B.; Dong, S. J. *Nanotechnology* 2006, 17, 4758.

- (90) Van de Broek, B.; Frederix, F.; Bonroy, K.; Jans, H.; Jans, K.; Borghs, G.; Maes, G. *Nanotechnology* 2011, 22.
- (91) Tam, J. M.; Murthy, A. K.; Ingram, D. R.; Nguyen, R.; Sokolov, K. V.; Johnston, K. P. *Langmuir* 2010, 26, 8988.
- (92) Tam, J. M.; Tam, J. O.; Murthy, A.; Ingram, D. R.; Ma, L. L.; Travis, K.; Johnston, K. P.; Sokolov, K. V. *ACS Nano* 2010, 4, 2178.
- (93) Murthy, A. K.; Stover, R. J.; Borwankar, A. U.; Nie, G. D.; Gourisankar, S.; Truskett, T. M.; Sokolov, K. V.; Johnston, K. P. *ACS Nano* 2013, 7, 239.
- (94) Pazos-Perez, N.; Garcia de Abajo, F. J.; Fery, A.; Alvarez-Puebla, R. A. *Langmuir : the ACS journal of surfaces and colloids* 2012, 28, 8909.
- (95) Pazos-Perez, N.; Wagner, C. S.; Romo-Herrera, J. M.; Liz-Marzan, L. M.; Garcia de Abajo, F. J.; Wittemann, A.; Fery, A.; Alvarez-Puebla, R. A. *Angew Chem Int Ed Engl* 2012, 51, 12688.
- (96) Zhao, Y.; Xu, L.; Liz-Marzán, L. M.; Kuang, H.; Ma, W.; Asenjo-García, A.; García de Abajo, F. J.; Kotov, N. A.; Wang, L.; Xu, C. *The Journal of Physical Chemistry Letters* 2013, 4, 641.
- (97) Luk'yanchuk, B.; Zheludev, N. I.; Maier, S. A.; Halas, N. J.; Nordlander, P.; Giessen, H.; Chong, C. T. *Nat. Mater.* 2010, 9, 707.
- (98) Murthy, A. K.; Stover, R. J.; Hardin, W. G.; Schramm, R.; Nie, G. D.; Gourisankar, S.; Truskett, T. M.; Sokolov, K. V.; Johnston, K. P. *J Am Chem Soc* 2013, 135, 7799.
- (99) Grzelczak, M.; Mezzasalma, S. A.; Ni, W.; Herasimenka, Y.; Feruglio, L.; Montini, T.; Pérez-Juste, J.; Fornasiero, P.; Prato, M.; Liz-Marzán, L. M. *Langmuir* 2012, 28, 8826.
- (100) Grzelczak, M.; Sánchez-Iglesias, A.; Mezerji, H. H.; Bals, S.; Pérez-Juste, J.; Liz-Marzán, L. M. *Nano Letters* 2012, 12, 4380.
- (101) Cheung, J. K.; Truskett, T. M. *Biophys J* 2005, 89, 2372.
- (102) Shen, V. K.; Cheung, J. K.; Errington, J. R.; Truskett, T. M. *Biophys J* 2006, 90, 1949.
- (103) Langille, M. R.; Personick, M. L.; Zhang, J.; Mirkin, C. A. *Journal of the American Chemical Society* 2012, 134, 14542.
- (104) Langille, M. R.; Zhang, J.; Personick, M. L.; Li, S.; Mirkin, C. A. *Science* 2012, 337, 954.
- (105) Valente, J. J.; Verma, K. S.; Manning, M. C.; Wilson, W. W.; Henry, C. S. *Biophys J* 2005, 89, 4211.

- (106) Hou, Y.; Cramer, S. M. J Chromatogr A 2011, 1218, 7813.
- (107) Scherer, T. M. J Phys Chem B 2013, 117, 2254.
- (108) Shukla, D.; Trout, B. L. The Journal of Physical Chemistry B 2010, 114, 13426.
- (109) Shukla, D.; Trout, B. L. J Phys Chem B 2011, 115, 1243.
- (110) Saito, S.; Hasegawa, J.; Kobayashi, N.; Kishi, N.; Uchiyama, S.; Fukui, K. Pharm. Res. 2012, 29, 397.

Chapter 2: Gold Nanoparticles with High Densities of Small Points on Nanocluster Cores with Strong NIR Extinction

Plasmonic nanoparticles with sizes well below 100 nm and high near infrared (NIR) extinction are of great interest in biomedical imaging. Herein ~60 nm Au nanoparticles with high NIR absorbance at wavelengths ranging from 700 nm to 1100 nm at low pH values are synthesized under kinetic control. A high surface density of points is grown on ~30 nm nanocluster cores, which are composed of ~10 nm primary particles. The high NIR extinction is produced by the close proximity of the primary particles in the cores, the high surface density of points, and the high aspect ratio of the size of the points to the size of the primary particles. When the Au precursor was reduced more slowly at a higher pH of 9.3, the growth was thermodynamically controlled and the nanocluster cores relaxed to spheres. For particles with spherical cores, longer points are required to obtain the same NIR extinction, resulting in larger particles.

2.1 INTRODUCTION

Gold nanoparticles with controlled optical and surface properties are of great interest in biomedical imaging and therapy,^{1,2} catalysis,³ energy,^{4,5} and plasmonic sensing.^{6,7} For biomedical imaging and therapy, the surface plasmon resonance (SPR) of Au nanocrystals may be tuned to the near infrared (NIR) region (800-1100 nm) where water, soft tissues, and blood absorb minimally.⁸ Furthermore, nanoparticles smaller than ~ 60 nm are of great interest for achieving desired blood residence times and cellular uptake through accumulation of nanoparticles in targeted sites including cancerous tumors and atherosclerotic plaques.⁹⁻¹⁴ For Au nanospheres in water, the SPR peak is seen to be at 520 nm.¹⁵ Upon introducing asymmetry in the morphology, hybridization

between dipoles and higher-order multipoles red shifts the SPR to the NIR region for various shapes of monolithic particles including Au nanorods,¹⁶⁻²⁰ nanoshells,^{1,21-23} nanocages,²⁴ and nanostars (as well as related geometries like nanoflowers and nanourchins).²⁵⁻⁴¹ In the case of nanostars, the size and number of points on the cores influence the SPR. For the simpler geometry of a single point on a spherical core, the hybridization of the individual SPRs is well understood theoretically with the points leading to a red shift in the SPR.^{42,43} For nanostars, the extent of the red shift of the hybridized SPR into the NIR region increases with the length of the points (due to increased aspect ratio of point length/sphere diameter) and the number of points per surface area on the spherical cores.^{25,43,44} In addition to studies of monolithic particles, recent efforts are underway to determine shifts in the SPR of self-assembled nanoclusters composed of very closely spaced primary nanoparticles with either random⁴⁵⁻⁴⁷ or controlled⁴⁸⁻⁵¹ spacing between the particles. Insight into the effects of complex geometry and multi-body interactions on the SPR may be gained from model systems composed of a pair of closely spaced particles as a function of the interparticle spacing.^{51,52}

Design rules are being developed to control the shape of monolithic Au by balancing thermodynamically controlled and kinetically controlled growth of Au on seeds.^{24,53-55} In the reaction-controlled regime, morphologies consist of higher surface energy facets compared to the facets seen in the thermodynamically favored regime, which is observed for slower reaction rates. For example, with an increase in the rate of reaction, Au morphologies range from truncated bitetrahedra with lower energy {111} facets to isooctahedra with higher energy {221} facets.⁵³ Moreover, NIR active high surface energy nanohexapods have been grown in the kinetic regime from a cubic Au seed, with a tip to tip distance of 60 nm.⁵⁶ Similarly shaped nanostars have been formed

by directed growth on facets of Au seeds, with polymers or surfactants used to block certain sites.²⁵⁻³⁶ The length of the points or arms on the stars may be controlled by varying the stoichiometric ratio of concentrations of Au precursor and the core particles along with the precursor reduction rate.²⁵

As an alternative to monolithic particles, nanoclusters have been formed by colloidal assembly of primary particles in aqueous media for Au coated iron oxide,^{2,57} Au spheres,⁴⁵⁻⁴⁷ and CdSe quantum dots,⁵⁸ and in organic media for TiO₂ nanospheres (3 nm) or rods (3 nm to 6 nm).⁵⁹ In some cases, the cluster size may be controlled by balancing long-ranged repulsion and short-ranged attraction. For example spherical Au particles were self-assembled into reversible (biodegradable) nanoclusters with sizes ranging from 30 to 100 nm by tuning colloidal interactions to achieve strong NIR extinction even at 1024 nm.⁴⁵⁻⁴⁷ Chains of Au particles were also formed by linking particles together using a polymerase chain reaction resulting in a shift of the absorbance to the NIR region.⁵⁰ Recent clusters formed from ~100 nm long Au nanorods⁶⁰ or ~100 nm long nanodumbbells⁶¹ have also been shown to shift the SPR peak into the NIR region out to 1500 nm. In a few rare cases, self-assembled nanostar-shaped particles have been synthesized from 10-40 nm primary particles which are colloidally unstable but with round and small arms on the cores resulting in low absorbance in the NIR region.⁶²

Despite advances in controlling the shape of monolithic nanocrystals and self-assembled nanoclusters, it remains highly challenging to introduce sufficient asymmetry into nanoparticle structures to generate high extinction coefficients for wavelengths ranging from 800-1100 nm, particularly for particles smaller than 60 nm.^{29,34,37,39,62} For Au nanostars, long points (and thus large particles) are required given the relatively large cores (~ 10 to 30 nm) in order to shift the SPR to the NIR..^{25,40,41,63-65} Indeed, only a few

studies report particles on the order of 50 nm with strong NIR absorbance from 700-800 nm, namely, nanohexapods,⁵⁶ nanocages²⁴ and nanoclusters.^{2,47} In each case, the absorbance drops significantly at wavelengths greater than 1000 nm. Consequently novel concepts are needed to synthesize nanoparticles with a sufficient degree of asymmetry for broad NIR absorbance in small particles (~50 nm).

Herein, ~ 60 nm Au nanoparticles exhibiting intense and broad NIR extinction from 700 to 1100 nm are synthesized by reduction of H₂AuCl₄ with hydroxylamine in the presence of either carboxymethyl dextran (CMD) or dextran. Reactions were performed at a pH 8.7 and below to attempt to achieve kinetic control and avoid relaxation of the growing particles to the thermodynamically favored state of spheres. The objective was to design small nanocluster cores formed by self-assembly of closely-spaced small primary particles and to further decorate the cores with a large number of small points as shown in Fig. 2.1. The large number of reactive sites on the ensemble of high surface area primary particles within the nanoclusters offers the opportunity to form a high density of points per nanocluster. In essence, concepts of kinetic versus thermodynamic control of growth from monolithic particles^{24,53,54} are adapted to growth of points on self-assembled nanoclusters. A weakly adsorbing polymer, CMD or dextran, is used to provide electrosteric stabilization of the nanoclusters. The low coverage of the weakly interacting polymer on Au is needed so that the primary particles are close enough together to produce strong NIR extinction. At higher pH, slower precursor reduction is shown to result in thermodynamically controlled growth to form spherical particles with low surface energy.

The hybridization of the large number of ~ 10 nm points on similarly sized ~ 10 nm primary particles (high aspect ratio of point length/primary particle diameter) is

shown to contribute to a large shift in the SPR, as anticipated from previous simulation studies with a point on a spherical core.^{25,43} The shift is further magnified by coupling between the surface plasmons of closely-spaced primary particles in the clusters, resulting in a high level of NIR extinction from 700 to 1100 nm in a small Au nanoparticle. This concept of producing nanoclusters via reaction, with strong asymmetry in the primary particles, may be expected to be applicable to a wide variety of systems by balancing kinetic and thermodynamic control, along with colloidal interactions to tune self-assembly resulting in unique morphologies.

2.2 MATERIALS AND METHODS

2.2.1 Materials

All reagents used were analytical grade. Ammonium hydroxide, hydroxylamine hydrochloride, and dextrose anhydrous were purchased from Fisher Chemicals (Fairlawn, NJ), carboxymethyl dextran sodium salt (MW = 10,000) and dextran (MW = 10,000) from Sigma Aldrich (St. Louis, MO), and tetrachloroauric acid trihydrate from MP Biomedicals LLC. (Solon, Ohio). 50 and 100 nm diameter gold nano urchins were purchased from Cytodiagnostics (Ontario, Canada).

2.2.2 Synthesis of Au Clusters - First Iteration

Au nanocluster synthesis followed a modified procedure utilized previously for making Au/iron oxide nanoclusters.² The primary difference in the new approach was that it did not use iron oxide nanoparticles. For carboxymethyl dextran coated nanoclusters, a 70.4 ml aqueous reducing solution was prepared at room temperature with

2.0 mM $\text{NH}_2\text{OH}\cdot\text{HCl}$, 0.3 mM carboxymethyl dextran, and 475 mM dextrose. Synthesis of dextran nanoclusters followed the same procedure with the same concentration (0.3 mM) of dextran. The pH of the solution was adjusted to pH 7.5, 8.7 or 9.3 using a solution of 7% ammonium hydroxide in water and was observed to decrease by about 0.1 units after addition of the precursor. Under rigorous stirring, a given volume of aqueous Au precursor at a concentration of 12.7 mM was rapidly injected into the reducing solution to achieve the desired Au^{3+} concentration. Reactions began to exhibit an initial blue color at ~2 min which transitioned to pink for pH 9.3 and remained blue for lower pH reactions. The reaction mixture was allowed to sit for about 10 minutes and the particles were recovered or additional iterations of Au were added. After each iteration, including the first one, ~10 minutes were allowed for reaction. The color was always seen to become constant within the ten minutes. For each iteration, a given amount of Au precursor solution (about 0.1 ml) at 12.7 mM Au^{3+} was injected in order to achieve the desired concentration of Au precursor in solution. Final samples were concentrated by centrifugation at 6,000 rpm for 7 min, after which the supernatant was decanted. The clusters were re-dispersed into about 0.5 ml of DI water with ~1 min bath sonication to help remove the particles stuck to the walls of the centrifuge tube. Finally, this concentrated dispersion was diluted in DI water to various levels depending upon the characterization procedure.

2.2.3 Quenching of reactions for temporal experiments

For stopping the reaction at intermediate stages to observe the temporal evolution of the Au nanoparticles, mercapto acetic acid was used to complex with the unreacted Au precursor. A stoichiometric excess of about 2:1 of the mercapto acetic acid was added to

the reaction mixture at the desired time point and upon this addition, the color transition was observed to stop immediately.

2.2.4 Materials Characterization

2.2.4.1 Dynamic light scattering measurements

Dynamic light scattering (DLS) measurements were performed in triplicate on a custom-made Brookhaven Instruments ZetaPlus apparatus at a scattering angle of 90° and temperature of 25 °C. Nanoparticle concentrations were adjusted using DI H₂O in order to get signal count rates between 150-400 kcps. Prior to DLS measurements, samples were bath sonicated for ~2 minutes. The autocorrelation functions (ACFs) were analyzed with a CONTIN algorithm to determine distributions by volume. In order to verify the DLS technique, commercially available nanostars were analyzed by the DLS and seen to give similar trends in the intensity and volume distributions of size as the particles in the current study which is further discussed in in Appendix A.1. The autocorrelation functions (ACF) and the size distributions for both the nanourchins and the particles from the current study are shown in Table A1.

2.2.4.2 Electron Microscopy

Low resolution transmission electron microscopy (TEM) imaging (FEI Tecnai Spirit BioTwin) was performed at an accelerating voltage of 80 kV. A drop of diluted particle dispersion was put on a 400 mesh ultrathin carbon-coated copper TEM grid. Excess liquid was blotted with a tissue and the grid was allowed to dry in 30 inch Hg vacuum. Next the samples on the grid were further washed by adding a drop of DI H₂O

on the grid and blotting it with a tissue. The grids were also run on a Hitachi S5500 SEM for obtaining SEM and STEM images. Particle sizing was conducted using the ImageJ software (NIH) for 100 particles.⁶⁶ The sized particles were screened to ensure that only single particles were being sized and aggregates were excluded.

2.2.4.3 Thermogravimetric analysis

Thermogravimetric analysis was performed using a Perkin-Elmer TGA 7 under a nitrogen atmosphere at a gas flow rate of 20 ml/min. Nanoparticle samples were dried to a powder in a low pressure environment at 30 in Hg vacuum. Samples were heated to 100 °C in the TGA instrument for 20 minutes to further remove moisture. The samples were then heated from 100 °C to 900 °C at a rate of 15 °C/min, and then held at 900 °C for 30 minutes to burn off any organic material.

2.2.4.4 Measurement of Au concentration

Measurements of Au concentrations in solution were obtained by first dissolving the nanoparticles in aqua regia. 0.25ml HNO₃ was added to a glass vial followed by 0.03mL of sample solution. 0.75 ml of HCl was injected into the mixture and the samples were allowed to sit overnight (~12 hr) in a fume hood, during which time the solutions turned colorless. Samples were then diluted with DI H₂O until Au concentration was estimated to be between 1 and 5 µg/ml. The concentrations were then measured with a GBC 908AA flame atomic absorption spectrometer (GBC Scientific Equipment Pty Ltd) equipped with an air-acetylene flame furnace which was calibrated using a gold standard solution. The absorption for Au was recorded at 242.8 nm to measure the concentration.

2.3 RESULTS AND DISCUSSION

2.3.1 Formation of clusters of Au primary particles

The nanoparticle synthesis was carried out at a Au precursor concentration of 0.018 mM which is much lower than the typically used values of ~1 mM or higher.^{25,35,67,68} At all three pH values studied (9.3, 8.7, and 7.5), initially ~5 nm primary Au particles formed (which are not directly observed) which then aggregated into small nanoclusters. A similar type of cluster formation has also been seen in other studies with semiconductor or metallic nanoparticles.^{59,67,69} The formation of the nanoclusters is evidenced by the appearance of blue color in the reaction solution, as quantified by the significant extinction in the > 600 nm wavelength region of the UV-visible spectrum shown in Fig. 2.2a. Here the reaction was stopped after 40 s at pH 9.3. The morphology of these particles as seen in TEM micrographs in Fig. 2.2b was that of a nanocluster composed of several closely spaced primary particles. The coupling of the surface plasmon resonances (SPR) of the closely spaced primary particles along with some formation of Au bridges between the primary particles will be shown to produce the large red-shift in the SPR.

In order to further understand the formation of these clusters, it is instructive to consider recent mechanisms from the literature. Both thermodynamic and kinetic aspects contribute to the assembly of the primary particles into clusters to form the starting nanoclusters shown on the left-hand side of Fig. 2.1. From a thermodynamic point of view, clusters may be formed through short ranged attraction between primary particles that cause them to aggregate until the net long ranged electrostatic repulsion between the charged primary particles in the cluster limits the cluster size.^{47,69-74} In the current study,

the polymeric stabilizer is only weakly adsorbing and thus the van der Waals forces may cause the primary particles to pack closely. For other cases where primary particles have high levels of polymeric stabilizers on the surface, the steric repulsion between the polymer chains will preclude close proximity of the primary particles. In summary, in an equilibrium sense, as the clusters grow larger, the size may be limited by the net electrostatic repulsion from all the particles in the cluster. However, cluster formation and growth would not be expected to be solely equilibrium driven, but various mechanisms of kinetic control are present. For example, reduction of Au^{3+} onto primary particles continues even as the primary particles aggregate (Figs. 2.1 and 2.2). The Au growth may fuse the primary particles together, resulting in the formation of permanent clusters as has been studied previously.^{2,35,65} Another kinetic aspect is passivation of the growth by adsorbed polymer on the nanocluster surface. Given the complexity of thermodynamic and kinetic aspects of the particle growth, it is instructive to attempt to regulate the kinetic growth rates with variables such as pH to better control the morphology and spectral properties.

2.3.2 Rapid kinetic growth generates points on primaries whereas slow growth results in equilibrium relaxation to spheres

At the highest pH of 9.3, the Au^{3+} reduction rate is the slowest. Thus, the initial nanoclusters relax towards the thermodynamically favored state of large single spheres to minimize surface area/volume as shown in the upper part of Fig. 2.1. The reaction mixture was initially blue at 30 s, as described above, but then underwent a slow color change from blue at 2 mins to purple at 2.5-3 mins and eventually to pink in 3-4 mins, after which there was no further color change. Due to thermodynamic driving forces, the

nanocluster formed fills in progressively to form a sphere, as shown by the TEM micrographs in Figs. 2.2c-e, in order to minimize the surface area per volume. The spheres have a high extinction at 530 nm but very little extinction in the NIR region as shown in Fig. 2.3a, as is known for the SPR for spheres. The diameter of the resulting particles is ~25 nm by dynamic light scattering (DLS) as shown in Fig. 2.3b. The size measured by DLS is in reasonable agreement with the average size of 34 nm measured for 100 particles from the TEM micrographs using the ImageJ software, with a histogram of the nanoparticle sizes shown in Fig. 2.3c.

In contrast to the slow reaction at pH 9.3, more rapid growth occurs in the kinetic regime at lower pH values (8.7 and 7.5). The reaction mixture remained blue in color and darkened with time, as indicated by the absence of a peak shift in the UV-visible spectra in Fig. A1. Additionally, the reaction occurred at a much faster rate, with the color change reaching the final state in 40 s at pH 8.7 and 25 s at pH 7.5 compared to 3-4 minutes for pH 9.3. The initial nanoclusters formed at the lower pH are similar in morphology and extinction properties (Figs. 2.1a and A1) to the ones formed at pH 9.3, as shown by the TEM micrograph in Fig. A2a (for pH 8.7). However, further growth at the lower pH conditions to produce points / spikes / branches / arms (henceforth referred to solely as points) on these initial nanoclusters (Figs. A2b and A2c) may be contrasted with the relaxation to equilibrium favored spheres at higher pH values. The retention of the asymmetric morphological characteristics is very likely responsible for the maintenance of the high NIR extinction and peak position at pH 8.7, as opposed to loss of the NIR extinction for the spheres observed at pH 9.3. The particle size of the nanoparticles synthesized at pH 8.7 was ~60 nm as measured by DLS (Fig. 2.3b), which agrees with the size determined by TEM as shown in the histogram in Fig. 2.3d. Here the

small particles are highly asymmetric with a very high number of points on a nanocluster core, as shown in TEM micrographs in Fig. 2.4a and Fig. A3. In contrast, the growth is uncontrolled at pH 7.5 and results in very large particles with a diameter of 180 nm by DLS (Fig. 2.3b) and 150 nm from TEM micrographs (Fig. 2.3e). Here, the morphology is large star shaped particles as shown in the TEM micrographs in Fig. 2.4b.

The large number of points on the highly asymmetric particles synthesized at pH 8.7 and pH 7.5 produce high extinction in the NIR region out to 1100 nm with the peak absorbance at 650 nm as shown in Fig. 2.3a. The high NIR absorbance will be shown below to be the result of plasmon hybridization for the points on the spherical cores.^{25,43} The difference in the extinction spectra of the particle dispersions is also evident visually in the photograph in Fig. 2.3f with the pink dispersion at pH 9.3 and the blue dispersions at pH 8.7 and 7.5. The NIR extinction properties of these particles which were synthesized with CMD as the stabilizing polymer are summarized in Table 2.1 along with the particle size by DLS. Furthermore, the particles are seen to have a highly negative zeta potential which probably arises from the adsorbed polymer on the surface (Table 2.1). Very similar morphologies were obtained for the particles synthesized using dextran in place of CMD (Fig. A4 and Table A2), despite the fact that CMD is anionic. Both CMD and dextran provided steric stabilization, and both were weakly bound to the Au surface given the loadings of 50 and 40 % by weight respectively as seen from thermogravimetric analysis (TGA) in Figs. 2.5 and A5.

Here the variation in the reduction rate of the Au precursor (HAuCl_4) as a function of pH of the solution which is seen in the data is explained. The hydroxyl ions replace the chloride ions in the Au^{3+} complex, with the complex becoming less reactive when a higher fraction of chloride ligands have been replaced by hydroxyl ligands.^{2,67,75}

At higher values of pH, the hydroxyl ion concentration is higher, which causes a shift in the equilibrium favoring increased replacement of chloride ions by hydroxyl ions according to Le Chatelier's principle. Therefore as the pH of the reaction mixture increases, the Au precursor becomes less reactive resulting in a slower reaction rate in agreement with our observation of the slowest reaction rate based on rate of color change at pH 9.3. The reaction rate is intermediate at pH 8.7 and fastest at pH 7.5, where the uncontrolled rapid growth forms particles that are too large for biomedical applications.

The particle formation mechanism versus pH in terms of the kinetic and thermodynamic aspects influences the particle morphology. At the lowest pH values, where the reduction rate is the fastest, the reduction of Au^{3+} is primarily in the kinetically controlled growth region. Here the reduced Au precursor is deposited rapidly on the surface with limited time to diffuse to a more thermodynamically favored site. The deposition of Au is thus limited more by the diffusion of the precursor to the Au surface, where it is reduced rapidly. Therefore, the precursor reduction can result in the formation of higher energy facets or non-equilibrium structures as a consequence of the high kinetic driving force. In the current study, under kinetically-controlled growth at pH 8.7 and 7.5, the high energy facets manifest themselves in the form of points shown in the bright field STEM images in Figs. 2.4a and b. Analogously, during the growth of monolithic particles by seeded reduction of Au, kinetically-controlled growth of higher energy facets can result in higher energy structures structures, for example icosahedra with 211 facets.^{53,54} Furthermore, the ability to preferentially grow higher energy structures through kinetically-controlled growth has also been used to direct the growth of specific shapes like hexapods through growing non-equilibrium shapes.⁵⁶

In the present study, this strategy of using kinetic growth to form high energy facets was extended to growth on nanoclusters, whereby the growth produced points on the primary particles. The behavior may be contrasted with kinetic growth on single monolithic particles that has been used to form a wide variety of non-equilibrium particle shapes. For nanostars (and nanourchins) the growth of points on a monolithic core can only occur on certain crystal facets.^{25,29,36,76} With only a single core for growth on a monolithic particle, the number of points that can be grown is limited. A similar phenomenon is seen in the growth of Pd shells on Au particles where Au particle cores of different shapes resulted in different Pd outer layer morphologies due to variation in the number of available facets for growth.⁷⁷ A higher number of dendritic petals of Pd grew on the Au cores with more vertices/faults present than on more regularly shaped cores.

In the current study, the points are grown on a nanocluster consisting of numerous primary particles, each of which has multiple available growth sites. Thus, the growth on nanoclusters enables the formation of more points per particle. In addition to the larger density of points per particle, the resulting points may also have a higher point length to core diameter aspect ratio than comparable nanostar particles.^{3,20-22} The higher aspect ratio is a consequence of growth of points on a 5 – 10 nm primary particle, relative to a larger core for the case of single monolithic cores as shown in the right parts of Fig. 2.1 for particles with a nanocluster core and Fig. 2.6 for monolithic cores. Therefore, the current study provides an alternative core, namely, a nanocluster core, for kinetically-controlled growth of points to form Au nanoparticles with a large number of points with a high point-to core ratio to manipulate the surface plasmon to generate extraordinary NIR extinction properties.

In order to utilize the kinetically controlled regime to produce sub 100 nm particles with strong NIR absorbance, it was necessary to prevent uncontrolled growth. To ensure that the particle size does not become too large, an unusually low Au precursor concentration of 0.018 mM was utilized. To highlight the importance of the low Au precursor concentration, the synthesis was carried out at pH 8.7 with a Au precursor concentration of 0.036 mM, twice the normal concentration, while keeping all other parameters constant. Particles about twice as large were formed as shown by TEM images in Fig. 2.7a and by the hydrodynamic diameter from DLS in Fig. 2.7b. The significant increase in particle size is likely the result of the autocatalytic nature of the growth of Au on Au.^{57,78-80} It is much more energetically favorable for the Au precursor to deposit on a pre-existing Au surface rather than to create a new Au surface. Therefore at higher Au³⁺ concentrations of 1 mM or greater, the more rapid growth on the Au nuclei leads to the larger particles. Even larger particles have been observed in previous studies at even higher Au precursor concentrations.^{29,35,81} Despite the near doubling of the nanoparticle size for the higher Au³⁺ concentration, the NIR extinction properties were not improved over the particles synthesized with lower Au³⁺ concentrations as can be seen in Fig 2.7c.

In contrast to the kinetically driven formation of points at low pH values, the reactions at higher pH proceed in a thermodynamically controlled regime. As a result of the lower reduction rate, the diffusion of precursor to the particle surface becomes relatively faster and the precursor reduction reaction was more rate-limiting. Therefore, an Au precursor diffuses to an energetically favorable site on the particle surface before being reduced. The deposition on energetically favorable sites enabled relaxation of the structure to spheres as shown by the TEM images in Figs. 2.2b-d with the lowest possible

surface area per volume. Analogously, during the growth of monolithic particles by seeded reduction of Au, thermodynamically controlled growth resulted in the formation of lower energy facets, e.g., formation of triangular bipyramids with 111 facets.^{53,54}

2.3.3 Morphology of points on the nanoclusters gives rise to high NIR extinction

The particles synthesized in the current study have a very high number of points per particle along with a high point length-to-core diameter aspect ratio, both of which will now be shown to raise NIR extinction. It is instructive to contrast these properties with those of nanostars with monolithic cores. A totally symmetric sphere exhibits surface plasmon resonance with a characteristic wavelength of around 520 nm. The growth of a point on a sphere influences the resonant frequency of the surface plasmon through hybridization of the dipoles in the sphere and the point to form multipoles with a red shift in the characteristic frequency of the resultant plasmon.^{25,43} The cross-section or amplitude of the absorbance is influenced by the core of the particle but the shift in the frequency is caused solely by the points.⁴³ As a result, a larger core is capable of producing higher amplitude of the SPR, but an aspect ratio of 1:1 of point length to core radius is needed for a strong NIR shift, leading to larger particles. In agreement with this, for typical monolithic nanostars with a relatively large core, the red-shift is produced primarily by the points and not the monolithic particle cores.^{25,29} In contrast, the initial nanocluster cores in the present study already produce extinction in the NIR (Fig. 2.2a), which is further enhanced by the formation of points. The proximity between the primary particles in the cluster interior results in plasmon hybridization between primary particles in the core, resulting in a red shift in the extinction peak.^{47,48,70,82-84}

For the particles synthesized at the lower pH values of 8.7 and 7.5, growth of points further contributes to the red-shift in their SPR (Fig. 2.3a), in addition to the contribution of the nanocluster cores (Figs. 2.2a) . The increased surface density of points, as explained earlier, also contributes to the enhanced NIR extinction. As the number of points per particle increases, a greater red shift is observed experimentally in the SPR.^{35,44,65} Additionally, the point length-to-core diameter aspect ratio strongly affects the extent of the red shift of the plasmon, with longer points leading to a bigger red shift in the SPR.^{25,43,44} In the current study, the aspect ratio is very large as the core is composed of small 5-10 nm primary particles, thus allowing a much higher shift in the plasmon compared to particles with a monolithic core. The shift is caused by a combination of the aspect ratio of the points to both the size of the primary particle to which it is connected and the size of the nanocluster core. Therefore the particle morphology in the current study with the very high number of high aspect ratio points per particle causes a big shift in the characteristic plasmon frequency to the NIR region.

2.3.4 Morphology of points on the nanoclusters gives rise to high NIR

To further place the results for the nanocluster cores containing a high density of points in perspective, points were also grown on the spherical particles synthesized at pH 9.3. The growth of points was enabled by additional aliquots of Au precursor (called iterations) which were reduced onto the particles. In this case, dextran was used as the stabilizing polymer instead of CMD to show that the technique is general. Very similar results would be expected for CMD. The first iteration produced the same particles as in Figs. 2.2d and e as shown by the TEM image in Fig. 2.8a. As additional iterations of the Au precursor were added, they resulted in the growth of points on the spheres as shown

in Fig. 2.6. Each additional iteration resulted in the elongation of the points as shown in Figs. 2.8b-d. The growth of these points is probably the result of a progressive decrease in the reaction mixture pH due to the addition of the acidic Au precursor, which pushes the reaction into the kinetically-controlled growth regime and allows the growth of the non-equilibrium point structures on the particles instead of equilibrium thermodynamic relaxation. The growth of these points increases the particle size as seen from the hydrodynamic diameter of the particle measured by DLS in Fig. 2.9a. As can be seen, the particle diameter is initially 25 nm and grows to 120 nm after 12 added iterations of Au precursor. The UV-vis extinction spectra for these particles shows that the plasmon peak becomes gradually more red shifted as more iterations of Au precursor are added, as evidenced in Fig. 2.9b. The red-shift results from the growth of points on the particles. As seen in earlier studies, the increased point length to core diameter aspect ratio due to the longer points increases the extent of the red shift of the plasmon.^{25,43,44} The intensity of NIR extinction for these particles, however, is much inferior to the particles synthesized at lower pH which have the asymmetric nanocluster cores (Fig. 2.3a). Therefore, it is clear that the growth of points on an asymmetric nanocluster core, as developed in the current study, is far more advantageous for obtaining a high NIR absorbance than the growth of points on a more conventional symmetric core at a similar size of ~ 60 nm.

2.4 CONCLUSIONS

The growth of a high density of high energy facets, in the form of points, on a nanocluster core substrate, results in particles with high NIR extinction up to wavelengths of 1100 nm, even for small diameters of ~ 60 nm. These particles were formed at pH 8.7 and 7.5 in a more kinetically controlled regime, to avoid relaxation to spheres in the more

thermodynamically controlled slow growth regime at higher pH. The large number of primary particles per cluster results in a greater number of reactive sites being available for growth of the points, relative to the case of a monolithic core. The high NIR extinction results from the close primary particle spacings in the initial nanocluster cores, the high density of points on the cores, and the high point length to primary particle diameter aspect ratio. In contrast, much larger points are required for nanoparticles with spherical or monolithic cores (e.g. nanostars) to achieve the same NIR extinction resulting in much larger particles. The strong NIR extinction for a particle with a small size is of interest in biomedical imaging including photoacoustic imaging and photothermal therapy.

pH	Hydrodynamic Diameter (nm)	Extinction ratio (800 nm/500 nm)	Zeta Potential (mV)
9.3	23 ± 4.2	0.034	-33.8 ± 1.9
8.7	36 ± 6.3	1.24	-33.9 ± 0.9
7.5	180 ± 30.4	1.31	-35.8 ± 2.3

Table 2.1: Summary of nanoparticle size, absorbance properties and zeta potential.

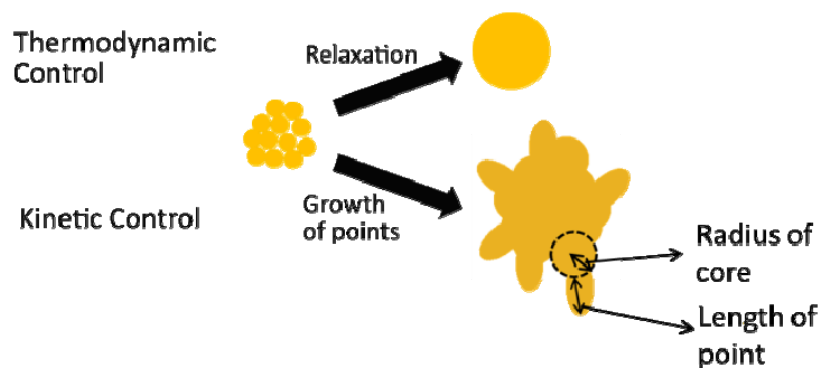


Figure 2.1: This schematic contrasts the thermodynamically and kinetically controlled growth. At high pH (9.3), the clusters fill in or relax to form regular spherical shaped particles while at low pH (8.7), the clusters have further faceted growth on them to form flower shaped particles. At even lower pH (7.5), there is further faceted growth leading to star shaped particles.

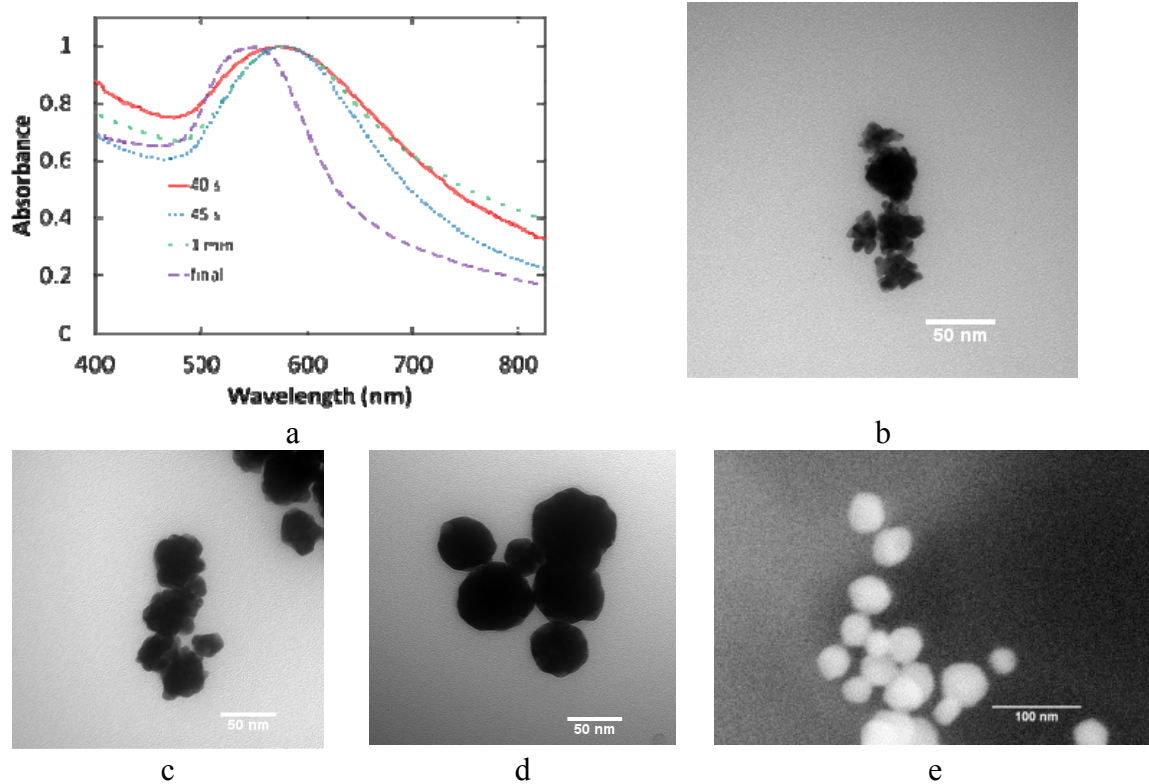
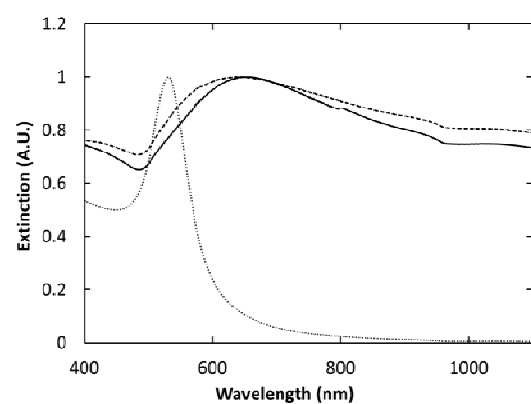
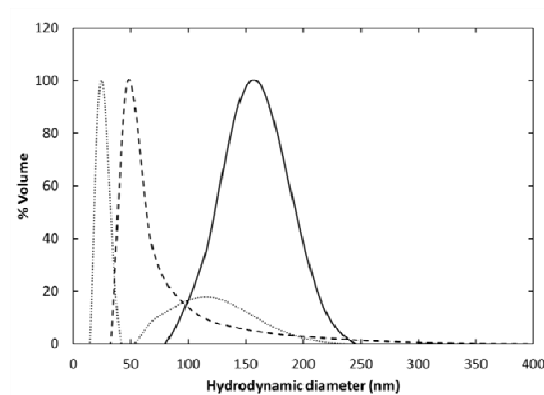


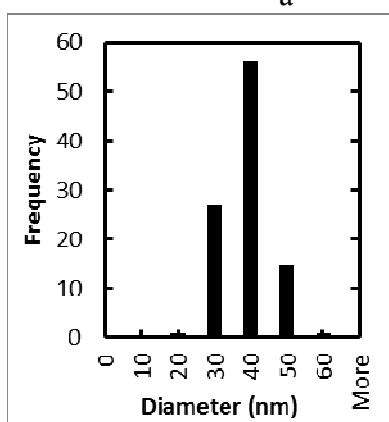
Figure 2.2: Aggregation of primary particles followed by relaxation for slow thermodynamically controlled growth captured by quenching with mercapto acetic acid at different time points is shown by TEM. a, UV-visible spectra for the nanoparticles as the reaction proceeds at pH 9.3. b, quenched at 40 s. c, quenched at 45 s. d, not quenched. e. SEM image of non-quenched particles.



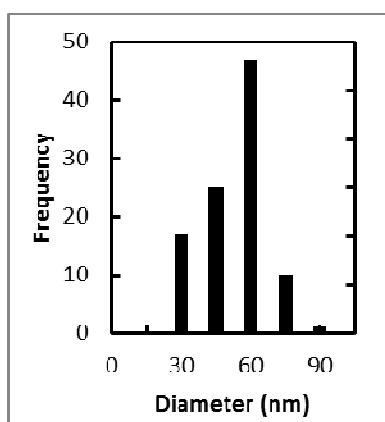
a



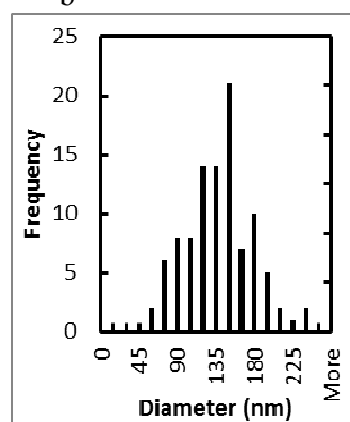
b



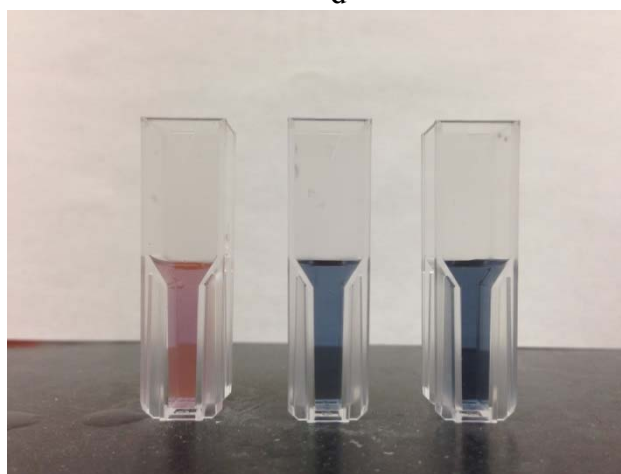
c



d



e



f

(Fig. 2.3 continued on the next page)

Figure 2.3: a. UV-vis-NIR spectra of final nanoparticles synthesized at 0.018 mM Au^{3+} at pH = 9.3 (dotted line), pH = 8.7 (dashed line) and pH = 7.5 (solid line). All spectra are normalized to an absorbance of 1 at the peak value. b. Hydrodynamic diameter of the nanoparticles synthesized with 0.018 mM Au^{3+} at pH = 9.3 (dotted line), pH = 8.7 (dashed line) and pH = 7.5 (solid line). Histograms showing size distributions for particles from TEM image analysis synthesized at c. pH 9.3, d. pH 8.7 and e. pH 7.5. f. Picture of dispersed particles showing the difference in color between the particles from part a with the pH decreasing from 9.3 on the left to 8.7 for the middle cuvette and 7.5 for the cuvette of the right.

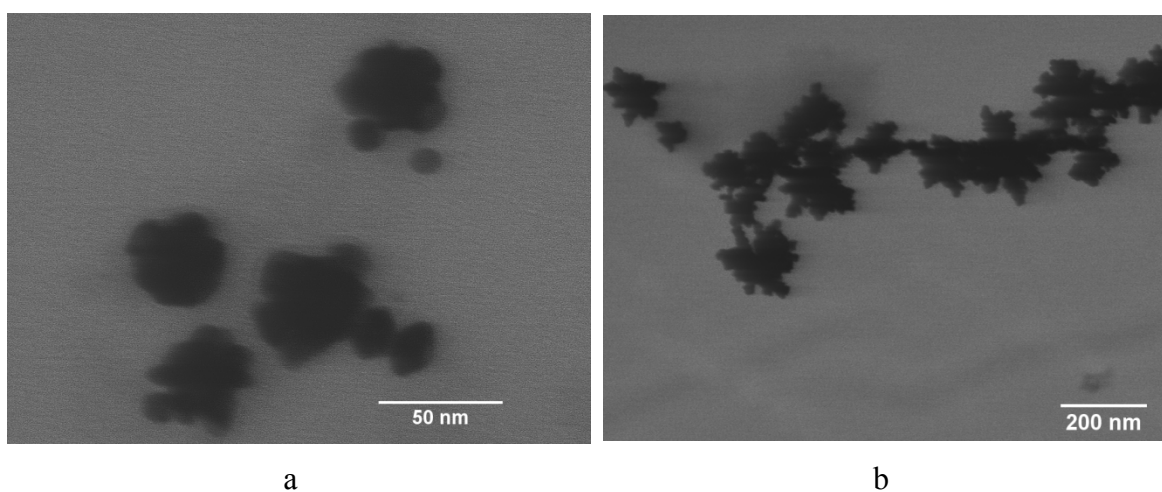


Figure 2.4: TEM images of nanoparticles synthesized with 0.018 mM Au^{3+} at a. pH = 8.7 (TEM image also included), b. pH = 7.5.

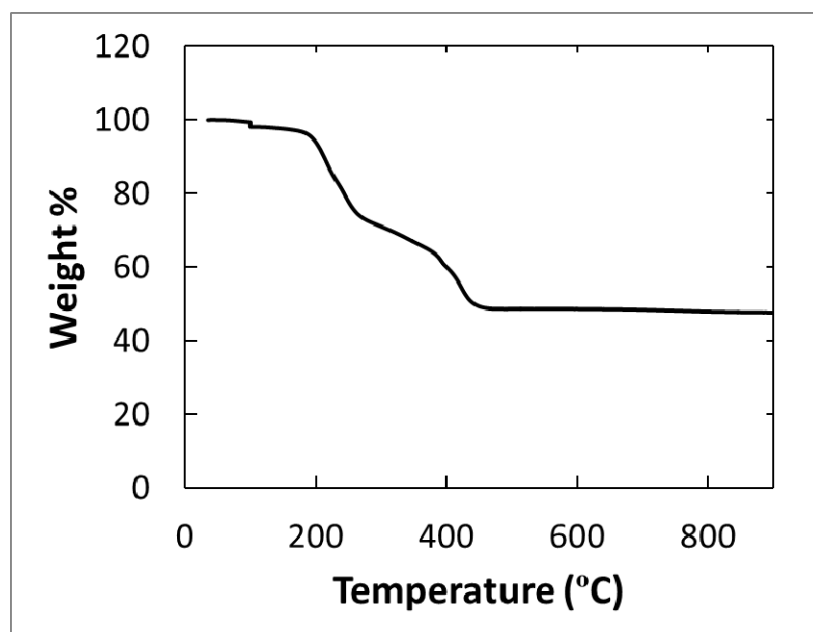


Figure 2.5: TGA profile of Au nanoparticles synthesized at 0.018 mM Au^{3+} with a CMD coating at pH 8.7.

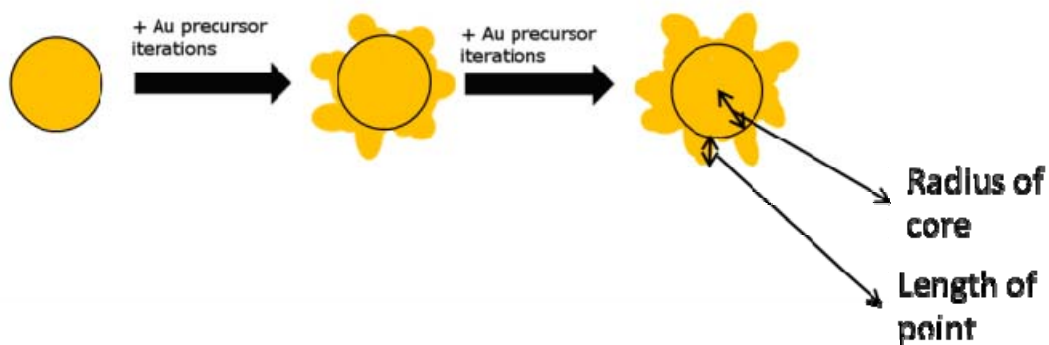


Figure 2.6: Scheme 2. Addition of more iterations of Au precursor to the reaction mixture at pH 9.3 leads to growth of points on the spherical core.

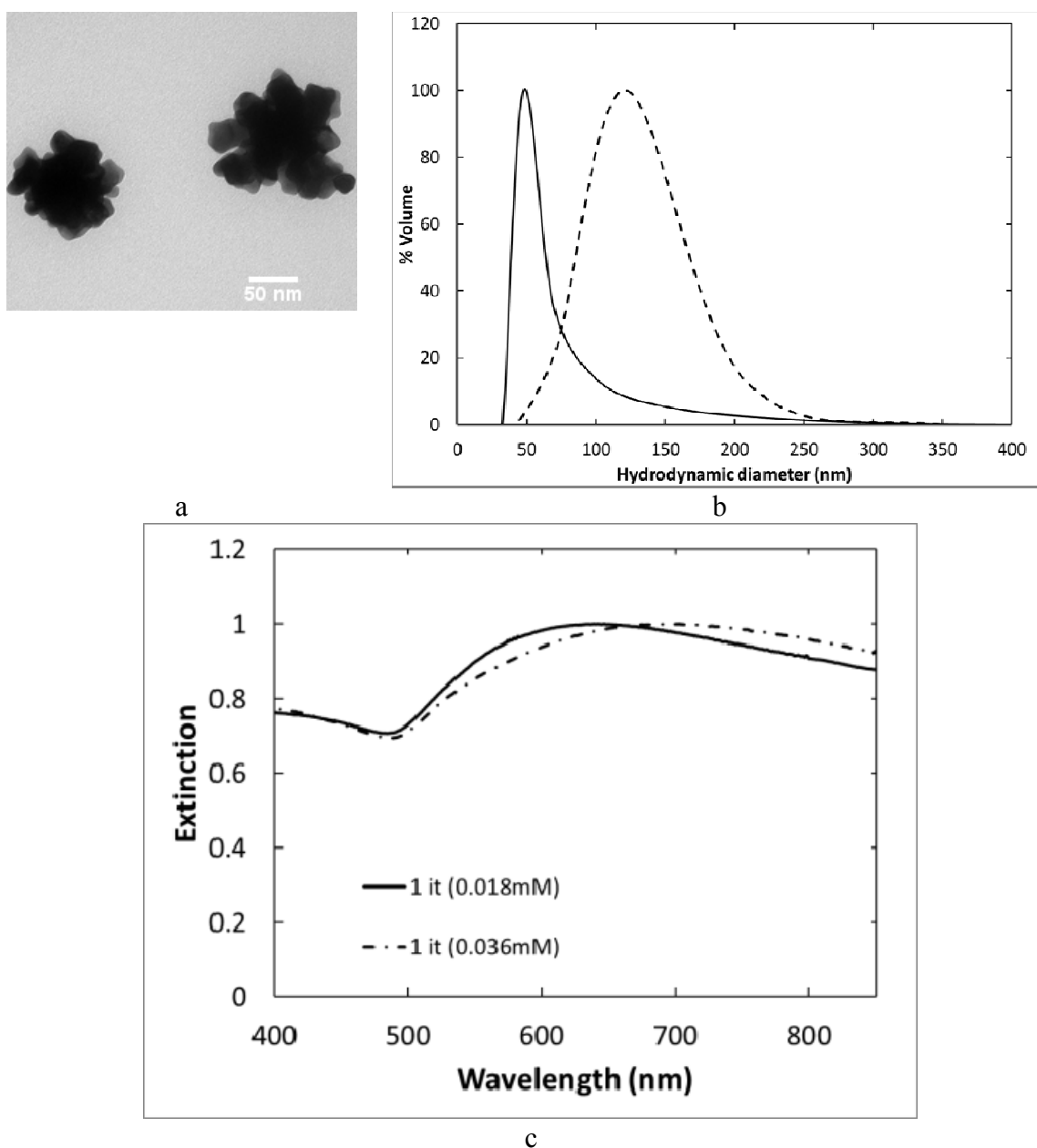


Figure 2.7: Effect of doubling concentration of Au precursor to 0.036 mM at pH 8.7 observed by a. Low resolution TEM of nanoclusters (scale bar is 50 nm), b. Hydrodynamic diameter by DLS and c. Extinction spectra by UV-vis spectroscopy. In both cases, the solid line denotes the 0.018 mM particles while the dashed line is for the 0.036 mM particles.

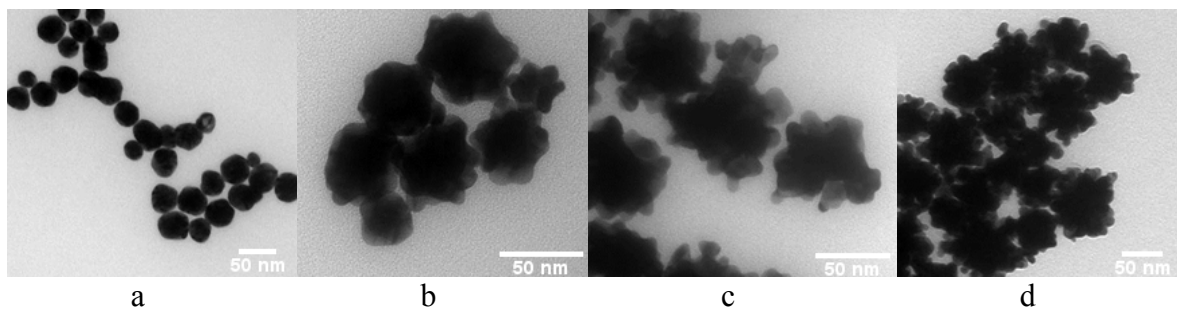
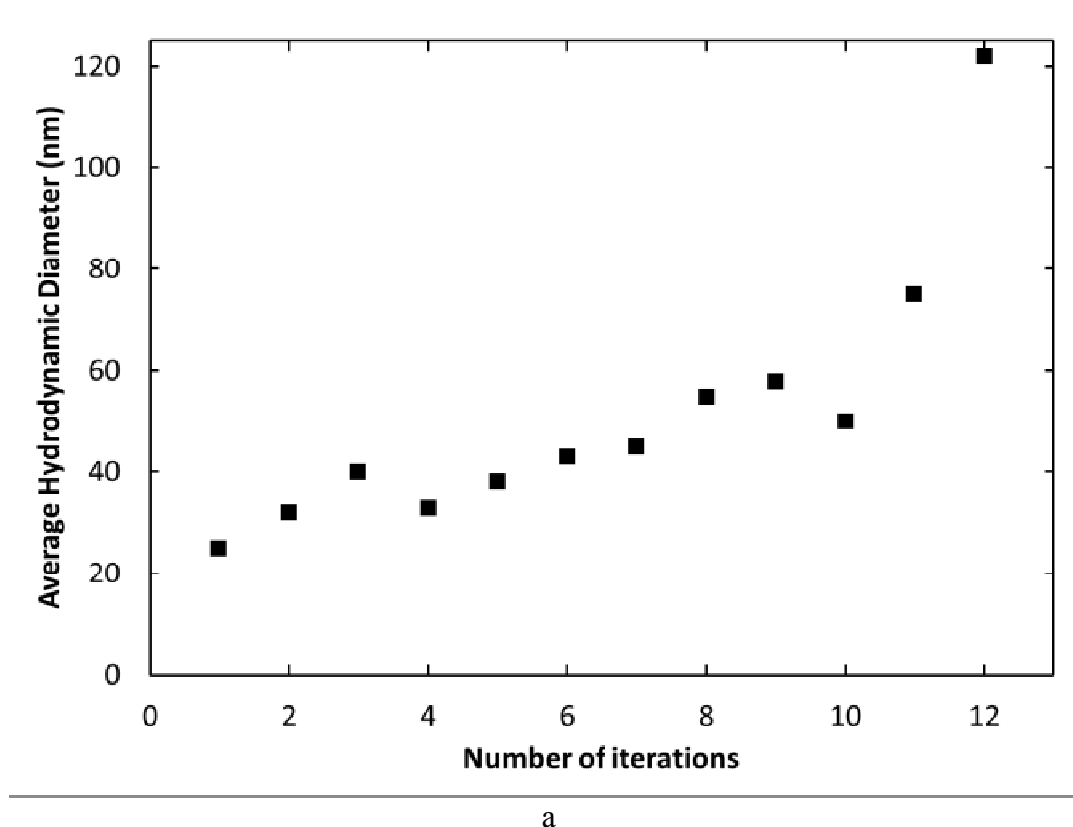
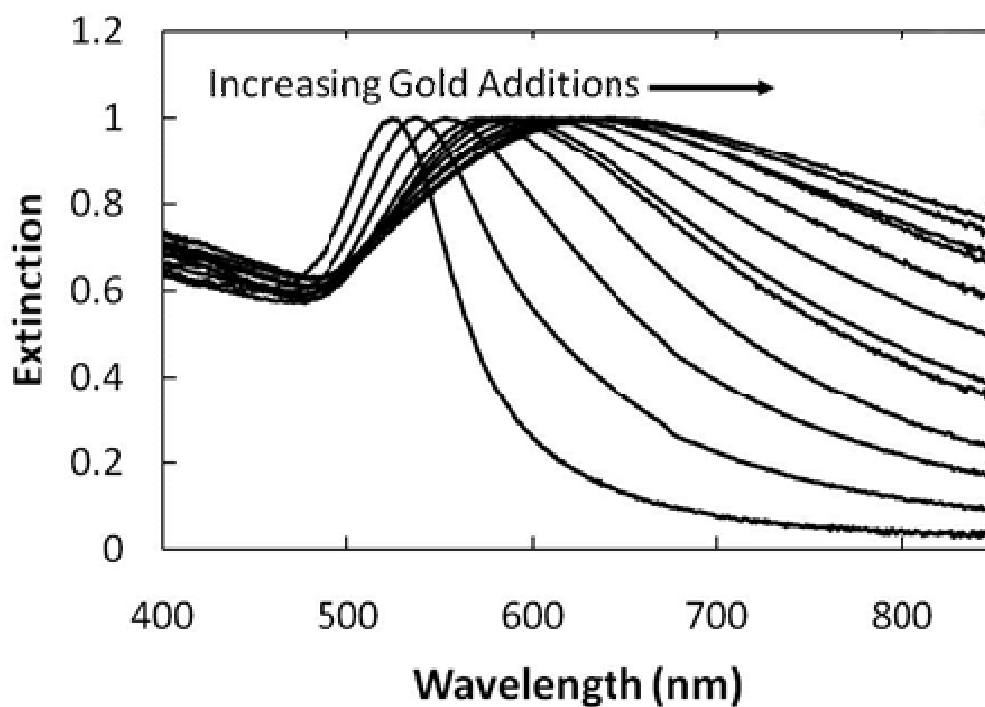


Figure 2.8: Low resolution TEM images of nanoparticles after different iterations synthesized with dextran (3 mM) at pH = 9.3 with a 50 nm scale bar. a, 1 iteration. b, 3 iterations. c, 7 iterations and d, 10 iterations.



(Fig. 2.9 continued on the next page)



b

Figure 2.9: Nanoparticles after 1-12 iterations at 0.018 mM Au^{3+} per iteration with dextran coating at pH=9.3 characterized by (a) DLS hydrodynamic diameter and (b) UV-Vis extinction spectra.

2.5 REFERENCES

- (1) Hirsch, L. R.; Stafford, R. J.; Bankson, J. A.; Sershen, S. R.; Rivera, B.; Price, R. E.; Hazle, J. D.; Halas, N. J.; West, J. L. *Proc. Nat. Acad. Sci.* 2003, 100, 13549.
- (2) Ma, L. L.; Feldman, M. D.; Tam, J. M.; Paranjape, A. S.; Cheruku, K. K.; Larson, T. A.; Tam, J. O.; Ingram, D. R.; Paramita, V.; Villard, J. W.; Jenkins, J. T.; Wang, T.; Clarke, G. D.; Asmis, R.; Sokolov, K.; Chandrasekar, B.; Milner, T. E.; Johnston, K. P. *Acs Nano* 2009, 3, 2686.
- (3) Zhang, J.; Sasaki, K.; Sutter, E.; Adzic, R. R. *Science* 2007, 315, 220.
- (4) Ferry, V. E.; Munday, J. N.; Atwater, H. A. *Adv Mater* 2010, 22, 4794.
- (5) Atwater, H. A.; Polman, A. *Nature Materials* 2010, 9, 865.

- (6) Anker, J. N.; Hall, W. P.; Lyandres, O.; Shah, N. C.; Zhao, J.; Van Duyne, R. P. *Nat. Mater.* 2008, 7, 442.
- (7) Stewart, M. E.; Anderton, C. R.; Thompson, L. B.; Maria, J.; Gray, S. K.; Rogers, J. A.; Nuzzo, R. G. *Chem. Rev.* 2008, 108, 494.
- (8) Weissleder, R. *Nat. Biotechnol.* 2001, 19, 316.
- (9) Kooi, M. E.; Cappendijk, V. C.; Cleutjens, K.; Kessels, A. G. H.; Kitslaar, P.; Borgers, M.; Frederik, P. M.; Daemen, M.; van Engelshoven, J. M. A. *Circulation* 2003, 107, 2453.
- (10) Ma, Y.; Li, N.; Yang, C.; Yang, X. R. *Analytical and Bioanalytical Chemistry* 2005, 382, 1044.
- (11) Arruebo, M.; Fernandez-Pacheco, R.; Ibarra, M. R.; Santamaria, J. *Nano Today* 2007, 2, 22.
- (12) Betancourt, T.; Brown, B.; Brannon-Peppas, L. *Nanomedicine* 2007, 2, 219.
- (13) Schipper, M. L.; Iyer, G.; Koh, A. L.; Cheng, Z.; Ebenstein, Y.; Aharoni, A.; Keren, S.; Bentolila, L. A.; Li, J. Q.; Rao, J. H.; Chen, X. Y.; Banin, U.; Wu, A. M.; Sinclair, R.; Weiss, S.; Gambhir, S. S. *Small* 2009, 5, 126.
- (14) Davis, M. E.; Chen, Z.; Shin, D. M. *Nat. Rev. Drug Discov.* 2008, 7, 771.
- (15) Daniel, M. C.; Astruc, D. *Chem. Rev.* 2004, 104, 293.
- (16) Huang, X.; El-Sayed, I. H.; Qian, W.; El-Sayed, M. A. *Journal of the American Chemical Society* 2006, 128, 2115.
- (17) Durr, N. J.; Larson, T.; Smith, D. K.; Korgel, B. A.; Sokolov, K.; Ben-Yakar, A. *Nano Letters* 2007, 7, 941.
- (18) Pissuwan, D.; Valenzuela, S. M.; Killingsworth, M. C.; Xu, X. D.; Cortie, M. B. *J. Nanopart. Res.* 2007, 9, 1109.
- (19) Qiu, L.; Larson, T. A.; Smith, D. K.; Vitkin, E.; Zhang, S. H.; Modell, M. D.; Itzkan, I.; Hanlon, E. B.; Korgel, B. A.; Sokolov, K. V.; Perelman, L. T. *Ieee Journal of Selected Topics in Quantum Electronics* 2007, 13, 1730.
- (20) Zhu, J.; Yong, K. T.; Roy, I.; Hu, R.; Ding, H.; Zhao, L. L.; Swihart, M. T.; He, G. S.; Cui, Y. P.; Prasad, P. N. *Nanotechnology* 2010, 21.
- (21) Adler, D. C.; Huang, S. W.; Huber, R.; Fujimoto, J. G. *Opt. Express* 2008, 16, 4376.
- (22) Loo, C.; Lowery, A.; Halas, N. J.; West, J.; Drezek, R. *Nano Letters* 2005, 5, 709.

- (23) Langille, M. R.; Personick, M. L.; Zhang, J.; Mirkin, C. A. *Journal of the American Chemical Society* 2011, 133, 10414.
- (24) Skrabalak, S. E.; Chen, J.; Au, L.; Lu, X.; Li, X.; Xia, Y. *Adv. Mater.* 2007, 19, 3177.
- (25) Barbosa, S.; Agrawal, A.; Rodriguez-Lorenzo, L.; Pastoriza-Santos, I.; Alvarez-Puebla, R. A.; Kornowski, A.; Weller, H.; Liz-Marzan, L. M. *Langmuir* 2010, 26, 14943.
- (26) Nehl, C. L.; Liao, H. W.; Hafner, J. H. *Nano Letters* 2006, 6, 683.
- (27) Senapati, D.; Singh, A. K.; Ray, P. C. *Chemical Physics Letters* 2010, 487, 88.
- (28) Mueller, M.; Tebbe, M.; Andreeva, D. V.; Karg, M.; Alvarez Puebla, R. A.; Pazos Perez, N.; Fery, A. *Langmuir* 2012, 28, 9168.
- (29) Grzelczak, M.; Liz-Marzán, L. M. *Langmuir* 2013, 29, 4652.
- (30) Casu, A.; Cabrini, E.; Donà, A.; Falqui, A.; Diaz-Fernandez, Y.; Milanese, C.; Taglietti, A.; Pallavicini, P. *Chemistry - A European Journal* 2012, 18, 9381.
- (31) Kedia, A.; Kumar, P. S. *Journal of Materials Chemistry C* 2013, 1, 4540.
- (32) Pallavicini, P.; Donà, A.; Casu, A.; Chirico, G.; Collini, M.; Dacarro, G.; Falqui, A.; Milanese, C.; Sironi, L.; Taglietti, A. *Chemical Communications* 2013, 49, 6265.
- (33) Su, Q.; Ma, X.; Dong, J.; Jiang, C.; Qian, W. *ACS Applied Materials & Interfaces* 2011, 3, 1873.
- (34) Wang, Z. D.; Zhang, J. Q.; Ekman, J. M.; Kenis, P. J. A.; Lu, Y. *Nano Letters* 2010, 10, 1886.
- (35) Nhung, T. T.; Bu, Y.; Lee, S.-W. *Journal of Crystal Growth* 2013, 373, 132.
- (36) Yi, S.; Sun, L.; Lenaghan, S. C.; Wang, Y.; Chong, X.; Zhang, Z.; Zhang, M. *RSC Advances* 2013, 3, 10139.
- (37) Lu, L. H.; Ai, K.; Ozaki, Y. *Langmuir* 2008, 24, 1058.
- (38) Yuan, H.; Ma, W.; Chen, C.; Zhao, J.; Liu, J.; Zhu, H.; Gao, X. *Chemistry of Materials* 2007, 19, 1592.
- (39) Kuo, C. H.; Huang, M. H. *Langmuir* 2005, 21, 2012.
- (40) Zou, X. Q.; Ying, E. B.; Dong, S. J. *Nanotechnology* 2006, 17, 4758.
- (41) Van de Broek, B.; Frederix, F.; Bonroy, K.; Jans, H.; Jans, K.; Borghs, G.; Maes, G. *Nanotechnology* 2011, 22.

- (42) Senthil Kumar, P.; Pastoriza-Santos, I.; Rodríguez-González, B.; Javier García de Abajo, F.; Liz-Marzán, L. M. *Nanotechnology* 2008, 19, 015606.
- (43) Stagg, L.; Zhang, S.-Q.; Cheung, M. S.; Wittung-Stafshede, P. *Proc Natl Acad Sci U S A* 2007, 104, 18976.
- (44) Senthil Kumar, P.; Pastoriza-Santos, I.; Rodriguez-Gonzalez, B.; Javier Garcia de Abajo, F.; Liz-Marzan, L. M. *Nanotechnology* 2008, 19, 015606.
- (45) Tam, J. M.; Murthy, A. K.; Ingram, D. R.; Nguyen, R.; Sokolov, K. V.; Johnston, K. P. *Langmuir* 2010, 26, 8988.
- (46) Tam, J. M.; Tam, J. O.; Murthy, A.; Ingram, D. R.; Ma, L. L.; Travis, K.; Johnston, K. P.; Sokolov, K. V. *ACS Nano* 2010, 4, 2178.
- (47) Murthy, A. K.; Stover, R. J.; Borwankar, A. U.; Nie, G. D.; Gourisankar, S.; Truskett, T. M.; Sokolov, K. V.; Johnston, K. P. *ACS Nano* 2013, 7, 239.
- (48) Pazos-Perez, N.; Garcia de Abajo, F. J.; Fery, A.; Alvarez-Puebla, R. A. *Langmuir : the ACS journal of surfaces and colloids* 2012, 28, 8909.
- (49) Pazos-Perez, N.; Wagner, C. S.; Romo-Herrera, J. M.; Liz-Marzan, L. M.; Garcia de Abajo, F. J.; Wittemann, A.; Fery, A.; Alvarez-Puebla, R. A. *Angew Chem Int Ed Engl* 2012, 51, 12688.
- (50) Zhao, Y.; Xu, L.; Liz-Marzán, L. M.; Kuang, H.; Ma, W.; Asenjo-García, A.; García de Abajo, F. J.; Kotov, N. A.; Wang, L.; Xu, C. *The Journal of Physical Chemistry Letters* 2013, 4, 641.
- (51) Luk'yanchuk, B.; Zheludev, N. I.; Maier, S. A.; Halas, N. J.; Nordlander, P.; Giessen, H.; Chong, C. T. *Nature Materials* 2010, 9, 707.
- (52) Frankamp, B. L.; Boal, A. K.; Rotello, V. M. *Journal of the American Chemical Society* 2002, 124, 15146.
- (53) Langille, M. R.; Personick, M. L.; Zhang, J.; Mirkin, C. A. *Journal of the American Chemical Society* 2012, 134, 14542.
- (54) Langille, M. R.; Zhang, J.; Personick, M. L.; Li, S.; Mirkin, C. A. *Science* 2012, 337, 954.
- (55) Chen, J.; Saeki, F.; Wiley, B. J.; Cang, H.; Cobb, M. J.; Li, Z.-Y.; Au, L.; Zhang, H.; Kimmey, M. B.; Li; Xia, Y. *Nano Letters* 2005, 5, 473.
- (56) Kim do, Y.; Yu, T.; Cho, E. C.; Ma, Y.; Park, O. O.; Xia, Y. *Angew Chem Int Ed Engl* 2011, 50, 6328.
- (57) Ma, L. L.; Borwankar, A. U.; Willsey, B. W.; Yoon, K. Y.; Tam, J. O.; Sokolov, K. V.; Feldman, M. D.; Milner, T. E.; Johnston, K. P. *Nanotechnology* 2013, 24.

- (58) Xia, Y.; Nguyen, T. D.; Yang, M.; Lee, B.; Santos, A.; Podsiadlo, P.; Tang, Z.; Glotzer, S. C.; Kotov, N. A. *Nat Nano* 2011, 6, 580.
- (59) Lu, Z.; Ye, M.; Li, N.; Zhong, W.; Yin, Y. *Angewandte Chemie International Edition* 2010, 49, 1862.
- (60) Grzelczak, M.; Mezzasalma, S. A.; Ni, W.; Herasimenka, Y.; Feruglio, L.; Montini, T.; Pérez-Juste, J.; Fornasiero, P.; Prato, M.; Liz-Marzán, L. M. *Langmuir* 2012, 28, 8826.
- (61) Grzelczak, M.; Sánchez-Iglesias, A.; Mezerji, H. H.; Bals, S.; Pérez-Juste, J.; Liz-Marzán, L. M. *Nano Letters* 2012, 12, 4380.
- (62) Zhao, L. L.; Ji, X. H.; Sun, X. J.; Li, J.; Yang, W. S.; Peng, X. G. *Journal of Physical Chemistry C* 2009, 113, 16645.
- (63) Trigari, S.; Rindi, A.; Margheri, G.; Sottini, S.; Dellepiane, G.; Giorgetti, E. *Journal of Materials Chemistry* 2011, 21, 6531.
- (64) Wilcoxon, J. P.; Martin, J. E.; Schaefer, D. W. *Phys. Rev. A* 1989, 39, 2675.
- (65) Xie, J.; Zhang, Q.; Lee, J. Y.; Wang, D. I. C. *Acs Nano* 2008, 2, 2473.
- (66) Schneider, C. A.; Rasband, W. S.; Eliceiri, K. W. *Nat Meth* 2012, 9, 671.
- (67) Goia, D. V.; Matijevic, E. *Colloids and Surfaces a-Physicochemical and Engineering Aspects* 1999, 146, 139.
- (68) Brust, M.; Walker, M.; Bethell, D.; Schiffrin, D. J.; Whyman, R. *Journal of the Chemical Society, Chemical Communications* 1994, 801.
- (69) Xia, Y. S.; Nguyen, T. D.; Yang, M.; Lee, B.; Santos, A.; Podsiadlo, P.; Tang, Z. Y.; Glotzer, S. C.; Kotov, N. A. *Nature Nanotechnology* 2011, 6, 580.
- (70) Murthy, A. K.; Stover, R. J.; Hardin, W. G.; Schramm, R.; Nie, G. D.; Gourisankar, S.; Truskett, T. M.; Sokolov, K. V.; Johnston, K. P. *J Am Chem Soc* 2013, 135, 7799.
- (71) Lu, Z.; Gao, C.; Zhang, Q.; Chi, M.; Howe, J. Y.; Yin, Y. *Nano Lett* 2011, 11, 3404.
- (72) Johnston, K. P.; Maynard, J. A.; Truskett, T. M.; Borwankar, A.; Miller, M. A.; Wilson, B.; Dinin, A. K.; Khan, T. A.; Kaczorowski, K. J. *ACS Nano* 2012.
- (73) Borwankar, A. U.; Dinin, A. K.; Laber, J. R.; Twu, A.; Wilson, B. K.; Maynard, J. A.; Truskett, T. M.; Johnston, K. P. *Soft Matter* 2013, 9, 1766.
- (74) Groenewold, J.; Kegel, W. K. *J. Phys. Chem. B* 2001, 105, 11702.

- (75) Ji, X.; Song, X.; Li, J.; Bai, Y.; Yang, W.; Peng, X. *Journal of the American Chemical Society* 2007, 129, 13939.
- (76) Giorgetti, E.; Trigari, S.; Rindi, A.; Margheri, G.; Sottini, S.; Dellepiane, G.; Brusatin, G.; Brigo, L.; Muniz-Miranda, M.; Timtcheva, I. *physica status solidi (b)* 2012, 249, 1188.
- (77) Jungjohann, K. L.; Bliznakov, S.; Sutter, P. W.; Stach, E. A.; Sutter, E. A. *Nano Letters* 2013, 13, 2964.
- (78) Minati, L.; Benetti, F.; Chiappini, A.; Speranza, G. *Colloids and Surfaces A: Physicochemical and Engineering Aspects* 2014, 441, 623.
- (79) Jana, N. R.; Gearheart, L.; Murphy, C. J. *Chem. Mat.* 2001, 13, 2313.
- (80) Watzky, M. A.; Finke, R. G. *Journal of the American Chemical Society* 1997, 119, 10382.
- (81) Xie, J.; Lee, J. Y.; Wang, D. I. C. *Chem Mater* 2007, 19, 2823.
- (82) Dreaden, E. C.; Alkilany, A. M.; Huang, X.; Murphy, C. J.; El-Sayed, M. A. *Chem. Soc. Rev.* 2012, 41, 2740.
- (83) Halas, N. J.; Lal, S.; Chang, W.-S.; Link, S.; Nordlander, P. *Chem. Rev.* 2011, 111, 3913.
- (84) Khlebtsov, N. G.; Dykman, L. A.; Krasnov, Y. M.; Mel'nikov, A. G. *Colloid Journal* 2000, 62, 765.

Chapter 3: Concentrated Dispersions of Equilibrium Protein Nanoclusters That Reversibly Dissociate into Active Monomers¹

Stabilizing proteins at high concentration is of broad interest in drug delivery, for treatment of cancer and many other diseases. Herein, we create highly concentrated antibody dispersions (up to 260 mg/ml) theorized to comprise of dense equilibrium nanoclusters of proteins [monoclonal antibody (mAb) 1B7, polyclonal sheep Immunoglobulin G (IgG) and bovine serum albumin (BSA)], which upon dilution *in vitro* or administration *in vivo*, remain conformationally stable and biologically active. The extremely concentrated environment within the nanoclusters (~700 mg/ml) could provide conformational stability to the protein through a novel self-crowding mechanism, as shown by computer simulation, while the primarily repulsive nanocluster interactions result in colloidally-stable, transparent dispersions. The nanoclusters are formed by adding trehalose as a co-solute which strengthens the short-ranged attraction between protein molecules. The diffusion coefficient of entities present in the dispersions was seen to be significantly lowered compared to the calculated value for the protein monomer which was interpreted as the nanocluster size and will be represented as such in this Chapter. The hypothesized protein nanocluster diameter was reversibly tuned from 50 to 300 nm by balancing short-ranged attraction against long-ranged electrostatic repulsion of weakly charged protein at a pH near the isoelectric point (pI). This behavior is described semi-quantitatively with a free energy model which includes the fractal

¹ Reproduced in large part with permission from: Johnston, K. P.; Maynard, J. A.; Truskett, T. M.; Borwankar, A. U.; Miller, M. A.; Wilson, B. K.; Dinin, A. K.; Khan, T. A.; Kaczorowski, K. J. *ACS Nano* **2012**, 6 (2) 1357-1369. Copyright 2012 American Chemical Society. A. U. Borwankar, A.K. Dinin, M.A. Miller, and B.K. Wilson conducted the experiments. T.A. Khan and K.J. Kaczorowski conducted the animal studies. A. U. Borwankar, A.K. Dinin, M.A. Miller, B.K. Wilson, K.P. Johnston and J.A. Maynard planned the experiments. A.U. Borwankar, K.P. Johnston and T.M. Truskett developed the free energy model. A.U. Borwankar, K.P. Johnston, T.M. Truskett and M. A. Miller wrote the manuscript.

dimension of the clusters. Upon dilution of the dispersion *in vitro*, the clusters rapidly dissociated into fully active protein monomers as shown with biophysical analysis (SEC, dynamic light scattering (DLS), circular dichroism (CD) and SDS-PAGE) and sensitive biological assays. Since the concept of forming nanoclusters by tuning colloid interactions is shown to be general, it is likely applicable to a variety of biological therapeutics, mitigating the need to engineer protein stability through amino acid modification. *In vivo* subcutaneous injection into mice results in indistinguishable pharmacokinetics *versus* a standard antibody solution. Stable protein dispersions with low viscosities may potentially enable patient self-administration by subcutaneous injection of antibody therapeutics being discovered and developed.

3.1 INTRODUCTION

The crowded macromolecular environment within cells (~400 mg/ml) is known to favor the compact native state of proteins over unfolded conformations.^{1,2} Proteins are stabilized against unfolding by the presence of other macromolecules as described with scaled particle theory,^{2,3} simulation,⁴⁻⁶ and experiment,^{2,7-11} not only in cells, but also *in vitro*.^{2,4,6-8,12,13} High volume fractions of molecules ($\phi \sim 0.3$ to 0.4) effectively “crowd out” (i.e., entropically penalize) more expanded, non-native protein conformations. Simulation and theory with coarse-grain models also predict that high concentrations ($c > 400$ mg/ml) of a single type of protein in solution would favor a compact state via a self-crowding mechanism.^{5,6} However, proteins are rarely soluble at these high concentrations as a result of which stable protein solutions at these ultrahigh concentrations have not been realized experimentally. Also even at intermediately high concentrations, proteins

tend to gel in part due to specific short-ranged attractive interactions, especially hydrogen bonding and hydrophobic interactions.^{2,14-18} In fact, at concentrations of 100 to 300 mg/ml, proteins in solution can become increasingly susceptible to irreversible aggregation,^{2,19,20} gelation and precipitation.^{14,16-18} Therefore to avoid gelation, while simultaneously attaining “local” protein concentrations high enough to stabilize the native conformation via self-crowding, novel types of stable and reversible protein assemblies (e.g., nanoclusters) are needed.

Insights into nanocluster formation and phase behavior of protein solutions may be obtained from considering model polymeric colloid suspensions.^{16,17,21-25} In the latter, tunable short-range colloidal attractions (e.g., cosolute-induced depletion interactions) are often present.^{21,25} Strengthening attraction (e.g., by increasing co-solute concentration) causes highly polydisperse particle assemblies to form, which can percolate and then gel near the colloid phase separation boundary.^{21, 25,26} Whereas phase separation and gelation can result from strong attraction between uncharged colloids at high concentrations,^{16,21,22} the physics change qualitatively when weak, longer-range electrostatic repulsion is also present between particles.^{16,25} In such cases, as predicted with an equilibrium model,^{27,28} long-lived and very large clusters of primary colloidal particles (i.e., cluster/particle diameter ratios of 5-10) have been observed in single-phase organic solvents (Fig. 3.1a).^{16,23,25,27,28} These clusters form due to the presence of both short and long-ranged interactions at the monomer scale which, in turn, produce diverse multi-scale (monomer-monomer, monomer-cluster, and cluster-cluster) interactions that affect both self-assembly and transport properties of the particles in dispersion.

Clusters of proteins observed to date in water have been small^{23,29} ($N \sim 10$, cluster/particle diameter ratio of 2.5), dilute,²⁶ and short-lived.^{29,30} Recently, reversible

clusters of 5 nm Au particles in water have been assembled with diameters from 30 to 100 nm (nanocluster/particle diameter ratios from 6 to 20) by tuning the charge on the Au particles with a weakly adsorbing non-electrolyte.^{31,32} More recently, nanoclusters have been reported for particles of CdSe.³³ It remains a challenge to properly balance the attractive and repulsive interactions to form large nanoclusters of proteins.

In analogy with the model colloid systems discussed above, the strength of effective protein-protein attractions in solution can also be tuned through the presence of co-solutes. For example, even co-solutes that interact weakly with the proteins still affect protein-protein interactions because of depletion attraction (Fig. B1).^{3,12,34} Depletion attraction is known to strongly influence the equilibrium behavior^{2,35} and rates^{2,36} of association of proteins into dimers or small oligomers. However, this behavior has received far less attention than other related crowding (i.e., excluded volume) effects that low^{3,9,10,12,37,38} and high^{2,4,8,13} molecular weight co-solutes have on protein folding or binding. The potential of mean force for depletion attraction between proteins, $V_{dep}(r)$ is proportional to the concentration of the co-solute c_E , as described with scaled particle theory^{3,12} or by the Asakura-Oosawa model.^{16,24,25,34,39-42} For model monomeric and oligomeric co-solutes at a fixed high concentration, V_{dep} can produce a strongly attractive osmotic second virial coefficient for a wide range in diameter ratio of extrinsic co-solute to that of protein monomer (0.02 to 1).^{21,22,39,40,43} An example of a diameter ratio of 0.1 would be a ~10 nm protein and a ~1 nm disaccharide. Thus, similar to the behavior of model colloids, depletion attraction due to co-solutes, such as trehalose at high concentrations could potentially be utilized to provide sufficient attraction to balance weak electrostatic interactions and form large protein nanoclusters.

Herein we assemble ~100 nm equilibrium clusters of proteins (mAb 1B7, polyclonal sheep IgG and BSA), which dissociate into stable protein monomer upon dilution in buffer. The nanocluster size is interpreted based on the lowered diffusion coefficient seen for the high co-solute samples which was converted to a cluster size based on the Stokes-Einstein equation. Although the validity of the above approach is not known, the current Chapter utilizes the above method of analysis to determine a cluster size. The nanoclusters are formed simply by gently mixing lyophilized protein powder containing trehalose, with buffer solution yielding protein concentrations up to 267 mg/ml for mAb 1B7, 350 mg/ml for IgG and 400 mg/ml for BSA. To drive formation of large clusters in water, we (1) minimize the net protein charge with a buffer pH near the pI to weaken electrostatic repulsion, and (2) add high concentrations of a co-solute, trehalose, to provide strong depletion attraction. The size of the nanoclusters is either increased or decreased reversibly over a continuum by varying the concentration of co-solute, as shown by DLS. The cluster size is predicted qualitatively by an extension of an earlier free energy model to account for the fractal dimension (δ_f) of the cluster. By adjusting co-solute volume fraction ϕ_E and the pH, hierarchical (protein-protein, protein-cluster, and cluster-cluster) interactions were generated to promote assembly of fluid dispersions of nearly monodisperse, weakly-interacting protein nanoclusters hypothesized to have ultra-high internal volume fractions ($\phi > 0.5$ or $c > 700$ mg/ml). The high internal ϕ stabilizes proteins in their folded state via self-crowding, as shown theoretically.^{5,6}

The protein stability after delivery as nanoclusters is of interest in protein therapeutics. After diluting the nanoclusters in buffer, they are shown to dissociate to monomeric protein by DLS,⁴⁴ SEC, and SDS-PAGE. The protein is demonstrated to be folded by CD, thermodynamically stable by determination of the apparent melting

temperature (T_m),⁴⁵ and biologically active by an ELISA.⁴⁶ Finally, the low viscosity of 40 cP, hypothesized to result from weak intercluster interactions, would allow for subcutaneous injection of the concentrated clusters at concentrations up to 267 mg/ml. As an indication of the ability of these nanoclusters to dissociate and deliver active proteins, an *in vivo* bioavailability study is performed with mice. The dispersed protein nanocluster dose delivered in blood is compared to that delivered by both subcutaneous and intravenous doses of dilute mAb solution, with activity of protein in the bloodstream quantified by both ELISA and an *in vitro* antibody neutralization assay.⁴⁷

3.2 METHODS

3.2.1 Formation of nanocluster dispersions

The murine IgG2a antibody 1B7 was expressed, purified and characterized as previously reported⁴⁶ and the isoelectric point (pI) determined via silver stained isoelectric focusing gel. Prior to lyophilization, the mAb 1B7 solution was buffer exchanged into a 20 mM histidine buffer (pH 5.5) using a 30,000 molecular weight cutoff (MWCO) Centricon filter and solid α,α -trehalose added to obtain a 1:1 protein: trehalose weight ratio as a cryoprotectant. The solution was filter-sterilized (0.22 μ m), diluted to 20 mg/ml protein with 20mM histidine buffer (pH 5.5), and transferred to a sterile 8 ml glass vial. It was frozen over 6 hours on a pre-cooled lyophilizer tray at - 40°C (VirTis Advantage Plus Benchtop Freeze Dryer) and then lyophilized at 150 mTorr with 12 hours of primary drying at - 40°C followed by a 6 hour ramp to 25°C and an additional 6 hours of secondary drying at 25°C. To create a dispersion, typically 56 mg \pm 0.02 mg of lyophilized protein powder was compacted into a pre-weighed 0.1 ml conical vial

(Wheaton Science Products). The total volume and volume fractions of the components were calculated assuming ideal mixing based on known masses, and hypothetical pure liquid protein (1.35 g/cm^3) and trehalose (1.64 g/cm^3) densities, from their partial molar volumes at infinite dilution^{48,49} to calculate the required buffer volume. After addition of the calculated 50 mM sodium phosphate buffer (pH 7.2) the resulting dispersion was stirred gently with a 25 gauge needle. The final protein concentration was verified using a BCA assay or A280 with a mass extinction coefficient of $1.37 \text{ L/g}\cdot\text{cm}$ (Nanodrop, Thermo Scientific).

3.2.2 Characterization of the nanocluster dispersions

The diffusion coefficients of protein monomers and nanoclusters were measured by dynamic light scattering (DLS) with a 632.8 nm (red) laser and an avalanche photodiode at $\sim 23^\circ\text{C}$ using CONTIN (Brookhaven BI-9000AT) and converted to hydrodynamic diameters using the Stokes-Einstein equation. According to a study of DLS and rheology of concentrated colloids, the assumption is relatively accurate at our highest ϕ of 0.25.⁴⁴ At higher ϕ s, interactions between particles during the time scale of the measurement may produce much larger deviations from the Stokes-Einstein equation. In this study, the scattering angles ranged from 135° to 165° to minimize multiple scattering⁴⁴ with the use of a 60 μl sample cell (Beckman Coulter). The scattering measurements for each sample of protein monomer or nanocluster were done at two separate angles consisting of 135° , 150° or 165° and the size was found to be within 5-10% between the two angles. For determining the fractal dimension of the IgG nanoclusters (Fig. B3), the scattered laser light intensity was measured at scattering

angles every 5° between 45° and 90° using a cylindrical 2 ml capacity ampoule for a static light scattering (SLS) measurement.

To prepare samples for scanning electron microscopy (SEM, Hitachi S-5500 at 30 kV), the dispersions were diluted to 40 mg/ml at a constant co-solute volume fraction of 0.18 (corresponding to original concentration of 220 mg/ml) using PEG 300 as a co-solute, placed on a copper TEM grid with a carbon film coated with formvar, blotted to remove the excess liquid, rapidly frozen by immersion in liquid nitrogen and lyophilized.

The viscosity of the nanocluster dispersions were measured in triplicate using a 25 gauge (ID = 0.1 mm) 1.5” long needle attached to a 1 ml syringe, according to the Hagen-Poiseuille equation. The time to draw the dispersion from a height from the bottom of the cone from 0.4” to 0.1”, corresponding to a volume of ~ 50 µL was determined from image analysis of a digital video.⁵⁰ A linear correlation between the time to draw 0.05 ml from the conical vial and the viscosity of various calibration fluids is shown in Fig. B7.^{50,51} The shear rate varied decreased with the viscosity and was 1000 s⁻¹ at a viscosity of 50 cp. The solvent or trehalose solution viscosities were calculated from Uchida et al.⁵²

3.2.3 Characterization of the protein structure and activity

To monitor antibody structure and ligand-binding activity, both the lyophilized protein powder and the protein dispersions were diluted to 1 mg/ml in phosphate buffered saline (PBS), prior to analysis by a battery of biophysical and biochemical assays with the original dilute protein solution as a control. Typically, the dilution was performed within ~4-6 hours of the formation of the dispersion. CD measurements were collected from 260 to 185 nm in 0.1 nm steps using a Jasco J-815 CD Spectrometer. The formation of insoluble and di-sulfide linked aggregates was monitored by analysis of 5 µg samples

of dilute protein on a 4-20% non-reducing SDS-PAGE. Formation of non-covalent aggregates was monitored by SEC, with 20 µg of diluted dispersion analyzed using a Waters Breeze high performance liquid chromatograph (HPLC). To analyze ligand-binding activity, an indirect PTx ELISA was performed as previously described⁴⁷ and reported as the ratio of 50% effective concentration values (EC_{50}) for the sample to the solution control. The T_m was quantified with using a 7900HT thermocycler from Applied Biosystems and SYPRO Orange Protein Gel Stain (Sigma-Aldrich).⁴⁵

3.2.4 In vivo bioavailability in BALB/c mice

An *in vivo* pharmacokinetic study of the mAb 1B7 dispersion and a control solution was performed over a 14 day period using 24-27g, female BALB/c mice. The three sample groups included (1) intravenous (IV) and (2) subcutaneous (SQ) control injections of 100 µl of a dilute mAb 1B7 solution and (3) a test condition, SQ injection of an antibody dispersion (235 mg/ml in a 1 µl volume to yield a 9.4 mg/kg dose). Serum samples (~20 µl) were collected from the tail vein prior to injection and then at eight additional time-points between 12 and 336 hours. At the terminal time-point, mice were anaesthetized and serum collected by cardiac puncture. This study was performed with approval by the Institutional Animal Care and Use Committee at the University of Texas at Austin (protocol #AUP-2010-00070) in compliance of guidelines from the Office of Laboratory Animal Welfare. To determine the concentration of active mAb 1B7 in each serum sample, an indirect PTx ELISA was performed as previously described.⁴⁶ Each plate included mouse serum (Sigma) as a negative control and a mAb 1B7 diluted in mouse serum to obtain a standard curve. SoftMax Pro v5 was used to calculate EC_{50} values based on the serum dilution using a 4 parameter logistic (4PL) model and total

concentrations of active mAb 1B7 present in serum samples calculated on the basis of the standard curve. An orthogonal antibody activity assay, based on *in vitro* chinese hamster ovary (CHO) cell neutralization of PTx, was performed using serum from the terminal time point.⁴⁶

3.3 RESULTS AND DISCUSSION

3.3.1 Nanocluster morphology and tunability with trehalose and dilution in buffer

Fig. 3.1b shows a colloiddally-stable, transparent dispersion of mAb 1B7⁴⁶ that were formed immediately upon gentle stirring of lyophilized protein powder (with a 1:1 mass ratio of trehalose to protein) in phosphate buffer solution at the pI (pH 7.2). The concentrations of protein, c , and extrinsic co-solute, trehalose, c_E , were each 220 mg/ml. The low turbidity is a consequence of the small D_c and small difference in refractive indices of the porous cluster and solvent. The SEM images of the dispersions after cryo-preparation revealed ~300 nm nanoclusters composed of primary particles about the size of protein monomer, ~11 nm (Fig. 3.1c and Fig. B1) although the sample preparation is somewhat questionable. The “halos” about the primary particle the nanoclusters are a result of trehalose deposition during SEM sample preparation, and thus of minor interest. An artist’s rendering of these clusters in dispersion in Fig. 3.1d. For $c = c_E = 220$ mg/ml, the average hydrodynamic diameter, D_c , of the nanoclusters from dynamic light scattering (DLS) was estimated to be 315 nm (std. dev. in peak width of 6% over the mean) in agreement with the SEM images (Fig. 3.2a). For the porous clusters, the volume fraction of protein within a cluster ϕ_{int} , was estimated to be 0.6 with static light scattering (SLS, Fig. B2), as a function of the fractal dimension (δ_f) (Eq. B9). The δ_f is the slope in

the log-log plot of the intensity against the scattering vector. The fractal dimension in the case of 50 nm IgG clusters was found to be 2.6 versus 3, 2 and 1 for completely space filled spheres, disks and long thin rods respectively, which suggests that the protein has a high volume fraction inside the nanoclusters.

Upon successive dilutions of the 220 mg/ml 1B7 dispersion in phosphate buffer to maintain a constant c/c_E ratio, D_c decreased over a continuum as proteins dissociated from the cluster (Figs. 3.2a and 3.2b). D_c then reached a plateau at ~ 12.3 nm for $I = c_E = 75$ mg/ml, the expected size of monomeric mAb. Similarly, dilution of c_E from 270 to 150 mg/ml with c fixed at 70 mg/ml was used to tune the cluster size until reaching a c_E below which only ~ 10 nm species, presumably antibody monomers, were observed (Fig. 3.2b and 3.2c). The trehalose concentration was decreased using pH 7.2 phosphate buffer along with small amounts of dispersion with $c = c_E = 100$ mg/ml to maintain a constant c . Upon subsequently increasing c_E back to 270 mg/ml, the original D_c values of ~ 300 nm were recovered. Similar experiments with a polyclonal sheep IgG mixture (Fig. 3.2d and Figs. A1b and A3) resulted in the same trends. Fig. B1b shows a nanocluster of sheep IgG from a dispersion at $c = c_E = 260$ mg/ml, which was diluted down to 50 mg/ml followed by cryo-preparation. The IgG nanocluster size decreased from ~ 80 nm at $c_E = 270$ mg/ml to ~ 10 nm (monomeric protein) for $c_E = 150$ mg/ml at a constant $c = 50$ mg/ml (Fig. 2d). (When increasing c_E , a 500 mg/ml trehalose solution in pH 6.4 phosphate buffer (pI of IgG) was used along with small amounts of dispersion with $c = c_E = 200$ mg/ml to maintain a constant c). Very similar values of D_c were observed upon either increasing or decreasing the trehalose concentration. This reversibility in nanocluster size suggests the nanoclusters were in an equilibrium state, based on the predictions from the free energy model. The cluster size for the sheep IgG also decreases

from 80 nm to 11 nm (monomeric protein) when the dispersion was sequentially diluted in pH 6.4 phosphate buffer from $c = c_E = 260$ mg/ml to $c = c_E = 47$ mg/ml as shown in Fig. B3. Taken together, these data theorize about a novel type of long-lived (tested for several hours) well-defined nanocluster in aqueous media, with reversible equilibrium behavior, which was unexpected.^{23,26,29}

To demonstrate further the generality of the technique, clusters were also formed with macromolecular co-solutes including PEG (M.W. 300), N-methylpyrrolidone (NMP) and dextran (M.W. 10,000). With sheep IgG at a concentration of 162 mg/ml with 162 mg/ml trehalose and 20% (v/v) PEG-300, the cluster diameter was 110 nm. For sheep IgG at a concentration of 157 mg/ml with 157 mg/ml trehalose, 10% (v/v) PEG-300 and 20% (v/v) NMP, the clusters were ~250 nm in diameter. Also 315 mg/ml BSA with 5% (v/v) PEG300 and 20% (v/v) ethanol yielded clusters of size 30 nm (BSA monomer is 4-5 nm). Whereas the focus of the current study was on a low molecular weight co-solute, trehalose, these examples with macromolecular co-solutes (data not shown in this dissertation), illustrate the generality of the technique. Apart from that, in order to demonstrate the possibility of using this technique at higher concentrations of protein as a proof of concept, higher concentration dispersions of proteins were prepared. Fig. 3.3 shows nanoclusters of BSA at a very high c of 400 mg/ml and $c_E = 240$ mg/ml which have a $D_c = 40$ nm. The number of protein monomers in this case, about 1000, in the cluster is of the same order as the clusters formed from mAb 1B7 and sheep IgG. Highly concentrated dispersions are also shown for sheep IgG in Fig. B4 where nanoclusters with D_c of ~100 nm were observed for $c = 300$ and 350 mg/ml and $c/c_E = 1:0.5$ where trehalose was the co-solute.

3.3.2 Protein stability after dilution of the nanoclusters

A major concern for protein formulations at high concentration is the potential for individual protein monomers to misfold and form irreversible aggregates. These events may result from the dynamic nature of proteins: at any given moment, a system of identical proteins will present an ensemble of related three-dimensional structures, some of which transiently expose normally buried hydrophobic patches. At low concentrations, proteins will frequently recover their native conformation, but at high concentration the probability of two proteins with exposed hydrophobic patches colliding and associating irreversibly is high.⁹ These misfolded and irreversibly aggregated proteins do not present the native structure and therefore exhibit reduced potency and, due to their modified apparent size and exposed surface charges, altered pharmacokinetics. Moreover, the presentation of these non-native surfaces to the immune system can induce a response against the therapeutic protein, which will in itself change biological activity and pharmacokinetics.⁵³

As discussed below, simulation results of earlier studies^{2,5,6} suggest that the folded state is strongly favored for model proteins at high concentrations (i.e., values comparable to the local protein concentration within the nanoclusters). To investigate this hypothesis, experimental studies on actual mAbs are needed to determine whether proteins in the nanoclusters are in the folded state upon dissociation of the nanoclusters to protein monomer. To determine whether irreversible protein aggregates are formed in our 1B7 nanocluster dispersions at 267 mg/ml, we performed a battery of biophysical and biochemical tests. The dispersions were diluted several hours after formulation, as long term storage stability is outside the scope of this work. However, proteins within the dispersion were stressed through viscosity testing earlier, as it was drawn through a 25

gauge needle, subjecting it to significant shear forces with a shear rate estimated to be as high as 9500 s^{-1} assuming a Newtonian fluid. Remarkably, after dilution to 1 mg/ml in PBS, we were unable to detect a change in protein conformation or activity relative to the control antibody in solution (Table 3.1). Prior to dispersion, analysis of a control 1B7 antibody solution in PBS exhibited a stability typical of monoclonal antibodies,⁵⁴ with an apparent thermal unfolding transition temperature (T_m) of 68 °C (Table 3.1) and an unfolding midpoint at 6.2 M urea. After dilution of the dispersion, the T_m was again measured to be 68 °C (Table 3.1). Since a T_m change of two-to-three degrees indicates a change in conformational stability, this data demonstrates that the average mAb 1B7 thermal stability was not altered meaning that its folded structure is probably unaffected.⁵⁵ CD was used to monitor the presence of secondary structural elements in proteins as a function of absorption of polarized light at particular wavelengths. Both the control solution and diluted dispersion retained the same strong negative signal at 217 nm, indicative of the folded β -sheet structure characteristic of antibodies (Fig. 3.4a and Table 3.2).⁵⁶ Table 3.2 shows the secondary structure as estimated by Dichroweb, using the CDSSTR fitting algorithm. It is generally accepted that a normalized root mean square deviation (NRMSD) of < 0.1 indicates a good fit.⁵⁷ As shown in Table 3.2 the calculated percent β -sheet structure (the predominant secondary structure in antibodies) does not differ between the mAb 1B7 control solution and the diluted dispersion.

Finally, two additional sizing methods were used to directly assess whether or not a small population of misfolded and larger molecular weight aggregates was present. HPLC-SEC and SDS-PAGE analyses of the diluted dispersions show a negligible increase in higher molecular weight aggregates, when compared with the initial solution control (Table 3.1 and Figs. B5 and B6). The presence of aggregates was also not

apparent by DLS in the sharp monomer peaks (Fig. 3.2a and 3.2c). HPLC-SEC is able to discriminate mAb monomers from non-covalent and covalent aggregates, while non-reducing SDS-PAGE detects covalent oligomers. Fig. B5 also shows the HPLC-SEC data for the intermediate steps in the dilution experiment for the 1B7 dispersion that are shown by DLS in Figs. 3.2a and 3.2c. In all cases, there was not an increase in aggregates over the initial solution control.

Although these biophysical tests (SEC, DLS, CD and SDS-PAGE) did not detect protein structural perturbations or aggregation, it is possible that the dispersed samples may have folded monomeric protein that does not retain biological activity. Thus, sensitive biological assays were used for determining activity that may be applied for protein concentrations < 10 ng/ml. To monitor ligand binding activity, indirect ELISAs using pertussis toxin as a capture molecule measured the mAb 1B7 activity in terms of the relative 50% effective concentration ($EC50_{disp}/EC50_{control}$). This ratio is the concentration of antibody resulting in 50% of the maximum ELISA response for the dispersion (after dilution to 1 mg/mL) to that for an unmodified control solution. Here, the diluted dispersion yielded a relative activity of 1.03 ± 0.20 , which is indistinguishable from measurements made with the solution control (Table 3.1).⁵⁸ This result demonstrates that antigen binding ability, a powerful measure of protein activity, is identical for antibody recovered upon diluting a dispersion and a solution control.

The experimentally demonstrated stability of the native protein state in the large self-crowded nanoclusters may be anticipated from coarse-grain globular protein models^{5,6} (Fig. 3.4b). Specifically, for ultrahigh volume fractions of proteins within the nanoclusters ($\phi_{int} \sim 0.6$), the fraction of folded protein approaches unity. This reflects the entropic self-crowding (inset in Figs. 3.4b, 3.1c and 3.1d) penalty for unfolding to more

expanded non-native conformations, which overwhelms other factors (e.g., the increase in both chain conformational entropy and favorable hydrophobic protein-protein interactions upon unfolding) that can otherwise destabilize the native state in less crowded environments. Importantly, the high ϕ_{int} within the clusters (> 400 mg/ml) strongly favors the native state via self-crowding, even for overall ϕ values where proteins aggregate and unfold when in solutions without clusters.

Although protein stability and conformation were not measured experimentally within the nanoclusters, upon dilution, mAb 1B7 was clearly active, stable, and monomeric. Thus irreversible aggregates were not present within the nanoclusters, despite the high protein concentrations. As discussed above, within the nanoclusters, the native conformation would be expected to be entropically stabilized by protein self-crowding. In addition, the relatively low mobility of the proteins in the clusters, given the high intraccluster concentrations of ~ 700 mg/ml, may kinetically frustrate protein conformational changes that could otherwise lead to contact between hydrophobic patches and stabilize non-native complexes and aggregated states.

During these in vitro dilution experiments, the rapid dissolution (estimated to be <1 msec, see Appendix B.2) also lowers the probability of protein collisions that may otherwise produce irreversible aggregates. Immediately upon dilution, concentration and solubility gradients will result in release of mAbs from the nanocluster surface, while those buried within the nanocluster remain self-crowded, thus favoring stable folded protein within the nanocluster. This hypothesis is supported by the absence of an increase in the aggregates based on HPLC-SEC data and SDS-PAGE data upon dilution of the clusters, which decreases D_c , as is shown in Figs. B5 and B6. Finally, the trehalose within the dispersion is present as the nanoclusters dissolve and promotes protein folding.

3.3.3 Mechanism of assembly of proteins into nanoclusters

Assembly of non-gelling dispersions of monodisperse protein nanoclusters relies on properly balancing hierarchical, multi-scale interactions. Proteins should attract one another (favoring cluster formation), individual proteins should interact neutrally with the clusters²⁷ (limiting cluster size), and nanoclusters should repel one another (avoiding gelation). Fig. 3.5a shows estimates for the contributions to the potential of mean force $V(r)$ for two mAb 1B7 molecules (the parameters used in this case are given in Table B1). For a dispersion pH 3 units away from pI, $V_{el}(r)$ is strongly repulsive. At these conditions, as should be expected, only very small clusters have been observed, as seen for lysozyme.²³ Near the pI, V_{el} becomes very weak and thus with a strong V_{dep} for $c_E = 220$ mg/ml, $V(r)$ is attractive. This attraction may now be shown to drive formation of clusters, as described by the equilibrium free energy model. To understand the cluster formation mechanism, consider an aqueous solution of protein and relatively concentrated co-solute at conditions near the protein's pI. Two proteins in this system will strongly attract one another because the magnitude of electrostatic repulsion between the weakly charged monomers is vanishingly small compared to the short-range depletion attraction (Fig. 3.1a and 3.5a). However, the interaction between a protein monomer and a cluster of proteins is more complex because the monomer feels, in addition to the short-range depletion attraction, the net effect of weak, longer-ranged repulsion from the multiple charged proteins within the cluster. This interaction can be attractive or repulsive depending on the size of the cluster.^{27,28} If the cluster is sufficiently large, then these repulsions balance the depletion attraction, limiting further cluster growth (Fig. 3.1a). The equilibrium cluster size increases with increasing strength of depletion interactions between the protein monomers (e.g., with increasing co-solute concentration)

and decreases with the increasing strength of the repulsive interactions (e.g., with number pH units away from the pI). Because of their collective electrostatic repulsions, it will be shown that fully grown clusters in solution do not attract one another.

The contours for protein cluster diameters, D_c , shown in Fig. 3.5b were computed from an extension of a simple equilibrium free energy model^{27,28} which has previously been applied to understand clustering of polymeric colloids in organic solvents.²⁵ In that model, D_c is determined by a balance between short-range interparticle attraction and weak, longer-range electrostatic repulsion. To understand the equilibrium model, consider n_c proteins of radius R that form a cluster of radius R_c in solution, as shown in Fig. 3.1a. In our analysis, the only attraction we explicitly consider is the co-solute-mediated depletion interactions, which (as explained above) is the dominant attractive interaction under strong clustering conditions. If the depletion interaction between two proteins is $-\varepsilon$, and each protein has C nearest neighbors in the cluster interior, then the effective depletion contribution to the free energy per protein molecule in the cluster interior will be $-\varepsilon C/2$. The “missing” depletion interaction pairs for proteins on the cluster surface are accounted for by adding an effective surface energy term ($4\pi R_c^2 \gamma$), where the surface tension is approximated as $\gamma = \varepsilon/4\pi R^2$. In other words, the depletion attractions contribute the following to the cluster free energy,

$$F_{att} = -\frac{\varepsilon C n_c}{2} + 4\pi R_c^2 \gamma \quad (3.1)$$

Assuming that the charges are negligibly screened within the cluster (Appendix B.4), their repulsive self-energy can be approximated by that of a uniform distribution of point charges in a spherical volume with the cluster radius R_c , i.e.,

$$F_{rep} = \frac{3\lambda k_B T n_c^2 q^2}{5R_c} \quad (3.2)$$

where λ is the Bjerrum length ($\lambda = e^2/4\pi\epsilon_r\epsilon_0 k_B T$), ϵ_r is the relative permittivity of the medium, and q is the charge per protein. The minimization of the $F = F_{att} + F_{rep}$ with respect to R_c (or n_c) gives

$$n_c = \frac{10\pi\gamma R^3}{3k_B T \lambda q^2} \quad (3.3)$$

This simple result illustrates that the equilibrium n_c increases with attraction and decreases with electrostatic repulsion. To further understand the cluster free energy in terms of the translational and combinatorial entropy of the counterions dissociating from the proteins, it is instructive to write²⁷

$$F_{entropic} = 2n_c q \left[\ln \left(q/q_0 \right) - 1 \right] \quad (3.4)$$

The quantity q_0 represents the charge per protein q that minimizes the overall cluster free energy (see also Eq. 3.5 below) for conditions corresponding to very low values of ζ potential (where $1/R_c \rightarrow 0$; i.e., the weakly charged systems of interest here). It can be expressed as

$$q_0 = (4\pi n_d / 3\phi)^{1/2} (R/b)^{3/2} e^{-\lambda/(2b-1)} \quad (3.5)$$

where n_d is the number of dissociable sites on a protein surface, b is the distance of closest approach between a counterion and a charge on the protein surface, and ϕ is the volume fraction of proteins in solution. As discussed extensively elsewhere,²⁷ higher values of ϕ generally result in lower q_0 because, with more proteins present in the system, fewer counterions per protein need to dissociate to achieve the same increase in counterion translational entropy. Combining terms, the free energy per protein of a cluster given by²⁸

$$\frac{f_c}{k_B T} = -\frac{\varepsilon C}{2k_B T} + \frac{4\pi R_c^2 \gamma}{k_B T n_c} + \frac{3\lambda n_c q^2}{5R_c} + 2q \left[\ln\left(\frac{q}{q_0}\right) - 1 \right] \quad (3.6)$$

To take into account the porosity of the protein cluster, we modify the original model by expressing the cluster radius as

$$R_c = \left(\frac{n_c}{k} \right)^{\frac{1}{\delta_f}} R \quad (3.7)$$

where δ_f is the fractal dimension (2.6 from Fig. B2) and k is a constant chosen as unity. The resulting modified free energy equation is

$$\frac{f_c}{k_B T} = \frac{\varepsilon C}{2k_B T} + \frac{\varepsilon n_c^{\left(\frac{2}{\delta_f}-1\right)}}{k_B T k^{2/\delta_f}} + \frac{3\lambda n_c^{\left(1-\frac{1}{\delta_f}\right)} q^2}{5R_c k^{1/\delta_f}} + 2q \left[\ln\left(\frac{q}{q_0}\right) - 1 \right] \quad (3.8)$$

Minimizing f_c with respect to n_c at $q = q_0$ gives the following estimate for the equilibrium aggregation number (n^*)

$$n^* = k^{\frac{3}{3-2\delta_f}} \left\{ \frac{5(\delta_f - 2)\varepsilon R}{3(\delta_f - 1)k_B T \lambda q_0^2} \right\}^{\frac{\delta_f}{2\delta_f - 3}} \quad (3.9)$$

As should be expected, the cluster size increases with increased strength of the attraction, ε . Since we are interested here in cases where V_{ssr} (hydrogen-bonding, hydrophobic interactions, etc.) is smaller in magnitude than the co-solute-mediated depletion attraction (Fig. 3.5a); we approximate ε as the contact value of the depletion potential from Appendix B.3 [$-\varepsilon(\phi_E, R/R_E) = V_{dep}(r = 2R)$]. In the limit of solid clusters with $\delta_f = 3$, Eq. 3.9 becomes Eq. 3.3 which is essentially the same as Eq. 23 given by Groenewold and Kegel.²⁷ The only difference is in the coefficient which is explained elsewhere.⁵⁹

Table B2 in summarizes input variables for the model to determine the R_c contours in Fig. 3.5b. The R_c is determined from setting n^* from Eq. 3.9 into Eq. 3.7. The total number of dissociable sites on the protein monomer at a given pH, n_d , was chosen as 50 based on previous estimates.⁵⁶ The fractal dimension is estimated as 2.6 based on the SEM images and SLS measurements (Fig. B2). The ε_r inside the clusters was chosen as 25 as explained in detail in Appendix B.4. The distance between opposite charges in an ionic bond is taken to be ~ 0.1 nm and the protein diameter is 11 nm (Table B2).⁶⁰

The effects of ϕ and ϕ_E on R_c are illustrated in Fig. 3.5b, from the equilibrium model for clustering of colloids,^{27,28} which has been extended to account for the fractal dimension of the cluster (see Eq. 3.9). We assumed based on Fig. 3.5a that short-range attractive interactions between proteins are dominated by depletion attractions (Appendix B.3) at high values of ϕ_E as is evident at contact. This attraction is balanced by weak long-ranged repulsions with negligible electrostatic screening within the dense clusters (Appendix B.3). On a horizontal pathway in Fig. 3.5b, increasing ϕ_E at fixed ϕ

strengthens V_{dep} (crowding) and hence increases R_c . This pathway raises the depletion attraction between protein monomers (higher ε) and therefore the numerator in Eq. 3.9 (and likewise Eq. 3.3) which increases R_c . The predictions of the model are in reasonable agreement with experimental data as shown in Fig. 3.2b and Fig. 3.2d where the cluster size increases with an increase in the c_E . In addition, on a vertical pathway increasing ϕ at fixed ϕ_E lowers the charge per protein in the cluster, because fewer counterions per protein must dissociate to obtain the same balance between entropy and energy in the system,²⁷ which also increases R_c . For the combined change whereby ϕ and ϕ_E decrease upon dilution along a diagonal slant, R_c decreases (Fig. 3.5b). Here both the decrease in depletion attraction and the lower ϕ and its effect on charge produce a decrease in R_c . Again this prediction is in agreement with the experimental data as shown in Figs. 3.2a-d. Our new model, as well as the one it is based on,^{27,28} is only meant to provide qualitative predictions. The model does not consider intracluster charge screening, differences in ε_r inside and outside the cluster, and variations in the attractive interaction with r . However, the simple equilibrium model substantiates the novel experimental discovery of reversible equilibrium nanoclusters and qualitatively predicts the experimental trends in D_c .

In contrast to the predominantly attractive interactions between individual proteins near their pI in Fig. 3.5a, the resulting nanocluster interactions are highly repulsive (Fig. 3.5c). The dominance of intercluster repulsions is due to the large number of weakly charged proteins per cluster (>1000 proteins/cluster and ~ 1 elementary charge/protein) and the longer range of V_{el} (Appendix B.3) which scales as R_c . In contrast, the range of V_{dep} and V_{ssr} (Appendix B.3) is < 1 nm, and thus almost negligible versus the intercluster spacing (Fig. 3.5c inset). Under conditions for which the electrostatic repulsion is insufficient to balance the attractive forces (i.e., very high co-

solute or protein concentrations), the protein can also form a gel.²¹ The spinodal instability associated with this transition in the context of the clustering model²⁸ can be defined as the locus of points where $d^2f_{cl}/dq^2 = 0$ (see gray line in Fig. 3.5b). Note that equilibrium clusters with various sizes may be formed before the gel phase boundary, according to the experimental data and the theoretical cluster size contours.

3.3.4 Viscosity of Nanocluster Dispersions

The very weak attraction between clusters led to a viscosity of the dispersion of mAb 1B7 at $c = 267$ mg/ml of only 40 cP which is a syringeable value (Table 3.3). Similarly, it was 63 cP for polyclonal sheep IgG at $c = 275$ mg/ml. The viscosity of the dispersion is commonly described as a function of the intrinsic viscosity, $[\eta]$, maximum volume fraction of particles, ϕ_{max} , and the solvent viscosity (including co-solute), η_0 , using the Krieger-Dougherty equation^{50,61}

$$\frac{\eta}{\eta_0} = \left[1 - \left(\frac{\phi_{eff}}{\phi_{max}} \right) \right]^{-[\eta]\phi_{max}} \quad (3.10)$$

η may be reduced by lowering η_0 , or $[\eta]$, which can be a minimum of 2.5 for hard sphere colloids, We chose $\phi_{max} = 0.64$, the value for random packed spheres.⁶² The value of effective cluster volume fraction ϕ_{eff} was defined as ϕ/ϕ_{int} , on the basis of the ϕ_{int} from SLS, ~ 0.6 . From Eq. 3.10, $[\eta]$ for both 1B7 and IgG clusters was found to be ~ 7 . At the present time, the variation of ϕ_{int} with nanocluster size is not well understood, thus we assumed a constant value of ϕ_{int} of 0.6 and therefore the values of ϕ_{eff} are only approximate.⁶³ If ϕ_{int} was lower, then the larger ϕ_{eff} would lead to an even smaller $[\eta]$.

Higher $[\eta]$ values of 11-20 are often observed for monoclonal antibody solutions.⁶⁴ Similarly, we observed for monomeric IgG (without trehalose as a co-solute) an $[\eta]$ of 18 at $c = 260$ mg/ml (Table 3.3). Finally at $c = 300$ mg/ml again for $c_E = 0$, the viscosity of the IgG solution was found to be not measureable as the solution was in the form of a gel that did not flow. This gelation was a manifestation of the high $[\eta]$ in solution resulting from attraction between proteins with small spacings. In contrast, the nanocluster dispersions did flow at this c with $c = c_E$, with a viscosity of 250 cP. In principle, this viscosity may be lowered by optimizing the composition of the extrinsic co-solute. More data about viscosity is provided in studies of mAb1 in Chapter 7.

3.3.5 In vivo study of protein stability and pharmacokinetics in mice

To test the potential for drug delivery of protein nanocluster dispersions, we performed an *in vivo* pharmacokinetics (PK) study in mice. Control groups received 100 μ l of dilute antibody solution via intravenous or subcutaneous injection to provide a baseline defined as full bioavailability. 1 μ l of a highly concentrated 235 mg/ml nanocluster dispersion was injected subcutaneously at pH 7.2 (Table 3.4). The viscosity of this dispersion was well below 40 cP (see Table 3.3), which is below the typical limit of 50 cP for subcutaneous injection. Remarkably, the resulting PK parameters, including normalized bioavailability ($AUC/dose$), $C_{max/dose}$, t_{max} and elimination kinetics were statistically indistinguishable from those of the two subcutaneous groups (Fig. 3.6). The similar bioavailabilities suggest that the mAs in the nanoclusters readily dissociated (the predicted time in buffer is 7 ms, Appendix B.2), were transported from the injection site and entered the blood stream, while identical alpha and beta rates indicates the presence of predominantly monomeric mAb in the blood. If mAbs were to aggregate or misfold

during dissolution, the molecular weight and surface properties would change, in turn affecting renal and hepatic clearance rates.⁵³ Finally, analysis of antibody activity in the terminal blood samples with an *in vitro* toxin neutralization test showed similar activities versus control antibody, indicating that, in addition to mAb conformation, activity was unaffected. It is likely this nanocluster drug delivery concept could be extended to even higher dosages, given that dispersion concentrations up to 400 mg/ml for BSA and 350 mg/ml for polyclonal IgG, were attained (Figs. 3.3 and B4). Whereas these tests provide a preliminary indication that the nanoclusters may potentially be used for subcutaneous delivery, further work is needed to address various practical questions beyond the scope of this study, for example, immune response to the injection.

3.4 CONCLUSIONS

Low viscosity dispersions of concentrated protein assumed to be in monodisperse equilibrium nanoclusters, with high conformational stability *in vitro* and high biological activity *in vivo* upon dilution, were formed simply by mixing lyophilized protein, an co-solute and buffer. The high degree of self-crowding of proteins within the nanoclusters at an unusually high concentration of 700 mg/ml is shown theoretically to favor folding, as confirmed experimentally upon dilution of mAb 1B7 nanoclusters. The size of the nanoclusters is tunable by adjusting protein and co-solute concentrations near the pI, as shown both experimentally and with a free energy model. The model proposes that the ability to simultaneously achieve self-crowded clusters and low viscosities results from a general concept of tuning the multi-scale interactions with: attraction dominant at the protein monomer level, repulsion dominant at the intercluster level. The intercluster repulsion favors colloidal stability and low viscosity without gelation. Remarkably, an

analysis with a variety of physical, chemical and biological assays indicated conformationally stable protein monomer without any loss of protein activity was obtained after dilution of the nanocluster dispersions. *In vivo* sub-cutaneous administration of dispersed mAb resulted in indistinguishable pharmacokinetics and activity compared to control antibody solutions. This general approach for formulating dispersions of protein nanoclusters with co-solutes and a pH near the isoelectric point, offers the potential of subcutaneous administration of a variety of therapeutic biologics, which would otherwise gel when formulated as solutions.

Sample	T_m (°C) [†]	% monomer (SEC)	EC ₅₀ (ELISA)
Control solution	67.7 ± 0.3	98.88 ± 0.04	1.00 ± 0.24
Diluted dispersion (from 267 mg/ml)	68.3 ± 0.3	98.59 ± 0.04	1.03 ± 0.20

Table 3.1: 1B7 stability and activity in nanocluster dispersion samples with $c = c_E = 267$ mg/ml diluted to 1 mg/ml in PBS prior to analysis. Error is ± s. d.

Sample	% α -helix	% β -strand	% Turn and Unordered	NRMSD ²
Control solution	0	39	63	0.006
Diluted dispersion (from 267 mg/mL)	1	40	60	0.006

Table 3.2: Estimation of 1B7 Secondary Structure from Circular Dichroism.

Protein concentration (c , mg/ml)	Trehalose concentration (c_E , mg/ml)	Viscosity (η , cP)	ϕ_{eff}	Intrinsic viscosity ($[\eta]$)	Hydrodynamic diameter	Hydro. Diam. St. Dev.
267 (1B7)	270	40	0.32	7.2	315	17
275 (IgG)	275	63	0.33	7.9	88.0	9.0
260 (IgG)	0	57	0.19	18	9.66	1.84

Table 3.3: η and D_c for mAb 1B7 and polyclonal sheep IgG mixture dispersions.

² NRMSD is the normalized root mean square deviations between the calculated and experimental CD spectra. The program CDSSTR was used for all secondary structure estimates via the Dichroweb online analysis.

Sample	C_{\max} / dose ($\mu\text{g/ml}$)/ (mg/kg)	$AUC_{0-\infty}$ / dose ($\mu\text{g}\cdot\text{hr/ml}$)/ (mg/kg)	t_{\max} (hrs)	$t_{1/2,\alpha}$ (hrs)	$t_{1/2,\beta}$ (hrs)	Relative neutralization titer
IV solution	25.5 ± 3.8	3582 ± 990	15.1 ± 0.7	45.7 ± 22.8	227.1 ± 24.9	2.3 ± 1.7
SQ solution	18.8 ± 4.4	2699 ± 583	18.9 ± 3.1	43.4 ± 17.3	210.0 ± 17.4	1.0 ± 1.8
SQ nanocluster dispersion	14.3 ± 3.1	3269 ± 291	21.4 ± 2.9	42.1 ± 24.8	243.2 ± 35.5	1.3 ± 0.5

Table 3.4: Pharmacokinetic parameters for curves shown in Fig. 3.6. Error is \pm s.d.

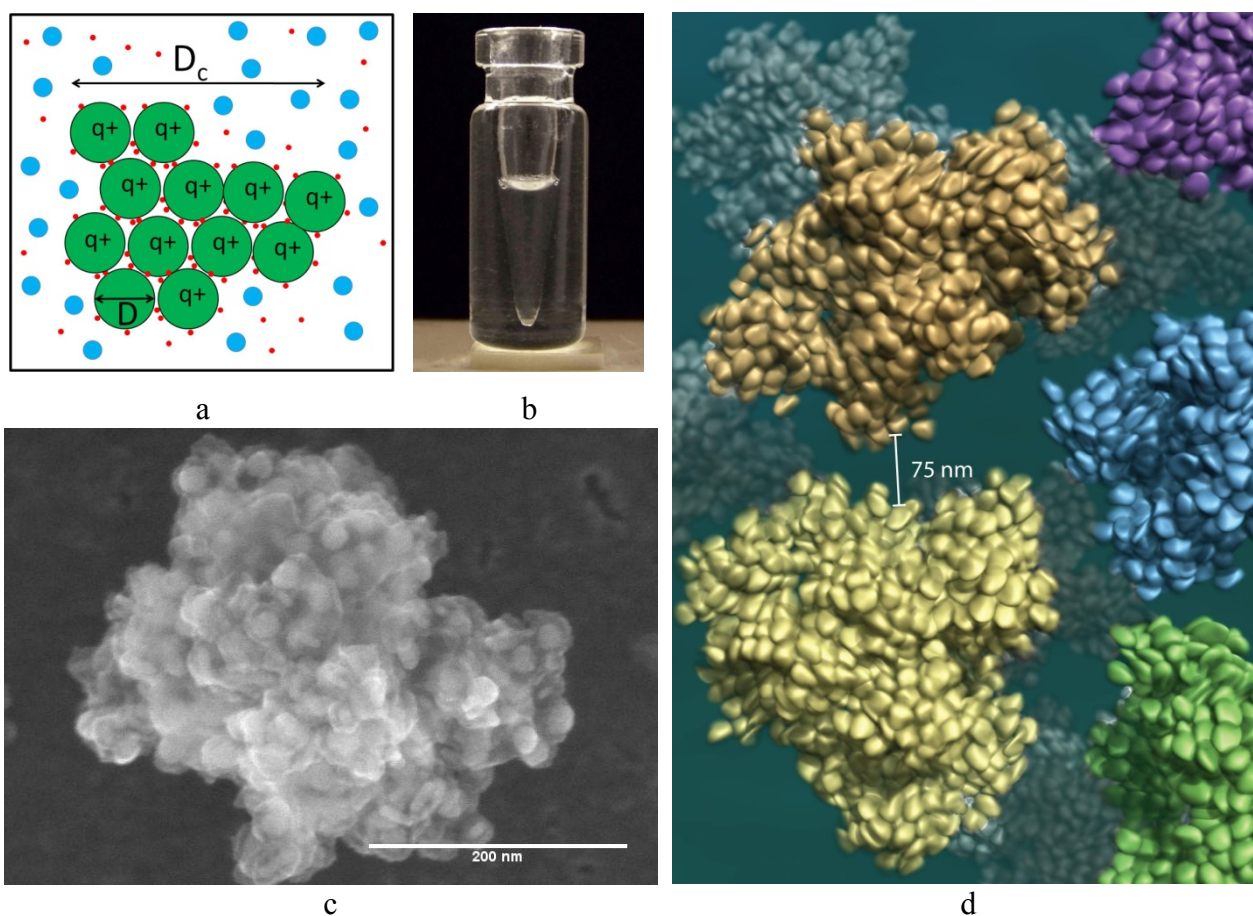


Figure 3.1: Nanocluster morphology for mAb 1B7 with trehalose as extrinsic co-solute. a. Schematic of a nanocluster where in the current study green circles represent proteins, red dots, counterions and blue circles, co-solutes. Similar clusters are observed for colloids in organic solvent. b. Transparent dispersion at $c = c_E = 220$ mg/ml. c. SEM image of 3.1b indicating closely-spaced, self-crowded protein. (The “halo” on the component particles is probably an artifact of trehalose deposition during sample preparation). d. Schematic of dispersion of nanoclusters drawn to scale.

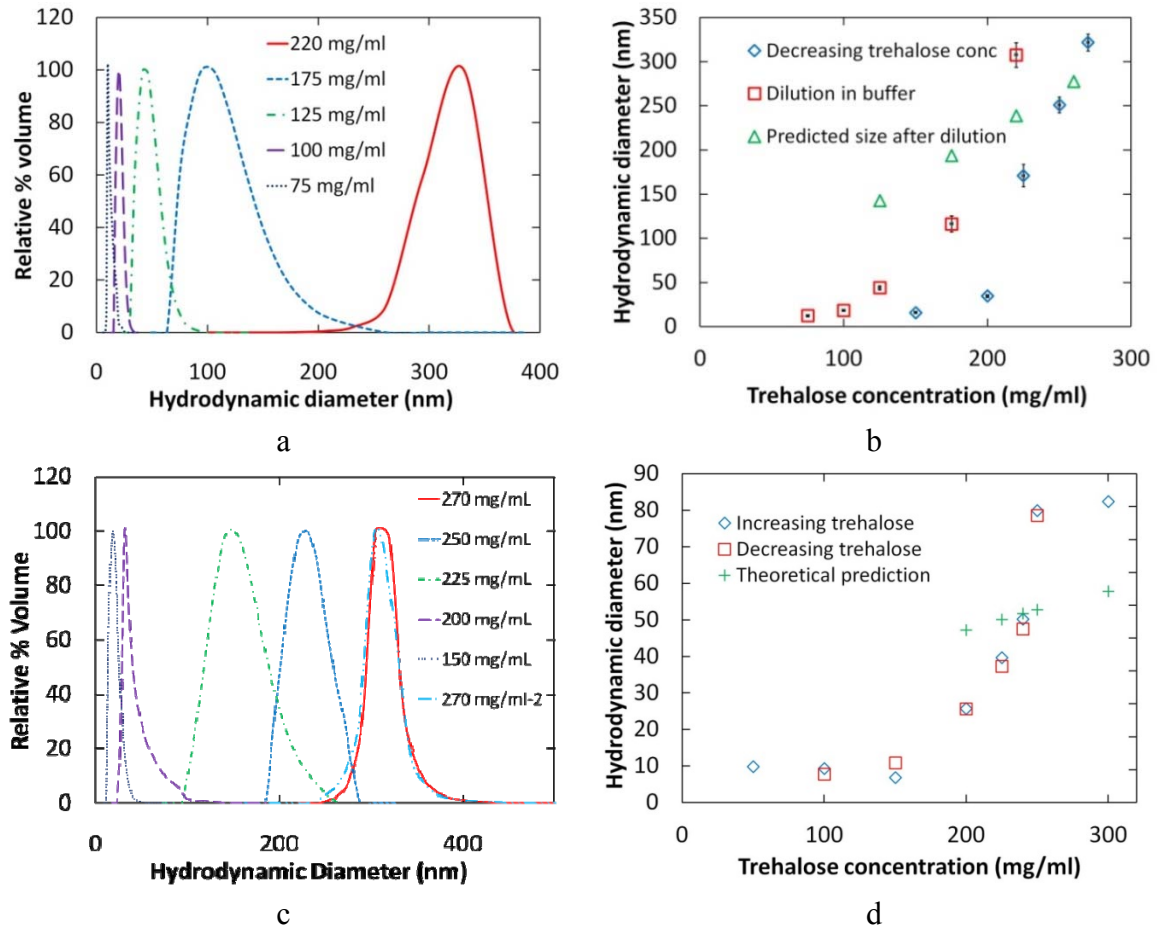


Figure 3.2: Calculated hydrodynamic diameter by DLS for 1B7 antibody and polyclonal sheep IgG with trehalose as extrinsic co-solute. a. 1B7: serial dilutions in buffer such that $c/c_E = 1$. b. 1B7: dilution in pH 7.2 phosphate buffer with starting $c = c_E = 220$ mg/ml as in Fig. 3.2a (squares) and decreasing c_E with a constant c of 70 mg/ml with a starting c_E of 270 mg/ml (diamonds). Error bars indicate \pm s. d. in peak width. The predictions of Eq. 9 are in qualitative agreement. c. 1B7: constant c of 70 mg/ml for decreasing c_E of trehalose from 270 to 150 mg/ml as shown in legend and then a final point where c_E is raised back to 270 mg/ml, labeled as 270 mg/ml-2. d. polyclonal sheep IgG: constant c of 50 mg/ml for increasing (diamonds) followed by decreasing (squares) trehalose concentration. The reversibility suggests equilibrium cluster behavior. The theoretical predictions of the free energy model are in qualitative agreement with the data.

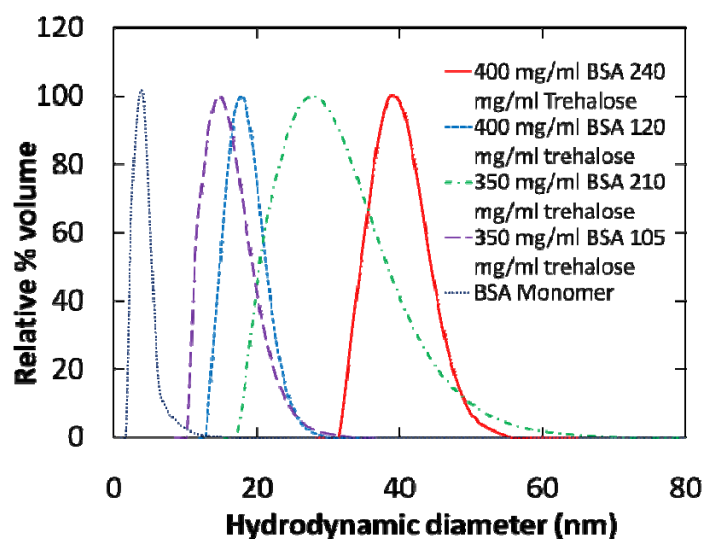
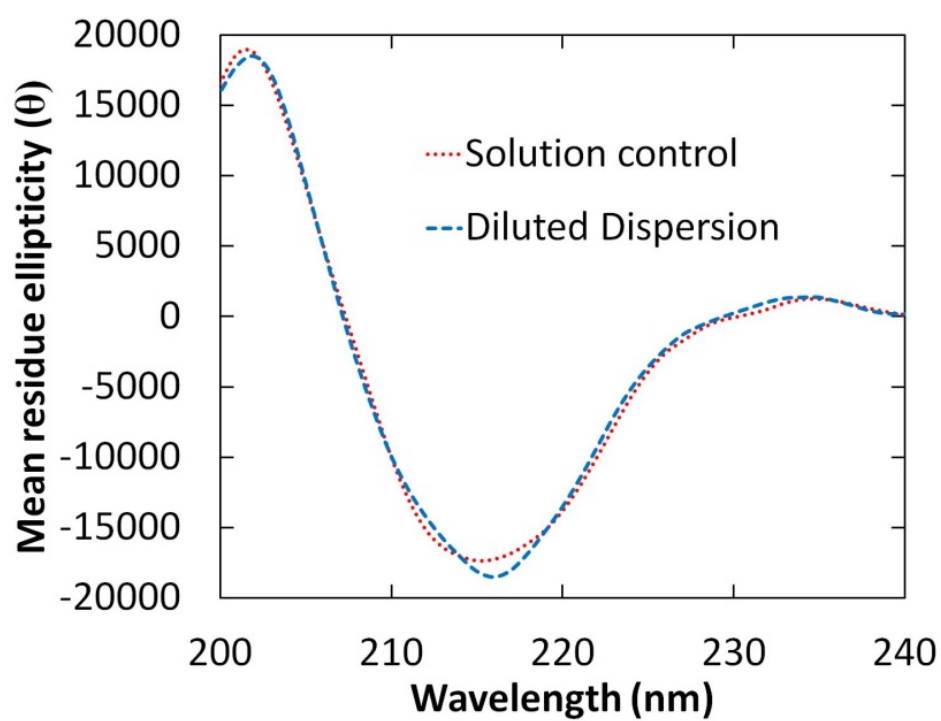
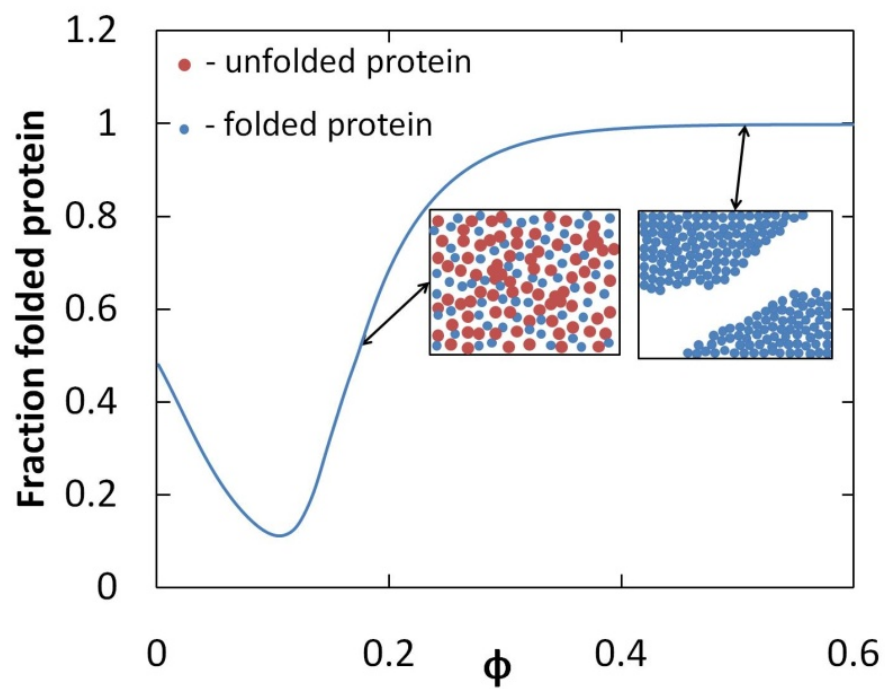


Figure 3.3: BSA nanocluster size for high protein concentrations. A high concentration BSA dispersion formulated at $c = 400$ mg/ml and $c_E = 240$ mg/ml contains nanoclusters with hydrodynamic diameter of 40 nm. Dispersions formulated with lower concentrations of BSA and/or trehalose yield progressively smaller nanoclusters. Also shown is BSA monomer which is 3-4 nm in diameter.



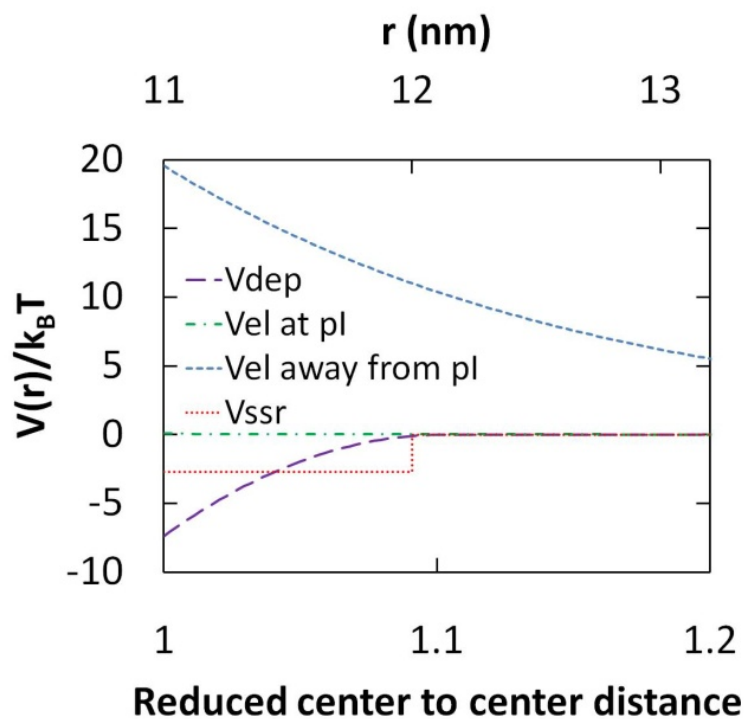
a



b

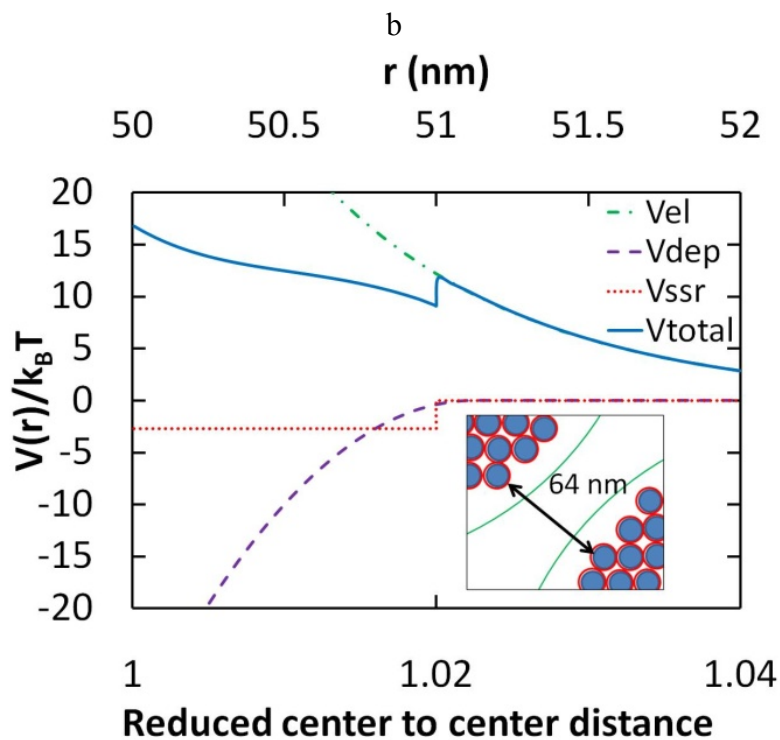
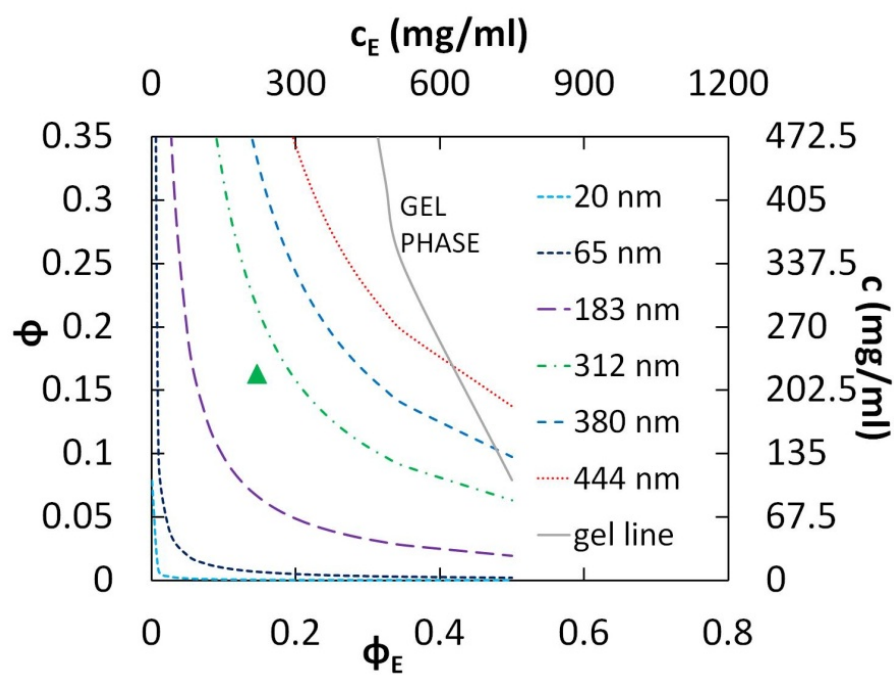
(Fig. 3.4 continued on the next page)

Figure 3.4: Antibody conformation and activity. a. Circular dichroism spectra of a mAb 1B7 control and 267 mg/ml dispersion. All samples were diluted to 0.1 mg/ml in PBS and analyzed on a Jasco J-815 CD Spectrometer. b. Theoretical prediction of the fraction of folded protein suggesting that the native state would be favored at high $\phi_{int} = 0.6$ found in antibody nanocluster. (extended from Shen et al. [5](#))



a

(Fig. 3.5 continued on the next page)



(Fig. 3.5 continued on the next page)

Figure 3.5: Protein-protein, protein-cluster and cluster-cluster hierarchical interactions in nanocluster dispersions. The potential of mean force includes specific short-ranged (ssr), depletion attraction (dep) and electrostatic (el) components: $V(r) = V_{ssr}(r) + V_{dep}(r) + V_{el}(r)$. **a.** Components of $V(r)$ for protein monomers at pI and 3 pH units away from pI. **b.** Predicted cluster diameter contours. The green triangle denotes the conditions of the injected dispersion into mice at $c = 235$ mg/ml for mAb 1B7 as given in Table B3. The diagonal pathway represents dilution of the dispersion (Fig. 3.2a). **c.** $V(r)$ for two 50 nm nanoclusters based on experimental zeta potential for polyclonal IgG (Appendix B.5). *Inset*, green arc depicts range of long-ranged repulsion at the edges of two clusters and red indicates short-ranged inter-cluster attraction.

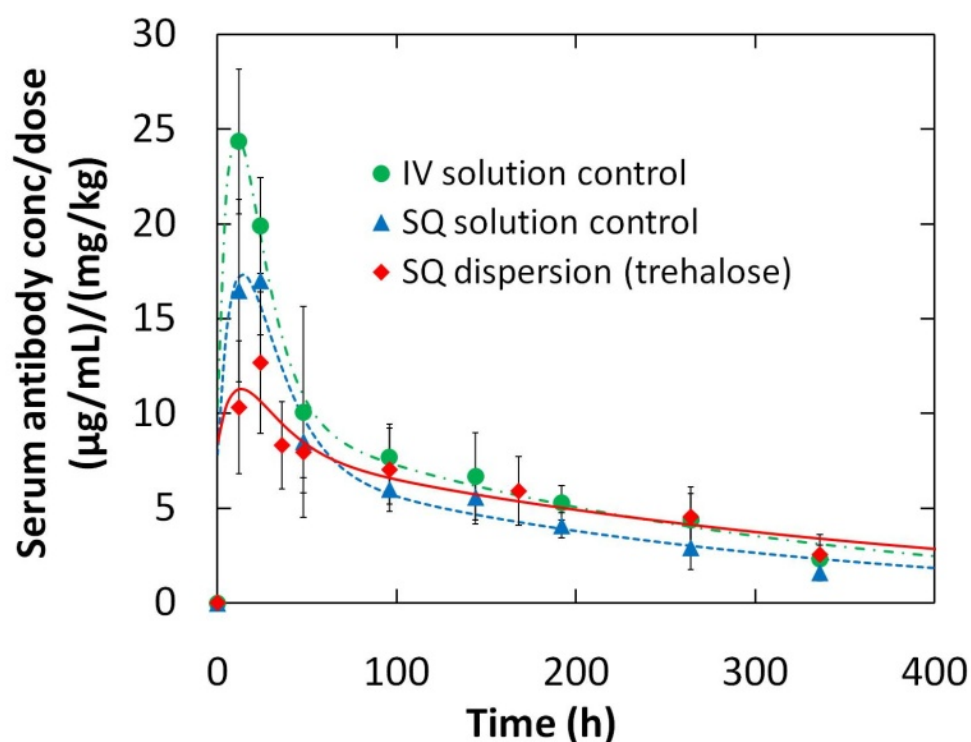


Figure 3.6: Pharmacokinetics of concentrated 1B7 dispersion and solution controls. Time course of serum antibody concentration normalized by dose after administration of intravenous solution, subcutaneous solution or subcutaneous dispersion. Serum samples were recovered from the tail vein and the mAb 1B7 concentration determined by activity from ELISA.

3.5 REFERENCES

- (1) Hartl, F. U.; Hayer-Hartl, M. *Science* 2002, 295, 1852.
- (2) Zhou, H. X.; Rivas, G.; Minton, A. P. *Annual Review of Biophysics* 2008, 37, 375.
- (3) Davis-Searles, P. R.; Saunders, A. J.; Erie, D. A.; Winzor, D. J.; Pielak, G. *J. Annu Rev Biophys Biomol Struct* 2001, 30, 271.
- (4) Hall, D.; Minton, A. P. *Biochimica et Biophysica Acta (BBA) - Proteins & Proteomics* 2003, 1649, 127.
- (5) Shen, V. K.; Cheung, J. K.; Errington, J. R.; Truskett, T. M. *Biophys. J.* 2006, 90, 1949.
- (6) Cheung, J. K.; Truskett, T. M. *Biophys. J.* 2005, 89, 2372.
- (7) Cheung, M. S.; Klimov, D.; Thirumalai, D. *Proc Natl Acad Sci U S A* 2005, 102, 4753.
- (8) Dhar, A.; Samiotakis, A.; Ebbinghaus, S.; Nienhaus, L.; Homouz, D.; Gruebele, M.; Cheung, M. S. *Proc Natl Acad Sci U S A* 2010, 107, 17586.
- (9) Kendrick, B. S.; Carpenter, J. F.; Cleland, J. L.; Randolph, T. W. *PNAS* 1998, 95, 14142.
- (10) Krishnan, S.; Chi, E. Y.; Webb, J. N.; Chang, B. S.; Shan, D.; Goldenberg, M.; Manning, M. C.; Randolph, T. W.; Carpenter, J. F. *Biochemistry* 2002, 41, 6422.
- (11) Stagg, L.; Zhang, S.-Q.; Cheung, M. S.; Wittung-Stafshede, P. *Proc Natl Acad Sci U S A* 2007, 104, 18976.
- (12) Oconnor, T.; Debenedetti, P.; Carbeck, J. *Biophys Chem* 2007, 127, 51.
- (13) Pielak, G. J.; Miklos, A. C. *Proceedings of the National Academy of Sciences* 2010, 107, 17457.
- (14) Shire, S. J.; Shahrokh, Z.; Liu, J. J. *Pharm. Sci.* 2004, 93, 1390.
- (15) Scherer, T. M.; Liu, J.; Shire, S. J.; Minton, A. P. *J Phys Chem B* 2010, 114, 12948.
- (16) Zaccarelli, E. *J Phys: Condens. Matter* 2007, 19, 323101.
- (17) Rosenbaum, D. F.; Zamora, P. C.; Zukoski, C. F. *Phys Rev Let* 1996, 76, 150.
- (18) ten Wolde, P. R.; Frenkel, D. *Science* 1997, 277, 1975.
- (19) Fields, G. B.; Alonso, D. O. V.; Stigter, D.; Dill, K. A. *Journal of Physical Chemistry* 1992, 96, 3974.

- (20) Young, T. M.; Roberts, C. J. *The Journal of Chemical Physics* 2009, 131, 125104.
- (21) Lu, P. J.; Zaccarelli, E.; Ciulla, F.; Schofield, A. B.; Sciortino, F.; Weitz, D. A. *Nature* 2008, 453, 499.
- (22) Lu, P. J.; Conrad, J. C.; Wyss, H. M.; Schofield, A. B.; Weitz, D. A. *Physical Review Letters* 2006, 96.
- (23) Stradner, A.; Sedgwick, H.; Cardinaux, F.; Poon, W. C. K.; Egelhaaf, S. U.; Schurtenberger, P. *Nature* 2004, 432, 492.
- (24) Gast, A. P.; Hall, C. K.; Russel, W. B. *J Colloid Interface Sci* 1983, 96, 251.
- (25) Sedgwick, H.; Egelhaaf, S. U.; Poon, W. C. K. *Journal of Physics: Condensed Matter* 2004, 16, S4913.
- (26) Pan, W. C.; Vekilov, P. G.; Lubchenko, V. *Journal of Physical Chemistry B* 2010, 114, 7620.
- (27) Groenewold, J.; Kegel, W. K. *Journal of Physical Chemistry B* 2001, 105, 11702.
- (28) Groenewold, J.; Kegel, W. K. *Journal of Physics-Condensed Matter* 2004, 16, S4877.
- (29) Porcar, L.; Falus, P.; Chen, W.-R.; Faraone, A.; Fratini, E.; Hong, K.; Baglioni, P.; Liu, Y. J. *Phys. Chem. Lett.* 2010, 1, 126.
- (30) Godfrin, P. D.; Valadez-Perez, N. E.; Castaneda-Priego, R.; Wagner, N. J.; Liu, Y. *Soft Matter* 2014, 10, 5061.
- (31) Tam, J. M.; Murthy, A. K.; Ingram, D. R.; Nguyen, R.; Sokolov, K. V.; Johnston, K. P. *Langmuir* 2010, 26, 8988.
- (32) Tam, J. M.; Tam, J. O.; Murthy, A.; Ingram, D. R.; Ma, L. L.; Travis, K.; Johnston, K. P.; Sokolov, K. V. *ACS Nano* 2010, 4, 2178.
- (33) Xia, Y. S.; Nguyen, T. D.; Yang, M.; Lee, B.; Santos, A.; Podsiadlo, P.; Tang, Z. Y.; Glotzer, S. C.; Kotov, N. A. *Nature Nanotechnology* 2011, 6, 580.
- (34) Ping, G.; Yang, G.; Yuan, J.-M. *Polymer* 2006, 47, 2564.
- (35) Minton, A. P. *Biophys J* 1999, 76, 176.
- (36) del Alamo, M.; Rivas, G.; Mateu, M. G. *J Virol* 2005, 79, 14271.
- (37) Lee, J. C.; Timasheff, S. N. *Journal of Biological Chemistry* 1981, 256, 7193.

- (38) Chi, E. Y.; Krishnan, S.; Kendrick, B. S.; Chang, B. S.; Carpenter, J. F.; Randolph, T. W. *Protein Science* 2003, 12, 903.
- (39) Asakura, S.; Oosawa, F. *Journal of Polymer Science* 1958, 33, 183.
- (40) Vrij, A. *Pure and Applied Chemistry* 1976, 48, 471.
- (41) Mutch, K. J.; van Duijneveldt, J. S.; Eastoe, J. *Soft Matter* 2007, 3, 155.
- (42) Sharma, A.; Walz, J. Y. *Journal of the Chemical Society, Faraday Transactions* 1996, 92, 4997.
- (43) Tuinier, R.; Vliegthart, G. A.; Lekkerkerker, H. N. W. *Journal of Chemical Physics* 2000, 113, 10768.
- (44) Horn, F. M.; Richtering, W.; Bergenholtz, J.; Willenbacher, N.; Wagner, N. J. *J Colloid Interface Sci* 2000, 225, 166.
- (45) Lavinder, J. J.; Hari, S. B.; Sullivan, B. J.; Magliery, T. J. *J Am Chem Soc* 2009, 131, 3794.
- (46) Sutherland, J. N.; Maynard, J. A. *Biochemistry* 2009, 48, 11982.
- (47) Sutherland, J. N.; Chang, C.; Yoder, S. M.; Rock, M. T.; Maynard, J. A. *Clinical and Vaccine Immunology* 2011, 18, 954.
- (48) Pilz, I.; Puchwein, G.; Kratky, O.; Herbst, M.; Haager, O.; Gall, W. E.; Edelman, G. M. *Biochemistry* 1970, 9, 211.
- (49) Miller, D. P.; dePablo, J. J.; Corti, H. *Pharm. Res.* 1997, 14, 578.
- (50) Miller, M. A.; Engstrom, J. D.; Ludher, B. S.; Johnston, K. P. *Langmuir* 2010, 26, 1067.
- (51) Liu, J.; Nguyen, M. D. H.; Andya, J. D.; Shire, S. J. *Journal of Pharmaceutical Sciences* 2005, 94, 1928.
- (52) Uchida, T.; Nagayama, M.; Gohara, K. *Journal of Crystal Growth* 2009, 311, 4747.
- (53) Tabrizi, M. A.; Tseng, C. M. L.; Roskos, L. K. *Drug Discovery Today* 2006, 11, 81.
- (54) Garber, E.; Demarest, S. J. *Biochem Biophys Res Commun* 2007, 355, 751.
- (55) Kumar, V.; Sharma, V. K.; Kalonia, D. S. *International Journal of Pharmaceutics* 2009, 366, 88.
- (56) Chari, R.; Jerath, K.; Badkar, A. V.; Kalonia, D. S. *Pharm. Res.* 2009, 26, 2607.

- (57) Wallace, B. A.; Janes, R. W.; Editors Modern Techniques for Circular Dichroism and Synchrotron Radiation Circular Dichroism Spectroscopy. [In: Adv. Biomed. Spectrosc., 2009; 1]; IOS Press, 2009.
- (58) Crowther, J. R.; Editor ELISA: Theory and Practice. [In: Methods Mol. Biol. (Totowa, N. J.), 1995; 42]; Humana, 1995.
- (59) Arfken, G. B.; Weber, H. J. Mathematical Methods for Physicists; 4 ed.; Academic Press: San Diego, 1995.
- (60) Harn, N.; Spitznagel, T.; Perkins, M.; Allan, C.; Shire, S.; Middaugh, C. R. In Current Trends in Monoclonal Antibody Development and Manufacturing; Shire, S. J., Ed.; Springer: New York, 2010, p 229.
- (61) Hiemenz, P. C.; Rajagopalan, R. Principles of Colloid and Surface Chemistry; 3rd ed.; Marcel Dekker, Inc.: New York, 1997.
- (62) Torquato, S.; Truskett, T. M.; Debenedetti, P. G. Physical Review Letters 2000, 84, 2064.
- (63) Chakrabarti, R.; Delannoy, J.-Y.; Couty, M.; Schweizer, K. S. Soft Matter 2011, 7, 5397.
- (64) Yadav, S.; Liu, J.; Shire, S. J.; Kalonia, D. S. J Pharm Sci 2010, 99, 1152.

Chapter 4: Tunable Equilibrium Nanocluster Dispersions at High Protein Concentrations³

Solutions of therapeutic proteins often gel and become too viscous to deliver via subcutaneous injection at high protein concentrations (> 200 mg/ml). Herein, we demonstrate that proteins can be crowded into colloiddally stable dispersions of distinct nanoclusters that exhibit hydrodynamic diameters larger than monomer (with the same assumptions as chapter 3) without gelation at very high concentrations (up to 320 mg/ml). The nanoclusters form spontaneously upon concentration of protein solutions in the presence of a co-solute, in this case, trehalose. Remarkably nanoclusters of the same size are produced by dilution of protein powder in buffer. Nanocluster size is stable for extended time periods, and upon frozen storage and thawing. Thus, the nanocluster diameter appears to be governed by equilibrium behavior arising from a balance of short and long-ranged monomer-monomer, monomer-cluster and cluster-cluster interactions, as calculated by a free energy model.

4.1 INTRODUCTION

The compact native folded state of a protein within a cell is favored by the crowded macromolecular environment (>400 mg/ml), as further characterized by in vitro studies.¹⁻³ According to computer simulations with coarse-grained models, native proteins of a single type could also stabilize each other against unfolding via “self-

³Reproduced in large part with permission from: Borwankar, A. U.; Dinin, A. K.; Laber, J. R.; Twu, A.; Wilson, B. K.; Maynard, J. A.; Truskett, T. M.; Johnston, K. P. *Soft Matter* **2013**, 9, 1766-1771. Copyright 2012 RSC Publishing. A. U. Borwankar, A.K. Dinin, J. R. Laber, A. Twu and B.K. Wilson conducted the experiments. A. U. Borwankar, A.K. Dinin, J.R. Laber, B.K. Wilson, K.P. Johnston, T.M. Truskett and J.A. Maynard planned the experiments. A.U. Borwankar, K.P. Johnston and T.M. Truskett developed the free energy model. A.U. Borwankar, K.P. Johnston, T.M. Truskett and A.K. Dinin wrote the manuscript.

crowding” when present at these ultra-high concentrations.⁴⁻⁶ However, even at concentrations of 100-200 mg/ml,^{7,8} proteins are often insoluble in buffer and undergo irreversible aggregation,^{1,9-11} gelation and precipitation^{8,12-14} due to specific short ranged attractive forces.^{1,8} To address these limitations, we recently designed a novel self-crowded environment for stabilizing native proteins within nanoclusters (internal protein concentrations of ~ 700 mg/ml) that were dispersed in aqueous buffer.⁷ Remarkably, transparent colloidal dispersions of these nanoclusters with diameters on the order of 100 nm were produced by diluting lyophilized powders containing equal amounts of protein and trehalose.⁷ mAb 1B7 nanoclusters upon dilution were found to dissociate *in vitro* and upon dilution were found to yield folded and biologically active protein monomers. Similarly, upon subcutaneous injection into mice active protein was found to be delivered into the bloodstream.

Despite the recent demonstration of nanoclusters of primary nanoparticles including proteins,⁷ gold,^{15,16} iron oxide¹⁷ and cadmium selenide¹⁸ in water and other high dielectric constant solvents, the assembly mechanism is not yet well understood. Charged proteins such as lysozyme form either small or transient clusters (cluster/particle diameter < 2) with lifetimes on the order of 100 ns as characterized by small-angle neutron scattering.^{19,20} Larger and longer-lived nanoclusters (cluster/primary particle diameter >5), characterized by DLS and SEM,⁷ have also been produced for three different proteins [mAb 1B7, polyclonal sheep Immunoglobulin G (IgG) and bovine serum albumin (BSA)] with low charge near their respective isoelectric points. For dilute protein concentrations of 50 (sheep IgG) and 70 mg/ml (mAb 1B7), the nanocluster diameters were varied reversibly by adjusting the trehalose concentration (and hence the effective inter-protein attraction), suggesting equilibrium behavior.⁷ At extremely high

volume fractions (> 0.2), however, aggregation and gelation is often observed for protein solutions⁸ behavior that is well established for model colloids.^{14,21,22} Protein nanoclusters have been reported at a concentration of 260 mg/ml, but the nanoparticle size was similar to that of the protein particles in the lyophilized starting material. Thus it was unknown if nanocluster size was controllable at high concentrations or influenced by colloidal interactions. It would be remarkable to show the existence of concentrated protein nanoclusters (200 to 400 mg/ml) governed by equilibrium behavior whereby the nanocluster diameter may be tuned via the colloidal interactions.

Transparent colloidal dispersions of concentrated protein nanoclusters were made (see Fig. 4.1a) with sizes found to be the same for assembly via multiple pathways indicating equilibrium behavior. The sizes are calculated based on the diffusion coefficient measured by DLS using the Stokes-Einstein equation. The assumption was used in this Chapter although it may not be very accurate at these high protein concentrations. As shown schematically in pathway C of Fig. 4.1b, concentration of dilute protein solutions in the presence of an extrinsic crowding agent, trehalose, produces protein nanoclusters with hydrodynamic diameters (D_c) of 35-80 nm and a morphology shown by SEM in Fig. 4.1c. Interestingly, nanoclusters with the same diameter are also formed by diluting lyophilized powders in buffer (LD pathway). The nanocluster diameters increase with protein concentration (c) and/or the concentration of an extrinsic crowding agent (c_E) as described by an equilibrium free energy model in terms of short and long-ranged monomer-monomer, monomer-cluster and cluster-cluster interactions.^{7,23,24} Furthermore, a dispersion of ~ 37 nm nanoclusters is formed with only 70 mg/ml trehalose (isotonic level) and a viscosity of 36 cP at a protein concentration of 220 mg/ml without gelation. Upon dilution, the nanoclusters dissociate to a solution of

stable protein monomer, further demonstrating reversibility. These nanoclusters pass through a 220 nm filter (enabling sterile filtration) and spontaneously re-disperse to nanoclusters with the expected equilibrium size upon thawing of the dispersion after frozen storage.

4.2 MATERIALS AND METHODS

4.2.1 Protein purification (FPLC)

The stock solution, typically with ~ 20 mg/ml of a polyclonal sheep Immunoglobulin G mixture (referred to as polyclonal sheep IgG, Rockland Immunochemicals) was further purified. The solution was passed through a fast protein liquid chromatography column (GE Healthcare HiLoad 16/60 Superdex 200 pg) using a buffer at pH 7 (100 mM phosphate and 300 mM NaCl) as the mobile phase. The monomer fractions observed with absorbance at 280 nm were collected and pooled, and the oligomers were discarded.

4.2.2 Buffer exchange

After the FPLC purification step, the ~4 mg/ml solution of polyclonal sheep IgG was buffer exchanged into 50 mM phosphate buffer with the desired amount of dissolved trehalose (typically 70-125 mg/ml). The buffer was formulated at the isoelectric point (pI) of the protein, which is 6.4 for the polyclonal sheep IgG. The buffer exchange was carried out using centrifugal filter tubes (Millipore, Amicon Ultracell 30K centrifugal filters) with a molecular weight cutoff of 30 kDa and a capacity of 12 ml. A desired amount (typically 6-8 ml) of the protein solution was added to the filter tube and the

volume was increased to 12 ml using the desired buffer for the dispersion. The buffer was forced through the membrane by centrifugal filtration at 4500 radial centrifugal force (rcf) for 12 minutes concentrating the protein solution in the retentate until the solution volume dropped to about 2 ml. Then the retentate protein solution was again diluted to 12 ml in the same buffer as before and concentrated down to 2 ml again. The dilution and centrifugation process was repeated 4 or more times until the permeate volume was 4-5 times the original solution volume, typically 40 ml and the original buffer accounted for < 1% of the sample volume. After buffer exchange, the solution was further concentrated so that the final solution volume was about 0.5 ml.

4.2.3 Centrifugal filtration of protein solution to form a dispersion of nanoclusters upon concentration

Tare weights were taken of a centrifugal filter assembly (Millipore Microcon, Ultracel YM-50 membrane, 50 kDa nominal molecular weight limit, diameter of filter, 0.25"). The desired volume (~0.5 ml) of protein solution, after buffer exchange and concentration, was pipetted into the retentate chamber. The filter assembly was then centrifuged (Eppendorf Centrifuge 5415D) at 10,000 rcf, typically in about 20-40 minute increments until the calculated final retentate volume for the desired final protein concentration was reached. The volume measurements were done using image analysis (ImageJ software) to determine the height of the liquid column in the retentate chamber. Additionally, the protein concentration in the retentate dispersion was measured by measuring out 2 μ l (\pm 0.08 μ l) of dispersion using an Eppendorf Research adjustable volume 0.5-10 μ l pipette and diluting it into a receiving vessel containing 998 μ l of the same buffer. For mixing, the solution was cycled 5 times into and back out of the pipette

tip followed by light agitation with the pipette tip. The absorbance of the resulting solution at 280 nm was measured using a Cary 3E uv-visible spectrophotometer in a cuvette (Hellma cells) with a path length of 1 cm, and converted to concentration assuming an extinction coefficient of $1.43 \text{ ml mg}^{-1} \text{ cm}^{-1}$. Once the desired concentration had been reached, the dispersion of protein nanoclusters in the retentate chamber was recovered by inverting the filter assembly into a retentate recovery tube, and centrifuging it for 3-4 minutes at 1,000 rcf. The resulting dispersion was transferred to a 0.1 mL conical vial (V-Vial, Wheaton), and the concentration was confirmed using 2 μL of the dispersion as described above.

4.2.4 Characterization of the protein nanocluster dispersion

4.2.4.1 Hydrodynamic diameters

The short-time mutual diffusion coefficient $D_s(q)$ of protein nanoclusters was extracted from intensity correlation functions measured using dynamic light scattering (Appendix C1). Measurements were taken at angle of 150° with a 632.8 nm laser ($q = 0.01918 \text{ nm}^{-1}$) and an avalanche photodiode at $\sim 23^\circ\text{C}$ using a custom apparatus (Brookhaven BI-9000AT and 60 μL Beckman Coulter sample cell)⁷ and analyzed with the CONTIN algorithm to generate a volume distribution. Hydrodynamic nanocluster diameters D_c were estimated from the $D_s(q)$ using Beenakker-Mazur theory²⁵ for $D_s(q)/D_0$, where $D_0 = kT / 3\pi\eta D_c$ and η is the shear viscosity of the buffer solvent with added excipients. This approach assumes that the protein nanoclusters act like suspended hard spheres occupying an effective packing fraction $\phi_c^{\text{eff}} = \phi / \phi_c^{\text{int}}$, where ϕ_c^{int} is the protein packing fraction within a nanocluster. In this work, we assumed $\phi_c^{\text{int}} = 0.60$, which is

consistent with light scattering data on protein nanoclusters reported previously.⁷ We also verified that an alternative approximation, $\phi_c^{\text{int}} = (D_c/2R)^{\delta_f-3}$ (where δ_f is the fractal dimension, taken as 2.6),⁷ resulted in similar nanocluster size estimates. The measured intensity correlation functions decayed on time scales between ~100 to 500 μs , consistent with short-time diffusion for nanoclusters with the diameters and mobilities reported here.

4.2.4.2 Size exclusion chromatography

For analysis of non-covalent aggregates, the sample was diluted in mobile phase (100 mM sodium phosphate, 300 mM sodium chloride, pH 7) to ~1 mg/ml. 20 μg of diluted dispersion was analyzed with a Waters Breeze HPLC, using TOSOH Biosciences TSKgel3000SWXL and TSKgel2000SW columns in series, with eluate monitored by absorbance at 214 nm.

4.2.4.3 Enzyme linked immunosorbent assay (ELISA)

An ELISA was performed by coating a 96-well Costar high binding polystyrene plate with anti-polyclonal sheep IgG (Sigma) in PBS at 1 $\mu\text{g}/\text{ml}$ at 4°C overnight. The sheep IgG samples were serially diluted in a 1:5 ratio starting at 10 $\mu\text{g}/\text{ml}$. The plate was then blocked with 5% milk in PBS for two hours at room temperature. Bound IgG was detected with anti-polyclonal sheep IgG conjugated with horseradish peroxidase (Sigma) in PBS added to each well in a 1:5000 ratio. The signal was developed with a TMB solution (Thermo Scientific) and the reaction was quenched with 1N HCl. The signal was detected using a spectrophotometer (Molecular Devices Spectramax M5) at an

absorbance of 450 nm. The data was fit to a four parameter logistic curve (MATLAB nonlinear curve fitting) and the half maximal effective concentration (EC50) reported.

4.2.4.4 Circular dichroism (CD)

Secondary structure was determined by diluting the dispersions to approximately 10 mg/ml in 5 mM phosphate buffer at pH 7.4. The samples were then placed in the JASCO J-815 circular dichroism spectrometer and the CD spectrum was measured from 260 nm to 190 nm. Data was analyzed with Dichroweb online analysis tool, using the CDSSTR function and reference set 4.²⁶

4.2.4.5 Viscosity

The viscosities of the nanocluster dispersions were measured in triplicate using a 25 gauge (ID = 0.1 mm) 1.5" long needle (Becton Dickinson & Co. Precision Glide Needle) attached to a 1 ml syringe (Becton Dickinson & Co. 1 mL syringe with Luer-Lok™ tip), according to the Hagen-Poiseuille equation.⁷ The flow rate of the dispersion through the needle was determined by correlating volume to the height of the liquid in the conical vial (using ImageJ software) and measuring the time taken for the dispersion column height to move between two points. The flow rate was correlated to viscosity from a calibration curve derived from a set of standards of known viscosities.⁷

4.2.4.6 Scanning Electron Microscopy (SEM)

Scanning electron microscopy (SEM, Hitachi S-5500 at 30 kV), was carried out on the dispersions in the concentrated state. A small drop of the dispersion was placed on

a copper TEM grid with a lacey carbon film coated with formvar, blotted to remove the excess liquid and form an extremely thin film which was too thin to see easily with the naked eye, rapidly frozen by immersion in liquid nitrogen and lyophilized.

4.3 RESULTS AND DISCUSSION

4.3.1 Recap of Equilibrium free energy model

To guide understanding of the experimental data, it is helpful to first consider some of the colloidal forces that can influence the nanocluster diameter as a function of dispersion composition. A more detailed explanation is provided below and in Appendix C.3 using results from a semi-quantitative free energy model⁷ which was used to produce the nanocluster diameter contours in Fig. 4.1b. Near the isoelectric point of the protein, electrostatic repulsion between two proteins is relatively weak, such that attractive forces between protein monomers can favor assembly of nanoclusters. To further drive nanocluster formation, a co-solute, trehalose, is added to produce excluded volume (i.e. osmotic depletion) attractions between proteins. As the concentration of co-solute (trehalose), c_E , is increased, stronger depletion attraction is expected to produce larger protein nanoclusters. As the nanoclusters grow, our hypothesis is that the accumulation of weak, longer-range electrostatic repulsions between the slightly charged proteins balance the attractions, resulting in an equilibrium nanocluster size.

4.3.2 Nanocluster formation by the centrifugal or concentration filtration pathway

To form nanoclusters by the filtration concentration pathway (C) in Fig. 4.1b, approximately 0.5 ml of a solution containing 40-60 mg/ml protein in 50 mM phosphate

buffer at pH 6.4 was concentrated by centrifugal filtration through a filter with a 50 kDa cutoff (Centrifugal filter units, Millipore) at 10000 rcf. The c_E remained approximately constant at 70 mg/ml, since the trehalose and the buffer components passed through the filter without a barrier while the protein (M.W. ~150 kDa) was retained. In each filtration experiment, a transparent dispersion (Fig. C2) formed spontaneously, composed of protein nanoclusters with a typical morphology shown in Fig. 4.1c by SEM (Additional SEM images shown in Fig. C3). The D_c measured at a scattering angle of 150° increased as a function of the final c (Figs. 4.2a and 4.2b, Table 4.1) from 18 nm at 120 mg/ml to 37 nm at 220 mg/ml. The peak width, which characterizes the polydispersity in diameter, was larger for nanoclusters in Fig. 4.2a for dispersions with c above 180 mg/ml (the corresponding calculation from the free energy model shown in Fig. 4.2b is explained below.) To our knowledge, this is the first demonstration of a dispersion of self-assembled, long-lived nanoclusters at high protein concentration (above 100 mg/ml) produced by concentrating a protein solution. Also upon dilution to 1 mg/ml protein was found to be 99.5% monomer by size exclusion chromatography (SEC) and the relative EC50 was found to be 1.133 ± 0.839 by ELISA (using a four parameter logistic fit, see Appendix C.2). To examine the reversibility of nanocluster formation, the above C 220:70 (defined in Table 4.1) nanoclusters were diluted in the same pH 6.4 phosphate buffer to maintain a constant c/c_E of 220/70 or 3.14:1, as shown in Fig. 4.2b, with full DLS distributions in Fig. C4 and Table C2. As expected, the D_c values at the same c measured along this dilution pathway were smaller than those obtained on the concentration filtration pathway at constant c_E . These results are placed in perspective with nearly all of the conditions investigated in this study in the global plot in Fig. 4.2c. The vertical filtration concentration pathway for nanocluster formation at 70 mg/ml (C

70) is shown along with a diagonal pathway for subsequent dilution of the C 220:70 sample with buffer. Reversibility in nanocluster diameter, increasing upon concentrating the protein and decreasing upon dilution in the diagonal direction, suggests equilibrium behavior.

In order to show that the nanocluster diameter depends only on c and c_E and is independent of formation pathway, nanoclusters were synthesized at a c_E of ~ 100 mg/ml by the two extremely different pathways namely, filtration concentration (C) and lyophilization dilution (LD). For the C pathway, a protein solution with a starting concentration of 50 mg/ml was concentrated to a dispersion with $c = 250$ mg/ml (C 250:100) and a measured D_c of 49 nm. A similar value of D_c of ~ 51 nm (see Table 4.1 and Fig. 4.2d) was observed by stirring (diluting) lyophilized protein and trehalose powder with a c/c_E ratio of 2.5:1, with 50 mM phosphate buffer at pH 6.4 (LD 250:100). As the lyophilized protein contacts the buffer, it disperses to form sub-100 nm nanoclusters nearly identical to those obtained from the concentration filtration pathway, without getting trapped in gel states during wetting. This similarity in D_c , as summarized in Figs. 4.2c and 4.2d, is another strong indicator of equilibrium behavior, especially given the extreme difference in the filtration and lyophilization dilution pathways. The LD 250:100 dispersion from Fig. 4.2d was diluted by mixing with buffer, such that the c/c_E ratio remained constant at 2.5, as shown by the diagonal pathway in Figs. 4.2c and 4.2e and with D_c distributions shown in Fig. 4.2d and Table C3. The D_c values decreased markedly as c reached 120 mg/ml and only monomer was present at 60 mg/ml. The % monomer in the original LD 250:100 dispersion upon dilution to ~ 1 mg/ml was 98.3% as verified by SEC and the relative EC50 was found to be 1.380 ± 0.474 . The trend is similar to that for the dilution of the C 220:70 nanoclusters described earlier, as expected

for equilibrium behavior given the similar c/c_E ratios. Additionally, concentration filtration was utilized to form nanoclusters with an ultra-high c of 320 mg/ml, with a D_c of 40 nm as shown in Table 4.1 and Fig. C5. Upon dilution, the % monomer was 99.3% indicating that irreversible aggregation did not occur even at these extremely high concentrations.

To explore the behavior at a high c_E of 250 mg/ml, both the C and LD pathways were used to form nanoclusters at a $c:c_E$ ratio of 1:1. As expected, the diffusion coefficient decreases much further and so larger nanoclusters were assumed to be formed with the stronger crowding forces (depletion attractions) at this higher c_E . This well-known depletion attraction between proteins is caused by a gain in accessible volume, and consequently entropy, for the trehalose as the excluded volumes of closely-spaced protein molecules overlap.²⁷⁻²⁹ The D_c value of 77 nm for the C 250:250 nanoclusters (Table C4 and Fig. C6) was similar to, and as expected slightly smaller than, the value of 95 nm for the lyophilization dilution (LD 270:270) nanoclusters which are at a slightly higher c and c_E . Furthermore, the D_c values were nearly identical during dilution of both types of nanoclusters in buffer (Figs. 4.2c and 4.2e). In summary, the similarity in D_c values at high c for the nanoclusters produced by both the filtration concentration and lyophilization dilution processes for different sets of c_E values, and upon dilution with buffer back down to monomer is highly suggestive of equilibrium behavior although the fraction of protein present in nanoclusters is unknown. The nanocluster diameters are consistent over a wide range of c and c_E state points, as shown on the global plots in Fig. 2c, and do not depend significantly on the pathway.

Additionally, for the C 250:100 dispersion stored at room temperature for 14 days, D_c was virtually unchanged at ~50 nm as is shown in Fig. C7 and Table C5.

Macroscopic phase separation was not present further indicating that the dispersions are colloidally stable at high protein concentration. Upon dilution of the stored dispersion in buffer to 1 mg/ml, the % monomer was constant at 98.5 % by SEC, indicating the protein did not form irreversible aggregates during the two weeks of storage. Additional examples of dispersions are given in Table C6.

4.3.3 Prediction of nanocluster size based on the free energy model

In our previous study of nanoclusters at high protein concentration which is of fundamental and technological interest, the size of the nanoclusters was similar to those of the particles in the lyophilized powders used to form them. Thus, it was not possible to determine the origin of the nanocluster size and whether the nanoclusters were reflecting an equilibrium state.⁷ In the current study, we now show that the D_c s of 50, 80 and 95 nm nanoclusters made by concentration of protein solutions (C pathway) match those made from dilution of lyophilized powders (LD pathway) for the 250:100, 250:250, and 270:270 ratios of $c:c_E$. Thus, both types of nanoclusters appear to be in the same equilibrium state, regardless of the starting state, i.e., whether a liquid solution or a powder comprised of nanoparticles. As mentioned above, relations between dispersion composition, protein interactions, and expected nanocluster diameter can also be estimated from an approximate equilibrium free energy model^{7,23,24} described in detail in Appendix C.3. Specifically, the model suggests that nanocluster diameters obey the following proportionality -

$$D_c \propto \left[\frac{\varepsilon/kT}{(\lambda/R)q^2} \right]^{\frac{1}{2\delta_f-3}} \quad (4.1)$$

where ε is the magnitude of the effective attraction between two adjacent proteins in the nanocluster, k is the Boltzmann constant, T is temperature, λ is the Bjerrum length, R is the protein radius, q is the charge per protein, and δ_f is the fractal dimension of the nanocluster. According to the model, stronger attraction ($\varepsilon/kT \gg 1$) and lower protein charge ($q^2 \ll 1$), and hence weaker electrostatic repulsion, produce larger self-assembled nanoclusters. Thus, choosing dispersion pH near the isoelectric point of the protein,^{30,31} as is done in this work, helps to minimize q and favor nanocluster formation.

The equilibrium free energy model also predicts that both ε/kT and q (and hence nanocluster diameter) can be tuned by varying the dispersion composition. In this case, we consider the attraction to be provided by depletion attraction and the repulsion to be provided by electrostatic repulsion between proteins. In the case of osmotic depletion interactions (see plot of potential of mean force between the protein molecules in Fig. C1), the attractive strength is expected to grow in proportion to the concentration of co-solute or depletant (trehalose), $\varepsilon \propto c_E kT$ as shown in Appendix C.3.^{29,32,33} At higher protein concentration c , the effect of depletion interaction is further enhanced. This is because higher protein concentration reduces the free volume in the dispersion, which in turn decreases the entropic driving force for proteins to dissociate from nanoclusters³⁴ and also for counterions to dissociate from a given protein.^{23,24} The former effect has been observed in suspensions of uncharged hard-sphere colloids, where the strength of polymer-mediated depletion interaction required to induce colloid clustering or phase separation was found to decrease with increasing colloid concentration.^{21,28,35-39} The latter effect of less counterion dissociation per protein at high protein concentration corresponds to lower protein charge and hence weaker electrostatic repulsion to balance the depletion attraction, also leading to larger protein nanoclusters. A simple equilibrium

site-binding model that estimates the translational and combinatorial entropy of counterion dissociation^{21, 22} predicts the dependence between charge and protein concentration to be $q \propto c^{-1/2}$ for low ζ -potential nanoclusters, like those expected to be observed near the isoelectric point. Together with eq. (4.1), these arguments suggest the following simple proportionality -

$$D_c \propto [c_E c]^{\frac{1}{2\delta_f - 3}} \quad (4.2)$$

This relation, while qualitative and (as discussed below) not expected to be quantitatively predictive, is consistent with the experimental data presented here. Specifically, it captures the observed increases in D_c with co-solute concentration c_E shown earlier in Fig. 4.2c and also with increasing protein concentration c evident from Figs. 4.2a, 4.2b and 4.2c. It further captures the various experimental trends when nanoclusters shrink in buffer along the various dilution pathways shown in Figs. 4.2c and 4.2e. The qualitative agreement between the predictions of the model using the parameters in Table C1 and the experiments further supports the idea that the dispersed protein nanoclusters may be in an equilibrium state. Quantitative agreement is likely not achieved, at least in part, because there are several assumptions in the model that are not expected to strictly hold in the experimental system. For example, the model does not account for fluctuations. It assumes monodisperse spherical nanoclusters with a single effective dielectric constant within the nanoclusters. It also ignores the entropic penalty due to the reduced translational degrees of freedom of the protein upon clustering. Furthermore, the site-binding charge model incorporated here provides one simple (albeit likely oversimplified) prediction for the effects of protein concentration. Protein

concentration effects on depletion interactions may also be important and are not considered here.

4.3.4 Colloidal and conformational stability of proteins

As discussed above, proteins in a highly crowded environment have an increased tendency to stay in their compact (osmotically favored) native folded state.^{1,4,5,33,40,41} During the course of the filtration concentration process, the high trehalose concentration may help mitigate protein unfolding and aggregation, particularly at intermediate c values in Figure 4.3. Inside the clusters, proteins are also expected to remain in their native state, stabilized by self-crowding.^{5,6} We find upon dilution that the protein is monomeric by SEC, biologically active by an ELISA (see Fig. C8 for details), and in its native conformation according to secondary structural characterization by CD (also see Table C7). These favorable results were obtained for both types of nanocluster dispersions, i.e., for the LD or C pathways. As further evidence of equilibrium behavior, the nanoclusters were found to retain their D_c after freezing the dispersion and storing it at -40°C for the duration of 2 ½ months as is shown in Table C8 and Fig. C9. Furthermore, upon dilution the % monomer from SEC was essentially unchanged. All of these support the concept of reversible equilibrium assembly.

The low trehalose concentrations in the current study were isotonic as shown in Table 4.1,⁴² and furthermore, produced a small D_c of 36 nm. The size was found to be small enough for sterile filtration through a 220 nm filter as demonstrated in Fig. C10 and Table C9. Finally, the viscosity of the C 220:70 dispersion was 36 cP, which is syringeable through a 25 gauge needle, commonly used for subcutaneous injection.⁸ The ability to tune the size of nanoclusters via equilibrium assembly, which dissociate

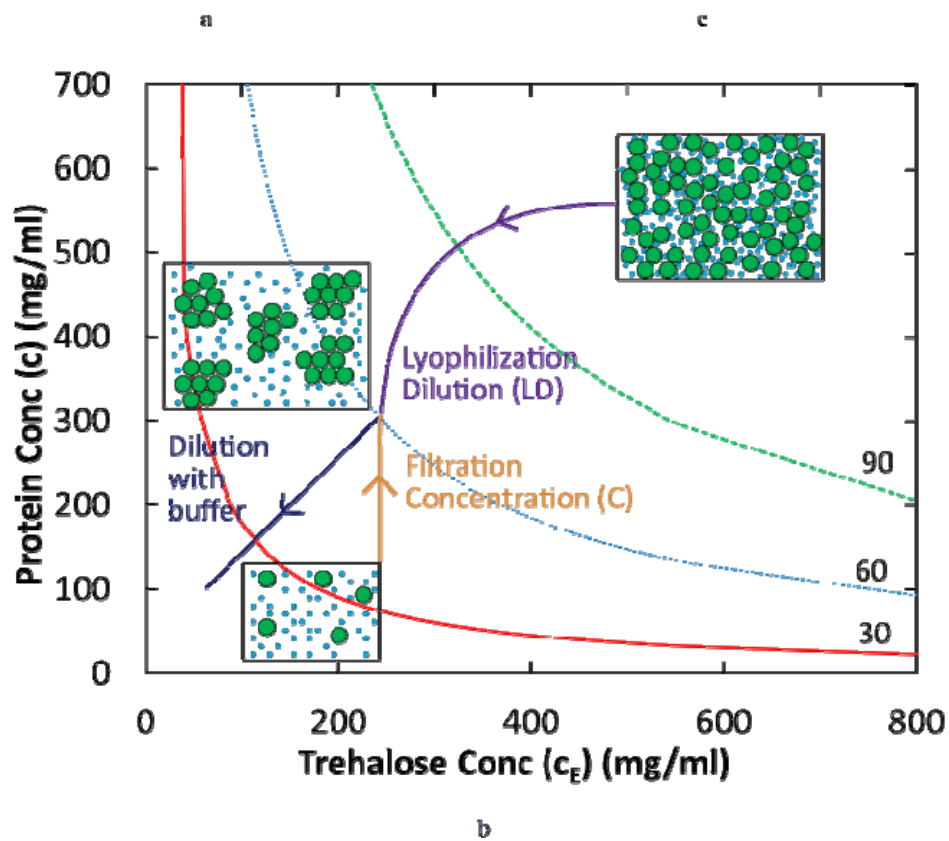
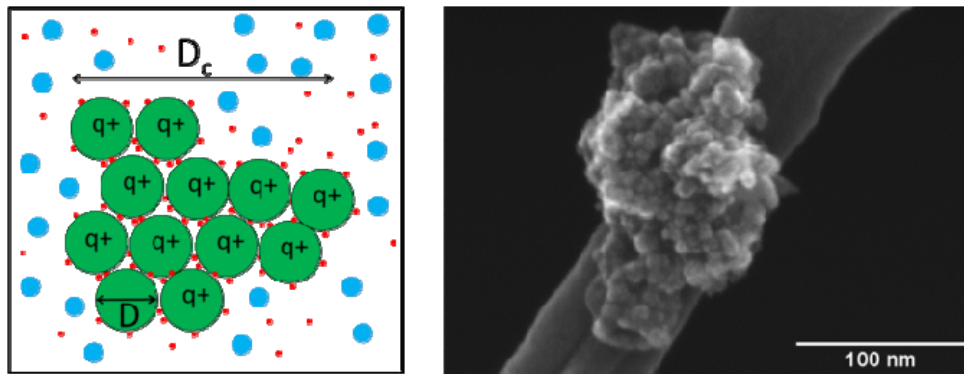
reversibly to primary particles may be expected to be of broad interest in practical applications including subcutaneous delivery of therapeutic proteins.

4.4 CONCLUSIONS

Transparent colloidal dispersions of concentrated protein nanoclusters were made (see Fig. 4.1a) with sizes found to be the same for assembly via multiple pathways indicating equilibrium behavior under the assumptions for determining the cluster size by DLS. Increasing the concentration of dilute protein solutions in the presence of an extrinsic crowding agent, trehalose, produced protein nanoclusters with hydrodynamic diameters (D_c) of 35-80 nm. Nanoclusters with the same diameter were formed by diluting lyophilized powders in buffer (LD pathway) and concentration filtration (C pathway). The theoretically calculated nanocluster diameters increase with protein concentration (c) and also with the concentration of an extrinsic crowding agent (c_E) as described by an equilibrium free energy model in terms of short and long-ranged monomer-monomer, monomer-cluster and cluster-cluster interactions. Furthermore, a dispersion of ~37 nm nanoclusters is formed with only 70 mg/ml trehalose (isotonic level) and a viscosity of 36 cP at a protein concentration of 220 mg/ml without gelation. Upon dilution, the nanoclusters dissociate to a solution of stable and active protein monomer evidencing that the protein is stable in the dispersion. These nanocluster dispersions can be sterile filtered and frozen without affecting the nanocluster size, viscosity and causing additional aggregate formation.

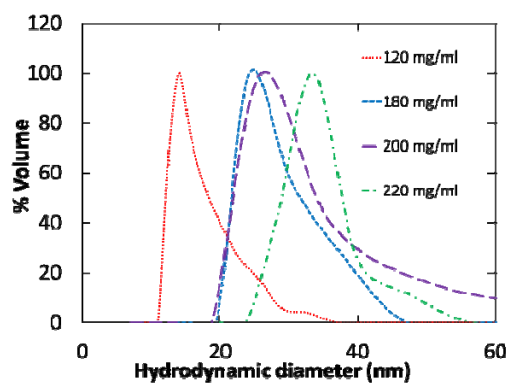
Process and $c:c_E$	Protein conc. (c) (mg/ml)	Trehalose conc (c_E) (mg/ml)	Osmolality/osmolality at isotonic conc.	D_c (nm)
C 220:70	220	70	0.92	37 ± 8
C 250:25	250	25	0.52	16 ± 5
LD 250:100	250	100	1.20	51 ± 9
C 320:70	320	70	0.92	40 ± 7

Table 4.1: Hydrodynamic diameters (D_c) of protein nanoclusters for various dispersions made by the filtration concentration (C) and lyophilization dilution (LD) processes shown in Fig. 4.1b.

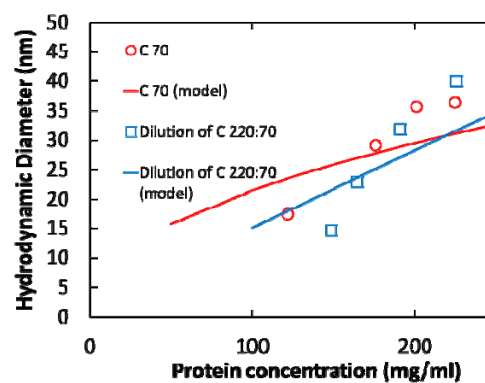


(Fig. 4.1 continued on the next page)

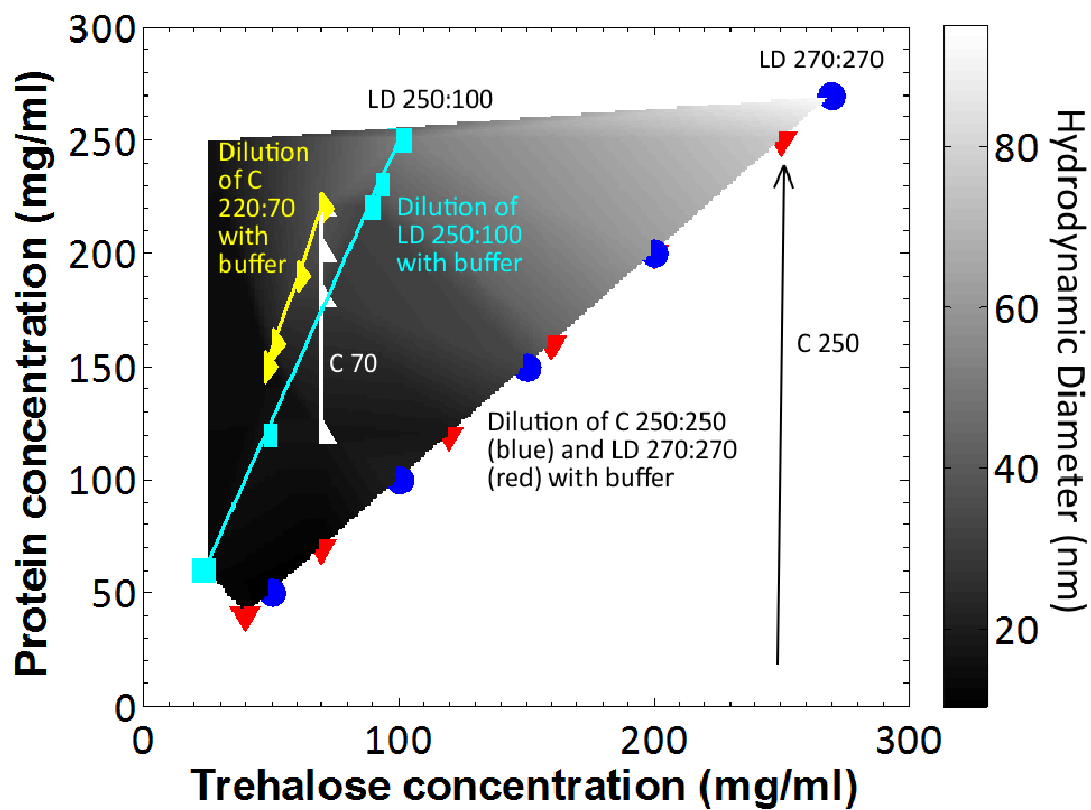
Figure 4.1: Nanocluster morphology and formation pathways. a, Schematic of a protein (green) nanocluster with trehalose molecules (co-solute, blue) and counterions of the protein (red). b, Nanocluster formation by two pathways: dilution of lyophilized power (LD) and concentration by filtration (C). Three nanocluster diameter contours (in nm) calculated by a free energy model (Appendix C.3) are shown. Additionally, the nanocluster diameter decreases to that of a protein monomer upon dilution in buffer (shown by diagonal pathway). c, SEM image of a nanocluster from a dispersion at $c = 270$ mg/ml and $c_E = 270$ mg/ml.



a



b



c

(Fig. 4.2 continued on the next page)

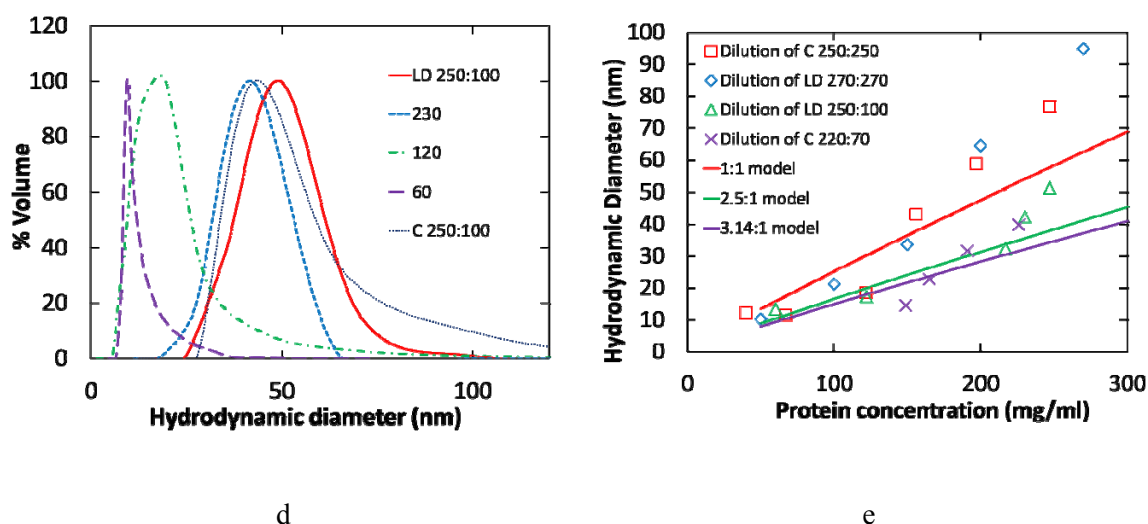


Figure 4.2: Nanocluster hydrodynamic diameters (D_c) for filtration concentration (C) and lyophilization dilution (LD) pathways. a, D_c of the nanoclusters for C pathway at 70 mg/ml trehalose for various final c values (C 70 pathway). b, Volume average D_c and the calculated diameter from the model (Appendix C.3) for the nanoclusters from panel a (C 70) and for dilution of the C 220:70 samples with buffer. c, D_c surface for the nanoclusters interpolated from the individual experimental points. d, D_c of the nanoclusters formed by dispersing lyophilized protein powder (LD 250:100) and after subsequent sequential dilutions with buffer to 230, 120 and 60 mg/ml IgG. A similar D_c was observed for the C 250:100 dispersion. e, D_c upon dilution of both LD and C dispersions with the calculated diameters from the model corresponding to the same protein:trehalose ratios.

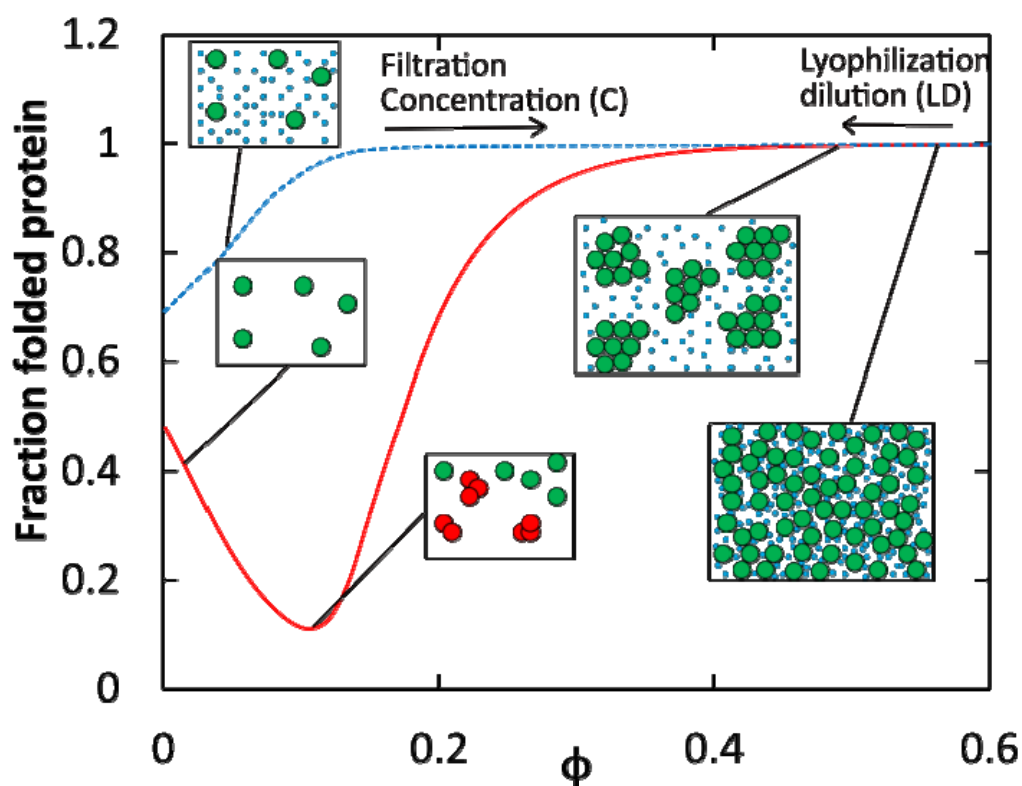


Figure 4.3: Fraction of folded protein adapted from simulations of Shen et al.⁴³ and schematic of LD and C pathways for nanocluster synthesis in the presence (blue curve) and absence (red curve) of crowder. Small red irreversible aggregates are shown at an intermediate ϕ without crowder (here $\phi = c/1400$, where ϕ is the volume fraction of protein which has a partial molar density of 1400 mg/ml)⁷

4.5 REFERENCES

- (1) Zhou, H. X.; Rivas, G.; Minton, A. P. Annual Review of Biophysics 2008, 37, 375.
- (2) Hartl, F. U.; Hayer-Hartl, M. Science 2002, 295, 1852.
- (3) Roosen-Runge, F.; Hennig, M.; Zhang, F.; Jacobs, R. M. J.; Sztucki, M.; Schober, H.; Seydel, T.; Schreiber, F. Proceedings of the National Academy of Sciences 2011, 108, 11815.

- (4) Cheung, J. K.; Shen, V. K.; Errington, J. R.; Truskett, T. M. *Biophysical Journal* 2007, 92, 4316.
- (5) Cheung, J. K.; Truskett, T. M. *Biophys J* 2005, 89, 2372.
- (6) Shen, V. K.; Cheung, J. K.; Errington, J. R.; Truskett, T. M. *Biophys J* 2006, 90, 1949.
- (7) Johnston, K. P.; Maynard, J. A.; Truskett, T. M.; Borwankar, A.; Miller, M. A.; Wilson, B.; Dinin, A. K.; Khan, T. A.; Kaczorowski, K. J. *ACS Nano* 2012.
- (8) Shire, S. J.; Shahrokh, Z.; Liu, J. J. *Pharm. Sci.* 2004, 93, 1390.
- (9) Rosenberg, E.; Hepbildikler, S.; Kuhne, W.; Winter, G. *Journal of Membrane Science* 2009, 342, 50.
- (10) Young, T. M.; Roberts, C. J. *J Chem Phys* 2009, 131, 125104.
- (11) Fields, G. B.; Alonso, D. O. V.; Stigter, D.; Dill, K. A. *Journal of Physical Chemistry* 1992, 96, 3974.
- (12) Rosenbaum, D. F.; Zamora, P. C.; Zukoski, C. F. *Phys Rev Let* 1996, 76, 150.
- (13) ten Wolde, P. R.; Frenkel, D. *Science* 1997, 277, 1975.
- (14) Zaccarelli, E. *J Phys: Condens. Matter* 2007, 19, 323101.
- (15) Tam, J. M.; Murthy, A. K.; Ingram, D. R.; Nguyen, R.; Sokolov, K. V.; Johnston, K. P. *Langmuir* 2010, 26, 8988.
- (16) Tam, J. M.; Tam, J. O.; Murthy, A.; Ingram, D. R.; Ma, L. L.; Travis, K.; Johnston, K. P.; Sokolov, K. V. *Acs Nano* 2010, 4, 2178.
- (17) Gindy, M. E.; Prud'homme, R. K. *Expert Opinion on Drug Delivery* 2009, 6, 865.
- (18) Xia, Y. S.; Nguyen, T. D.; Yang, M.; Lee, B.; Santos, A.; Podsiadlo, P.; Tang, Z. Y.; Glotzer, S. C.; Kotov, N. A. *Nature Nanotechnology* 2011, 6, 580.
- (19) Liu, Y.; Porcar, L.; Chen, J.; Chen, W.-R.; Falus, P.; Faraone, A.; Fratini, E.; Hong, K.; Baglioni, P. *The Journal of Physical Chemistry B* 2011, 115, 7238.
- (20) Stradner, A.; Sedgwick, H.; Cardinaux, F.; Poon, W. C. K.; Egelhaaf, S. U.; Schurtenberger, P. *Nature* 2004, 432, 492.
- (21) Lu, P. J.; Zaccarelli, E.; Ciulla, F.; Schofield, A. B.; Sciortino, F.; Weitz, D. A. *Nature* 2008, 453, 499.
- (22) Sedgwick, H.; Egelhaaf, S. U.; Poon, W. C. K. *Journal of Physics: Condensed Matter* 2004, 16, S4913.

- (23) Groenewold, J.; Kegel, W. K. J. Phys. Chem. B 2001, 105, 11702.
- (24) Groenewold, J.; Kegel, W. K. Journal of Physics-Condensed Matter 2004, 16, S4877.
- (25) Beenakker, C. W. J.; Mazur, P. Physica A 1984, 126, 349.
- (26) Whitmore, L.; Wallace, B. A. Biopolymers 2008, 89, 392.
- (27) Asakura S.; Oosawa F. J. Chem. Phys. 1954, 22.
- (28) Lekkerkerker, H. N. W.; Tuinier, R. Colloids and the Depletion Interaction; Springer: New York, 2011; Vol. 833.
- (29) Vrij, A. Pure and Applied Chemistry 1976, 48, 471.
- (30) Chari, R.; Jerath, K.; Badkar, A. V.; Kalonia, D. S. Pharm. Res. 2009, 26, 2607.
- (31) Moody, T. P.; Kingsbury, J. S.; Durant, J. A.; Wilson, T. J.; Chase, S. F.; Laue, T. M. Analytical Biochemistry 2005, 336, 243.
- (32) Asakura, S.; Oosawa, F. Journal of Polymer Science 1958, 33, 183.
- (33) Davis-Searles, P. R.; Saunders, A. J.; Erie, D. A.; Winzor, D. J.; Pielak, G. J. Annu Rev Biophys Biomol Struct 2001, 30, 271.
- (34) Jiang, T.; Wu, J. Physical Review E 2009, 80.
- (35) Bergenholtz, J.; Poon, W. C. K.; Fuchs, M. Langmuir 2003, 19, 4493.
- (36) Ramakrishnan, S.; Fuchs, M.; Schweizer, K. S.; Zukoski, C. F. J Chem Phys 2002, 116, 2201.
- (37) Ilett, S.; Orrock, A.; Poon, W.; Pusey, P. Physical Review E 1995, 51, 1344.
- (38) Kulkarni, A. M.; Dixit, N. M.; Zukoski, C. F. Faraday Discussions 2003, 123, 37.
- (39) Lewus, R. A.; Darcy, P. A.; Lenhoff, A. M.; Sandler, S. I. Biotechnology progress 2011, 27, 280.
- (40) Lee, J. C.; Timasheff, S. N. Journal of Biological Chemistry 1981, 256, 7193.
- (41) Kreilgaard, L.; Frokjaer, S.; Flink, J. M.; Randolph, T. W.; Carpenter, J. F. J Pharm Sci 1999, 88, 281.
- (42) Windholz, M.; Editor The Merck Index: An Encyclopedia of Chemicals and Drugs. 9th Ed; Merck and Co., Publ. Dept., 1976.

- (43) Shen, V. K.; Cheung, J. K.; Errington, J. R.; Truskett, T. M. Journal of biomechanical engineering 2009, 131, 071002.

Chapter 5: Characterization of structures in protein formulations with high co-solute concentrations by small angle x-ray scattering

The diffusion coefficient as measured by DLS in the high co-solute samples was seen to be significantly lower than that for protein monomer while that for the low co-solute samples is close to the monomer value even at protein concentrations up to 230 mg/ml. The lowering of the diffusion coefficient was theorized to be through the formation of nanoclusters. The presence of the nanostructures in protein formulations with a high concentration of a mixture of trehalose, histidine and citric acid as co-solutes was studied by SAXS to bolster the DLS data. Larger entities are shown to be present by SAXS in protein formulations at 125 mg/ml mAb1 containing high co-solute concentrations. In contrast, low co-solute formulations do not show evidence of structures larger than ~15 nm which corresponds to monomer size. The co-solutes may cause assembly of the nanostructures by giving rise to strong short-ranged depletion attraction which drives proteins together into nanoclusters with the cumulative long-ranged electrostatic repulsion between proteins in the nanoclusters limiting the nanocluster size. Additionally these high co-solute samples are seen to have a lower viscosity than low co-solute samples at the same mAb concentration.

5.1 INTRODUCTION

Recently, large and long-lived protein nanostructures at very high protein concentrations (>200 mg/ml) were studied by dynamic light scattering (DLS).^{1,2} Proteins were forced together through depletion attraction by adding trehalose as a co-solute which assembled the proteins into the nanostructures as discussed in Chapters 3 and 4. The accumulation of proteins into nanostructures was opposed by the longer ranged

electrostatic repulsions between the proteins in the low dielectric constant environment of the clusters.^{2,3} The balance of the two opposing forces determined the size of the nanostructure. Similar larger structures were also observed in other cases by DLS although the fraction of protein contained in these bigger entities is typically low.⁴⁻⁶ The formation of these nanostructures through the addition of high co-solute concentrations was hypothesized to lower viscosity when compared to conventional monomer solutions with low levels of co-solutes. The nanostructures were also shown to dissociate into stable, active and monomeric protein molecules after dilution in vitro and in vivo.¹ The cluster size was determined from the diffusion rates measured by the DLS while assuming that the species diffused through a medium which had the same viscosity as that of the solvent in which they were formulated using the Stokes Einstein model.^{1,2} Also it was assumed that in the duration of the measurement that the clusters did not interact with each other or with free monomer which may have been present in the sample. However at high protein concentration above 200 mg/ml, these assumptions may or may not hold true.⁷ Therefore, the cluster size at these high protein concentrations needs to be verified by other independent methods to ensure that the DLS technique used yielded reasonable results. Also DLS does not quantify the structure of the protein while it is still inside the clusters which would be an interesting phenomenon to explore using methods capable of seeing it to verify the results reported for protein folding at high volume fractions using cross-grained models.^{8,9}

Small angle x-ray scattering (SAXS) is routinely used in order to explore the crystal structure of proteins to enable determination of protein structure, sequence, etc.¹⁰⁻¹² Additionally protein oligomerization particularly for monoclonal antibodies (mAbs) resulting in the formation of dimers, trimers and larger species has also been explored by

SAXS.^{13,14} The apparent molecular weight and the radius of gyration resulting from the scattering profile increased as protein concentration was increased from 1 to 5 mg/ml indicating that the oligomeric content of the sample is also raised.¹³ The dimerization at higher concentrations was studied by means of small angle neutron scattering (SANS) and neutron spin echo characterization which showed a behavior similar to the critical micellar concentration for surfactants where the sample contained mainly dimeric species at concentrations above 10 mg/ml with a gradual increase in the dimer concentration until that point.¹⁴ These clusters had a detrimental effect on the viscosity of the mAb solutions with viscosity increasing as the size of these oligomers increased.^{13,14} Additionally, small clusters of lysozyme present at relatively high lysozyme concentrations of greater than 100 mg/ml have been studied by SAXS showing that it is well established for studying the formation of higher order structures in proteins.^{15,16} A single SAXS experiment can investigate a continuum of length scales providing both monomer-monomer and cluster-cluster structural pair correlations.¹⁷ The structure of proteins inside the nanoclusters can also be probed in terms of obtaining the size of the protein monomer via the primary scattering peak. Additionally, the structure factor can be modelled in order to determine what structures are present in the sample in terms of their size and persistence.¹⁸ Upon changing density, strong protein-protein attraction augments the low q scattering via the drive to form a protein rich condensed phase (either macrophase or microphase) while if repulsion dominates a low q depression is found as the fluid becomes less compressible. One, more approximate guideline suggesting whether attraction or repulsion dominates is if the low q structure factor is above or below 1 respectively. Interactions between proteins contained in the nanoclusters and between the nanoclusters themselves can therefore be studied using SAXS lending to a better understanding of the cluster

morphology and interactions. The size and other properties measured by SAXS are unaffected by the temporal dynamics of the sample like diffusion since it is a static measurement. Therefore, as the measurements are based on different principles, agreement between the DLS and the SAXS data about the presence of larger species would be much more convincing evidence for the presence of nanoclusters. SAXS can also be used to visualize the interactions between structures at different length scales by determining the structure factor.¹⁹⁻²¹ To further bolster the structural study, contrasting monomer scattering profiles with scattering profiles of nanocluster samples will help to compare and contrast the structures in the monomer and nanocluster samples.

5.2 MATERIALS AND METHODS

5.2.1 Materials

The monoclonal antibody (called mAb1) used in this study was obtained from Abbvie at ~120 mg/ml in a proprietary buffer composition henceforth called the original buffer. Histidine, sodium monophosphate, sodium biphosphate, citric acid and HCl were purchased from Fisher Scientific, Fairlawn, NJ. Trehalose was purchased from Ferro Pfanstiehl Laboratories Inc., Waukegan, IL.

5.2.2 Preparation of dispersion samples

The samples were prepared by tangential flow filtration (TFF) with diafiltration for buffer exchanging into the correct buffer followed by an ultrafiltration step to concentrate the sample. More dilute samples were prepared by subsequent dilution into buffer. For tangential flow filtration, the buffers with the desired composition were first

prepared by dissolving the co-solutes in DI water. The buffers were sterile filtered with the Celltreat bottle top PES filters and then degassed under vacuum for 30 minutes. The frozen mAb stock (25 ml in 5 vials) was thawed in a 4°C water bath and diluted with an equal volume (25 ml) of the buffer, resulting in a mAb concentration of 65 mg/ml. The diluted mAb solution was gently mixed in a 50-ml centrifuge tube, which served as the retentate reservoir during the TFF experiments. In certain experiments, the diluted mAb solution was additionally sterile-filtered using the 0.22 μm bottle top filters and degassed.

The diluted mAb solution was then buffer-exchanged at constant concentration with permeation of six diavolumes (150 ml) of the desired formulation buffer with a KrosFlo Research II TFF system (Spectrum Labs, Rancho Dominguez, CA) operated in a constant-volume mode. The TMP was maintained at 0.80 bar using a KrosFlo automatic backpressure valve (Spectrum Labs, Rancho Dominguez, CA), which regulated the pressure by constricting the retentate line. The feed cross-flow rate was set at 100 ml/min corresponding to calculated wall shear rates inside each fiber of 1415 s^{-1} respectively. The retentate reservoir was gently mixed throughout the process using a Vari Mix Platform Rocker (Thermo Fisher Scientific, Fair Lawn, NJ) set at the maximum speed and rocking angle along with periodic mixing through swirling by hand. The buffer-exchanged solution was recovered and sterile filtered, then stored overnight at 4°C, after which it was concentrated to ~250 mg/ml the following day.

The buffer-exchanged mAb solution was concentrated from 65 mg/ml to 250 mg/ml by ultrafiltration using the 1.0 mm ID hollow fiber module. The feed cross-flow rate was initially kept at 100 ml/min and the TMP was maintained at 0.80 bar. When the mAb solution became too viscous ($> 150\text{ cP}$), the TMP could no longer be regulated so the feed cross-flow rate was decreased. The rocker angle for the Vari Mix Platform

Rocker was gradually reduced over time as the fluid level in the retentate reservoir decreased in order to keep the feed and retentate return lines submerged. The retentate concentration at any given time was estimated based on the mass of the permeate which was monitored real time assuming no permeation of mAb through the membrane and the filtration was stopped at a mAb concentration of 250 mg/ml.

5.2.3 Characterization of the protein formulations

5.2.3.1 Measurement of formulation viscosity

The viscosity of the nanocluster dispersion was measured in triplicate with a 25 gauge (ID = 0.1 mm) 1.5” long needle (Becton Dickinson & Co. Precision Glide Needle) which was attached to a 1 ml syringe (Becton Dickinson & Co. 1 ml syringe with Luer-Lok™ tip), using to the Hagen-Poiseuille equation. The dispersion flow rate through the needle was determined using the volume left in the vial, which had been previously correlated to the height of the liquid, at two different time points during drawing up the protein formulation. The measured flow rate was then correlated to viscosity from a calibration curve derived from a set of standards of known viscosities as described previously.²

5.2.3.2 Measurement of diffusion coefficient by DLS

The effective CONTIN diffusion coefficient of protein monomers and nanoclusters were measured by dynamic light scattering (DLS) at an angle of 150° with a 632.8 nm laser and an avalanche photodiode at ~23°C using the CONTIN algorithm (Brookhaven BI-9000AT). The samples were pipetted into a 60 µl sample cell (Beckman

Coulter) which was then mounted on the instrument to conduct three replicate runs of 2 minutes each. All reported diffusion coefficients are the average of three runs. The diameter of the entities was calculated using the Stokes-Einstein model.

5.2.3.3 Determination of protein concentration

For determining the concentration of the dispersions, 2 μl of dispersion was measured out and diluted into a receiving vessel containing 998 μl of 50 mM pH 6.4 phosphate buffer mixing well with the pipette tip. The diluted samples were prepared in duplicate. The absorbance of the resulting solution was measured using a Cary 3E uv-visible spectrophotometer in a cuvette (Hellma cells) with a path length of 1 cm. Then using Beer's law ($A = \epsilon b c$, where ϵ = extinction coefficient = $1.43 \text{ ml mg}^{-1} \text{ cm}^{-1}$, b = path length = 1 cm), knowing the absorbance, the concentration of the protein in the solution was calculated.

5.2.3.4 Small angle x-ray scattering measurements of formulations

The SAXS measurements were performed on the National Synchrotron Light Source's X9 beamline at Brookhaven National Laboratories, NY or on a Nanostar U (Bruker-AXS) instrument equipped with a VANTAC 2000 detector and rotating copper anode. The scattering data for the X-9 beamline were collected using a charge-coupled device (CCD) area detector for the X-rays. The data are presented as either the background corrected angular averaged one dimensional scattering intensity profile $P(q)$ or the structure factor $S(q)$ vs scattering vector, $q = (4\pi/\lambda)\sin(\theta/2)$, where θ is the scattering angle. The values of q were determined by calibration with silver behenate (q_1

= 0.1076 Å⁻¹) prior to the measurement. Samples were run for 10 s with 3 replicates measured for each sample.

5.3 RESULTS AND DISCUSSION

5.3.1 Nanostructure characterization for protein concentration of 125 mg/ml

Fig. 5.1 shows the SAXS intensity profile for a dilute mAb solution at 3 mg/ml in the original buffer. The profile does not have any prominent features and is in excellent agreement with the profiles previously seen for dilute monomeric mAb solutions.^{13,14,19,22} The featurelessness of the profile originates because there is not much structure in the sample apart from protein monomer in addition to a very minor contribution from interactions due to its very dilute nature. Therefore, the intensity profile from Fig. 5.1 was assumed to be the form factor ($FF(q)$) and was used to compute the structure factor ($S(q)$) of the samples as shown in Eq. 5.1.

$$P(q) = FF(q) \times S(q) \dots (5.1)$$

where $P(q)$ is the scattered intensity, $FF(q)$ is the form factor and $S(q)$ is the structure factor.

Fig. 5.2a shows the SAXS intensity profile for a mAb solution at 120 mg/ml in the original buffer (called P1) which contains a very low level of co-solutes. Fig. 5.2a also displays the scattering profile for a mAb dispersion at 125 mg/ml with 40 mg/ml trehalose, 50 mg/ml histidine and 17 mg/ml citric acid at pH 6 prepared by dilution of a sample in the same buffer at 250 mg/ml by TFF (P2). The viscosities of the samples are shown in Table 5.1 with the dispersion being significantly less viscous than the solution. Also as Fig. 5.2a shows, the monomer scattering profile has a prominent peak at a q of

about 0.04 \AA^{-1} corresponding to a length scale of $\sim 15 \text{ nm}$. The cluster sample does not have a peak in the same q range but it forms a plateau at a much higher intensity than the monomer sample and at lower q values of $\sim 0.01 \text{ \AA}^{-1}$ corresponding to a length scale of $\sim 50 \text{ nm}$. Fig. 5.2b shows the effect of increasing protein concentration on the structure in the original buffer through the structure factor. The peak at 0.04 \AA^{-1} from the intensity profile is much amplified indicating that the peak may be due to strong repulsion at the length scale of $\sim 15 \text{ nm}$ which closely corresponds to a length scale of the monomer size of 11 nm in the solution. Therefore the monomers in solution seem to have a net repulsive interaction at close spacing although at longer distances, the interaction seems to become more neutral with a small peak at around 50 nm which may indicate the presence of some minor (likely transient) aggregates or possibly micelles of Tween-80 which is present in the sample. The data for P1 run on a rotating anode SAXS instrument instead of a synchrotron beamline is shown in Fig. D1 with reasonable agreement between the synchrotron and rotating anode data.

The structure factor for the cluster sample (Fig. 5.2c), on the other hand displays a much weaker repulsive interaction on the monomer level as is evident from the scattering profile with the peak also shifted to slightly lower q meaning that the interaction is at longer length scales. However, unlike the monomer sample, the structure factor here climbs to a peak at a higher length scale of $\sim 50 \text{ nm}$ hinting at the presence of larger species in the sample supporting the data obtained by dynamic light scattering. The peak value of 3.2 is higher than the threshold value of 2.7 which is the value of the structure factor at which the higher-order species must be long-lived (non-transient).¹⁸ Therefore the addition of co-solutes to mAb formulations seems to lead to the formation of some higher order species in the system. The reason for the difference in the shape of the peak

corresponding to the monomer compared to the monomer sample itself could be the changed interactions between the monomer proteins as a result of the added excipients. Histidine binds to and blocks interacting sites on proteins likely altering the nature of the monomer-monomer interactions. Further, trehalose will give rise to some osmotic depletion attraction between protein monomers both inside and outside the clusters thus further perturbing the structure factor. The crowded environment in the interior of the nanocluster may also affect the structure of proteins (likely through a net compression of the protein which tends to favor the native state). All the factors mentioned above may therefore result in the wider and shorter peak for the monomer seen in the sample with excipients present.

DLS of the sample shows that the high co-solute sample has much higher relaxation times and, thereby, likely contains larger structures as seen from the D/D_0 values (ratio of measured diffusion coefficient to the calculated diffusion coefficient for a monomer equivalent hard sphere with a diameter of 11 nm diffusing through the same solvent) shown in Table 5.1 and the ACFs shown in Fig. D2 with the average sizes and standard deviations in Table 5.1. Based on the D/D_0 values, the low co-solute sample seems to contain species diffusing at a rate indicating that they are in the 5-10 nm length scale while the high co-solute sample has species 2.5 times that of the monomer. Therefore, we speculate that the addition of the excipients to a protein solution causes depletion attraction to arise between proteins and causes them to assemble into nanoclusters or undergo micro-phase separation. The nanocluster size increases until equilibrium is reached when the net repulsion from all proteins present in the clusters leads to a net repulsion between the monomers and the cluster.^{1,2} The viscosity decrease for the high excipient cluster samples which was mentioned earlier is probably due to the

largely neutral interactions between the species in solution compared to the strong interactions between proteins. The previous hypothesis is based on a trend seen for low co-solute protein solutions where viscosity decreases as the interactions become more strongly repulsive for mAbs.^{23,24}

5.3.2 Characterization of higher protein concentration formulations

Fig. 3a shows the SAXS scattering profiles for other formulations at higher concentrations of 250 mg/ml to contrast against the data at 120 mg/ml from Fig. 5.2. The detailed compositions, viscosities and average DLS sizes is shown in Table 5.1. As can be seen, all the samples except for P4 have an upturn in intensity at a q value of 0.126 corresponding to a correlation length of > 50 nm. For P3 there is an upturn in the intensity at the q range of 40-60 nm while their D/D_0 is ~ 0.35 indicating entities of a size around 30 nm (Fig. 5.3b) seemingly agreeing with each other within ~ 10 -20 nm. The upturn is especially prominent for P5 which is a sample of a different mAb (mAb2) which had the largest nanostructures ($D/D_0 = 0.17$) by DLS as shown in Fig. 5.3b. The profile for P4 seems to be relatively flat with no upturn in the intensity at lower q values indicating that there are no larger species in this sample in agreement with the DLS data which shows no significant decrease in the D/D_0 . Therefore the trends in the features present in the samples as surmised from the SAXS profile seem to agree with the trend in D/D_0 seen for these samples in Table 5.1 for which the ACFs are shown in Fig. D3. Low co-solute monomer samples were not studied at 250 mg/ml since they were extremely viscous and prone to gelation and aggregation (gelling within a day). The scattering profile data for P3 obtained from a rotating anode SAXS instrument instead of a

synchrotron beamline is shown in Fig. D1 with reasonable agreement between the synchrotron and rotating anode data.

At these high concentrations of mAbs, the SAXS intensity is depressed as is evidenced by the structure factor for concentrated protein formulations evidenced in other studies.^{15,25,26} The trend of lowered intensity at lower q values is more obvious in the structure factor for the concentrated cluster samples (Fig. D4). The structure factor for P4 is seen to be even lower than that for the other samples as the size of nanostructures contained in this sample is seen to be very small. Interestingly, the peak for the monomer structure seems to be shifted to lower values of ~ 5 nm for these samples which may be indicative of proteins being compressed at the high concentration inside the nanocluster due to self-crowding. The depression seen for the other samples is not as severe as it is for P4 due to the presence of larger species in the other samples as indicated by the DLS measurements. The reason for this depression is not clear, but it may be due to interfering multi-body interactions from proteins/nanoclusters in close proximity. Also, at these high concentrations, the particles are very close to each other which may make it difficult to distinguish the structures clearly apart from each other. Another factor may be that the structures are not very long lived which leads to the depression in structure factor with increased density as has been theorized previously.¹⁸ However, more experiments are needed to conclusively understand this behavior of the samples at high concentration.

5.4 CONCLUSIONS

The protein nanoclusters and monomer samples seem to have structures on different size scales present in them as is evident from the SAXS profiles. The high co-solute cluster samples have significantly higher intensity of scattering at lower q values

corresponding to higher sizes which can be seen more clearly in the structure factor plots. The high co-solute cluster samples show the characteristic peak seen in the concentrated low co-solute monomer samples at around 15 nm, although it is shifted to lower q values and depressed which indicates modified interactions and structure. The cluster samples contain species in the > 50 nm range at both 125 mg/ml and 250 mg/ml while the monomer sample has species in the 15 nm size range.

Na me	Prote in conc (mg/ ml)	Exc 1	Exc 1 conc (mg/ ml)	Exc 2	Exc 2 conc (mg/ ml)	Exc 3	Exc 3 conc (mg/ ml)	p H	D_c (n m)	D_c st dev (n m)	D/D_0	Visco sity (cP)
P1	120	origi nal buffe r						6	11. 5	3.7	0.9 6	5
P2	125	tre	40	his	50	cit	17	5. 8	25	5	0.4 4	3
P3	242	tre	40	his	50	cit	17	6	31. 9	3.7	0.3 5	53
P4	249	imid	150	HCl	65.6			6. 3	15. 1	2.3	0.7 3	37
P5	220	tre	220	phosph ate	50 mM			8. 2	66	5.0	0.1 7	90

Table 5.1: Compositions, DLS data and viscosities of samples from the current Chapter.

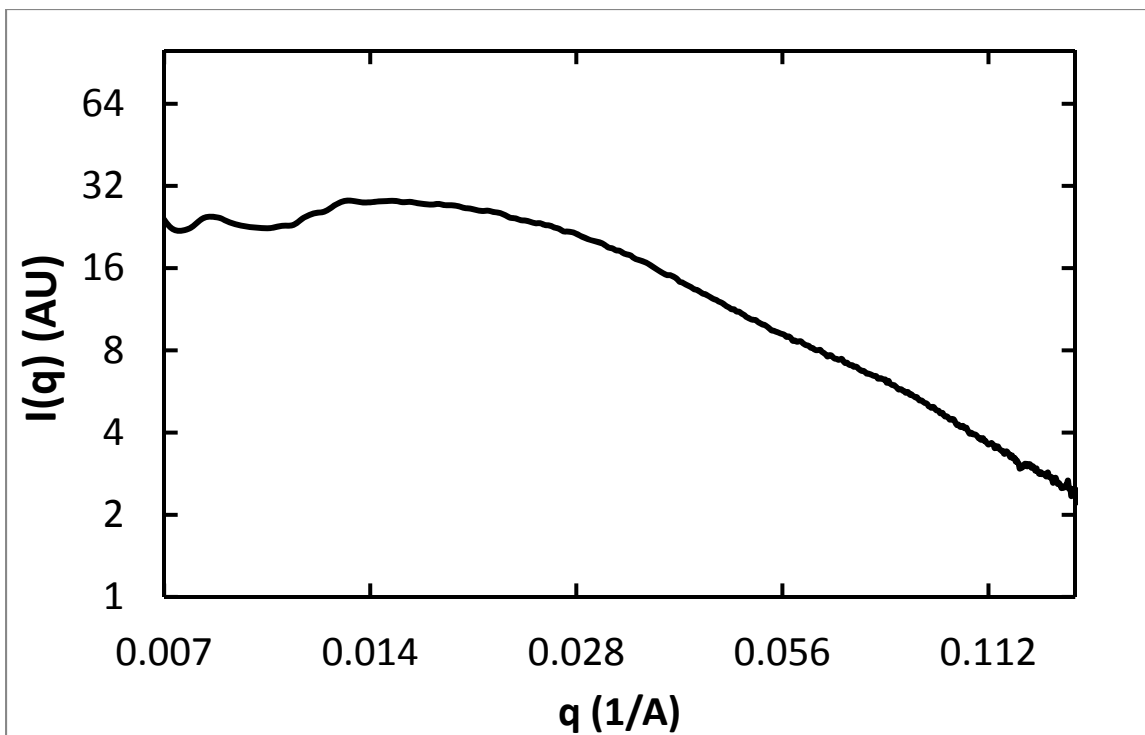
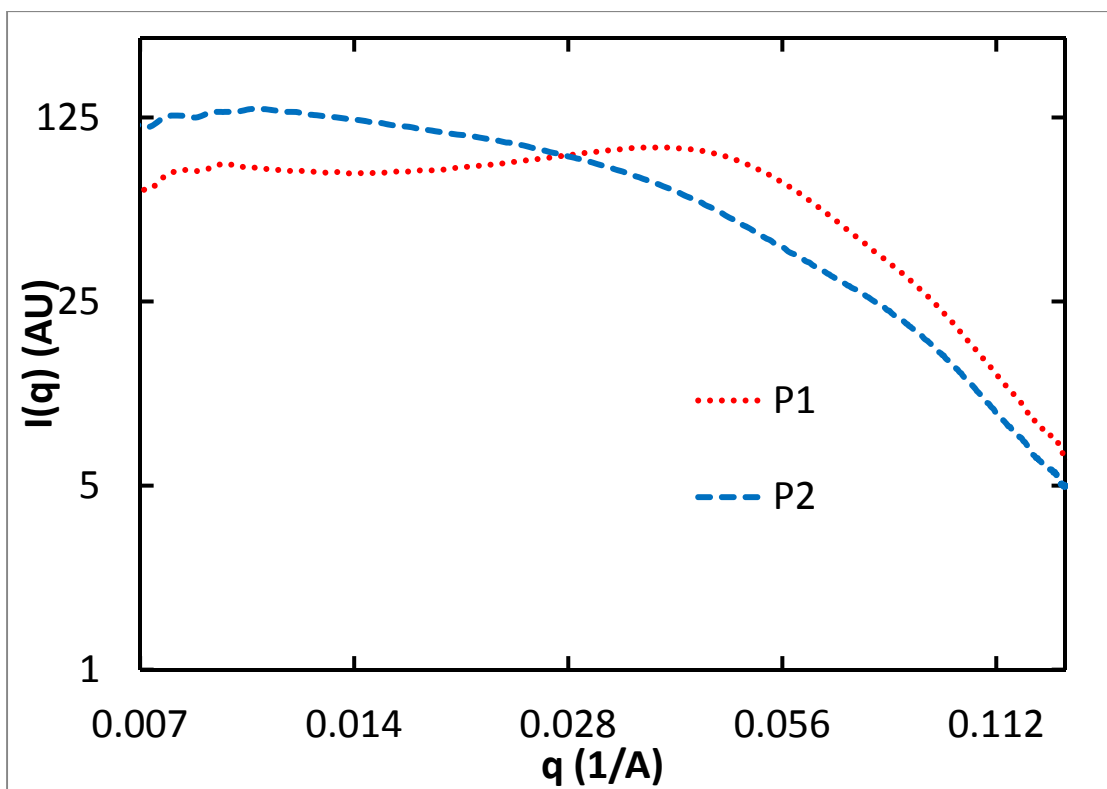
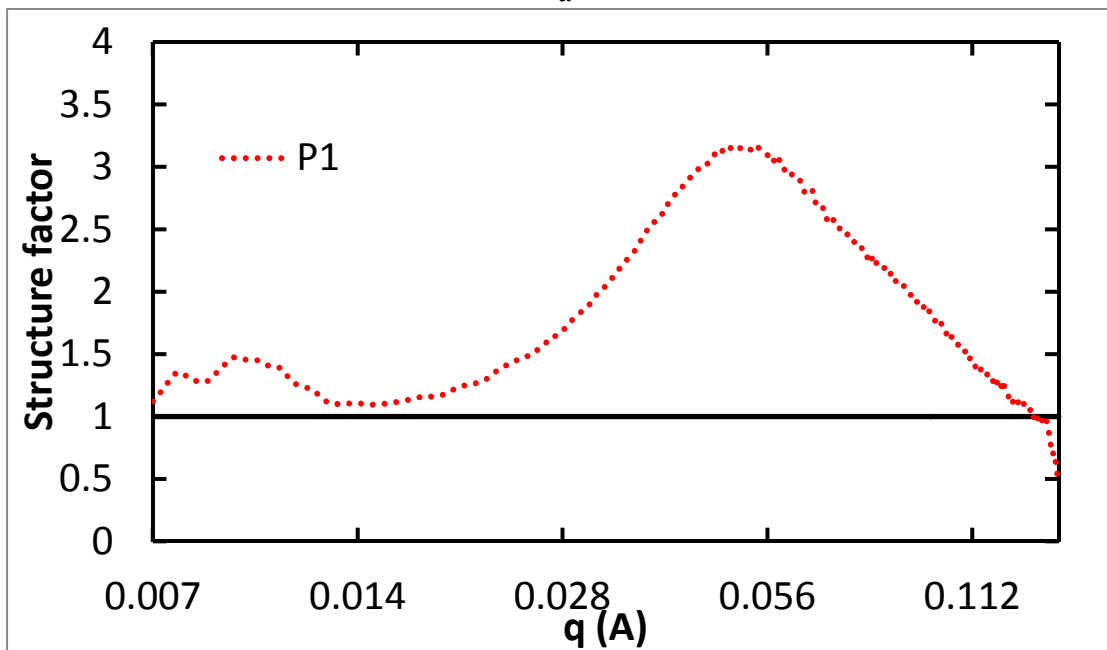


Figure 5.1: Scattering profile for a dilute protein solution at 3 mg/ml in the original formulation buffer which was used as the form factor.



a



b

(Fig. 5.2 continued on the next page)

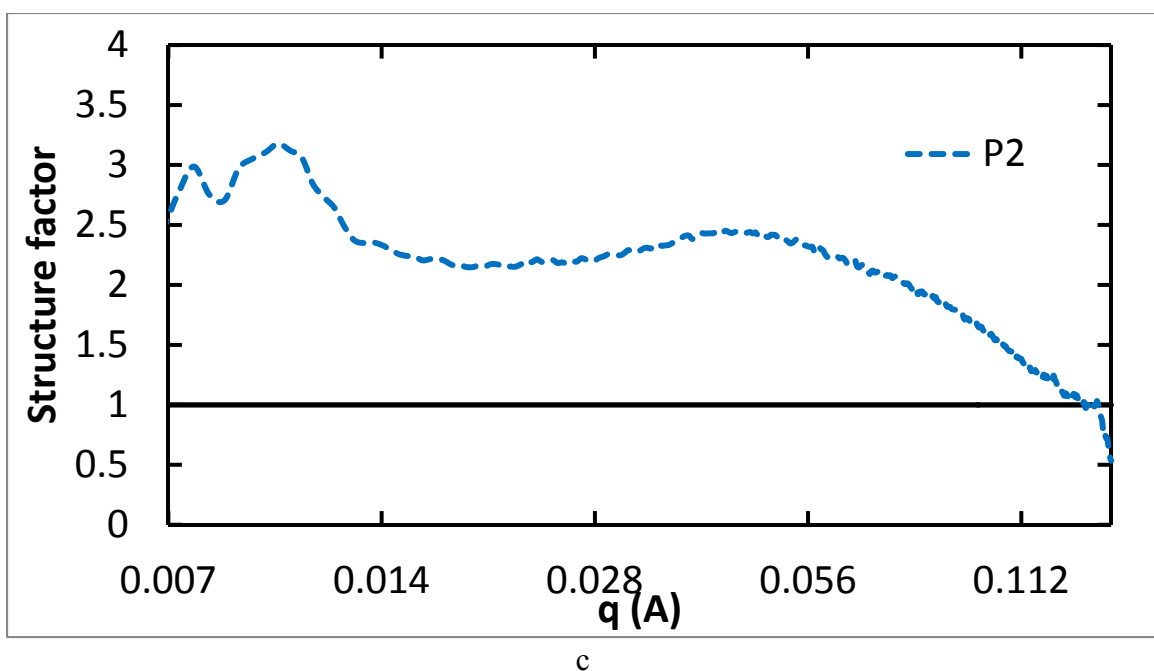


Figure 5.2: Monomer (P1, red dots) and cluster (P2, blue dashes) samples show a very different structure at the same concentration. b. Structure factor for low co-solute monomer sample from 5.2a. c. structure factor for high co-solute cluster sample in 5.2a.

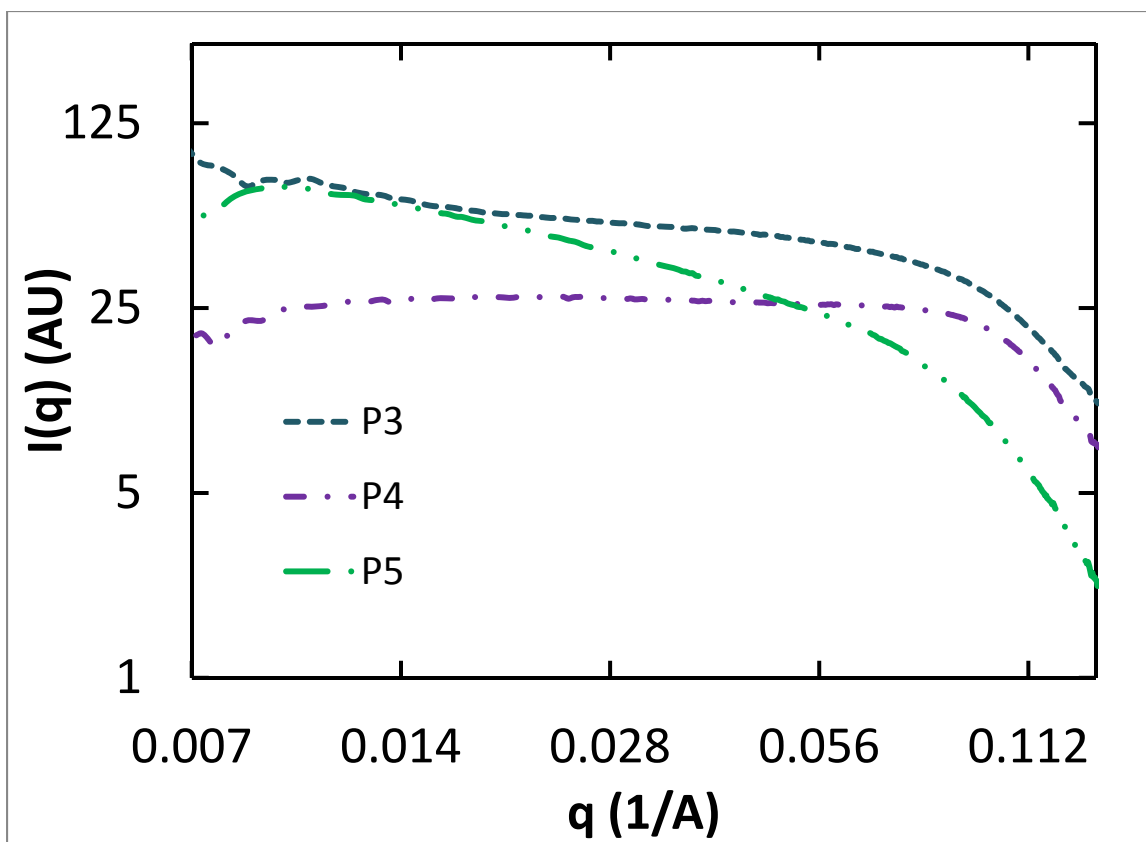


Figure 5.3: SAXS profiles for protein dispersions at 250 mg/ml.

5.5 REFERENCES

- (1) Johnston, K. P.; Maynard, J. A.; Truskett, T. M.; Borwankar, A.; Miller, M. A.; Wilson, B.; Dinin, A. K.; Khan, T. A.; Kaczorowski, K. J. *ACS Nano* 2012.
- (2) Borwankar, A. U.; Dinin, A. K.; Laber, J. R.; Twu, A.; Wilson, B. K.; Maynard, J. A.; Truskett, T. M.; Johnston, K. P. *Soft Matter* 2013, 9, 1766.
- (3) Groenewold, J.; Kegel, W. K. *J. Phys. Chem. B* 2001, 105, 11702.
- (4) Li, Y.; Lubchenko, V.; Vekilov, P. G. *Rev Sci Instrum* 2011, 82, 053106.
- (5) Pan, W. C.; Vekilov, P. G.; Lubchenko, V. J. *J. Phys. Chem. B* 2010, 114, 7620.

- (6) Soraruf, D.; Roosen-Runge, F.; Grimaldo, M.; Zanini, F.; Schweins, R.; Seydel, T.; Zhang, F.; Roth, R.; Oettel, M.; Schreiber, F. *Soft Matter* 2014, 10, 894.
- (7) Horn, F. M.; Richtering, W.; Bergenholtz, J.; Willenbacher, N.; Wagner, N. J. *J Colloid Interface Sci* 2000, 225, 166.
- (8) Cheung, J. K.; Truskett, T. M. *Biophys J* 2005, 89, 2372.
- (9) Shen, V. K.; Cheung, J. K.; Errington, J. R.; Truskett, T. M. *Journal of biomechanical engineering* 2009, 131, 071002.
- (10) Hura, G. L.; Menon, A. L.; Hammel, M.; Rambo, R. P.; Poole, F. L.; Tsutakawa, S. E.; Jenney, F. E.; Classen, S.; Frankel, K. A.; Hopkins, R. C.; Yang, S. J.; Scott, J. W.; Dillard, B. D.; Adams, M. W. W.; Tainer, J. A. *Nat. Methods* 2009, 6, 606.
- (11) Forster, F.; Webb, B.; Krukenberg, K. A.; Tsuruta, H.; Agard, D. A.; Sali, A. *J Mol Biol* 2008, 382, 1089.
- (12) Rozycki, B.; Kim, Y. C.; Hummer, G. *Structure* 2011, 19, 109.
- (13) Lilyestrom, W. G.; Yadav, S.; Shire, S. J.; Scherer, T. M. *J Phys Chem B* 2013, 117, 6373.
- (14) Yearley, E. J.; Godfrin, P. D.; Perevozchikova, T.; Zhang, H.; Falus, P.; Porcar, L.; Nagao, M.; Curtis, J. E.; Gawande, P.; Taing, R.; Zarraga, I. E.; Wagner, N. J.; Liu, Y. *Biophys J* 2014, 106, 1763.
- (15) Cardinaux, F.; Zaccarelli, E.; Stradner, A.; Bucciarelli, S.; Farago, B.; Egelhaaf, S. U.; Sciortino, F.; Schurtenberger, P. *J Phys Chem B* 2011, 115, 7227.
- (16) Kowalczyk, P.; Ciach, A.; Gauden, P. A.; Terzyk, A. P. *J Colloid Interface Sci* 2011, 363, 579.
- (17) Spinozzi, F.; Maccioni, E.; Teixeira, C. V.; Amenitsch, H.; Favilla, R.; Goldoni, M.; Di Muro, P.; Salvato, B.; Mariani, P.; Beltramini, M. *Biophys J* 2003, 85, 2661.
- (18) Godfrin, P. D.; Valadez-Perez, N. E.; Castaneda-Priego, R.; Wagner, N. J.; Liu, Y. *Soft Matter* 2014, 10, 5061.
- (19) Mosbaek, C. R.; Konarev, P. V.; Svergun, D. I.; Rischel, C.; Vestergaard, B. *Pharm. Res.* 2012, 29, 2225.
- (20) Gelamo, E. L.; Itri, R.; Alonso, A.; da Silva, J. V.; Tabak, M. *J Colloid Interface Sci* 2004, 277, 471.
- (21) Zhang, F.; Roosen-Runge, F.; Skoda, M. W.; Jacobs, R. M.; Wolf, M.; Callow, P.; Frielinghaus, H.; Pipich, V.; Prevost, S.; Schreiber, F. *Phys Chem Chem Phys* 2012, 14, 2483.

- (22) Castellanos, M. M.; Pathak, J. A.; Leach, W.; Bishop, S. M.; Colby, R. H. *Biophys J* 2014, 107, 469.
- (23) Connolly, B. D.; Petry, C.; Yadav, S.; Demeule, B.; Ciaccio, N.; Moore, J. M.; Shire, S. J.; Gokarn, Y. R. *Biophys J* 2012, 103, 69.
- (24) Saito, S.; Hasegawa, J.; Kobayashi, N.; Kishi, N.; Uchiyama, S.; Fukui, K. *Pharm. Res.* 2012, 29, 397.
- (25) Stradner, A.; Sedgwick, H.; Cardinaux, F.; Poon, W. C. K.; Egelhaaf, S. U.; Schurtenberger, P. *Nature* 2004, 432, 492.
- (26) Cardinaux, F.; Stradner, A.; Schurtenberger, P.; Sciortino, F.; Zaccarelli, E. *Europhysics Letters (EPL)* 2007, 77, 48004.

Chapter 6: Cryo-SEM for direct visualization of high concentration protein formulations at high and low co-solute concentration

The diffusion coefficient as measured by DLS in the high co-solute formulations was seen to be significantly lower than that for protein monomer while that for the low co-solute samples is close to the monomer value even at protein concentrations up to 230 mg/ml. The lowering of the diffusion coefficient was theorized to be through the formation of nanoclusters. The presence of nanostructures in protein formulations containing a high concentration of a mixture of trehalose, histidine and citric acid as co-solutes was somewhat supported by SAXS in Chapter 5 to bolster the DLS data. Larger entities are also observed by SANS in protein formulations at 125 and 250 mg/ml mAb1 containing high co-solute concentrations. In contrast, low co-solute formulations and buffer solutions which were imaged as controls did not show evidence of any structures as the monomer size is probably below the threshold for detection by cryo-SEM. Cryo-SEM preserves structures present in the liquid state through the freezing process allowing direct observation of those structures. The controls provide support that the structures present in the high co-solute samples were not formed as an artifact of the sample preparation prior to imaging. The co-solutes may cause assembly of these structures by giving rise to strong short-ranged depletion attraction which drives the proteins together into nanoclusters with the cumulative long-ranged electrostatic repulsion between proteins in the nanoclusters limiting the nanocluster size. Additionally these high co-solute samples are seen to have a lower viscosity than low co-solute samples at the same mAb concentration probably as a result of modified interactions.

6.1 INTRODUCTION

High concentration protein formulations are of growing interest for the rapidly expanding field of mAb therapeutics and related biologics. The high concentration formulations with greater than 200 mg/ml mAb can aid use of sub-cutaneous self-injection for administration instead of medically supervised intravenous injection.^{1,2} At this high mAb concentration, the small surface to surface distances between proteins of ~1-5 nm allow attractive protein-protein interactions to have the detrimental effect of causing aggregation, unfolding and gelation.^{1,3-12} The formation of aggregates can affect the macroscopic properties of protein formulations like low shear viscosity for example.^{5,6} Studies have also theorized that formation of reversible clusters in mAb formulations is responsible for the elevation in the viscosity at high protein concentrations due to the attractive interactions responsible for causing the association of these proteins.¹³⁻¹⁵

The clusters responsible for the above elevation in viscosity were typically small oligomers forming due to specific attractive interactions between proteins due to alignment of oppositely charged patches or hydrophobic patches.^{13,14,16,17} These oligomers were studied using the scattering profiles generated by either small angle X-ray scattering (SAXS) or small angle neutron scattering (SANS).^{13,14} The SAXS studies were bolstered with supporting techniques for size determination like static light scattering (SLS)¹³ or neutron spin echo analysis¹⁴ to determine the size of the cluster entity. The cluster size was seen to increase with the concentration of salt added to screen attractive electrostatic interactions.¹³ On the other hand, the cluster size was found to be relatively invariant with increasing protein concentration by neutron spin echo techniques analogous to the critical micellization phenomenon where all added monomeric species

above a certain concentration are incorporated into the collective entities which in the case of the mAb in this study are dimers. SAXS and SANS studies have also been used for studying cluster formation in other proteins like lysozyme although there is some debate on the lifetime of the lysozyme clusters and also in the interpretation of the data for the purpose of determining the cluster size.¹⁸⁻²²

Alternatively larger nanocluster species were observed by DLS in mAb formulations containing high concentrations of a co-solute, trehalose.^{23,24} Trehalose provides depletion attraction between proteins due to the entropy gain for trehalose as a result of pushing proteins together leading to increased available volume for its motion due to overlapping of the excluded hard sphere volume of proteins.²⁵⁻²⁷ Proteins contained in a nanocluster can repel any protein being added to the cluster resulting in a progressively increasing repulsion which eventually balances the attractive forces responsible for adding protein to the nanocluster and therefore limiting the nanocluster size. These nanoclusters were only sized by DLS with the cluster diffusion being assumed to occur through a medium with the effective viscosity of the solvent and then applying the Stokes-Einstein equation. The size determined by DLS is biased towards larger particles because larger particles scatter light more than smaller particles in the Rayleigh regime [Intensity \sim (diameter)⁶] and therefore have a higher contribution in the measured signal from the scattered light. Also the assumption that the diffusion follows the Stokes-Einstein model may not hold at these high protein concentrations despite using a correction because the nanoclusters formed are most probably not hard spheres.²⁴

Cryogenic scanning electron microscopy (cryo-SEM) is a technique that has been widely used for studying the structures present in liquid systems by means of vitrification of the sample and imaging the structure in the frozen state.²⁸⁻³¹ The most common

application of cryo-SEM is to image samples where changing the sample concentration or some other modifications in the sample can cause the sample morphology to change.²⁸ The freezing of the sample is carried out using either liquid ethane or slushed liquid nitrogen for rapid freezing to prevent convective forces from changing the sample morphology.^{28,32} The most common application of cryo-SEM is to image micro-emulsions of hexane in water or water in hexane to preserve the morphology which is very sensitive to the concentration of the various components even when these samples have higher viscosities that limit cryo-TEM imaging.³¹ The imaging has the capability of resolving structures as small as ~10 nm although smaller features tend to be obscured due to the metallic sputter coating needed for allowing the sample to be visualized.³³ The sputter coating helps to visualize samples with low contrast very easily. While cryo-TEM has been commonly used to visualize protein structures including micelles, cryo-SEM has rarely been used to visualize protein nanostructures because typically protein samples being imaged can be diluted.³⁴⁻³⁶ Cryo-TEM however is difficult to apply at higher particle concentrations because there can be overlap between particles leading to complications in distinguishing between multiple structures.^{36,37} Also, it is very difficult to get a thin film of liquid at the higher viscosity of the samples typically present in this dissertation.³¹

Herein we study high co-solute protein formulations by cryo-SEM for determining the size and presence of nanostructures in the same. Nanostructures will be imaged at different compositions of co-solutes and different protein concentrations in order to study the effect of variations in the same on the size and shape of the potential nanostructures. The sizes measured for the nanostructures were also compared with the expected sizes based on the measured diffusion coefficients for these high excipient

samples. For ensuring that the structures were not artifacts formed during processing, controls were also imaged with low co-solute concentrations where no decrease in the D/D_0 was observed with DLS in addition to the high co-solute buffers alone without proteins. The viscosities of the various formulations were also compared to examine the effect of the formation of the nanostructures on the macroscopic viscosity properties of the formulation.

6.2 MATERIALS AND METHODS

6.2.1 Materials

The monoclonal antibody (called mAb1) used in this study was obtained from Abbvie at ~120 mg/ml in a proprietary buffer composition henceforth called the original buffer. Histidine, sodium monophosphate, sodium biphosphate, citric acid and HCl were purchased from Fisher Scientific, Fairlawn, NJ. Trehalose was purchased from Ferro Pfanstiehl Laboratories Inc., Waukegan, IL.

6.2.2 Preparation of dispersion samples

The samples were prepared by TFF as described in Chapter 5.

6.2.3 Characterization of the protein formulations

6.2.3.1 Measurement of formulation viscosity

The viscosity of the nanocluster dispersion was measured in triplicate with a 25 gauge (ID = 0.1 mm) 1.5” long needle (Becton Dickinson & Co. Precision Glide Needle)

which was attached to a 1 ml syringe (Becton Dickinson & Co. 1 ml syringe with Luer-Lok™ tip), using to the Hagen-Poiseuille equation. The dispersion flow rate through the needle was determined using the volume left in the vial, which had been previously correlated to the height of the liquid, at two different time points during drawing up the protein formulation. The measured flow rate was then correlated to viscosity from a calibration curve derived from a set of standards of known viscosities as described previously.²⁴

6.2.3.2 Measurement of diffusion coefficient by DLS

The effective CONTIN diffusion coefficient of protein monomers and nanoclusters were measured by dynamic light scattering (DLS) at an angle of 150° with a 632.8 nm laser and an avalanche photodiode at ~23°C using the CONTIN algorithm (Brookhaven BI-9000AT). The samples were pipetted into a 60 µl sample cell (Beckman Coulter) which was then mounted on the instrument to conduct three replicate runs of 2 minutes each. All reported diffusion coefficients are the average of three runs. The diameter of the entities was calculated using the Stokes-Einstein model.

6.2.3.3 Determination of protein concentration

For determining the concentration of the dispersions, 2 µl of dispersion was measured out and diluted into a receiving vessel containing 998 µl of 50 mM pH 6.4 phosphate buffer mixing well with the pipette tip. The diluted samples were prepared in duplicate. The absorbance of the resulting solution was measured using a Cary 3E uv-visible spectrophotometer in a cuvette (Hellma cells) with a path length of 1 cm. Then

using Beer's law ($A = \epsilon b c$, where ϵ = extinction coefficient = $1.43 \text{ ml mg}^{-1} \text{ cm}^{-1}$, b = path length = 1 cm), knowing the absorbance, the concentration of the protein in the solution was calculated.

6.2.3.4 Cryo-SEM sample preparation and imaging

Cryo-SEM imaging was done with two different microscopes each with different cryo-prep systems. Most of the images are with the Quanta 650 FEG SEM with a PolarPrep 200 cryo system from Quorum Technologies. The broad end of a rivet (Electron Microscopy Services part no. 328116510) was made rough by abrading it with a file. The other end was sealed by dipping it in Tissue-Tek™. Then the rivet was fixed into a slot on the microscope stage (broad end up) and carefully filled with the sample until there was a convex meniscus of a drop extending over the top of the rivet. The broad end of another rivet was similarly roughened with a file and then the rivet was gently put on top of the filled rivet so that the sample droplet entered the upper rivet. Additional sample was added onto the narrow end of the top rivet and gently forced into the rivet assembly with a needle to ensure that there was a continuous column of liquid between the rivets while taking care to not dislodge the sandwiched rivet assembly. The stage was tilted till the rivets were sideways to ensure that they were stuck together due to a combination of the surface tension and viscosity of the sample. The rivet and stage assembly was then plunged into slushed liquid nitrogen (prepared by pulling a vacuum over liquid nitrogen) and held there for about a minute to ensure complete vitrification of the sample. The assembly was then rapidly transferred to the cryo-prep chamber which was maintained at -180°C and under 10^{-6} mTorr vacuum and locked in place on the stage holder. The top rivet was then knocked off with a knife to create a fresh fracture surface

of the sample. The sample was then sputter coated with platinum under an atmosphere of argon at 0.05 mTorr for 1 minute at a current of ~10 mA. The sample was then transferred to the microscope and imaged at an accelerating voltage of 10 kV.

The remaining images are with a Zeiss Supra 40 VP SEM with a custom Leica cryo-prep system. The sample prep for this was very similar except instead of using rivets, planchettes were used for containing the sample. A drop of sample was loaded onto a planchette and another planchette was placed on top of it to create a planchette sandwich. Also liquid nitrogen that was not slushed was used for freezing the sample. After freezing, the sample was etched by sublimation by warming it up to -100°C and holding it at that temperature for 5 minutes under vacuum. The sample was then sputter coated with Pt in an argon atmosphere and then imaged at an accelerating voltage of 2 kV.

6.3 RESULTS AND DISCUSSION

6.3.1 High mAb concentration formulations containing 60-80 nm species

Figs. 6.1a-c show the images obtained by cryo-SEM for samples containing 250 mg/ml mAb1 along with 100 mg/ml pro and 50 mg/ml His.HCl as co-solutes. The presence of these co-solutes may give rise to depletion attraction between mAbs leading to the assembly of the nanostructures seen in the figures.^{23,24} The proportion of the visible area of the sample covered by the nanostructures is also very high indicating that a high fraction of the protein may be present in the nanostructures. Although, the technique does not show the presence of much monomeric protein between the nanostructures it does not rule out the possibility that a substantial fraction of the protein may be monomer. The

current technique used for cryo-SEM imaging does not have sufficient resolution to easily resolve monomeric protein. Also the thickness of the layer of Pt coating on ghte sample may be enough to obscure any monomers that could be present. The species seen in the images were sized by ImageJ yielding the histogram of the size distribution shown in Fig. 6.1d (the actual sizing data and sizing for the individual images is shown in Fig. E1). The average size of the nanostructures contained in the sample is ~ 50 nm which is much larger than the expected size for the monomeric protein. Monomeric protein would be expected to have dimensions of 20 nm x 12 nm x 6 nm being Y-shaped from images obtained by negative staining transmission electron microscopy (TEM) imaging and by molecular simulations of mAbs based on the amino acid sequence.³⁸⁻⁴⁰ The holes seen in the sample in the images are the result of beam damage from the impacting electrons heating up the sample from loss of momentum causing sublimation of the ice which disrupts the Pt sputter coating on the sample in the absence of which the sample will appear dark. In order to have a supplemental size measurement by a different technique, the diffusion coefficient of the entities in the same formulation was measured by DLS. The values for the D/D_0 and the effective hydrodynamic diameter assuming that the Stokes-Einstein theory holds true with the Beenakker-Mazur correction are shown in Table 6.1.²⁴ The size measured by DLS for the sample in Fig. 1 is 40 nm with a solvent viscosity of 1.25 cP which is slightly smaller than the size measured from the cryo-SEM imaging. The difference may be explained partly by the Pt coating on the sample which causes an increase in the particle size as explained in scheme 1 with the thickness of the coating layer being around ~ 5 -10 nm. Also the assumptions involved in the DLS lend a degree to the size measured by DLS. Therefore, the measured size by both techniques is in excellent agreement for the two techniques when accounting for the uncertainties.

Images for another mAb1 formulation at 250 mg/ml, but with a different co-solute composition (40 mg/ml trehalose, 50 mg/ml histidine and 17 mg/ml citric acid) are shown in Figs. 6.2a-c. The appearance of the particles is different in the different images since they are from different sections of the sample. However, all the images seem to show similar 60 nm structures present in them which are much larger than the expected size for the protein monomer. To determine the reproducibility of the technique, a different sample with the same composition was imaged as shown in Figs. 6.2d-f. These images are obviously not focused as well as the images in Fig. 6.2a-c. The ability to focus the image seemed to depend on the amount of time for which the sample could survive beam damage without undergoing any change.^{30,41} It was observed that different samples had different thicknesses of protective platinum sputter coating on them and so they would disintegrate at different rates. The strategy used to focus the beam on these samples to obtain an image was to focus on one small part of the sample irrespective of the beam damage it underwent. Once the image was completely focused, the beam was moved to an adjacent undamaged pristine area of the sample and an image was immediately captured without changing the settings. Even with this method the ability to focus was limited because the sample changed during the focusing process due to ongoing beam damage. Also the optimal focus conditions at two different locations on a sample may be different due to different sample depths and from factors involved in movement of the stage and focusing mechanism. However, despite the limitations in the ability to focus the image, the measured sizes for the two sets of images, shown in Figs. 6.2g and 6.2h (the actual sizing data and sizing for the individual images is shown in Figs. E2 and E3) displayed excellent agreement with each other showing excellent reproducibility between samples. The measured size in this case is also much larger than the size from the DLS

data which is given in Table 6.1. The difference between the sizes measured by the two techniques could be partially due to the coating and partially due to assumptions involved in measuring the size by DLS. DLS assumes that the clusters are diffusing independently of each other according to the Stokes-Einstein model which at high concentration may not be accurate.

6.3.2 Dilution of mAb retains nanostructures

The sample at 250 mg/ml was diluted to 125 mg/ml in the same buffer in which mAb1 was originally dispersed in order to observe the effect of high co-solute concentration at lower protein concentrations. The images for the diluted sample are shown in Figs. 6.3a-c. 50-60 nm structures are also seen in the images similar to the ones observed at higher concentrations. These images were obtained with the Zeiss Supra SEM unlike the other ones which were obtained with the Quanta SEM. The image on the right was seen to have some ice deposited on the sample which can be seen as the white material in stark contrast to the rest of the sample. The cracks developed on the sample are the result of the sample heating up as discussed earlier. The particles in the sample are seen as the lighter patches against the dark background, but unlike the ice mentioned above, these particles are embedded in the bulk matrix of the sample. The same images are displayed in the supplemental section showing the sizing method for this sample and all the previously mentioned samples also. All the images in the current study were sized manually since automatic sizing had trouble distinguishing between two particles that were close to each other and tended to obfuscate them into one for the purpose of sizing them. There was some disagreement between the size measured by DLS and that measured by SEM for this particular sample also as can be seen in Table 6.1 and Fig.

6.3d respectively (the actual sizing data and sizing for the individual images is shown in Fig. E4). The diluted sample was imaged in order to have a better comparison to the control low excipient samples.

6.3.3 Imaging of control samples: Low co-solutes and buffer without protein

In order to eliminate the possibility that the particles seen were formed due to the freezing process or some other factor involved in the cryo-SEM imaging process, a control low excipient sample at 100 mg/ml mAb1 in DI water was also imaged as shown in Figs. 6.4 a-d. The images show no clear features or particles in the sample. The size from DLS shown in Table 6.1 is in agreement with that of the monomer which may not be easily visible at the resolution available for the microscope.^{23,24,42} A low excipient sample at a higher mAb concentration of 250 mg/ml comparable to the samples from Figs. 6.1 and 6.2 could not be run on the cryo-SEM because the samples tended to be very highly viscous > 200 cP and also formed a gel upon overnight storage. All of these factors made it very difficult to prepare a sample for imaging by cryo-SEM. These samples upon sizing by DLS yielded sizes similar to those obtained for the more dilute samples and so we may speculate that the sample does not contain significantly larger entities. An additional control that was run was the buffer in which the mAbs were dispersed without any protein in it as a blank shown in Fig. 6.5. The buffer sample did not show any features confirming that the structures seen in the high crowder protein samples were not the result of formation of species from the buffer and were formed from the proteins present in the formulations.

6.3.4 Limitations and factors affecting size measurement by cryo-SEM

The resolution of the images obtained for cryo-EM could be improved in the future by using cryo-TEM instead of cryo-SEM which has been used to elucidate the structure of viruses or other protein based particles in the dilute state.^{34,35,37,43-45} However, it is not possible to use cryo-TEM in the case of these samples since the viscosity of these samples is too high > 5 cP.^{30,31} Dilution of the samples to a low enough is not a viable approach for imaging since it causes the larger species dissociating into monomer based on DLS.^{23,24} Also overlap between the species at a high concentration may cause cryo-TEM to be unviable due to close proximity in the highly concentrated sample.³⁶ Another factor which may cause the difference in observed size between the cryo-SEM and DLS measurement which has not been mentioned yet is the location of the fracture surface. Since the sample was fractured before imaging by knocking off the top rivet/planchette, the location of the fracture is not specifically controlled, the sample would tend to fracture along the most energetically favorable or structurally weakest part of the sample.⁴⁶ Since there is phase discontinuity between the protein particles and the ice phase, the fracture would tend to propagate across the sample while selectively passing through the larger particles as less ice surface has to be created and a lower cross section and therefore lower strength part of the sample needs to yield. Therefore, the fracture surface may possibly expose the larger particles over the smaller particles which may be responsible to some extent for the observed trend of the size measured by cryo-SEM being larger than that by DLS. Also, the samples were not etched or sublimed in the current study as is common for SEM sample preparation in order to avoid artifacts.^{30,35,41,47,48} At the very high protein concentration that these samples were prepared at, the protein particles would tend to be very abundant and if not held in place

by the surrounding ice matrix, they could possibly aggregate together and form some sort of superstructure which would otherwise not be actually present in the formulation. Future studies could be conducted to observe the effect of sublimation on the observed morphology. To prove the consistency of the sample preparation and sizing, data for additional samples is shown in Table. E1 with similar sizes obtained for replicates of the same sample. Additional samples with different compositions that were attempted are also listed in Table E2.

High co-solute concentration can give rise to depletion attraction between proteins causing them to assemble together with the assembly limited by the longer-ranged electrostatic repulsion whose magnitude increases as more proteins are assembled together into nanoclusters as discussed in more detail in Chapters 3 and 4.^{23,24} The formation of nanoclusters may explain the presence of particles in the SEM images with sizes larger than that of the monomer samples. Larger species of ~50 nm in agreement with the size from cryo-SEM were detected for protein formulations with the same composition by SAXS through a peak in the low q region which was not seen for the low excipient samples as described in Chapter 5. Therefore particles of a size larger than the monomer were detected by three different techniques therefore validating that there are species of larger size in the high excipient samples.

6.4 CONCLUSIONS

Nanostructures of a size larger than monomeric protein were observed by cryo-SEM in multiple mAb1 formulations with different compositions and a high concentration of co-solutes with the size estimated to range from ~50-80 nm. The measured sizes from cryo-SEM are in some agreement with the measured D/D_0 for these

samples as measured by DLS. As a control, samples with low co-solute concentration showed no evidence of these larger species in the cryo-SEM micrographs in contrast to the high excipient samples. A high co-solute buffer was also imaged with no features seen in the micrographs proving that the larger species seen in the high co-solute samples were not artifacts of sample preparation. An additional effect was the lowered viscosity for the high co-solute formulations compared to the low co-solute formulations which could be the result of the formation of larger structures in the high excipient samples which modify the interactions present between mAbs in the system.

Fig. No.	mAb conc (mg/ml)	Exc 1	Exc 1 conc (mg/ml)	Exc 2	Exc 2 conc (mg/ml)	Exc 3	Exc 3 conc (mg/ml)	pH	D/D_0 (Diameter in nm)	SEM Diameter (nm)	SEM Diameter st dev (nm)	Viscosity (cP)
1	249	pro	100	His. HCl	50			5	0.35 (31)	46	4.7	83
2	242	tre	40	his	50	cit	17	6	0.35 (31)	60	12.3	52
3	125	tre	40	his	50	cit	17	6	0.42 (26)	54	13.3	3
4	120	-						6	0.96 (11)	-	-	11
5	0	tre	40	his	50	cit	17	6	-	-	-	1.25

Table 6.1: Summary of the samples contained in the current study (cit stands for citric acid).

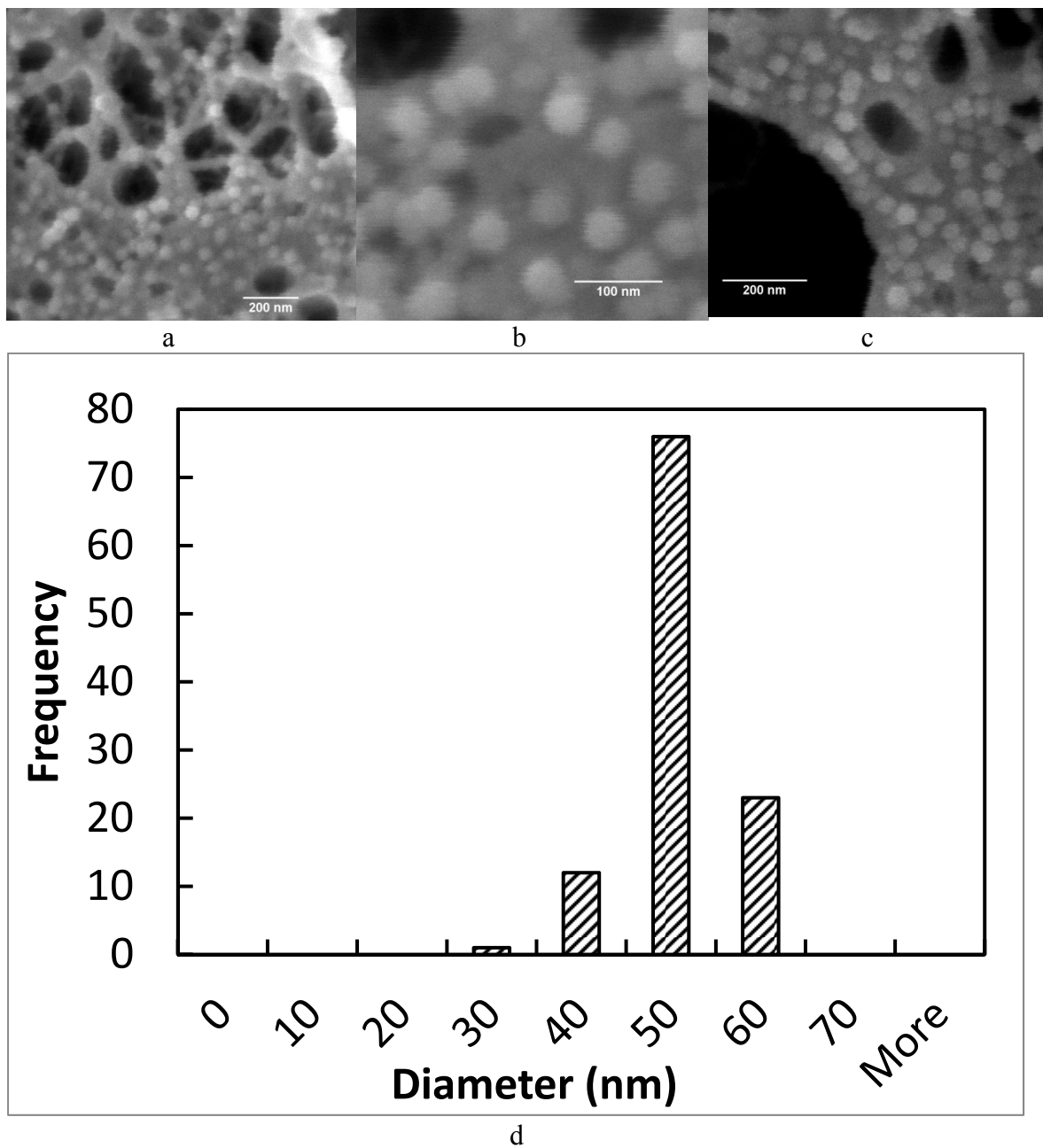
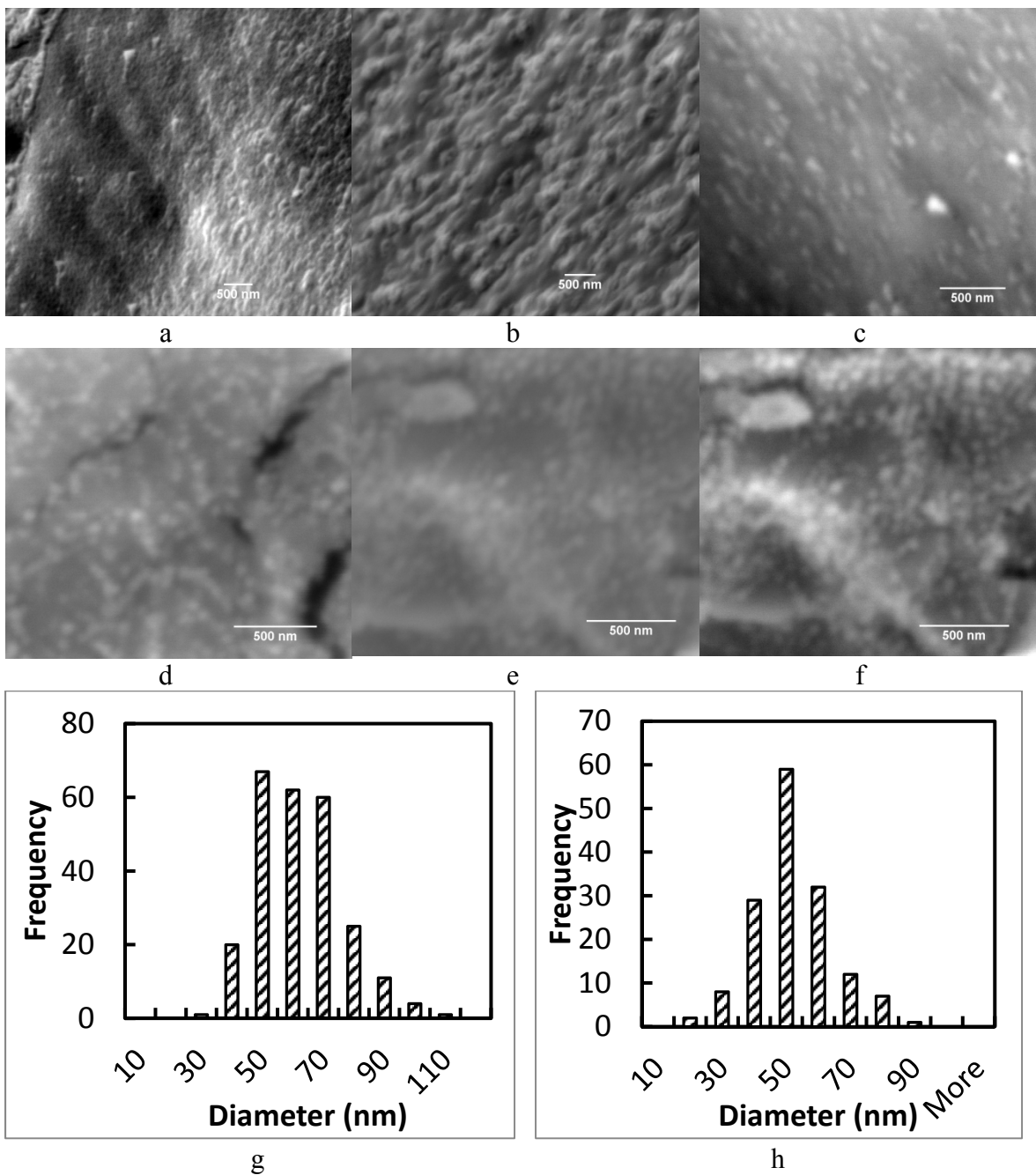


Figure 6.1: a, b and c. Cryo-SEM micrographs of protein clusters with 250 mg/ml mAb1, 100 mg/ml proline and 50 mg/ml his.HCl. d. Histogram of particle sizes as measured by SEM.



(Fig. 6.2 continued on the next page)

Figure 6.2: a, b, and c. Cryo-SEM micrographs of protein clusters with 250 mg/ml mAb1, 40 mg/ml trehalose and 50 mg/ml his and 17 mg/ml citric acid. d, e and f. Cryo-SEM micrographs of a replicate of the same cluster sample. g. Histogram of particle sizes as measured by SEM for images from a, b and c. h. Histogram of particle sizes as measured by SEM for images from d, e and f.

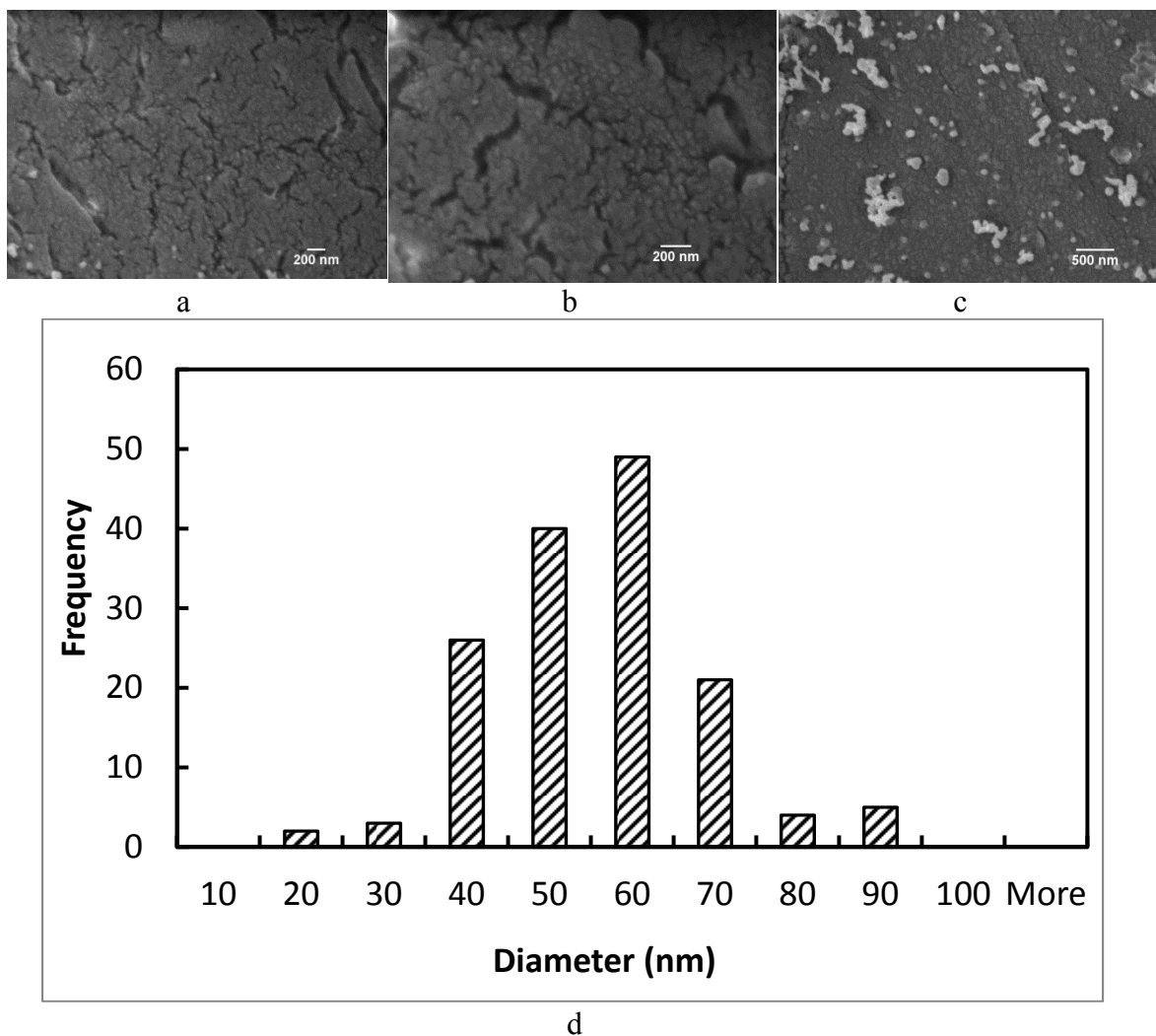


Figure 6.3: a, b, and c. Cryo-SEM micrographs of protein clusters with 125 mg/ml mAb1, 40 mg/ml trehalose and 50 mg/ml his and 17 mg/ml citric acid. d. Histogram of particle sizes as measured by SEM.

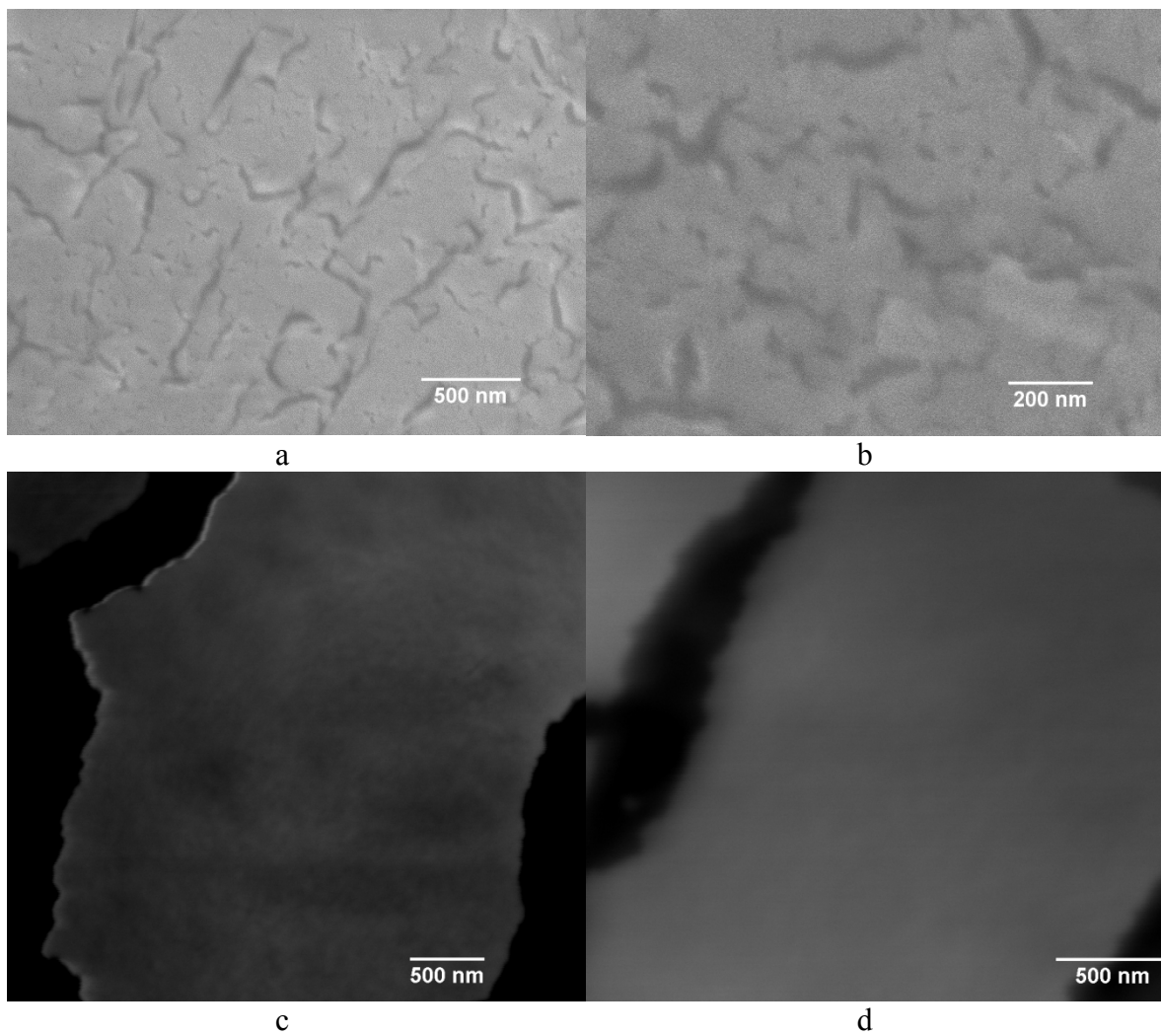


Figure 6.4: a, b, c and d. Cryo-SEM micrographs of protein monomer at 120 mg/ml in DI water.

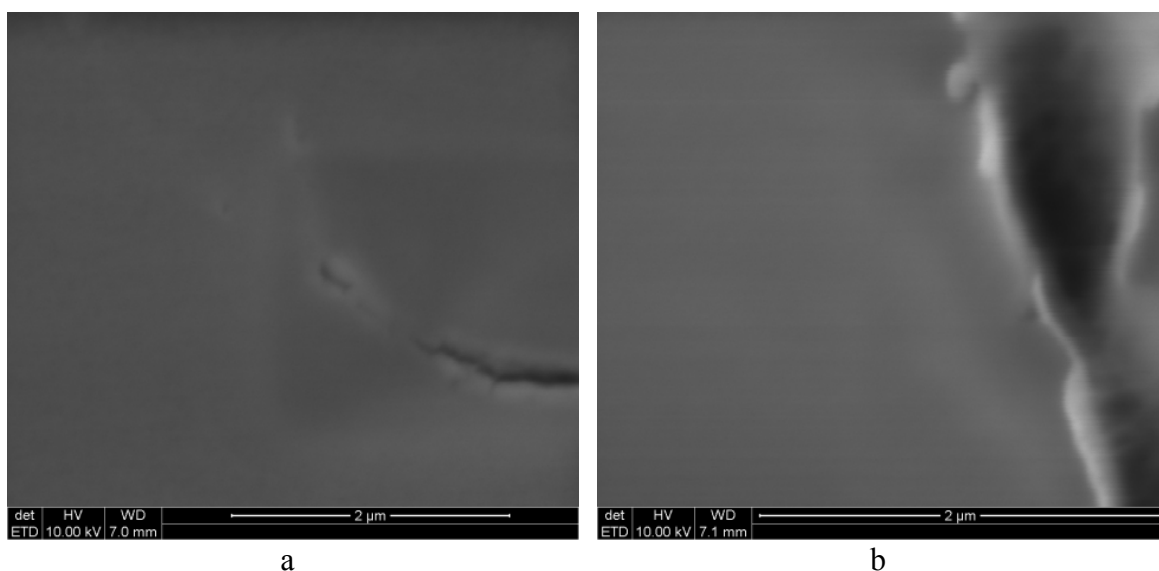


Figure 6.5: a and b. Cryo-SEM micrographs of buffer solution with 40 mg/ml tre, 50 mg/ml his and 17 mg/ml cit at pH 6

6.5 REFERENCES

- (1) Shire, S. J.; Shahrokh, Z.; Liu, J. J. *Pharm. Sci.* 2004, 93, 1390.
- (2) Saluja, A.; Kalonia, D. S. *International Journal of Pharmaceutics* 2008, 358, 1.
- (3) Baglioni, P.; Fratini, E.; Lonetti, B.; Chen, S. H. *Journal of Physics: Condensed Matter* 2004, 16, S5003.
- (4) Burckbuchler, V.; Mekhloufi, G.; Giteau, A. P.; Grossiord, J. L.; Huille, S.; Agnely, F. *Eur J Pharm Biopharm* 2010, 76, 351.
- (5) Castellanos, M. M.; Pathak, J. A.; Colby, R. H. *Soft Matter* 2014, 10, 122.
- (6) Castellanos, M. M.; Pathak, J. A.; Leach, W.; Bishop, S. M.; Colby, R. H. *Biophys J* 2014, 107, 469.
- (7) Fields, G. B.; Alonso, D. O. V.; Stigter, D.; Dill, K. A. *Journal of Physical Chemistry* 1992, 96, 3974.
- (8) Rosenbaum, D. F.; Zamora, P. C.; Zukoski, C. F. *Phys Rev Let* 1996, 76, 150.

- (9) ten Wolde, P. R.; Frenkel, D. *Science* 1997, 277, 1975.
- (10) Young, T. M.; Roberts, C. J. *J Chem Phys* 2009, 131, 125104.
- (11) Zaccarelli, E. *J Phys: Condens. Matter* 2007, 19, 323101.
- (12) Zhou, H.-X.; Rivas, G.; Minton, A. P. *Annual Review of Biophysics* 2008, 37, 375.
- (13) Lilyestrom, W. G.; Yadav, S.; Shire, S. J.; Scherer, T. M. *J Phys Chem B* 2013, 117, 6373.
- (14) Yearley, E. J.; Godfrin, P. D.; Perevozchikova, T.; Zhang, H.; Falus, P.; Porcar, L.; Nagao, M.; Curtis, J. E.; Gawande, P.; Taing, R.; Zarraga, I. E.; Wagner, N. J.; Liu, Y. *Biophys J* 2014, 106, 1763.
- (15) Zarraga, I. E.; Taing, R.; Zarzar, J.; Luoma, J.; Hsiung, J.; Patel, A.; Lim, F. J. *J Pharm Sci* 2013, 102, 2538.
- (16) Yadav, S.; Liu, J.; Shire, S. J.; Kalonia, D. S. *J Pharm Sci* 2010, 99, 1152.
- (17) Yadav, S.; Shire, S. J.; Kalonia, D. S. *J Pharm Sci* 2012, 101, 998.
- (18) Stradner, A.; Sedgwick, H.; Cardinaux, F.; Poon, W. C. K.; Egelhaaf, S. U.; Schurtenberger, P. *Nature* 2004, 432, 492.
- (19) Shukla, A.; Mylonas, E.; Di Cola, E.; Finet, S.; Timmins, P.; Narayanan, T.; Svergun, D. I. *Proc Natl Acad Sci U S A* 2008, 105, 5075.
- (20) Pan, W. C.; Vekilov, P. G.; Lubchenko, V. J. *Phys. Chem. B* 2010, 114, 7620.
- (21) Liu, Y.; Porcar, L.; Chen, J.; Chen, W. R.; Falus, P.; Faraone, A.; Fratini, E.; Hong, K.; Baglioni, P. *J Phys Chem B* 2011, 115, 7238.
- (22) Cardinaux, F.; Zaccarelli, E.; Stradner, A.; Bucciarelli, S.; Farago, B.; Egelhaaf, S. U.; Sciortino, F.; Schurtenberger, P. *J Phys Chem B* 2011, 115, 7227.
- (23) Johnston, K. P.; Maynard, J. A.; Truskett, T. M.; Borwankar, A.; Miller, M. A.; Wilson, B.; Dinin, A. K.; Khan, T. A.; Kaczorowski, K. J. *ACS Nano* 2012.
- (24) Borwankar, A. U.; Dinin, A. K.; Laber, J. R.; Twu, A.; Wilson, B. K.; Maynard, J. A.; Truskett, T. M.; Johnston, K. P. *Soft Matter* 2013, 9, 1766.
- (25) Lekkerkerker, H. N. W.; Tuinier, R. *Colloids and the Depletion Interaction*; Springer: New York, 2011; Vol. 833.
- (26) Vrij, A. *Pure and Applied Chemistry* 1976, 48, 471.
- (27) Davis-Searles, P. R.; Saunders, A. J.; Erie, D. A.; Winzor, D. J.; Pielak, G. J. *Annu Rev Biophys Biomol Struct* 2001, 30, 271.

- (28) Bellare, J. R.; Davis, H. T.; Scriven, L. E.; Talmon, Y. *J Electron Microsc Tech* 1988, 10, 87.
- (29) Glaeser, R. M. *Rev Sci Instrum* 2013, 84, 111101.
- (30) Issman, L.; Talmon, Y. *J Microsc* 2012, 246, 60.
- (31) Koifman, N.; Schnabel-Lubovsky, M.; Talmon, Y. *J Phys Chem B* 2013, 117, 9558.
- (32) Desbois, G.; Urai, J. L.; Burkhardt, C.; Drury, M. R.; Hayles, M.; Humbel, B. *Geofluids* 2008, 8, 60.
- (33) Nijse, J.; Walther, P.; Hoekstra, F. A. *Seed Science Research* 2004, 14, 117.
- (34) Bachar, M.; Mandelbaum, A.; Portnaya, I.; Perlstein, H.; Even-Chen, S.; Barenholz, Y.; Danino, D. *J Control Release* 2012, 160, 164.
- (35) Boerakker, M. J.; Botterhuis, N. E.; Bomans, P. H.; Frederik, P. M.; Meijer, E. M.; Nolte, R. J.; Sommerdijk, N. A. *Chemistry* 2006, 12, 6071.
- (36) Moren, A. K.; Regev, O.; Khan, A. *J Colloid Interface Sci* 2000, 222, 170.
- (37) González-Pérez, A.; Olsson, U. *Soft Matter* 2008, 4, 1625.
- (38) Tong, H.; Zhang, L.; Kaspar, A.; Rames, M. J.; Huang, L.; Woodnutt, G.; Ren, G. *Sci Rep* 2013, 3, 1089.
- (39) Zhang, L.; Ren, G. *Journal of Physical Chemistry & Biophysics* 2012, 02.
- (40) Zhang, L.; Tong, H.; Garewal, M.; Ren, G. *Biochim Biophys Acta* 2013, 1830, 2150.
- (41) Walther, P.; Muller, M. *J Microsc* 1999, 196, 279.
- (42) Ahrer, K.; Buchacher, A.; Iberer, G.; Josic, D.; Jungbauer, A. *Journal of Chromatography A* 2003, 1009, 89.
- (43) Baker, M. L.; Hryc, C. F.; Zhang, Q.; Wu, W.; Jakana, J.; Haase-Pettingell, C.; Afonine, P. V.; Adams, P. D.; King, J. A.; Jiang, W.; Chiu, W. *Proc Natl Acad Sci U S A* 2013, 110, 12301.
- (44) Dai, W.; Fu, C.; Raytcheva, D.; Flanagan, J.; Khant, H. A.; Liu, X.; Rochat, R. H.; Haase-Pettingell, C.; Piret, J.; Ludtke, S. J.; Nagayama, K.; Schmid, M. F.; King, J. A.; Chiu, W. *Nature* 2013, 502, 707.
- (45) de Kruif, C. G.; Huppertz, T.; Urban, V. S.; Petukhov, A. V. *Adv Colloid Interface Sci* 2012, 171-172, 36.
- (46) Ge, H.; Zhao, C.-L.; Porzio, S.; Zhuo, L.; Davis, H. T.; Scriven, L. E. *Macromolecules* 2006, 39, 5531.

- (47) Win, K. Y.; Feng, S. S. *Biomaterials* 2005, 26, 2713.
- (48) Adams, D. J.; Butler, M. F.; Frith, W. J.; Kirkland, M.; Mullen, L.; Sanderson, P. *Soft Matter* 2009, 5, 1856.

Chapter 7: Reduction of mAb viscosity at 250 mg/ml by addition of high arg concentrations to modify protein-protein interactions

Monoclonal antibodies (mAbs) are of great interest in the pharmaceutical field as therapeutics for the treatment of a variety of disorders and diseases. To enable subcutaneous self-injection of mAbs, it is necessary to develop low viscosity dispersions of mAbs at high concentration. The viscosity of mAb1 dispersions at 250 mg/ml was reduced by about 6 times compared to low co-solute protein dispersions in buffer by the addition of high concentrations of co-solutes, namely, arg with either glu or HCl. Arg binds to proteins and reduces both the hydrophobic and localized electrostatic attraction between proteins. Lowered interactions between entities in the dispersion can have the effect of lowering the viscosity. The viscosity was observed to decrease as the total concentration of arg and glu was increased at a fixed pH and fixed ratio of arg to glu as evidenced by the inherent viscosity. The ratio of arg to glu or HCl was also varied to affect the dispersion pH with the viscosity observed to reach a maximum around pH 9 which is the isoelectric point of mAb1. The importance of the binding and interactions of co-solutes with proteins was examined by comparing the protein dispersions with arg to those containing a non-interacting co-solute, namely trehalose which had no impact on the dispersion viscosity. The absence of protein specificity of the effect of co-solutes on the dispersion properties was demonstrated through a viscosity of 17 cP at 258 mg/ml for a polyclonal sheep IgG mixture. For all high co-solute dispersions, the diffusion coefficient as measured by DLS decreased while that for the low co-solute monomer samples remained comparable to that of the monomer in dilute conditions even at high concentrations of protein. The lowered diffusion coefficient was in contrast to the

lowering of dispersion viscosity. Upon dilution, the high co-solute dispersions were determined to yield monomeric protein by both DLS and SEC.

7.1 INTRODUCTION

Monoclonal antibodies (mAbs) are of great interest for the treatment of many diseases and disorders including various types of cancer, rheumatoid arthritis, Alzheimer's disease, asthma, and Crohn's disease. There are currently more than 40 mAbs that are either currently under review or have already been approved by the drug administrations in either the United States or the European Union.¹ The most common method of administration through an intravenous drip (IV) of a dilute solution is time consuming and requires medical supervision, in contrast with subcutaneous (subQ) self-injection.^{2, 3} Due to the limited volume of ~1-2 ml for subQ administration, the recommended dosage may require use of concentrations greater than 150 mg/ml mAb where viscosities can exceed the desired level of 20-50 cP.^{2, 4} The elevated viscosities often arise as a result of protein-protein interactions between the Fab (antibody binding fragment) regions of mAbs, specifically between CDRs (complementarity determining regions).⁴⁻⁶ The viscosity at high concentration has been shown to increase markedly for a series of mAbs as the interactions (measured at low concentration by dynamic or static light scattering) change from repulsive to attractive, for a given buffer/co-solute system.^{5,}

7-10

Often mAbs with isoelectric points between pH 7 and 9 are formulated in a buffer solution at pH 5-6, for example, 20-30 mM his/his.HCl and in relatively few cases with a saccharide.^{2, 5-9, 11, 12} The pH is chosen to be a few units away from the isoelectric point

such that the net charge provides electrostatic repulsion to favor stability against aggregation. The distribution of charged and hydrophobic patches on proteins in concentrated (150 to 300 mg/ml) dispersions in these buffers may produce highly complex anisotropic interactions, given a small average surface-to-surface separation of ~1-5 nm. Here, the hydrophobic, electrostatic (between oppositely charged patches) and charge-dipole interactions may produce aggregation, which is of concern with regard to immunogenicity in addition to protein unfolding and gelation.¹³⁻¹⁶ These interactions can cause formation of protein oligomers, where dimers have been found in some case to be the most common species.^{12, 17} These oligomeric structures may produce a large increase in the viscosity given that they occupy a greater volume than monomeric protein as a function of the fractal dimension.^{12, 17} Here, the viscosity may be elevated at low shear rates and then undergo shear thinning up to shear rates of $\sim 1000 \text{ s}^{-1}$ encountered in subQ injection, as the network structure of reversible aggregates is disrupted due to the higher shear energy from flow.^{6, 18} Even irreversible aggregates composed of a few proteins may cause shear thinning behavior as seen for bovine serum albumin (BSA) and for low concentration mAbs.^{15, 16, 19}

A common approach for reducing the viscosity of mAb formulations is to engineer the amino acid sequence to weaken the aforementioned attractive interactions.^{7, 18} However, this approach is time consuming, highly specific to the particular mAb under consideration and may even influence the mAb therapeutic efficacy.^{7, 18} Salts may be used to reduce the Debye length and screen electrostatic interactions including charge dipole interactions.^{5, 12, 20-22} In some cases, strongly chaotropic salts disrupt the water structure at the protein surface and suppress mAb attractive interactions, therefore reducing the viscosity to a much greater degree compared to kosmotropic salts.^{6, 20} Also,

salts containing large hydrophobic ions at concentrations of 0.5 M were shown to lower the viscosity up to 3-fold for BSA and bovine γ - globulin, likely by weakening the hydrophobic interactions, even in cases where hydrophilic salts had little effect.²⁰ Finally, low viscosities have been observed for micron-sized particulates of mAbs dispersed in organic solvents^{3, 23} or aqueous buffers containing a high organic solvent fraction²⁴ which lowers protein solubility so that the suspended particles do not dissolve.

Recently, there has been significant interest in utilizing organic co-solutes to modify protein-protein interactions to attempt to lower the viscosity.²⁵⁻²⁸ High concentrations of a neutral co-solute, trehalose, were used to tune the depletion attraction between proteins resulting in a lowered diffusion coefficient as indicated by dynamic light scattering (DLS).^{25, 26, 29} On the basis of a free energy model, it was proposed that self-limited protein nanoclusters may be formed near the isoelectric point for slightly charged proteins, as the short ranged depletion attraction between proteins was balanced by the long ranged repulsion between proteins.^{25, 26, 30, 31} Similarly, protein clusters were formed for highly concentrated lysozyme and BSA by light scattering with the measured fraction of clusters ranging from 10^{-5} to 0.8.³²⁻³⁵ Even at low concentrations trehalose is known to be preferentially excluded from the protein surface favoring a compact folded state of the protein sometimes termed as osmotic compression.^{36, 37} Together, the depletion attraction from the concentrated co-solutes and the high concentration of proteins may be expected to favor folding and thus enhance protein stability.^{38, 39} After diluting the protein dispersions, aggregates were not observed by SEC and the protein was active *in vitro* and *in vivo* upon dilution into buffer.^{25, 29}

Unlike trehalose, the effect of co-solutes that interact strongly with proteins on protein stability and the viscosity of protein dispersions has received little attention. The

addition of arg.HCl at 600 mM to mAb dispersions was hypothesized to reduce hydrophobic interactions in addition to mediating electrostatic interactions via charge screening.²⁷ The reduction of attractive hydrophobic interactions between mAbs occurs through the binding of arg to hydrophobic patches effectively making them more hydrophilic.^{21, 22, 27, 28, 40-45} Similarly, the positively charged arg also binds to charged patches on mAbs through hydrogen bonding which changes the charge distribution on mAbs causing reduced attractive interactions between oppositely charged patches.^{8, 20-28} Arg.HCl at an even higher concentration of 1 M was seen to lower the viscosity of polyclonal antibody mixtures slightly from 60 cP to ~45-50 cP through the mediation of attractive interactions in this manner.²⁸ Alternatively, arg.HCl at 200 mM has been used in mAb formulations to lower interactions and viscosity to some extent at mAb concentrations of 175 mg/ml.⁷ It remains to be determined if strongly interacting co-solutes may produce large decreases in viscosity at moderate concentrations.

Herein, we examine how high concentrations of arg and glu or HCl influence the viscosity of protein dispersions from pH 5 to 11 by modifying protein-protein interactions. Specifically, the viscosity of a dispersion of mAb1 is reduced from ~160 cP at 230 mg/ml in histidine buffer to as low as ~30 cP at 250 mg/ml in the presence of arg and glu as co-solutes at total concentrations ranging from 75 to 150 mg/ml. The binding and interactions of these co-solutes with proteins may reduce both localized anisotropic electrostatic or hydrophobic protein-protein interactions that otherwise often produce high viscosities.^{7, 10, 21, 22, 27, 40, 45, 46} The pH was varied to affect the interactions of the co-solutes with mAbs in order to modify charge distributions of the mAbs. Co-solute concentrations were also varied to modify protein-protein interactions and to add depletion attraction. Trehalose, which does not interact specifically with proteins, was

chosen as a control to isolate the effect of depletion attraction alone on viscosity.^{25, 26} For arg and glu at the high concentrations in this study, depletion attraction may be expected to modify the various protein interactions. The diffusion coefficient was measured by DLS and compared with the calculated value for mAbs in a monomeric state with an effective spherical diameter of 11 nm diffusing through the solvent. The osmotic compression effect arising from co-solutes may also favor folding of proteins to reduce the molecular volume as has been demonstrated before^{25, 36} which may help reduce aggregation. Finally, we show test the stability of mAb dispersions upon dilution using size exclusion chromatography (SEC) after storage for up to 8 weeks.

7.2 MATERIALS AND METHODS

7.2.1 Materials

The monoclonal antibody used in this study (mAb1) was obtained from Abbvie at ~120 mg/ml in a proprietary buffer composition. Arginine, glutamic acid, lysine, acetic acid, sodium glutamate, arginine hydrochloride, proline, glycine, histidine, sodium monophosphate, sodium biphosphate, sodium bicarbonate and HCl were purchased from Fisher Scientific, Fairlawn, NJ. Trehalose was purchased from Ferro Pfanstiehl Laboratories Inc., Waukegan, IL. Amicon Ultra-15 Ultracel – 30K and Amicon Ultra 0.5 Ultracel – 50K centrifugal filters were purchased from Merck Millipore Ltd. Ireland.

7.2.2 Buffer exchange

0.4 ml of the 120 mg/ml mAb1 solution was initially diluted to 4 mg/ml in a buffer containing desired concentrations of co-solutes (12 ml total, initial buffer

volumetric fraction is 3.33% (0.4 ml out of 12)). The resulting solution was then filtered using a Millipore Centricon centrifugal concentrator tube with a molecular weight cutoff of 30 kDa and a capacity of 12 ml at a spin speed of 4500 rcf for 12 minutes. The protein solution was concentrated till the solution volume dropped to about 5 ml and a protein concentration of ~ 10 mg/ml. Then the retained protein solution was again diluted using the desired dispersion buffer to make up the volume to 12 ml (initial buffer volume fraction reduced to 1.4% (3.33% out of 5 ml in 12 ml)) and then centrifuged again. This process was repeated 4 or more times until the volume of flow through was about 40 ml and the volumetric fraction of initial buffer was less than 1% assuming ideal mixing. After this the solution was further concentrated by continuing the centrifugation so that the final volume was about 0.5 ml at about 80 mg/ml. Alternatively, in Tables 7.1 and 7.2, buffer exchange was carried out by Tangential Flow Filtration using a Microkros hollow fiber module manufactured by Spectrum Labs (part no. C02-E050-05-N) with polyethersulfone as the filter material, 50 kD pores and a membrane area of 20 cm². The module was connected to a micokros pump (KrosFlo® Research Iii Tangential Flow Filtration System) using silicone tubing (Masterflex, HV-96410-14) with an ID of 1.6 mm. The buffer exchange was carried out in a continuous manner with continuous addition of DI water until 6 diavolumes of buffer had been permeated through.

7.2.3 Centrifugal concentration to >200 mg/ml

Tare weights were taken of the individual components (filter, permeate tube and retentate tube) of the centrifugal filter assembly (Millipore Microcon, Ultracel YM-50 membrane, 50 kD nominal molecular weight limit, 0.5 ml capacity). The desired volume of protein solution in the dispersion buffer post buffer exchange and concentration to 80

mg/ml was pipetted into the retentate chamber. The filter assembly was then centrifuged (Eppendorf Centrifuge 5415D) at either 5000 or 10,000 rcf, typically for about 40 minutes in 5-10 minute increments with volume monitoring at every stop until the calculated final volume for the desired final concentration was reached. The volume measurements were done using image analysis to determine the height of the liquid column in the filter which had been calibrated to correspond to the volume of liquid in the filter using ImageJ software⁴⁷ and also by weighing both the retentate and permeate having previously tare weighted filter components.

Once the desired concentration had been reached, the protein dispersion in the retentate was recovered by inverting the filter assembly into a retentate recovery tube, and centrifuging it for 2 minutes at 1,000 rcf. The resulting dispersion was transferred to a 0.1 mL conical vial (V-Vial, Wheaton), and the concentration was verified spectrophotometrically by withdrawing a small sample (2 μ l) of the dispersion (described in more detail below). The dispersion composition would not be expected to change significantly during the course of the run for the high co-solute samples as explained in the supplemental section. Further evidence supporting this is that there was no change observed in the pH of the high co-solute samples during the concentration step (pH was 5.48 at both the start and end for an example run as measured by a pH meter). In contrast, the pH of an example low co-solute sample drifted by \sim 0.2 units from 5.48 at the start to 5.67 at the end of the run.

In cases where a larger sample was needed to examine the effect of sterile filtration on the properties of the dispersions, the entire centrifugal filtration run was conducted in the larger centrifuge tubes. A larger amount of protein (\sim 170 mg) was initially loaded onto the filter at the start of buffer exchange. Instead of transferring the

sample to the smaller 0.5 ml centrifugal filters, it was transferred to another Millipore Centricon centrifugal concentrator tube and then concentrated to the desired final volume. The sample was characterized in the same way as the smaller samples and then sterile filtered using a 1 ml syringe (Becton Dickinson & Co. with Luer-Lok™ tip) and a syringe filter with a 220 nm cutoff. The sample was also weighed before and after filtration to determine the yield for the sterile filtration step. The sample was then characterized after sterile filtration in a similar way to the smaller samples.

7.2.4 Characterization of the protein nanocluster dispersion

7.2.4.1 Viscosity measurement

The viscosities of the nanocluster dispersions were measured in triplicate using a 25 gauge (ID = 0.1 mm) 1.5” long needle (Becton Dickinson & Co. Precision Glide Needle) attached to a 1 ml syringe (Becton Dickinson & Co. 1 mL syringe with Luer-Lok™ tip), on the basis of the Hagen-Poiseuille equation. The flow rate of a dispersion through the needle was determined using the estimated volume which was correlated to the height of the liquid in the conical vial (Fig. F4) and measuring the time taken for the dispersion meniscus height to move between two points. This flow rate was correlated to viscosity from a calibration curve derived from a set of standards of known viscosities as shown in Fig. F5. Cone and plate rheometry experiments were conducted on a standard torsional rheometer (AR2000EX, TA Instruments) with a 40 mm diameter cone with 2° of angle and a truncation gap of 55 µm. The cone-and-plate geometry is selected for the constant shear rate in the tool-plate gap. Sample temperature was controlled by a lower Peltier plate set to 25°C.

7.2.4.2 DLS and diffusion interaction parameter measurements

The effective CONTIN diameters of protein monomers and nanoclusters were measured by dynamic light scattering (DLS) at an angle of 150° with a 632.8 nm laser and an avalanche photodiode at ~23°C using the CONTIN algorithm (Brookhaven BI-9000AT) or at an angle of 90° with a Brookhaven ZetaPlus. The samples were pipetted into a 60 µl sample cell for the samples measured at 150° (Beckman Coulter) or a Uvette® (Eppendorf) for the samples measured at 90° which was then mounted on the instrument to conduct three replicate runs of 2 minutes each. All reported D/D_0 values are the average of three runs. Additionally measurements of the diffusion interaction parameter (k_d) were conducted on dilute protein samples at 5, 10, 15 and 20 mg/ml. The diffusion coefficient in these dilute protein solutions was measured with the Brookhaven ZetaPlus at a scattering angle of 90° and fit with the equation $D = D_0(1 + k_d c)$ where D is the measured diffusion coefficient, D_0 is the diffusion coefficient at infinite dilution and c is the protein concentration.

7.2.4.3 Size Exclusion Chromatography

For analysis of non-covalent aggregates, the sample was diluted in mobile phase (100 mM sodium phosphate, 300 mM sodium chloride, pH 7) to 1 mg/ml. A volume of the diluted sample containing 20 µg of mAb1 was analyzed with a Waters Breeze HPLC, using TOSOH Biosciences TSKgel3000SW_{XL} and TSKgel2000SW columns in series, with eluate monitored by absorbance at 214 nm.

7.2.4.4 Protein Concentration determination in the dispersion

For determining the concentration of the dispersions, 2 μl of dispersion was measured out and diluted into a receiving vessel containing 998 μl of 50 mM pH 6.4 phosphate buffer mixing well with the pipette tip. The diluted samples were prepared in duplicate. The absorbance of the resulting solution was measured using a Cary 3E uv-visible spectrophotometer in a cuvette (Hellma cells) with a path length of 1 cm. Then using Beer's law ($A = \epsilon b c$, where ϵ = extinction coefficient = $1.42 \text{ ml mg}^{-1} \text{ cm}^{-1}$, b = path length = 1 cm), knowing the absorbance, the concentration of protein in the solution was calculated.

7.2.4.5 Sample storage

Samples were stored in the 0.1 ml conical vials sealed with the lid and parafilm. Samples were stored in a -40°C freezer, in a refrigerator at 4°C and on the bench at room temperature. The sample for each time-point was taken from a separate vial which was then discarded.

7.3 RESULTS

7.3.1 Effect of co-solutes on viscosity at $\sim 150 \text{ mg/ml}$ mAb concentration

To provide a basis for understanding the viscosity experiments at $\sim 250 \text{ mg/ml}$ protein we begin with experiments at a lower protein concentration of $\sim 150 \text{ mg/ml}$. Various co-solutes at $\sim 150 \text{ mg/ml}$ were added to a 150 mg/ml solution of mAb1 in DI water which had been previously prepared by the tangential flow filtration (TFF) to attempt to lower the viscosity (η). To partially remove the effects of protein concentration

(c) and solvent viscosity (η_0), the inherent viscosity (η_{inh} , mg/ml) was determined for all dispersions.

$$\eta_{inh} = \frac{\ln(\eta/\eta_0)}{c} \dots (7.1)$$

The inherent viscosities at 130 mg/ml mAb1 are shown in Table 7.1 along with η and D/D_0 from DLS (where D_0 is the calculated diffusion coefficient for protein monomer with an effective spherical diameter of 11 nm in the same solvent). mAb1 upon formulation in DI water in the absence of any co-solutes had a η of 19 cP at ~150 mg/ml and a pH of 5.5 with a D/D_0 of 1.4. The η decreased only a small amount at pH 7 (50 mM phosphate buffer) compared to pH 5.5 where D/D_0 was close to 1. Upon addition of arg titrated with either acetic or hydrochloric acid, the η_{inh} dropped by 30% and 60% respectively, at a concentration of ~130 mg/ml. The η_{inh} was much smaller for arg.HCl than for all of the other systems. In contrast, sodium glutamate did not reduce η_{inh} compared to the controls. However, for a 1:1 mixture of sodium glutamate and arg.HCl, η_{inh} and D/D_0 decreased a similar extent as observed for lysine or proline. For all of the high co-solute systems, the D/D_0 was below unity and as low as 0.53 suggesting slower diffusion for the scattering entities. However, these dispersions were not filtered. Also, it was not possible to resolve from DLS what fraction of protein was in the monomer state at these conditions or to determine the polydispersity given how close D/D_0 was to unity and the complexity of diffusion at high concentrations and viscosities.⁴⁸

Additional experiments are presented for systems containing trehalose (tre) in Table 7.2 for a mAb concentration of ~150 mg/ml. The η and η_{inh} for the two buffer controls with no co-solutes were relatively high. Tre is well-known to favor folding of proteins by minimizing the surface area because it is preferentially excluded from the

protein surface.^{11, 36, 49} However, the addition of tre to the pH 8 solution did not affect η or η_{inh} significantly while at pH 5.5, it decreased the $\eta_{inh} \sim 20\%$. The mAb concentration was maintained at 150 mg/ml by addition of lyophilized mAb1 powder (with 1:1 mAb1 to tre by weight) to compensate for dilution due to co-solute addition. The addition of arg.HCl along with tre decreased η_{inh} by almost 30% with η reduced by almost 2 fold. Unlike the case for arg.HCl, the addition of glycine with tre at pH 5.5 did not reduce η_{inh} significantly more than tre by itself. All the subsequent experiments were conducted with the use of some arg in the dispersion along with an acid such as glutamic acid (glu) or HCl to modulate the sample pH as arg was the most effective co-solute at reducing η .

7.3.2 Effect of co-solutes on viscosity at ~250 mg/ml mAb concentration at pH ~5.5

Experiments were conducted over a wide range of mAb1 concentrations as shown in a semi-log plot in Fig. 7.1a. for a 20 mM low co-solute his/his.HCl buffer control along with a high co-solute system containing 78.6 mg/ml of arg and 71.4 mg/ml of glu, both at pH 5.5. The detailed data with η_{inh} are shown in Table F1 and Table F2. The reproducibility for was within $\sim 10\%$ for the two replicates shown for each sample at higher concentrations. The η s for both the low co-solute buffer and high co-solute samples were well below 10 cp at low mAb concentrations. The η of high co-solute samples was ~ 35 cP at 250 mg/ml and several times lower than 150 cP at ~ 230 mg/ml measured for the buffer samples. Two control samples with low histidine at the same pH of 5.5 were prepared to examine the reproducibility as shown in Table 7.3. These samples exhibited trends observed in Fig. 7.1a with a $\eta > 150$ cP much larger than for the high co-solute dispersions. Upon adding 150 mM NaCl to screen electrostatic interactions, the η_{inh} decreased significantly by about 15%, in contrast with a decrease of about 40% for

the high co-solute dispersions. The D/D_0 decreased significantly upon the addition of salt probably as a result of lowered overall charge repulsion leading to proteins assembling into larger structures, even though an organic depletant was not added at high concentration. The yield for rows 1 and 3 is lower than row 2 possibly due to more loss to the larger filters used for their preparation compared to the smaller filters used for row 2. The most concentrated samples were diluted to explore the reversibility of the η and are shown by the open symbols. The η of the diluted samples although slightly elevated was within experimental error of 20% for η_{inh} . For Fig. 7.1a, curves were fit with the Ross-Minton equation which is a modified version of the Mooney equation.^{5, 6, 50}

$$\eta = \eta_0 \exp\left(\frac{c[\eta]}{1-(k/v)c[\eta]}\right) \dots (7.2)$$

where $[\eta]$ is the intrinsic viscosity in ml/mg, k is the crowding factor and v is the Simha parameter (shape determining factor). The regressed values of the $[\eta]$ and k/v were 0.0053 ml/mg and 0.46 respectively for the high co-solute samples and 0.0054 ml/mg and 0.61 for the low co-solute samples. The 25% decrease in k/v for the high co-solute samples may suggest a significant reduction in the strength of mAb-mAb interactions based on the results from Kanai et al.^{5, 6} The $[\eta]$ is related primarily to the molecular volume and consequently was relatively invariant.^{5, 6}

The low co-solute samples have D/D_0 values nearly independent of protein concentration (Fig. 7.1b). Meanwhile, the D/D_0 for high co-solute samples varied from ~0.5 for the lowest protein concentrations with a gradual decrease to 0.3 as the protein concentration reached 250 mg/ml. It seems counterintuitive that the scattering entities diffused more slowly when the η of the dispersion decreased. It is possible that an unknown fraction of reversible protein aggregates or clusters were present along with

protein monomer since these dispersions were not filtered. Upon dilution of the highest concentration samples with high co-solute concentration from Fig. 7.1 to 0.5 mg/ml, the D/D_0 reverted to ~ 1 as shown in Table 7.4 indicating that any clusters were reversible yielding monomers with additional data shown in Table F3.

The effect of total concentration of arg and glu (75 to 150 mg/ml) on η was also studied by fixing the pH at 5.5 with a fixed ratio of arg to glu as 1.1:1 with a mAb concentration of ~ 250 mg/ml (Table 7.5). The η_{inh} decreased with increasing total co-solute concentration as shown in Fig. 7.2 with replicate data shown in Table F4. Additional data in Fig. 7.2 were taken from Table 7.6. The η was as low as 30 cP at 263 mg/ml for the 150 mg/ml total co-solute. Over this range of co-solute concentration (75 to 150 mg/ml) the overall η decreased by $\sim 45\%$ despite the $\sim 25\%$ increase in η_0 suggesting a weakening of protein-protein interactions. The yield for all the samples was $> 80\%$ which is acceptable considering the potential for protein adsorption to the walls and filter membranes along with the multiple transfer steps that were conducted.

The experiments were scaled up in Table 7.6 to ~ 500 μ l samples by using 15 ml filters to enable sterile filtration of the dispersions. Four pairs of rows are shown where the first is before filtration and the second in bold is after sterile filtration. In each case the protein concentration dropped about 10% due to losses from adsorption to the filter while the sterile filtration yield was $\sim 60\%$ due to losses to filter hold-up. Although this reduction in concentration lowered η , η_{inh} and D/D_0 did not change significantly. Therefore, η data for all other dispersions in this study was obtained by making ~ 120 μ l samples, which were not filtered to conserve protein, as they would be expected to follow this behavior. The D/D_0 was larger for the lower co-solute samples (50 mg/ml arg+glu) than for the higher co-solute samples. Additionally the extinction for the dispersions was

measured and is reported as the turbidity divided by the mAb concentration at 350 nm with the entire spectrum shown in Fig. F1. The turbidities were nearly twice as high for the 50 mg/ml arg+glu samples. It is possible that the higher turbidity was produced by reversible aggregates that also raised the η , but the structures of such aggregates have rarely been measured.^{12, 17, 51}

7.3.3 Effect of pH on co-solutes on viscosity at ~250 mg/ml mAb concentration

The effect of pH was examined for a series of dispersions containing a total concentration of 150 mg/ml arg and glu since arginine properties would be expected to change with pH as its charge varies from +1 from pH 5 to 8, neutral between pH 8-11 and negative above pH 11. The η increases with protein concentration at all pH values as expected (Fig. 7.3). Apart from pH 8.5 where it was the highest, the η was relatively insensitive to pH and ranged from 30-50 cP at 250 mg/ml in agreement with the samples from Fig. 7.1a. Fig. 7.4 shows η and η_{inh} for mAb1 samples containing arg titrated with HCl instead of glu (additional data in Table F5). The η progressively increases from pH 6.4 to 8 and even more at pH 10 where it peaks and then decreases as the pH is raised to 11, as was also observed for the systems with arg and glu. The lowest η was obtained at pH 11 although this pH is too alkaline for subcutaneous delivery. The η_{inh} also went through a maximum at pH 10 and was lowest at pH 11. The η_{inh} for the samples with arg and glu were modestly lower than for those with HCl (highlighted in Table F6). Additionally the samples containing glu have the advantage of a lower tonicity (row 4 in Table 7.5 is 935 mOsm/kg, 283% of isotonic concentration) compared to the samples with HCl (1688 mOsm/kg, 618% of isotonic concentration, for the pH 8 sample with arg.HCl from Fig. 7.4).⁵²

The effect of pH on η was also determined for low co-solute samples as shown in Table 7.7. The η_{inh} decreased to a minimum at pH 6.5 and then increased with pH up to pH 11. At a concentration of 200 mg/ml, η for high co-solute samples was as low as ~ 10 cP (Fig. 7.1a), which is about 6 fold lower than these low co-solute samples. The D/D_0 was close to 1 at pH 5.5, but then decreased to 0.6-0.73 closer to the isoelectric point where reversible aggregates may have formed. These samples permeated through the filter faster than the high co-solute samples in the lower range of mAb concentrations as expected from the lower η_0 . However, the permeation decayed rapidly once the mAb concentration approached 200 mg/ml, down to ~ 0.1 $\mu\text{l}/\text{min}$ from ~ 10 $\mu\text{l}/\text{min}$, as dispersion η increased markedly. As a result, the final concentrations for these samples were only about 200 mg/ml below the intended target concentration of 250 mg/ml.

To quantify the effect of co-solutes on protein-protein interactions, k_d measurements were conducted on dilute protein samples (5-20 mg/ml) in the buffers used in the previous measurements in this study with k_d values shown in Table 7.8 with the detailed data in Fig. F2. Protein-protein interactions for mAb1 in 30 mM histidine buffer, were weakly repulsive with a k_d of ~ 4 ml/mg because proteins would have some net charge being far from its isoelectric point of 9 which would lead to electrostatic repulsion between proteins. The addition of a high concentration of arg and glu decreases k_d making the interactions net attractive with a k_d of ~ -7 ml/mg.

For polyclonal sheep IgG, the viscosities were well below those for mAb1, down to 17 cp at 258 mg/ml (Table 7.9). Increasing the concentration of arg and glu to 200 mg/ml did not seem to further lower η . The centrifugation time for the higher arg concentration sample is higher probably because of the higher η_0 .

In order to further examine the effect of arg and glu on the interactions of mAb1, the shear rate dependence of η was measured with a cone and plate rheometer. The sample was prepared by combining samples from runs in 4 separate 0.5 ml centrifugal filters together. The mAb1 solution in 20 mM histidine with 0.05% Tween 80 was observed to be shear thinning with η decreasing over 2 orders of magnitude from 0.1 to 1000 s⁻¹. mAb dispersions with low co-solute concentrations are routinely observed to shear thin due to the presence of mAb clusters formed due to associative forces or entanglement of molecules.^{6, 8, 9, 18} The Tween-80 was added at a concentration well above its critical micellar concentration (CMC) to saturate the air-water interface and prevent the complication of a viscoelastic protein layer on the interface.⁵³ There is a possibility that some of the shear thinning observed may be the result of protein adsorption at the air/water interface even with the surfactant present. In contrast, the dispersion containing 78.6 mg/ml arg and 71.4 mg/ml glu was nearly Newtonian and underwent very little shear thinning over the same shear rate range, despite the lack of surfactant. This result suggests weaker interactions between proteins consistent with the lower viscosity. The syringe η data and D/D_0 data for the runs are shown in Table F7 and also plotted in Fig. 7.5 with the shear rate calculated using the measured flow rate and known needle diameter in the Hagen-Poiseuille equation. The measured η by the syringe viscometer at the same shear rate appears to be ~20 and 10 % higher for the his-Tween 80 and arg-glu systems, respectively relative to the cone and plate rheometer.

7.3.4 Effect of a preferentially excluded co-solute trehalose on viscosity

To place the results with arg in perspective, tre was chosen as a non-electrolyte co-solute without acidic or basic sites. In Table 7.10, dispersions contained tre as the

only co-solute at pH values ranging from 6.4-8 using a 50 mM phosphate buffer. Tre by itself does not reduce η_{inh} significantly in contrast with the behavior for arg. The D/D_0 values are very low for the samples with very high tre suggesting that depletion attraction may have produced relatively large reversible aggregates. The lack of a viscosity reduction for mAb1 suggests that tre does not modify the attractive specific protein-protein interaction for mAb1 sufficiently. In contrast with these results low viscosities were observed for a mAb 1B7 and sheep IgG in systems with a high concentration of tre co-solute in previous studies for dispersions buffered with histidine and phosphate together.²⁵ In that study, depletion attraction was proposed to assemble proteins into nanoclusters based on a free energy model for hard spheres with a uniform charge. This behavior may be part of the reason for the lowered D/D_0 . However, the model does not predict the fraction of proteins in the monomeric state surrounding the nanoclusters or provide information about the polydispersity of the nanoclusters.^{25, 26, 30, 31}

In order to add charge screening along with depletion attraction, ammonium sulfate was added to mAb1 dispersions containing tre as shown in Table 7.11. The addition of salt did not lower the η or η_{inh} significantly, in contrast with the behavior in Table 7.3 for NaCl with dilute histidine buffer. Thus, in the former case, the depletion attraction somehow negated the potential lowering of viscosity by electrostatic screening. Given tre or tre with NaCl did not lower the viscosity, we now examine how tre influences protein dispersions containing high concentration of arg and glu. Table 7.12 shows the effect of adding tre to a dispersion with a constant ratio of tre to arg and glu with replicates in Table F8. The η decreases by ~45% at ~240 mg/ml mAb1 as the total concentration of co-solutes is increased from 75 mg/ml to 200 mg/ml. The addition of tre increases η slightly compared to the dispersions containing only arg and glu at similar

concentrations, as can be seen by comparing row 2 of Table 7.12 with row 1 of Table 7.5 or row 3 of Table 7.12 with row 2 of Table 7.5. The viscosities for these samples containing tre alone at a given concentration are much higher than those for the samples with arg and glu at similar total co-solute concentrations as can be seen by comparing row 3 in Table 7.12 and rows 2-4 in Table 7.10. However, the increase is mainly due to the higher η_0 as η_{inh} remains essentially constant with added tre. The D/D_0s for the dispersions from Table 7.12 are also much lower than unity. The additional tre affects the osmolality of the sample but to a lesser extent than arg and glu, e.g., for samples with 200 mg/ml co-solute with arg, glu and tre from row 3 in Table 7.12 the osmolality is 1006 mM (311% of isotonic concentration) while that for tre at 200 mg/ml from rows 2-4 in Table 7.10, the osmolality is 529 (119% of isotonic concentration).⁵²

7.3.5 Stability of mAb dispersion upon storage and dilution

The dissociation of any reversible aggregates is evidenced by size exclusion chromatography (SEC) of diluted mAb1 dispersions at 1 mg/ml in Table 7.13. The SEC trace of the original material without any processing except for dilution before running SEC indicated > 99% monomer. For the 250 mg/ml dispersion from row 4 of Table 7.5, after dilution the % monomer was almost identical to that of the starting material (Fig. F3) thus corroborating the evidence from DLS that monomeric mAb is obtained upon dilution. A preliminary study of the stability of mAb1 in dispersion was also conducted by storing a high co-solute sample of mAb1 at -40° C, 4°C and room temperature for 8 weeks as shown in Table 7.14. The samples stored under all three conditions were seen to be stable with no significant decrease in the % monomer over the course of 8 weeks.

7.4 DISCUSSION

7.4.1 mAb dispersions without co-solute

In systems without added co-solutes, η has been studied as a function of the protein sequence, buffer composition or concentration of added salts.^{12, 17} In particular, Connolly et al. demonstrated that mAb sequence may be modified to decrease the attractive interactions and thus reduce η for the charged mutant compared to the wild-type mAb.^{7, 8, 18} For a series of mAbs in a given buffer, a direct correlation was observed between η at high concentration and the second virial coefficient (B_2) or the diffusion interaction parameter (k_D) at low concentration.^{7, 10} The slightly positive k_d for mAb1 (control with no added co-solute) at pH 5.5 in 30 mM histidine buffer (Table 7.8) is in the middle of Connolly's range. Thus the observed relatively high $\eta > 150$ cp in Table 7.3 is consistent with the measured k_d .⁷ Since high η s were seen for mAb1 dispersions with no co-solute over a variety of pH values in Table 7.7, the buffers probably do not modify protein-protein interactions to a sufficient extent for lowering η .

Even when proteins do not aggregate according to small angle neutron scattering (SANS), neutron spin echo (NSE),⁵⁴ small angle x-ray scattering (SAXS) or static light scattering (SLS), attraction between proteins may still produce a relatively high η of ~20 cP at 150-175 mg/ml. The η will likely be even higher when attractive hydrophobic or anisotropic electrostatic and charge-dipole forces form clusters or oligomers of mAbs.^{7-9, 12, 17, 18, 27} Since elevated volume fraction of mAb in solution due to the void volume present in oligomers is a major culprit for high η , disrupting the oligomer structure can potentially lower η .^{12, 32} For a strongly interacting mAb which dimerizes, addition of 200 mM NaCl was shown to lower η five-fold from ~300 cP to ~60 cP at 150 mg/ml by breaking up dimers, as shown by NSE measurements of protein diffusion.¹² The

oligomers may be disrupted by electrostatic screening of the anisotropic interactions between oppositely charged patches and charge-dipole interactions.^{8, 9, 18, 55, 56} As shown in Table 7.3 η for mAb1 was seen to decrease by a little more than two-fold upon the addition of 150 mM NaCl to a mAb1 dispersion in 30 mM histidine buffer. However, depending on whether the net or the localized electrostatic interactions are dominant for determining η , addition of salt can lower,^{4, 6, 18, 57} not influence^{5, 12} or in some cases even raise¹⁷ η depending on the particular mAb in question.

7.4.2 Modification of electrostatic interactions between mAbs by arg to lower η

The net charge on mAbs can cause repulsion between mAbs for pH values away from the isoelectric point and is an important factor governing protein-protein interactions. Between pH 5 and 8, the carboxylic acid group is negatively charged while the amino and guanidyl groups are positively charged giving arg a net +1 charge. Screening of the net electrostatic interactions by increased ionic strength can lead to a reduction in repulsive forces between mAbs which would explain the negative k_d value for mAb1 upon addition of a high concentration of arg and glu as co-solutes (Table 7.8). At these low concentrations, the anisotropic electrostatic and dipolar interactions will be less important than at the high protein concentrations. Arg and glu raise the ionic strength of mAb1 dispersions and therefore can have a similar η lowering effect as NaCl. However, the carboxylic acid, amino and guanidyl groups of arg can bind to a variety of polar or charged amino acid residues on proteins through hydrogen bonds, electrostatic or charge-dipole interactions.^{21, 22, 40-42, 46, 58} Therefore between pH 5-8, bound arg can increase the magnitude of positive charge on positively charged sites, lend a positive charge to neutral sites and neutralize the negative charge on negatively charged sites. As

a result, a majority of the localized charge patches will be positively charged leading to weak attraction between oppositely charged patches, which may explain the lowered η at pH 5 to 7. Although the overall electrostatic interactions are more attractive as evidenced by the measured k_d values via diffusion coefficient (Table 7.8), the localized oppositely charged interactions may be made less attractive by arg as evidenced by the elevated k_d measured by self-interaction chromatography⁴⁵ and weakened protein binding to ion-exchange columns.^{21, 22} The specific binding of arg to charged sites on proteins could be partially responsible for the greater decrease in η seen for the dispersions containing arg (Table 7.5 and Fig. 7.1) compared to those containing NaCl (Table 7.3). At pH values above 8 where arg becomes uncharged, the protein charge modification by arg will be lessened along with the effect of ionic strength. Consequently, an increase in anisotropic electrostatic interactions would be expected to increase η at pH 8.5 as observed in Figs. 7.3 and 7.4. Arg starts becoming negatively charged along with the protein at pH > 11 as the guanidyl group becomes deprotonated. Here arg H-bonds to proteins will make the protein surface more negative and increase electrostatic repulsion, which would be expected to lower η as observed in Figs. 7.3 and 7.4.

7.4.3 Modification of hydrophobic interactions between mAbs by salt and arg to lower η

Interactions between hydrophobic patches on proteins are known to produce elevated η s and ultimately precipitation.^{5, 20, 27} For example, addition of salts with organic ions can reduce η of BSA and γ -globulin solutions by up to 4 times at high protein concentration by binding to the hydrophobic patches.²⁰ In addition to H-bonding to mAbs, the guanidyl group of arg also interacts with hydrophobic residues allowing arg to

interact with hydrophobic patches on proteins.^{21, 22, 27, 28, 40-44} Guanidium chloride (Gdn.HCl) contains the guanidium cation, a strong base ($pK_a = 13.6$) that denatures proteins at much higher concentrations ($>5M$).^{59, 60} Unlike guanidine, arg binding to hydrophobic sites is much weaker due to the carboxylic acid group, and this weakened binding causes less unfolding.^{44, 46} Alternatively, simulations of arg.HCl at high concentrations show that three arg ions tend to stack on top of each other with the guanidium groups aligned with each other and the ethylene groups form a hydrophobic patch which binds to hydrophobic patches on proteins.^{40, 41, 44, 45} Arg binding to hydrophobic patches on a local scale decreases attraction and can potentially increase repulsion.²⁷ The reduction in hydrophobic interactions between proteins upon adding arg is evidenced by reduced protein binding on hydrophobic columns^{21, 22} and an increased k_d through addition of arg.⁴⁵ Partially because of this blocking of hydrophobic interactions, arg lowers η to a greater extent than screening of electrostatic interactions alone with NaCl, as evidenced by comparing Tables 7.3 and 7.5. Additionally, as the concentration of arg is increased, a greater number of hydrophobic and charged patches can be blocked leading to weaker interactions and therefore a low η explaining the observed trend in Fig. 7.2 and Table 7.5.

7.5 CONCLUSIONS

This study expands our previous studies of high co-solute protein dispersions^{25, 26, 29} with low viscosities to include interacting co-solutes and for pH values away from the isoelectric point. The viscosity of concentrated ~ 250 mg/ml mAb1 dispersions was decreased up to 6 fold by the addition of high concentrations of arg titrated with glu or HCl as co-solutes, compared to a control at the same pH of 5.5 in histidine buffer. At a

constant pH of 5.5 (fixed ratio of arg/glu), increasing the total concentration of arg and glu lowered the inherent viscosity and viscosity significantly, reaching 0.0129 ml/mg and 43 cP at 261 mg/ml mAb1 after sterile filtration, which is sufficiently low for injection through a 28G needle. Similar reduction is viscosity for arg/HCl suggesting that arg played a more important role than glu. For a polyclonal sheep IgG mixture at 258 mg/ml, η and η_{inh} reached 17 cp and 0.0097 ml/mg respectively. The viscosity for mAb1 dispersions with high arg and glu concentrations was seen to actually be the highest near the isoelectric point in this case and low over a wide range of pH values away from the isoelectric point. Specific interactions of arg with proteins reduce the localized electrostatic, hydrogen bonding, charge-dipole and hydrophobic patch interactions between proteins, which lowers the viscosity.^{21, 22, 45} The importance of these specific interactions is evident in the inability of tre, a non-interacting co-solute, to lower the viscosity. The diffusion coefficient ratio D/D_0 by DLS decreased well below 1 with the addition of almost all of the co-solutes, and to a greater extent for tre than arg/glu. Upon dilution in buffer, no significant increase was observed in % aggregates by SEC relative to the initial protein solution, despite exposing the protein to high co-solute and protein concentrations.

Protein conc (mg/ml)	Co-solutes	Co-solute conc (mg/ml)	pH	η_0 (cP)	η (cP)	η_{inh} (ml/mg)	D/D_0
146	-	-	5.5	1.0	18.5 ± 1.4	0.0175	1.43
140	50 mM phosphate buffer	-	7.4	1.0	15.5 ± 2.0	0.0197	1.06
130	Arg acetate	153	6	1.5	7.9 ± 0.3	0.0128	-
132	Arg.HCl	144	7	1.5	3.6 ± 0.4	0.0067	0.62
129	Lysine.HCl	159	7	1.3	5.7 ± 0.5	0.0103	0.53
130	Proline	130	6.5	1.25	6.0 ± 0.5	0.0124	0.61
135	Sodium glutamate	144	7.5	1.5	18.4 ± 0.3	0.0186	-
135	Sodium Glutamate and arg.HCl (1:1 by wt)	72 each	7	1.5	5.4 ± 1.2	0.0095	0.72

Table 7.1: Viscosity of mAb1 dispersions at ~130 mg/ml after addition of 150 mg/ml of amino acids as co-solute.

Protein conc (mg/ml)	Co-solutes	Co-solute conc (mg/ml)	pH	η_0 (cP)	η (cP)	η_{inh} (ml/mg)
146	-	-	5.5	1.0	18.5 ± 1.4	0.0175
150	50 mM phosphate buffer	-	8.2	1.0	12.6 ± 0.2	0.0144
136	Tre	137	5.5	1.3	11.8 ± 0.3	0.0152
162	Tre	155	8	1.3	14.9 ± 0.5	0.0150
155	Tre and arg.HCl	86 tre and 74 arg.HCl	7.5	1.4	8.0 ± 1.0	0.0111
135	Tre and glycine (1:1 by weight)	72 each	5.5	1.3	8.4 ± 0.3	0.0138

Table 7.2: Viscosity of mAb1 dispersions at ~ 150 mg/ml containing ~150 mg/ml mixtures of tre with and without amino acids as co-solutes.

Protein conc (mg/ml)	His buffer conc (mM)	η_0 (cP)	η (cP)	η_{inh} (ml/mg)	D/D_0	% yield	Cfg time (min)
238 ± 7.2	30	1.0	193 ± 8	0.0219	1.01	54	54
228 ± 16.2	20	1.0	152 ± 19.2	0.0219	0.98	78	30
229 ± 2.8	30 (+150 mM NaCl)	1.0	66.7 ± 3.4	0.018	0.29	51	69

Table 7.3: Viscosity for mAb1 dispersions in low concentration histidine (his to his.HCl was 0.18:1 by mass in both cases) buffers at pH 5.5 run at a centrifugation speed of 5000 rcf. Rows 1 and 3 were run in Centricon centrifugal concentrator tubes with a centrifugation speed of 4500 rcf.

Protein conc (mg/ml)	Original D/D_0	Effective CONTIN Diameter after dilution (nm)
249	0.32	13 ± 2.0
236	0.34	12 ± 3.0

Table 7.4: D/D_0 for dilution of mAb1 dispersions (0.5 mg/ml) with 78.6 mg/ml arg and 71.4 mg/ml glu from Fig. 7.1.

Protein conc (mg/ml)	Arg conc (mg/ml)	Glu conc (mg/ml)	η_0 (cP)	η (cP)	η_{inh} (ml/mg)	% yield	Cfg time (min)
246 ± 17.7	39.3	35.7	1.20	54 ± 1.9	0.0155	87	48
245 ± 24.4	52.4	47.6	1.33	38 ± 2.2	0.0137	81	45
241 ± 0.2	65.5	59.5	1.42	39 ± 4.8	0.0127	89	50
263 ± 13.4	78.6	71.4	1.5	30 ± 1.5	0.0111	92	63

Table 7.5: Viscosity of mAb1 dispersions as a function of increasing conc of arg/glu. The pH of all of the samples was 5.5 and the centrifugation speed was 5000 rcf. The uncertainty is \pm one std. dev. over multiple measurements in both concentration and viscosity.

Protein conc (mg/ml)	Arg conc (mg/ml)	Glu conc (mg/ml)	pH	η_0 (cP)	η (cP)	η_{inh} (ml/mg)	D/D_0	Turbidity/ conc (ml mg ⁻¹ cm ⁻¹)	% yield	Cfg time (min)
288 ± 1.5	78.6	71.4	5.49	1.5	105 ± 29.1	0.0148	0.33	0.0013	80	105
261 ± 2.2	78.6	71.4	5.51	1.5	43 ± 13.8	0.0129	0.43	0.0020	*	-
288 ± 18.7	75	75	5.01	1.5	118 ± 22.5	0.0152	0.33	0.0013	77	105
269 ± 7.5	75	75	5.02	1.5	74 ± 4.6	0.0145	0.35	0.0015	*	-
260 ± 18.2	26.2	24.8	5.5	1.2	519 ± 51.9	0.0232	0.58	0.0023	68	90
241 ± 7.7	26.2	24.8	5.5	1.2	358 ± 31.6	0.0236	0.67	0.0030	*	-
283 ± 15.4	26.2	24.8	5.49	1.2	303 ± 29.6	0.0196	0.72	0.0018	82	90
239 ± 23.9	26.2	24.8	5.5	1.2	192 ± 30.8	0.0213	0.76	0.0026	*	-

Table 7.6: Viscosity, DLS (D/D_0) and turbidity/concentration at 350 nm of mAb1 dispersions made with the large 15 ml Centricon centrifugal concentrator tubes with a centrifugation speed of 4500 rcf and a temperature of 20 °C. The second row in each pair shown in bold is the result after sterile filtration of the row above it.

Protein conc (mg/ml)	Buffer	Buffer conc (mM)	pH	η_0 (cP)	η (cP)	η_{inh} (ml/mg)	D/D_0	% yield	Cfg time (min)
197 ± 15.2	none	-	5.5	1.0	64 ± 4.2	0.0212	0.96	95.5	50
191 ± 1.0	phosphate	50	6.5	1.0	71 ± 4.5	0.0196	0.77	85.5	45
206 ± 1.0	phosphate	50	8	1.0	108 ± 13.9	0.0228	0.60	88.5	45
185 ± 8.2	carbonate	50	11	1.0	147.6 ± 9.2	0.0271	0.73	84.7	45

Table 7.7: Viscosity of low co-solute mAb1 dispersions at various pH values all at a centrifugation speed of 5000 rcf.

Protein formulation	pH	k_d (ml/mg)
30 mM histidine	6	3.8
78.6 mg/ml arg 71.4 mg/ml glu	5.5	-7.0

Table 7.8: Diffusion interaction parameter k_d values for various dilute protein solutions as measured by DLS using the CONTIN algorithm.

Protein conc (mg/ml)	Arg conc (mg/ml)	Glu conc (mg/ml)	pH	η_0 (cP)	η (cP)	η_{inh} (ml/mg)	% yield	Cfg time (min)
252	75	75	5	1.5	17 ± 5.6	0.0097	100	45
258	108.5	91.5	6	1.8	20 ± 0.3	0.0101	94	55

Table 7.9: Low viscosities for sheep IgG dispersions with high co-solute concentrations at a centrifugation speed of 10000 rcf.

Protein conc (mg/ml)	Tre conc (mg/ml)	pH	η_0 (cP)	η (cP)	η_{inh} (ml/mg)	D/D_0	Yield (%)	Cfg time (min)
229	70	8.2	1.2	241 ± 41.8	0.0230	0.25	80	30
246	200	8.2	1.4	190 ± 8.3	0.0198	0.13	76	90
200	200	7.2	1.4	191 ± 15.7	0.0244	0.18	66	30
229	200	6.4	1.4	160 ± 77.6	0.0206	-	82	95

Table 7.10: Viscosity and D/D_0 of mAb1 dispersions with tre as the only co-solute. All samples were formulated in 50 mM phosphate buffer to set the pH. The centrifugation speed was 10000 rcf.

Protein conc (mg/ml)	Tre conc (mg/ml)	$(\text{NH}_4)_2\text{SO}_4$ conc (mM)	η_0 (cP)	η (cP)	η_{inh} (ml/mg)	Cfg time (min)
228	200	25	1.4	130 ± 4.0	0.0197	20
243	200	100	1.4	195 ± 37.3	0.0202	40

Table 7.11: Viscosity of mAb1 dispersions with tre as the only co-solute with ammonium sulfate added to screen electrostatic interactions. All samples were formulated in 50 mM pH 8.2 phosphate buffer. The centrifugation speed was 10000 rcf.

Protein conc (mg/ml)	Arg conc (mg/ml)	Glu conc (mg/ml)	Tre conc (mg/ml)	η_0 (cP)	η (cP)	η_{inh} (ml/mg)	D/D_0	Yield (%)	Cfg time (min)
241	27.5	22.5	25	1.2	71 ± 14.0	0.0167	-	71	95
252	36.7	30	33.3	1.4	66 ± 16.5	0.0154	0.27	61	75
238	73.4	60	66.7	1.7	40 ± 2.5	0.0137	0.34	80	65

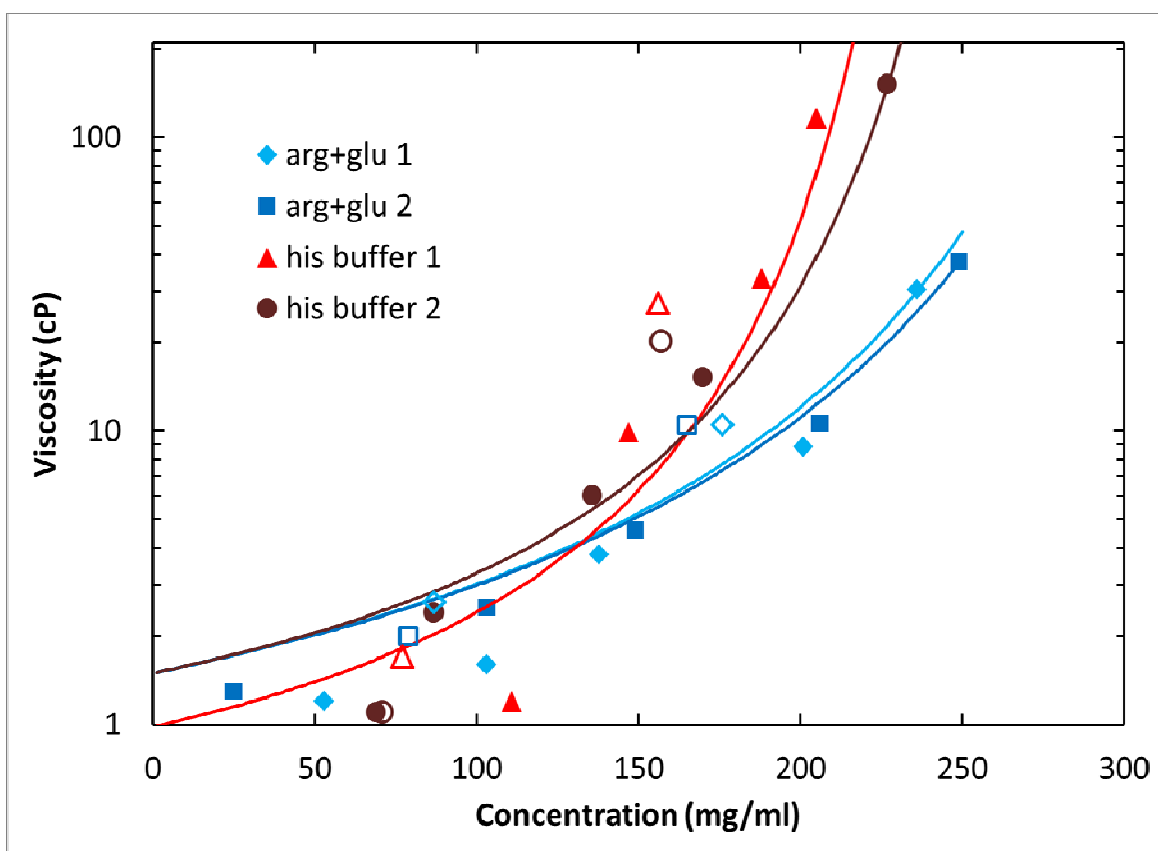
Table 7.12: Viscosity of mAb1 dispersions including tre with arg and glu at pH 7.1. The centrifugation speed was 5000 rcf.

Sample	% monomer in the sample
Monomer control (no processing)	99.89
Sample with arg:glu (row 4 from Table 7.5)	99.86

Table 7.13: SEC for diluted mAb1 dispersions compared to the monomer control.

Week	Frozen storage at -40 °C	Refrigerated storage at 4 °C	Room temperature storage
1	99.86	99.87	99.86
1.5	99.87	99.90	99.84
2	99.85	99.91	99.83
4	99.77	99.86	-
8	99.90	99.88	99.75

Table 7.14: SEC for mAb1 dispersions stored for 8 weeks. The values in the table are the % monomer in the sample measured by the area under the curve for the SEC. The ~250 mg/ml dispersion contained 81.4 mg/ml arg and 68.6 mg/ml glu (pH 7.1) and was 99.89% monomer pre-storage.



a
(Fig. 7.1 continued on the next page)

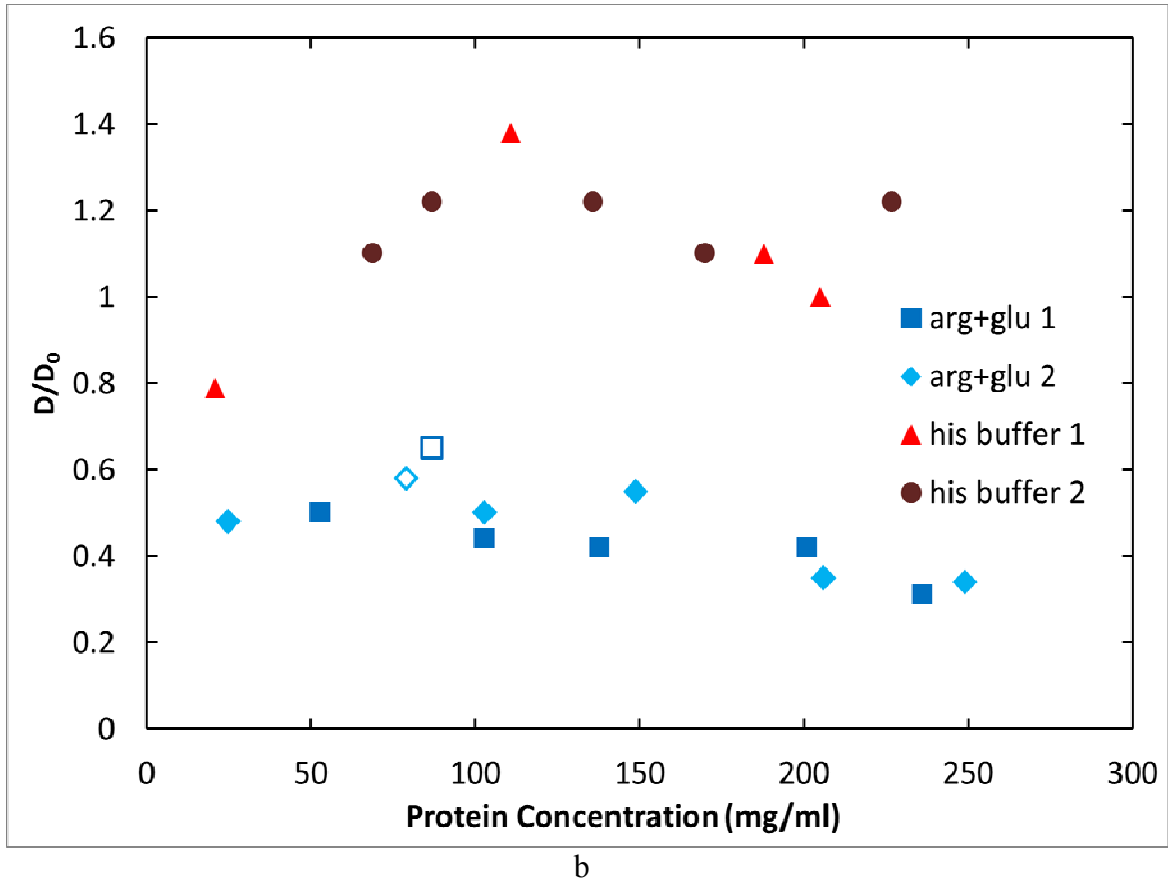


Figure 7.1: Viscosity of mAb1 dispersions as a function of the protein concentration. a. The arg glu samples had 78.6 mg/ml arg and 71.4 mg/ml glu while the histidine buffer samples were in pH 5.5 histidine buffer at 20 mM. The lines are fits with the Ross-Minton equation in terms of both $[\eta]$ and k/v . b. D/D_0 from DLS. For both a and b, the open symbols show the data for samples prepared by dilution of the highest concentration samples.

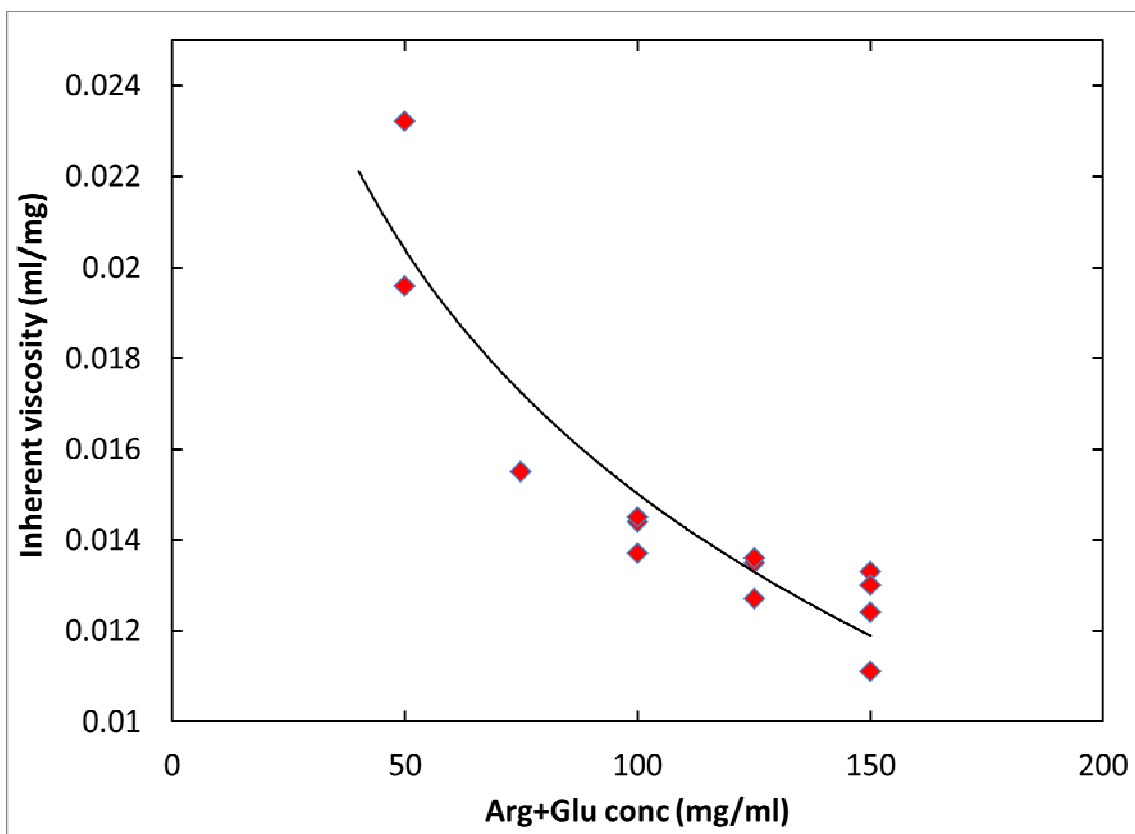


Figure 7.2: Decrease in inherent viscosity of mAb1 dispersions as the concentration of arg + glu is increased from 75 to 150 mg/ml for the data in Tables 7.4 and 7.5 at pH 5.5. The line is a guide to the eye.

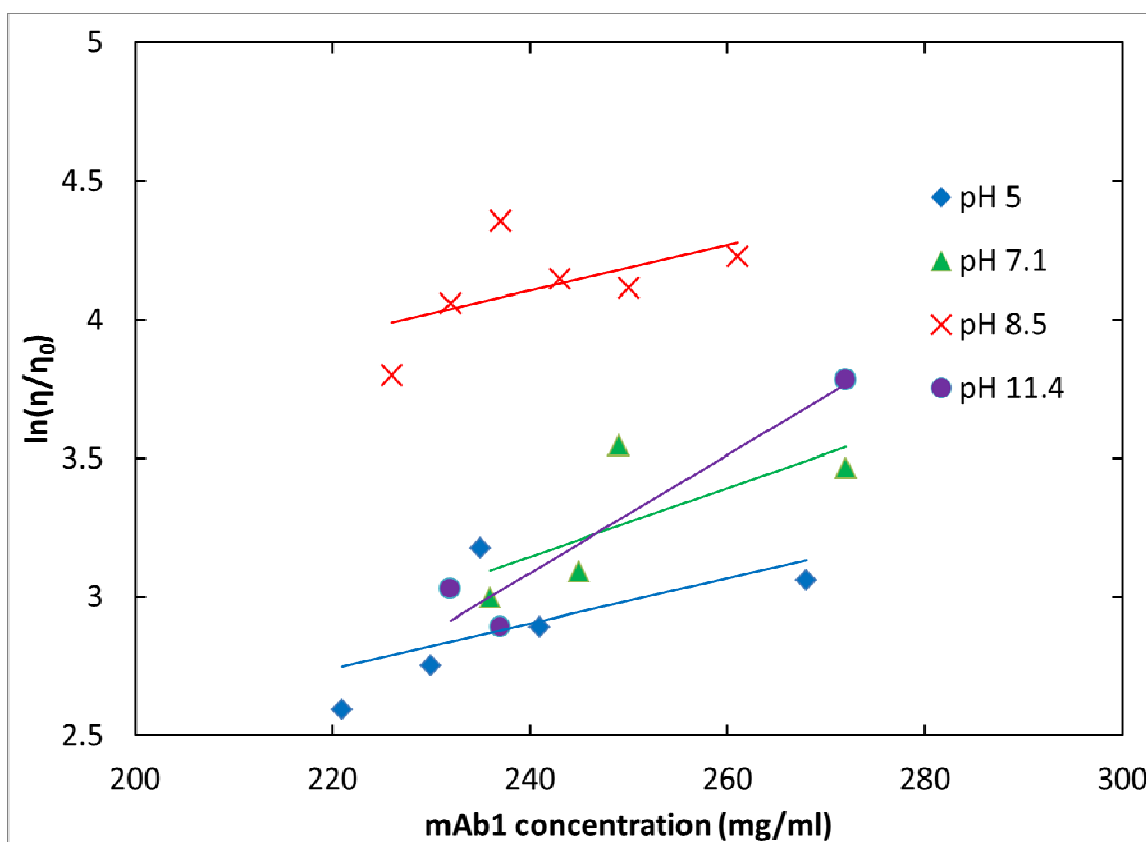


Figure 7.3: Viscosity of mAb1 dispersions as a function of pH at a constant arg and glu concentration of 150 mg/ml. The ratio of arg to glu was varied to change the pH.

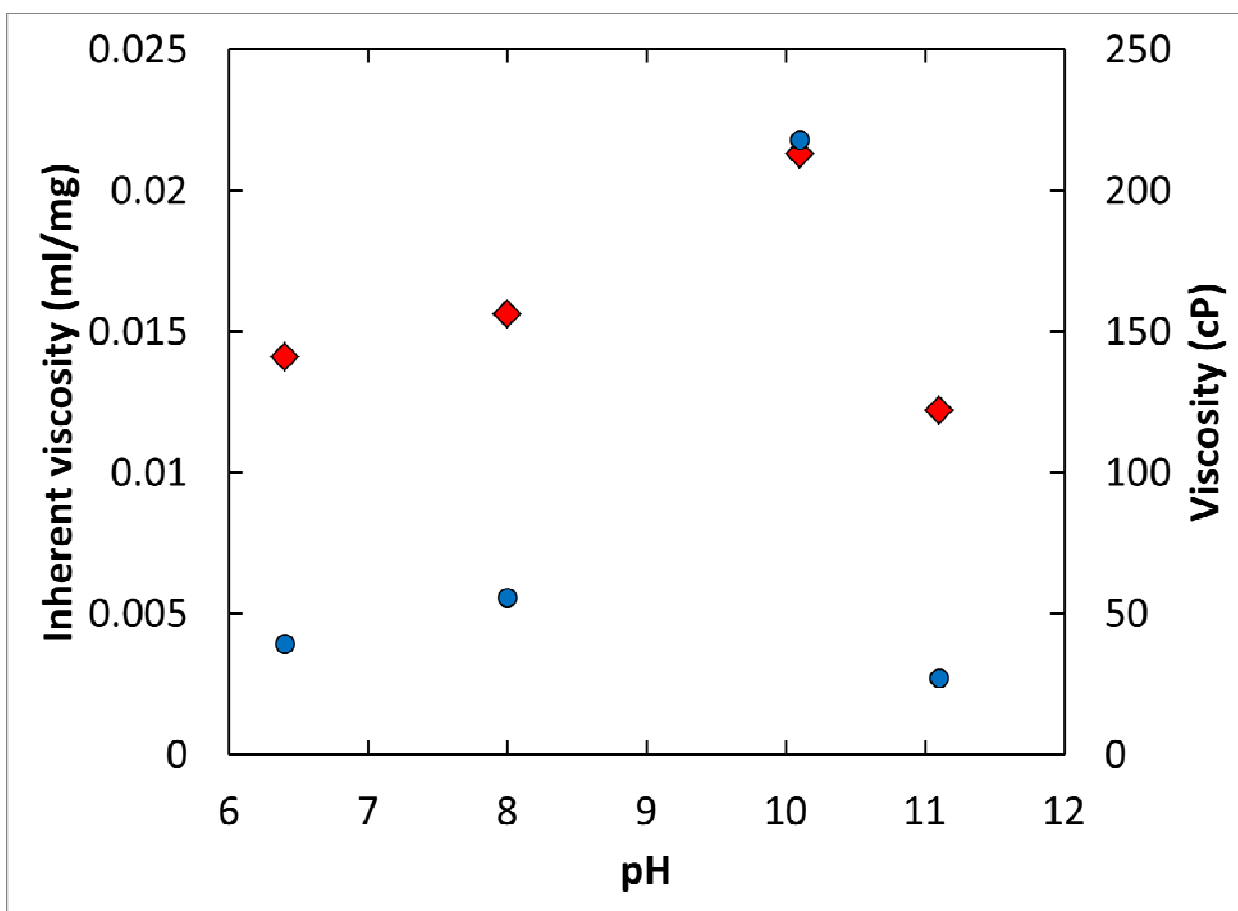


Figure 7.4: Inherent viscosity (red diamonds) and viscosity (blue circles) for mAb 1 dispersions with 150 mg/ml arg titrated with HCl from Table F5. Centrifugation speed was 10000 rcf. The viscosity goes through a maximum near the isoelectric point, pH 9.

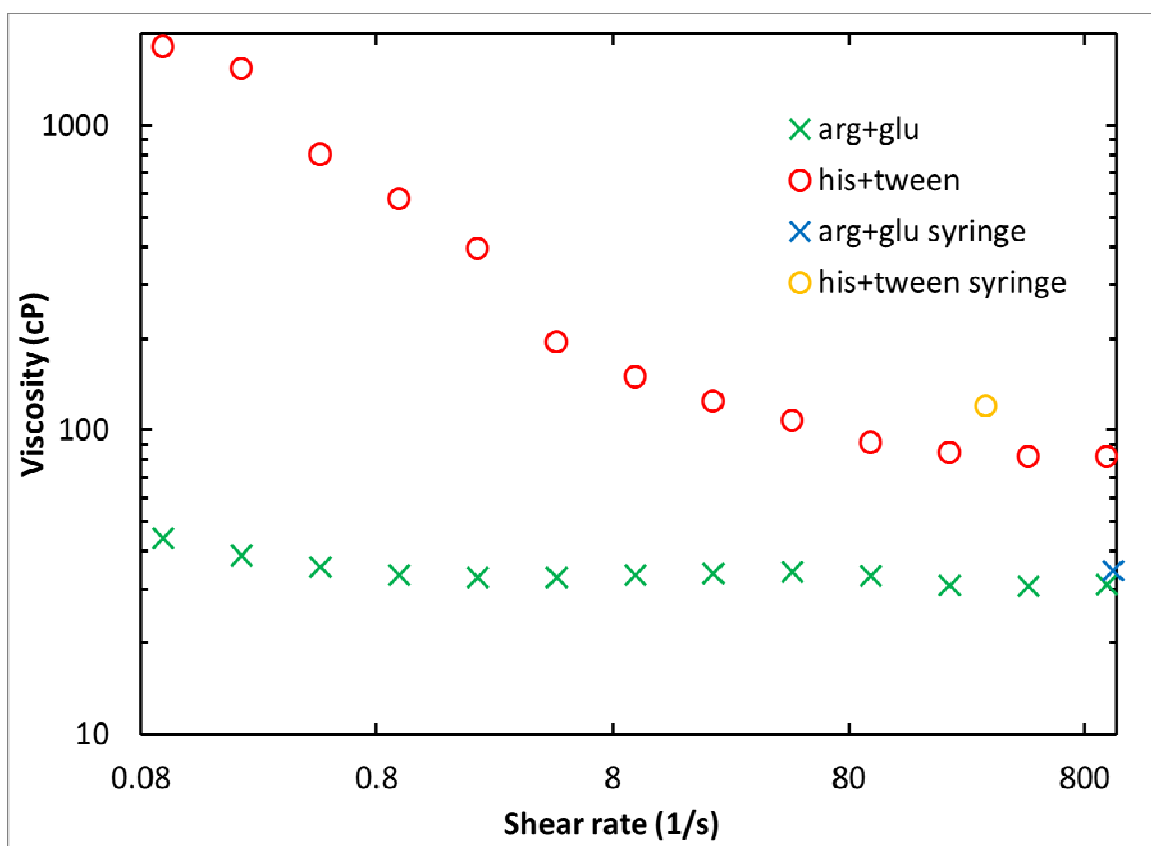


Figure 7.5: Effect of shear rate on viscosity of mAb1 dispersions at ~228 mg/ml with 20 mM histidine and 0.05% Tween 80 (red circles) and 269 mg/ml with 78.6 mg/ml arg and 71.4 mg/ml glu (green crosses).

7.6 REFERENCES

1. Therapeutic monoclonal antibodies approved or in review in the European Union or United States. http://www.antibodysociety.org/news/approved_mabs.php (9/27/2014),
2. Shire, S. J.; Shahrokh, Z.; Liu, J. J. Pharm. Sci. 2004, 93, (6), 1390-1402.
3. Srinivasan, C.; Weight, A. K.; Bussemer, T.; Klibanov, A. M. Pharmaceutical Research 2013, 30, (7), 1749-57.
4. Saluja, A.; Kalonia, D. S. International Journal of Pharmaceutics 2008, 358, (1-2), 1-15.

5. Kanai, S.; Liu, J.; Patapoff, T. W.; Shire, S. J. *J Pharm Sci* 2008, 97, (10), 4219-4227.
6. Liu, J.; Nguyen, M. D. H.; Andya, J. D.; Shire, S. J. *Journal of Pharmaceutical Sciences* 2005, 94, (9), 1928-1940.
7. Connolly, B. D.; Petry, C.; Yadav, S.; Demeule, B.; Ciaccio, N.; Moore, J. M.; Shire, S. J.; Gokarn, Y. R. *Biophysical journal* 2012, 103, (1), 69-78.
8. Yadav, S.; Shire, S. J.; Kalonia, D. S. *Journal of pharmaceutical sciences* 2012, 101, (3), 998-1011.
9. Yadav, S.; Liu, J.; Shire, S. J.; Kalonia, D. S. *J Pharm Sci* 2010, 99, (3), 1152-1168.
10. Saito, S.; Hasegawa, J.; Kobayashi, N.; Kishi, N.; Uchiyama, S.; Fukui, K. *Pharmaceutical Research* 2012, 29, (2), 397-410.
11. He, F.; Woods, C. E.; Litowski, J. R.; Roschen, L. A.; Gadgil, H. S.; Razinkov, V. I.; Kerwin, B. A. *Pharmaceutical Research* 2011, 28, (7), 1552-60.
12. Yearley, E. J.; Godfrin, P. D.; Perevozchikova, T.; Zhang, H.; Falus, P.; Porcar, L.; Nagao, M.; Curtis, J. E.; Gawande, P.; Taing, R.; Zarraga, I. E.; Wagner, N. J.; Liu, Y. *Biophysical journal* 2014, 106, (8), 1763-70.
13. Baglioni, P.; Fratini, E.; Lonetti, B.; Chen, S. H. *Journal of Physics: Condensed Matter* 2004, 16, (42), S5003-S5022.
14. Burckbuchler, V.; Mekhloufi, G.; Giteau, A. P.; Grossiord, J. L.; Huille, S.; Agnely, F. *European journal of pharmaceutics and biopharmaceutics : official journal of Arbeitsgemeinschaft fur Pharmazeutische Verfahrenstechnik e.V* 2010, 76, (3), 351-6.
15. Castellanos, M. M.; Pathak, J. A.; Colby, R. H. *Soft Matter* 2014, 10, (1), 122-31.
16. Castellanos, M. M.; Pathak, J. A.; Leach, W.; Bishop, S. M.; Colby, R. H. *Biophysical journal* 2014, 107, (2), 469-76.
17. Lilyestrom, W. G.; Yadav, S.; Shire, S. J.; Scherer, T. M. *The journal of physical chemistry. B* 2013, 117, (21), 6373-84.
18. Zarraga, I. E.; Taing, R.; Zarzar, J.; Luoma, J.; Hsiung, J.; Patel, A.; Lim, F. J. *Journal of pharmaceutical sciences* 2013, 102, (8), 2538-49.
19. Pathak, J. A.; Sologuren, R. R.; Narwal, R. *Biophysical journal* 2013, 104, (4), 913-23.
20. Du, W.; Klibanov, A. M. *Biotechnology and bioengineering* 2011, 108, (3), 632-6.
21. Hou, Y.; Cramer, S. M. *Journal of chromatography. A* 2011, 1218, (43), 7813-20.

22. Holstein, M. A.; Parimal, S.; McCallum, S. A.; Cramer, S. M. *Biotechnology and bioengineering* 2012, 109, (1), 176-86.
23. Miller, M. A.; Engstrom, J. D.; Ludher, B. S.; Johnston, K. P. *Langmuir* 2010, 26, (2), 1067-1074.
24. Johnson, H. R.; Lenhoff, A. M. *Molecular pharmaceutics* 2013, 10, (10), 3582-91.
25. Johnston, K. P.; Maynard, J. A.; Truskett, T. M.; Borwankar, A.; Miller, M. A.; Wilson, B.; Dinin, A. K.; Khan, T. A.; Kaczorowski, K. J. *Acs Nano* 2012.
26. Borwankar, A. U.; Dinin, A. K.; Laber, J. R.; Twu, A.; Wilson, B. K.; Maynard, J. A.; Truskett, T. M.; Johnston, K. P. *Soft Matter* 2013, 9, (6), 1766-1771.
27. Scherer, T. M. *The journal of physical chemistry. B* 2013, 117, (8), 2254-66.
28. Inoue, N.; Takai, E.; Arakawa, T.; Shiraki, K. *Molecular pharmaceutics* 2014, 11, (6), 1889-96.
29. Miller, M. A.; Khan, T. A.; Kaczorowski, K. J.; Wilson, B. K.; Dinin, A. K.; Borwankar, A. U.; Rodrigues, M. A.; Truskett, T. M.; Johnston, K. P.; Maynard, J. A. *Journal of Pharmaceutical Sciences* 2012, 101, (10), 3763-3778.
30. Groenewold, J.; Kegel, W. K. *Journal of Physical Chemistry B* 2001, 105, (47), 11702-11709.
31. Groenewold, J.; Kegel, W. K. *Journal of Physics-Condensed Matter* 2004, 16, (42), S4877-S4886.
32. Godfrin, P. D.; Valadez-Perez, N. E.; Castaneda-Priego, R.; Wagner, N. J.; Liu, Y. *Soft Matter* 2014, 10, (28), 5061-71.
33. Li, Y.; Lubchenko, V.; Vekilov, P. G. *The Review of scientific instruments* 2011, 82, (5), 053106.
34. Pan, W. C.; Vekilov, P. G.; Lubchenko, V. *Journal of Physical Chemistry B* 2010, 114, (22), 7620-7630.
35. Soraruf, D.; Roosen-Runge, F.; Grimaldo, M.; Zanini, F.; Schweins, R.; Seydel, T.; Zhang, F.; Roth, R.; Oettel, M.; Schreiber, F. *Soft Matter* 2014, 10, (6), 894-902.
36. Lee, J. C.; Timasheff, S. N. *Journal of Biological Chemistry* 1981, 256, (14), 7193-7201.
37. Kreilgaard, L.; Frokjaer, S.; Flink, J. M.; Randolph, T. W.; Carpenter, J. F. *Journal of Pharmaceutical Sciences* 1999, 88, (3), 281-290.
38. Shen, V. K.; Cheung, J. K.; Errington, J. R.; Truskett, T. M. *Journal of biomechanical engineering* 2009, 131, (7), 071002-071002.
39. Cheung, J. K.; Truskett, T. M. *Biophysical Journal* 2005, 89, (4), 2372-2384.

40. Shukla, D.; Trout, B. L. *The journal of physical chemistry. B* 2011, 115, (5), 1243-53.
41. Shukla, D.; Schneider, C. P.; Trout, B. L. *Advanced drug delivery reviews* 2011, 63, (13), 1074-85.
42. Arakawa, T.; Ejima, D.; Tsumoto, K.; Obeyama, N.; Tanaka, Y.; Kita, Y.; Timasheff, S. N. *Biophysical chemistry* 2007, 127, (1-2), 1-8.
43. Schneider, C. P.; Trout, B. L. *The journal of physical chemistry. B* 2009, 113, (7), 2050-8.
44. Vagenende, V.; Han, A. X.; Mueller, M.; Trout, B. L. *ACS chemical biology* 2013, 8, (2), 416-22.
45. Valente, J. J.; Verma, K. S.; Manning, M. C.; Wilson, W. W.; Henry, C. S. *Biophysical Journal* 2005, 89, (6), 4211-8.
46. Shukla, D.; Trout, B. L. *The Journal of Physical Chemistry B* 2010, 114, (42), 13426-13438.
47. Schneider, C. A.; Rasband, W. S.; Eliceiri, K. W. *Nat Meth* 2012, 9, (7), 671-675.
48. Horn, F. M.; Richtering, W.; Bergenholtz, J.; Willenbacher, N.; Wagner, N. J. *Journal of colloid and interface science* 2000, 225, (1), 166-178.
49. Mutch, K. J.; van Duijneveldt, J. S.; Eastoe, J. *Soft Matter* 2007, 3, (2), 155.
50. Ross, P. D.; Minton, A. P. *Biochemical and biophysical research communications* 1977, 76, (4), 971-976.
51. Rosenberg, E.; Hepbildikler, S.; Kuhne, W.; Winter, G. *Journal of Membrane Science* 2009, 342, (1-2), 50-59.
52. Windholz, M.; Editor, *The Merck Index: An Encyclopedia of Chemicals and Drugs*. 9th Ed. Merck and Co., Publ. Dept.: 1976; p 1937 pp.
53. Sharma, V.; Jaishankar, A.; Wang, Y.-C.; McKinley, G. H. *Soft Matter* 2011, 7, (11), 5150.
54. Grimaldo, M.; Roosen-Runge, F.; Zhang, F. J.; Seydel, T.; Schreiber, F. *Journal of Physical Chemistry B* 2014, 118, (25), 7203-7209.
55. Allmendinger, A.; Fischer, S.; Huwyler, J.; Mahler, H. C.; Schwarb, E.; Zarraga, I. E.; Mueller, R. *European journal of pharmaceutics and biopharmaceutics : official journal of Arbeitsgemeinschaft fur Pharmazeutische Verfahrenstechnik e.V* 2014, 87, (2), 318-28.
56. Roberts, C. J.; Blanco, M. A. *The journal of physical chemistry. B* 2014.
57. Salinas, B. A.; Sathish, H. A.; Bishop, S. M.; Harn, N.; Carpenter, J. F.; Randolph, T. W. *Journal of pharmaceutical sciences* 2010, 99, (1), 82-93.

58. Vondrášek, J.; Mason, P. E.; Heyda, J.; Collins, K. D.; Jungwirth, P. *The Journal of Physical Chemistry B* 2009, 113, (27), 9041-9045.
59. Chi, E. Y.; Krishnan, S.; Kendrick, B. S.; Chang, B. S.; Carpenter, J. F.; Randolph, T. W. *Protein Science* 2003, 12, (5), 903-913.
60. Liu, W.; Cellmer, T.; Keerl, D.; Prausnitz, J. M.; Blanch, H. W. *Biotechnology and bioengineering* 2005, 90, (4), 482-90.

Chapter 8: Solubilization of α -Chymotrypsinogen by interaction modification with arginine and glutamic acid

Some proteins tend to be insoluble at higher concentrations due to high degrees or hydrophobicity or a tendency to aggregate in solution. α -Chymotrypsinogen is typically not very soluble in buffers at neutral pH at high concentrations. A mixture of arginine and glutamic acid is used as a co-solute to solubilize α -CGN at protein concentrations above 200 mg/ml and form transparent dispersions. The solubilization of α -CGN seems to need a minimum total concentration of arginine and glutamic acid of 100 mg/ml as there may be a minimum number of sites that need to be blocked by co-solutes on proteins before solubilization. Also formulation pH values below 7 were seen to be incapable of solubilizing the protein. Below this apparent threshold concentration of co-solutes or below the threshold pH, the protein formulations at high concentration were seen to be turbid with large chunks of protein present in them. The presence of these interacting co-solutes also yields very low viscosities of protein formulations similar to that of mAb1 although there is no easy comparison as α -CGN is otherwise insoluble at these high concentrations. The diffusion coefficient as measured by DLS is also seen to be depressed relative to that calculated for monomeric protein for high co-solute concentration in the case of α -CGN. Additionally the high concentrations of arginine and glutamic acid are seen to stabilize α -CGN at high protein concentration as determined by melting temperature and enzymatic tests.

8.1 INTRODUCTION

α -Chymotrypsinogen (α -CGN) is a small globular protein with a molecular weight of about 26 kD. It is the inactive zymogen precursor of α -chymotrypsin (α -CT)

which is a digestive enzyme involved in protein digestion. α -CGN can be activated by a different enzyme, trypsin which cuts out 2 short peptides of 3 amino acids each. The removal of the peptide groups results in the α -CGN splitting into 3 peptide chains connected only by disulfide bonds which is α -CT. α -CGN is commonly used to study the kinetics and structural aspects of protein aggregation particularly for the formation of amyloid fibers.¹⁻⁴ In the case of these studies, the protein solutions are typically formulated in sodium citrate buffer at a highly acidic pH between 3 and 4. α -CGN is rarely formulated at a buffer pH near physiological conditions or nearer to its isoelectric point of 9.2.

Proteins when formulated have the lowest solubility near their isoelectric point than anywhere else over the entire pH range. Proteins have zero net charge at the isoelectric point as a result of which protein-protein attraction is the highest. The attraction between the oppositely charged patches on proteins will cause molecular orientation in a way so as to minimize the free energy with the lowest amount of repulsion.⁵⁻⁸ The attraction between hydrophobic patches is also unchanged leading to very highly attractive protein-protein interactions near the isoelectric point provided the samples are at low salinity so as to not eliminate electrostatic attractions.⁹⁻¹² These attractive forces for colloids in general, can lead to the formation of networks or associated protein species which will affect the dispersability of the colloidal species greatly.¹³ The networks can also cause increased viscosity and exacerbate observed shear thinning behavior for the protein formulations due to the need for breaking up the network to generate flow.^{5-7,14} Additionally, the tendency of proteins towards aggregation is elevated due to the lowered repulsion between proteins allowing for the attractive forces to bring them together allowing them to come close to each other and aggregate

especially at high concentrations. Therefore typical protein solutions at high concentration tend to gel, unfold, aggregate and in some cases even phase separate.¹⁵⁻¹⁸ Other proteins like α -CGN are not even soluble at concentrations above ~100 mg/ml.

Typically, to increase the solubility of proteins to higher concentrations above 100 mg/ml which are desired, protein engineering approaches for modifying the protein sequence are used.^{14,19} The technique is usually very complicated and time consuming with the possibility of reducing the protein activity and additionally it may not be effective or even possible for all proteins. Preparation of micron sized particles in organic solvents or aqueous buffers mixed with large fractions of organic solvents which act as anti-solvents have been developed for formulation of proteins at high concentrations.^{20,21} The approach has promise for proteins with low solubility because it actually works on the basis of desolubilizing the protein. However, there is limited knowledge about protein stability and in vivo effects of these large entities especially with regards to immune reactions.

Proteins were assembled into ~30-300 nm nanostructures detected by DLS by using a co-solute, namely, trehalose as an osmotic depletant to generate depletion attraction between proteins.²²⁻²⁴ The size of the nanocluster is limited by the long ranged electrostatic repulsion between proteins. The hypothesis of the approach is to lower the viscosity by increasing the inter-particle separation between nanoclusters, leading to weak, net-repulsive interactions between them compared to the strongly attractive interactions between mAbs in solution. Protein contained inside the nanostructures may have been stabilized due to self-crowding^{25,26} or through osmotic compression by trehalose^{27,28} as supported by the nanoclusters dissociating into active stable protein both in vitro and in vivo upon dilution into buffer. The nanoclusters could also be a

microphase of “liquid” protein dispersed in a more dilute “gaseous” phase of protein in solution. Proteins have also been assembled into large clusters ranging from 100-200 nm which were detected by light scattering, although in most cases the clusters account for a very small fraction of the protein present in the system.²⁹⁻³¹ Therefore there is no robust approach towards increasing the concentration of formulations of proteins where proteins retain their stability.

Herein, we use a mixture of arginine and glutamic acid as co-solutes to solubilize α -CGN at a concentration above 200 mg/ml and form transparent dispersions. The arginine and glutamic acid act as interacting co-solutes blocking sites on proteins reducing both the local electrostatic attraction and hydrophobic patch interactions which may be responsible for lack of protein solubility. The solubilization of proteins seems to need a minimum concentration of the charged co-solutes of 100 mg/ml as there may be a minimum number of sites that need to be blocked on proteins before it can be solubilized. Also it was necessary for the pH of the dispersing medium to be above 7 for achieving protein solubilization. Below the threshold concentration of co-solutes or below the threshold pH, the protein formulations at high concentration were seen to be turbid with large chunks of proteins in them. The presence of these interacting co-solutes yields very low viscosities of the protein formulations demonstrating the ability of arginine and glutamic acid to generate low viscosities. Additionally the high concentrations of arginine and glutamic acid are seen to stabilize proteins against degradation to α -CT demonstrating the ability of the high co-solute protein formulations to preserve protein structure.

8.2 MATERIALS AND METHODS

8.2.1 Materials

α -Chymotrypsinogen A was purchased in powder form from Alfa Aesar and used without any further purification. Trehalose was purchased from Ferro Pfanstiehl Laboratories Inc., Waukegan, IL. Arginine, glutamic acid, sodium monophosphate, sodium biphosphate, citric acid and sodium hydroxide were purchased from Fisher Scientific, Fairlawn, NJ.

8.2.2 Methods

8.2.2.1 Dispersion preparation

For a typical experiment, 25 mg of α -Chymotrypsinogen A was weighed out in a 0.1 mL conical vial (V-Vial, Wheaton). After correcting for the protein volume using the protein internal volume fraction, 81.5 μ L of the desired buffer containing pre-dissolved arginine and glutamic acid was added to the vial. The protein was then dispersed in the buffer by gentle stirring using a needle.

8.2.2.2 Viscometry for the protein nanocluster dispersion

The viscosity of the nanocluster dispersions were measured in triplicate using a 25 gauge (ID = 0.1 mm) 1.5" long needle (Becton Dickinson & Co. Precision Glide Needle) attached to a 1 mL syringe (Becton Dickinson & Co. 1 mL syringe with Luer-Lok™ tip), according to the Hagen-Poiseuille equation. The flow rate of the dispersion through the needle was determined using the volume measurement by correlating it to the height of the liquid in the conical vial and measuring the time taken for the dispersion column

height to move between two points. This flow rate was correlated to viscosity from a calibration curve derived from a set of standards of known viscosities as described previously.²³

8.2.2.3 Measurement of diffusion coefficient by DLS

The effective CONTIN diameters of protein monomers and nanoclusters were measured by dynamic light scattering (DLS) at an angle of 150° with a 632.8 nm laser and an avalanche photodiode at ~23°C using the CONTIN algorithm (Brookhaven BI-9000AT). The samples were pipetted into a 60 µl sample cell (Beckman Coulter) which was then mounted on the instrument to conduct three replicate runs of 2 minutes each. All reported diameters are the average of three runs.

8.2.2.4 Protein Concentration determination in the dispersion

For determining the concentration of the dispersions, 2 µl of dispersion was measured out and diluted into a receiving vessel containing 998 µl of 50 mM pH 6.4 phosphate buffer mixing well with the pipette tip. The diluted samples were prepared in duplicate. The absorbance of the resulting solution was measured using a Cary 3E uv-visible spectrophotometer in a cuvette (Hellma cells) with a path length of 1 cm. Then using Beer's law ($A = \epsilon b c$, where ϵ = extinction coefficient = 2.05 ml mg⁻¹ cm⁻¹, b = path length = 1 cm), knowing the absorbance, the concentration of the protein in the solution was calculated.

8.2.2.5 Measurement of protein enzymatic activity and stability

Chymotrypsinogen both before and after activation with trypsin (0.16 µg/ml) was diluted into an assay mixture of 38 mM Tris, 30% (v/v) methanol, 53 mM calcium chloride, 0.03 mM hydrochloric acid and 1.43 µg/ml chymotrypsinogen with varying amounts of N-benzoyl-L-tyrosine ethyl ester at a concentration of approximately 0.55 mM.³² After measuring the absorbance at 256 nm, the data was to fit a line and the k_{cat}/K_m was found. The α -CGN samples were then diluted to 100 µg/ml with 2.5 µL of Applied Biosystems, Inc. orange dye in their respective buffers and run on an Applied Biosystems ViiA-7 Real-time PCR machine to find the melting temperature.³² 2 micrograms of diluted protein were loaded onto a 12% SDS-PAGE gel in both reducing and non-reducing conditions and run at 80 V for 120 minutes.³²

8.3 RESULTS

8.3.1 Protein solubilization by addition of arginine and glutamic acid

Fig. 8.1 shows the effect of increasing arginine and glutamic acid concentration on α -CGN formulations at 250 mg/ml with a fixed mass ratio of arginine to glutamic acid of 1.5:1 which yields a pH of ~7.5 for all the dispersions contained in the images. The needle which is present in the picture was used to gently stir the samples to enable protein dissolution. As can be seen from the images, at low total concentration of arginine and glutamic acid, the samples appear very turbid due to the undissolved protein present in the formulation which is suspended in the sample due to mixing. The dispersions of α -CGN at 0, 25 and 50 mg/ml total concentration of arginine and glutamic acid in Figs. 8.1a, 8.1b and 8.1c respectively are seen to be milky or turbid due to the undissolved pieces of α -CGN. In these dispersions, the turbidity decreases slightly as the total co-

solute concentration in increased and disappears at 100 mg/ml of co-solutes (Fig. 8.1d) indicating that 100 mg/ml is the threshold concentration for the solubilization effect to occur. Dispersions with concentrations of arginine and glutamic acid higher than 100 mg/ml (Fig. 8.1e and 8.1f) were also not turbid with same level of transparency seen for all the formulations with co-solute concentrations above 100 mg/ml.

Table 8.1 shows the viscosities of the dispersions formulated with 100 mg/ml total added arginine and glutamic acid with different mass ratios of arginine to glutamic acid used for varying the sample pH. The viscosities of all the samples in Table 8.1 are very low being ~5-10 cP at a protein concentration of ~ 250 mg/ml. It is difficult to observe a clear trend in the viscosities as a function of the pH because the protein concentration is not constant between the various samples making comparison across samples difficult. Therefore, viscosities (η) of the different samples can be compared in a better manner by calculating the inherent viscosities (η_{inh}) to allow for easy comparison by compensating for the differences in the solvent viscosity (η) and the protein concentration (c) which impact the overall viscosity. The inherent viscosity is given by –

$$\eta_{inh} = \frac{\ln(\eta/\eta_0)}{c} \dots (8.1)$$

The inherent viscosity showed a clear trend being lower at pH values of 8 and 9 while being higher at the other pH values in both the more acidic and more basic range. At the pH values below 7.4, the samples were seen to be visibly turbid with some undissolved α -CGN dispersed in the sample similar to the samples with concentrations of arginine and glutamic acid which are too low from Fig. 8.1. The arginine concentration is lower at lower pH values since arginine is the basic component and less of it is needed to generate

lower pH values as seen in Table 8.1. Therefore, the lowered arginine concentration may be the cause for the lack of solubilization of α -CGN. The effective diffusion coefficient was measured for all samples by DLS using the CONTIN algorithm and corrected using the Beennakker-Mazur theory as described by Borwankar et al.²³ Throughout the current study, the value will be expressed as the ratio of the measured diffusion coefficient to the diffusion coefficient of the monomer in the same medium (D/D_0) to offer better perspective on the size range of the diffusing entities. The value of D/D_0 is seen to go through a minimum at pH 8 and 9 where the inherent viscosity is seen to be the lowest indicating that the samples with the lowest viscosities contain the slowest diffusing entities. The value of D/D_0 indicates that the rate of diffusion of the species in this high arginine and glutamic acid system is lower than that of monomer by at least 4 times hinting that these samples may contain some much larger entities. The trends in the inherent viscosity and diameter are further shown in a graphical form in Fig. 8.2 where the minima in both the properties can be seen more clearly.

The overall landscape of the trends seen for the inherent viscosity as a function of the pH and the total concentration of arginine and glutamic acid is shown in Fig. 8.3. Similar to the trends at pH 7.5, the α -CGN does not get solubilized at total arginine and glutamic acid concentrations below 100 mg/ml. Also the α -CGN is not solubilized at pH values below 7 even with total concentration of arginine and glutamic acid higher than 100 mg/ml. The experimental space that can be explored by varying the pH and the co-solute concentration in this case is limited by the solubility of the co-solutes. Glutamic acid has a relatively low solubility (<20 mg/ml)³³ while the solubility of arginine is higher (~150 mg/ml).³⁴ Arginine and glutamic acid have the synergistic effect of increasing each other's solubility through an acid-base neutralization reaction forming the

arginine glutamate salt. However, in the extreme values of pH, the concentration of one of them is too low leading to a large excess of one of them which cannot form the salt. The inherent viscosity is seen to be at a minimum between the pH values of 8-9 for all total concentrations of arginine and glutamic acid in agreement with the trend seen at 100 mg/ml. The inherent viscosity is seen to increase with increased total concentration of the co-solutes. Therefore, the solubilization effect and viscosity lowering effects both seem to have an optimal total co-solute concentration of ~ 100 mg/ml. The trend of increasing inherent viscosity with increased arginine and glutamic acid concentration is further highlighted in Table 8.2 although the absolute values of all the viscosities are still very low. The D/D_0 values measured for these samples all range from 0.2 to 0.16 again displaying a slowed rate of diffusion for the entities in the sample.

8.3.2 Effect of trehalose on dispersion viscosity and D/D_0

The effect of addition of trehalose to the α -CGN samples containing arginine and glutamic acid is shown in Table 8.3. The arginine and glutamic acid concentrations were maintained at 60 and 40 mg/ml respectively yielding a total concentration of 100 mg/ml and a pH of 7. Increasing the trehalose concentration increases the overall viscosity of the α -CGN but the inherent viscosity remains the same. Therefore the increased total viscosity is probably only the result of the increased solvent viscosity from the addition of trehalose. The D/D_0 decreases with increased trehalose concentration indicating that the diffusing species grow larger as the trehalose concentration is increased. The trend in D/D_0 before and after sterile filtration of the samples is shown by Fig. 8.4. The value of D/D_0 does not change significantly even after the sample is sterile filtered confirming that the observed decrease in D/D_0 is not the result of species larger than 200 nm skewing the

average size. The auto-correlation functions and their fits for the DLS measurements are shown in Table G1. The effect of increased arginine and glutamic acid concentration at a constant trehalose concentration is similar to that seen for the samples with no trehalose with the inherent viscosity increasing as the concentration of arginine and glutamic acid is increased as shown in Table 8.4. As the total concentration of arginine and glutamic acid is increased from 100 mg/ml to 200 mg/ml, the inherent viscosity increases by 20%. The value of the viscosity increases more sharply than the change in inherent viscosity would imply because the solvent viscosity is greatly increased with the addition of more co-solute. The value of D/D_0 is seen to remain more or less constant with the changing co-solute concentrations indicating that the diffusion speed of the entities in the sample remains fairly similar throughout.

8.3.3 Protein stability upon dilution of dispersions

To ensure that the α -CGN was maintained through the process of dispersion preparation and in the dispersion itself, the diluted α -CGN was tested for enzymatic activity, T_m and aggregation. As shown in Fig. 8.5a, the enzymatic activity of the protein upon dilution remains low and is comparable to that of the dilute solution controls. α -CGN typically contains small amount of trypsin as an impurity which may activate the α -CGN thereby raising the enzymatic activity. The retention of low viscosity indicates that the trypsin degradation is not enhanced at the high protein concentration in the formulations. Also, to test for protein degradation which can occur due to the trypsin impurity, diluted proteins were tested with SDS-PAGE as shown in Fig. 8.5b. SDS-PAGE showed little change in protein structure from the formation of the high co-solute formulations. To further ensure protein stability the melting temperature (T_m) was

measured for the diluted dispersions and dilute solution controls as shown in Fig. 8.5 with the result seemingly unchanged indicating that the high co-solute concentrations are capable of stabilizing α -CGN at high concentration.

8.4 DISCUSSION

8.4.1 Arginine interactions with α -CGN

α -CGN has low solubility at pH values greater than 4 with studies typically using sodium citrate buffers at a pH around 3.¹⁻⁴ The isoelectric point of α -CGN is 9.2 as a result of which, α -CGN has a low net charge at near neutral pH on proteins. The low charge may affect the ability of α -CGN to dissolve in water due to lowered colloidal stability stemming from the lowered electrostatic repulsion. α -CGN has prominent charged patches with one half of the protein being predominantly negatively charged while the other half is positively charged as shown in Fig. 8.6. Therefore, closer to the isoelectric point α -CGN molecules may align with the oppositely charged patches near each other due to their mutual attraction possibly leading to the overall protein-protein interactions being attractive especially at high concentration. The attractive forces in the previous hypothesis are analogous to the attraction seen from alignment of charged patches for BSA and mAbs.^{5-7,14} If α -CGN is similarly aligned when in the lyophilized powder state it was obtained in, it may be very stable in the lyophilized powder and resist solubilization.

Arginine consists of four main functional groups, namely, the guanidyl group, the alkyl chain, the carboxyl and amino groups. All of these various parts of α -CGN interact on the basis of very different forces with species having very different structures.

Arginine can bind to polar or charged groups on amino acid residues on α -CGN through hydrogen bonding. Hydrogen bonding can occur through either the guanidyl group, amino group or the carboxyl group on arginine.³⁵⁻³⁷ At or near neutral pH, a high fraction of arginine is positively charged as all the three functional groups mentioned above are charged being more than 2 units away from their respective pK_a s. Therefore, arginine binding to protein leads to the protein charge distribution changing as the negatively charged patches will be neutralized by positively charged arginine. The magnitude of positive charge on the positively charged patches will increase. The result would be that the protein-protein attractive interactions through charged patches on the proteins aligning would be much weakened. The increased net charge on proteins would also lead to the protein-protein interactions becoming more repulsive from electrostatic repulsion between the molecules.

The guanidyl group is the most strongly interacting group part of the arginine molecule and is usually in its protonated cation form at all pH values under consideration. The guanidyl group is present in guanidium chloride (Gdn.HCl) as the guanidium cation which is a strong base (pK_a 13.6). Gdn.HCl is known to denature proteins at high concentrations ($>5M$) through interactions with the backbone of proteins.³⁸ The guanidine group stabilizes the hydrophobic patches which are contained in the protein backbone and are usually concealed in the interior of proteins.^{38,39} As a result protein structure is disrupted into an unfolded non-native state by binding of guanidine to the protein backbone. However, arginine binding is weaker compared to guanidine binding due to the carboxylic acid group present in arginine.^{40,41} The lowered degree of binding prevents arginine from disrupting the protein structure although some arginine is still bound to hydrophobic patches on proteins due to the guanidyl group. Additionally,

simulation studies have shown that at high concentrations of arginine.HCl, arginine ions tend to stack on top of each other forming a stack of three molecules. The alkyl chains stay next to each other creating a hydrophobic surface which is capable of interacting with the hydrophobic patches on proteins making them more hydrophilic. The reduction in interactions between proteins as an effect of the addition of arginine⁴² has been observed through studies of the second virial coefficient or the attractive potential between proteins by various methods including self-interaction chromatography.^{37,43} Similar effects of lowered interactions are also seen in reduced binding of proteins to hydrophobic and ion-exchange resins due to addition of arginine to the protein sample.^{44,45}

Glutamic acid also interacts with proteins through hydrogen bonding although it has only been studied in conjugation with arginine so that its independent effects are unknown. When used with arginine, glutamic acid increases the effectiveness of arginine in reducing intermolecular interactions through some synergistic effect which is not fully understood.^{36,43} The interaction of arginine and glutamic acid mixtures with proteins can also serve to solubilize proteins through modification of interactions.⁴⁶ There may be a minimum number of sites that need to be blocked by arginine for enabling solubilization of proteins. The phenomenon of a minimum amount of arginine being needed to solubilize protein which has been observed experimentally in this Chapter may be explained by the above hypothesis. Similarly for low pH formulations, the amount of arginine contained in the sample may be too low for effective solubilization since the lower pH samples have a lower arginine concentration required for keeping the pH lower. The lowered interactions due to the addition of arginine can also lower the viscosity of the protein formulation as demonstrated for mAbs, and human or bovine gamma-

globulin.⁴⁷ The viscosities of α -CGN samples containing high arginine are observed to be very low ranging from 5-10 cP at ~250 mg/ml. There is no good way for comparing these viscosities with those for a low co-solute sample since α -CGN is not soluble at similarly high concentrations. The inherent viscosity and the actual viscosity are observed to be low nearer to the isoelectric point. Although, the net charge on proteins is lowest at the isoelectric point, the absolute number of charges on proteins is the highest. Therefore, the number of binding sites for arginine is the highest. The higher amount arginine bound to proteins may allow for more positive charge on proteins and therefore more net repulsive interactions between proteins. The more repulsive the interactions between proteins, the lower is the viscosity as seen by studies of the diffusion interaction parameter (k_D) or the second virial coefficient (B_2) for mAbs.^{19,48} Therefore the elevated arginine binding may be responsible for the comparatively lower viscosities at or near the isoelectric point.

8.4.2 Trehalose interactions with α -CGN

Contrary to arginine and glutamic acid which interact strongly with proteins, trehalose does not interact specifically with proteins. Trehalose is preferentially excluded from the surface of proteins due to preferential hydration.^{27,28} The preferential exclusion causes proteins to attempt to reduce their surface area thus forcing proteins to remain in a more compact state.²⁷ While trehalose has a stabilizing effect on proteins, it has not been shown to contribute to protein solubilization. Also, trehalose does not have a significant effect on viscosity as can be seen by comparing the inherent viscosity of samples with and without trehalose. The actual viscosity increases due to the elevated solvent viscosity as a result of the higher solute content in the liquid. The viscosity being unaffected is expected because the specific protein-protein interactions are not much affected by the

addition of trehalose as explained earlier. Therefore the depletion attraction may play some role in α -CGN solubilization, but it is likely a minor role although it probably is involved in stabilizing proteins. Arginine and glutamic acid are large enough to have a similar osmotic compression effect as trehalose and could also provide this stabilizing effect.⁴²

8.4.3 Stability of α -CGN in high concentration protein formulations with high co-solute concentrations

α -CGN is activated by reacting with trypsin which is another enzyme and removes two peptides consisting of 3 amino acids each from α -CGN to convert it into α -CT. The α -CT is the active digestive enzyme which is responsible for the enzymatic activity with α -CGN not having any enzymatic activity. Therefore increased enzymatic activity indicates that more of the α -CGN molecules are converted to α -CT and the reduced activity from the addition of arginine and glutamic acid indicates that α -CGN is stabilized in its inactive form by the addition of the co-solutes despite the high concentration. The activated protein (α -CT) can be distinguished from the inactive form (α -CGN) by SDS-PAGE because the inactive form consisting of three peptide chains connected by disulfide bonds splits into three smaller parts while the inactive protein remains in one piece. Since there is no change in the SDS-PAGE properties between the high co-solute and high protein concentration samples when compared to the low concentration protein samples. Arginine may bind to α -CGN on the activation peptides since the activation peptides consist exclusively of polar or charged amino acids which tend to heavily favor arginine binding.^{42,49} Therefore, the trypsin binding to the site will be affected due to modified charge in the binding region in addition to changing the

shape of the binding site preventing the activation peptides from being excised by trypsin. Additionally, the osmotic compression may compact the protein molecules into conformations where the activation peptides are not easily accessible to the trypsin for reacting.

8.4.4 Origin of lowered D/D_0 high concentration protein formulations with high co-solute concentrations

An alternate reason for the observed changes in the properties of α -CGN could be the formation of nanoclusters. Previously, in systems with concentrated protein and trehalose molecules formation of nanoclusters assembled from proteins was observed using dynamic light scattering.^{22,23,50} It was hypothesized that proteins were pushed together by depletion attraction due to the co-solute/crowder molecules with the cluster size being limited by the net repulsion between the protein molecules. Analogously, arginine and glutamic acid may provide depletion attraction to assemble these clusters either through micro-phase separation or formation of a structure of associated proteins that diffuse together. The structure of these nanostructures of proteins however would be more complicated than the previous studies due to the presence of charged depletants instead of neutral species. The associated motion, nanostructuring or micro-phase formation would explain the reduction in D/D_0 observed for all the samples containing high co-solute concentrations. The micro-phase separation may also help to keep the α -CGN dispersed in water without actually dissolving in water as it is in its own micro-phase, thus eliminating the need for elevated solubility for forming a high concentration formulation. Also the nanostructures were hypothesized to have more repulsive and weaker interactions due to the greater separation between them and the cumulative charge

on the protein molecules contained within them which can lead to a reduction in viscosity.^{22,23} The nanostructures may also limit access to α -CGN molecules contained inside the nanostructure for the trypsin simply through lack of unoccupied space around the protein. As a result, the ability of trypsin to degrade the α -CGN can be limited explaining the continued lower enzyme activity of the α -CGN samples with high co-solute.

8.5 CONCLUSIONS

α -CGN was solubilized at concentrations exceeding 200 mg/ml using a mixture of co-solutes, namely arginine and glutamic acid, as solubilization agents. The solubilizing effect of arginine and glutamic acid was probably through their ability to reduce both the hydrophobic and electrostatic attractions between proteins which may stabilize proteins in the aqueous environment. Arginine can also bind to the charged patches on proteins through hydrogen bonding and with the hydrophobic patches through the guanidyl group making them more hydrophilic thus easing their ability to disperse in water. At least 100 mg/ml total of arginine and glutamic acid was required to ensure the formation of clear dispersions devoid of any turbidity from undissolved protein present in the system. Similarly a sample pH above 7 is necessary for proteins to be dispersed in the solvent without any turbidity present because at lower pH the fraction of arginine in the co-solute mixture is too low leading to lower total arginine concentration. Samples with high amounts of arginine and glutamic acid as excipients in them also exhibit low viscosities ranging from 10-15 cP at 200-250 mg/ml α -CGN probably as a result of the reduced interactions resulting from the added co-solutes. The addition of trehalose does not affect the inherent viscosity although the overall solution viscosity is increased due to

increased solvent viscosity. Also, the arginine and glutamic acid reduce the measured diffusion coefficient of the species in the sample to 16-25% of the monomer diffusion coefficient. This may indicate the presence of larger associated species composed of proteins i.e. nanoclusters in the sample. The addition of arginine and glutamic acid also seems to preserve the protein structure for high co-solute samples.

Protein conc (mg/ml)	Arg Conc (mg/ml)	Glu Conc (mg/ml)	pH	Viscosity (cP)	st dev in visc (cP)	Solvent Visc (cP)	Inherent visc (ml/mg)	D/D_0	Turbid
240	50	50	4.54	6	1.2	1.35	0.0059	-	Y
207	55.6	44.4	5.35	5	0.4	1.35	0.0062	-	Y
264	60	40	7.43	10	1.0	1.35	0.0074	0.23	N
228	66.7	33.3	8.44	4	0.3	1.35	0.0043	0.17	N
258	80	20	9.13	5	0.2	1.35	0.0053	0.16	N
234	100		9.99	5	0.8	1.35	0.0056	0.19	N

Table 8.1: pH does not greatly affect the viscosity, but low pH dispersion are turbid and there seems to be a maximum in the size around pH 9 which is the isoelectric point.

Protein conc (mg/ml)	Arg Conc (mg/ml)	Glu Conc (mg/ml)	pH	Viscosity (cP)	st dev in visc (cP)	Solvent Visc (cP)	Inherent visc (ml/mg)	D/D_0
228	66.7	33.3	8.44	4	0.3	1.35	0.0043	0.17
231	100	50	8.56	5	0.4	1.5	0.0050	0.21
212	133.3	66.7	8.58	8	0.4	1.9	0.0066	0.18
258	80	20	9.13	5	0.2	1.35	0.0052	0.16
224	120	30	9.10	6	0.3	1.5	0.0059	0.2
224	160	40	9.18	10	1.9	1.9	0.0074	0.17

Table 8.2: Increased arginine and glutamic acid concentrations at pH 8.5 and pH 9 which is the optimized pH range for low viscosity results in increased viscosity but no change in cluster size.

Protein conc (mg/ml)	Arg Conc (mg/ml)	Glu Conc (mg/ml)	Tre Conc (mg/ml)	pH	Viscosity (cP)	st dev in visc (cP)	Solvent Visc (cP)	Inherent visc (ml/mg)	D/D_0
225	60	40	0	7.2	6	0.2	1.35	0.0064	0.27
228	60	40	50	7.0	10	1.4	1.5	0.0072	0.20
242	60	40	100	7.0	10	0.6	1.65	0.0076	0.15
221	60	40	150	7.0	11	0.7	1.8	0.0080	0.15
252	60	40	200	7.3	15	0.2	2	0.0080	0.14
236	60	40	250	7.3	25	1.8	2.2	0.0104	0.11

Table 8.3: Effect of increased trehalose concentration on viscosity and cluster size of α -CGN. Increased trehalose concentration does not significantly increase the dispersion inherent viscosity. Increased solvent viscosity causes the dispersion viscosity to increase. The cluster size increases with increased trehalose concentration.

Protein conc (mg/ml)	Arg Conc (mg/ml)	Glu Conc (mg/ml)	Tre Conc (mg/ml)	pH	Viscosity (cP)	st dev in visc (cP)	Solvent Visc (cP)	Inherent visc (ml/mg)	D/D_0
238	60	40	50	7.5	7	0.1	1.5	0.0064	0.23
224	90	60	50	7.5	9	0.6	1.9	0.0067	0.28
223	120	80	50	7.5	17	0.2	2.4	0.0086	0.28

Table 8.4: Dispersion viscosities for samples from Fig. 8.3 showing very low viscosities for α -CGN dispersions. The inherent viscosity increases with the concentration of arginine and glutamic acid. For lower concentrations though, the α -CGN is in the form of very large particles as evidenced by the turbidity. Cluster size does not change greatly.

Formulations	Average T_m	St. Dev. in T_m
chymo pH 3.8 free	65.6	0.3
chymo pH 8.2 free	65.1	0.8
chymo pH 8.2 disp free	66.1	0.7

Table 8.5: T_m data for the α -CGN dispersions and dilute solution controls.

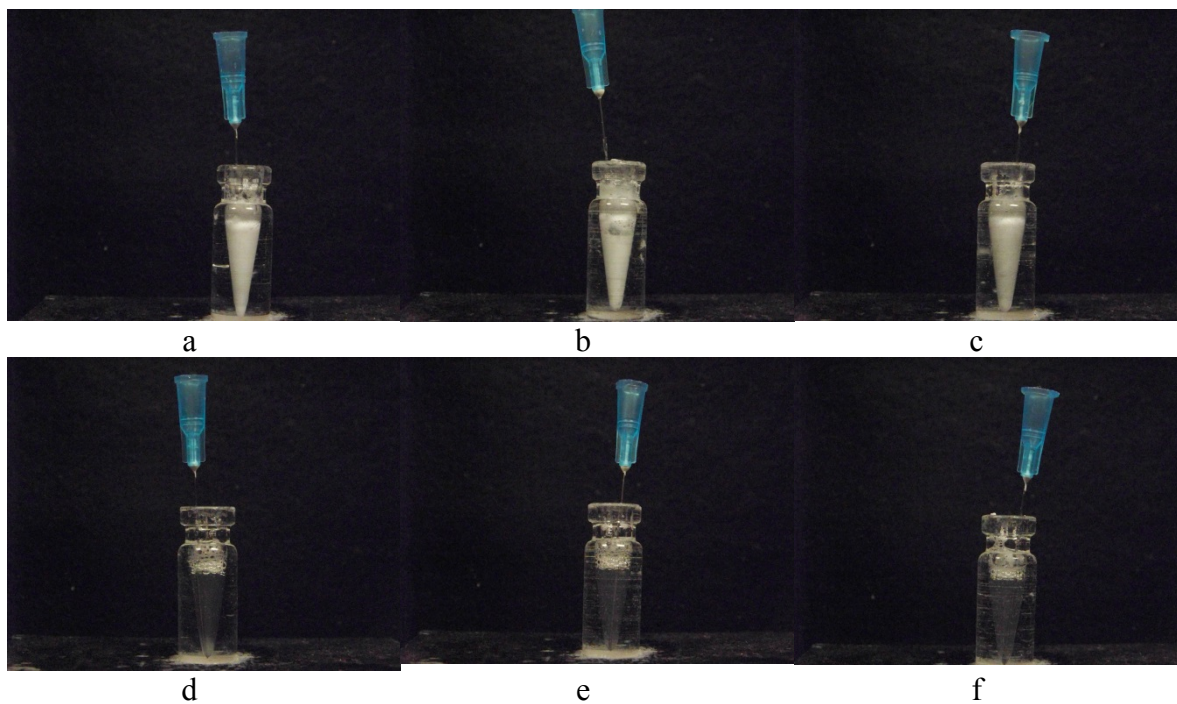


Figure 8.1: Increasing concentration of arg+glu in α -CGN dispersions leads to improved dispersibility of α -CGN. α -CGN concentration in each case was targeted to be 250 mg/ml. Arg+glu concentrations are a. 0 mg/ml, b. 25 mg/ml, c. 50 mg/ml, d. 100 mg/ml, e. 150 mg/ml and f. 200 mg/ml. As can be seen the solutions with low arg+glu are turbid while those with higher arg+glu are clear.

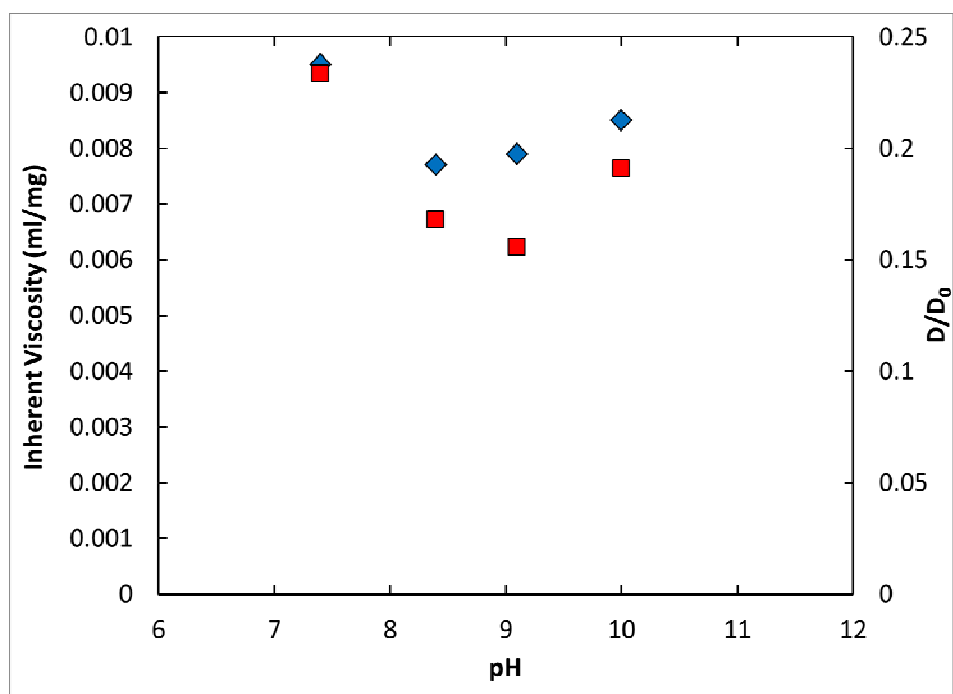


Figure 8.2: Dispersion viscosities for samples from Table 8.1 showing very low inherent viscosities for α -CGN dispersions. The inherent viscosity (blue diamonds) is lowest around pH 8-8.5 while the D/D_0 ratio (red squares) is also minimum at around pH 9.

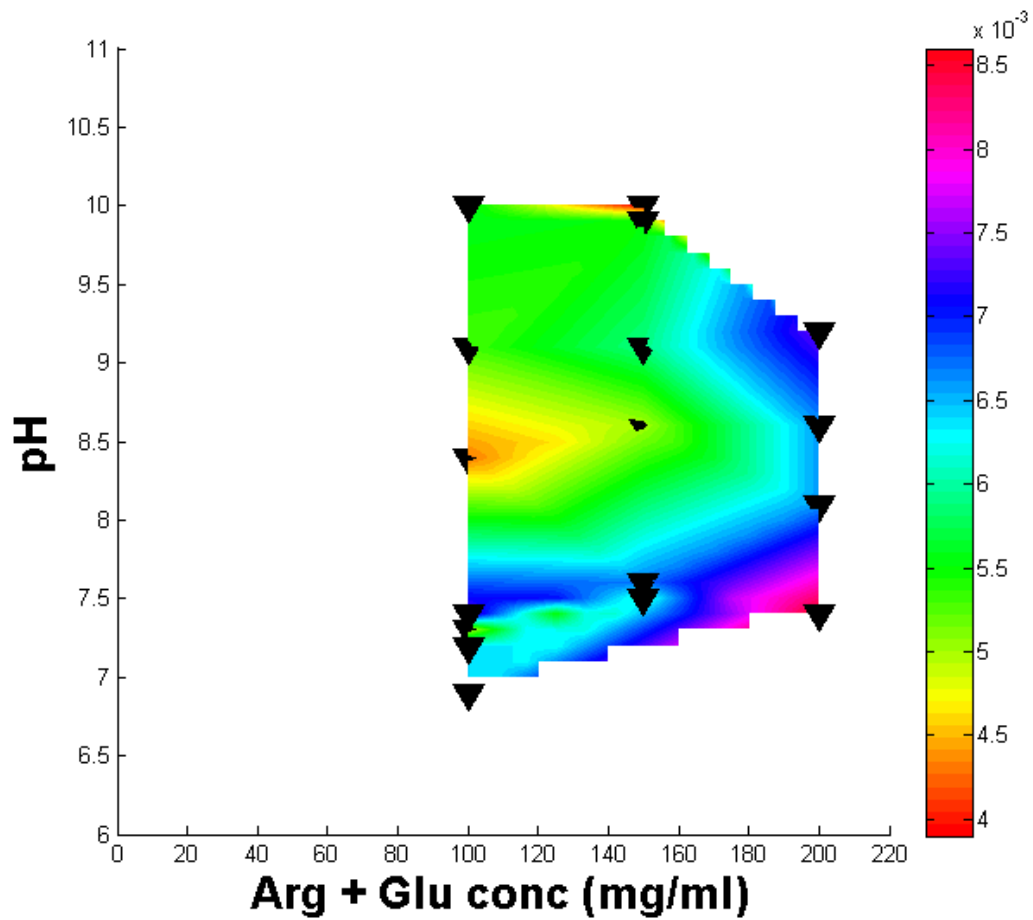


Figure 8.3: Inherent viscosity has a minimum at around pH 8-8.5 and an optimum for arg+glu conc of 100 mg/ml. Space that can be explored is limited by the solubility of the excipients.

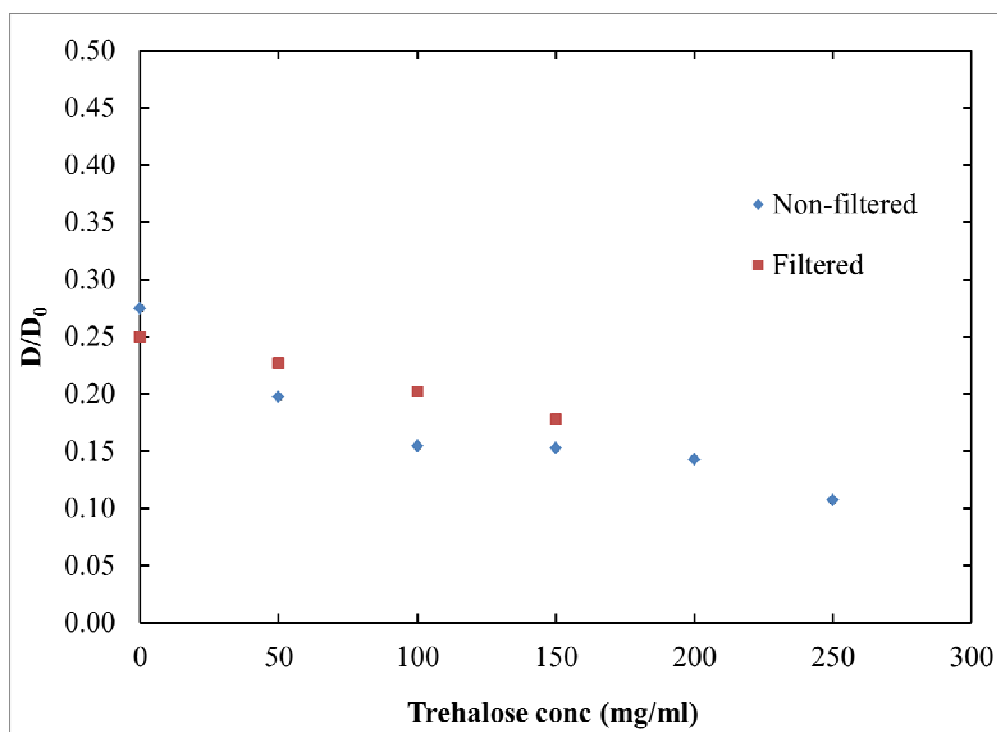
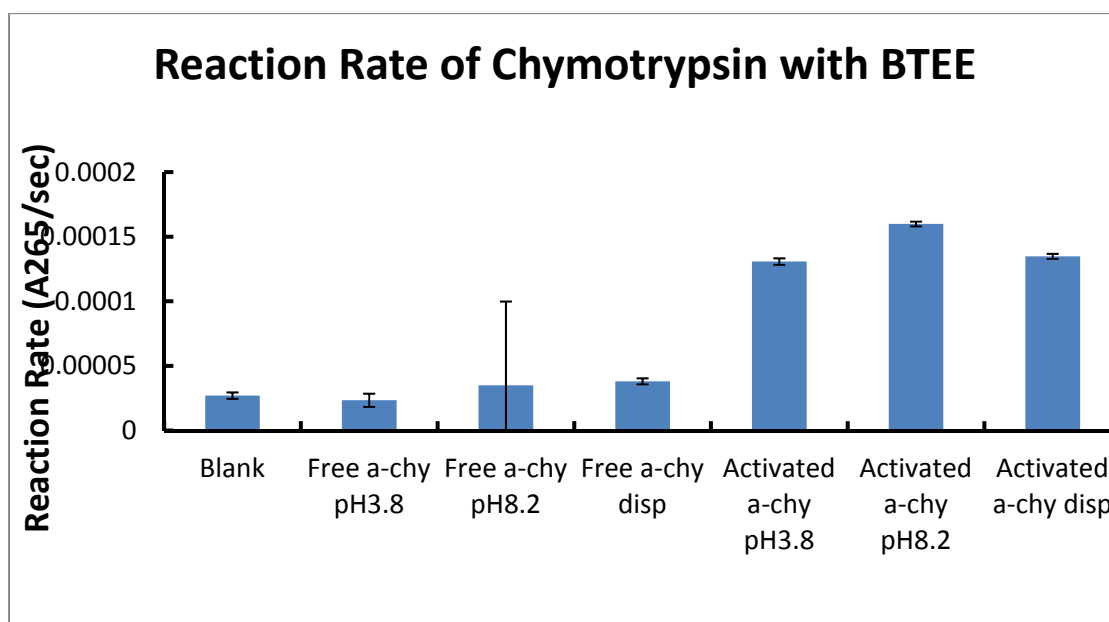
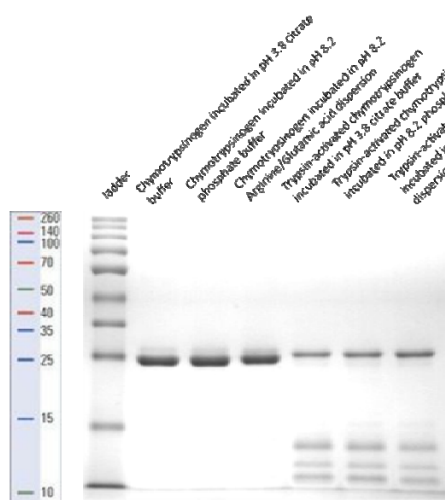


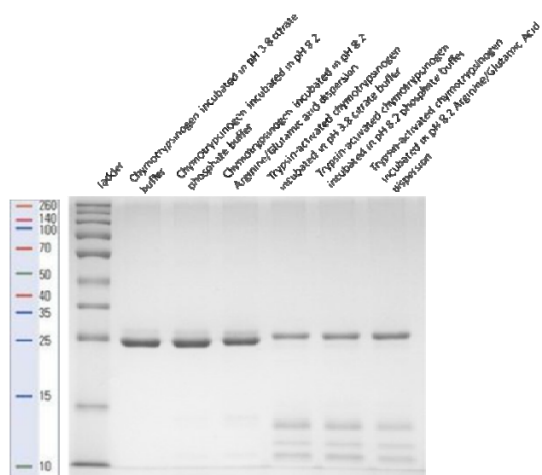
Figure 8.4: Sterile filtration of the clusters by centrifugal filtration does not significantly affect the D/D_0 .



a



b



c

(Fig. 8.5 continued on the next page)

Figure 8.5: a. Reaction rate of diluted α -CGN dispersions compared to dilute solution controls along with that for protein activated with trypsin. b. SDS-PAGE gel under reducing conditions and c. SDS-PAGE gel under non-reducing conditions for analysis of aggregates and degradants for α -CGN dispersions compared to dilute solution controls along with that for protein activated with trypsin

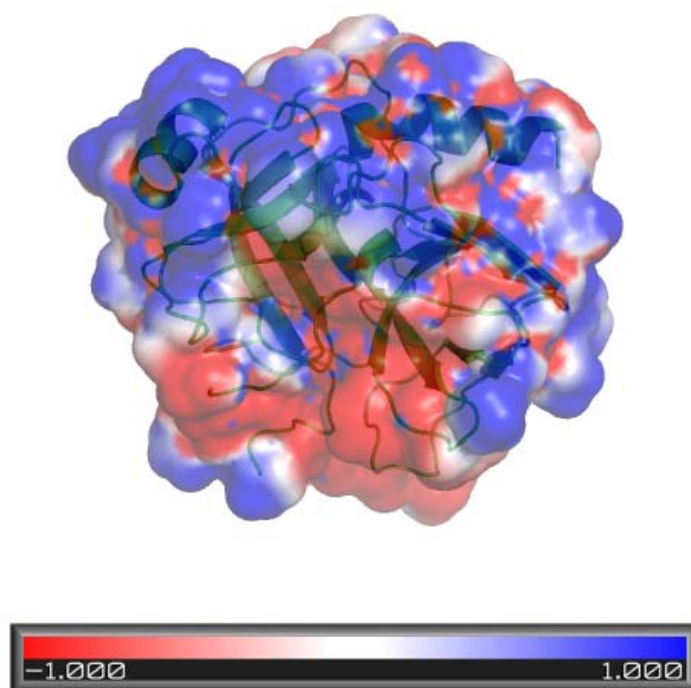


Figure 8.6: Electrostatic charge map of α -CGN shows distinct charged patches. The surface is drawn where the electrostatic repulsion is ± 1 kT with red being negative charge and blue being positive charge.

8.6 REFERENCES

- (1) Weiss, W. F. t.; Hodgdon, T. K.; Kaler, E. W.; Lenhoff, A. M.; Roberts, C. J. *Biophys J* 2007, 93, 4392.
- (2) Blanco, M. A.; Perevozchikova, T.; Martorana, V.; Manno, M.; Roberts, C. J. *J Phys Chem B* 2014, 118, 5817.

- (3) Kroetsch, A. M.; Sahin, E.; Wang, H. Y.; Krizman, S.; Roberts, C. J. *J Pharm Sci* 2012, 101, 3651.
- (4) Andrews, J. M.; Roberts, C. J. *Biochemistry* 2007, 46, 7558.
- (5) Yadav, S.; Liu, J.; Shire, S. J.; Kalonia, D. S. *J Pharm Sci* 2010, 99, 1152.
- (6) Yadav, S.; Shire, S. J.; Kalonia, D. S. *Pharm. Res.* 2011, 28, 1973.
- (7) Yadav, S.; Shire, S. J.; Kalonia, D. S. *J Pharm Sci* 2012, 101, 998.
- (8) Roberts, C. J.; Blanco, M. A. *J Phys Chem B* 2014.
- (9) Sule, S. V.; Cheung, J. K.; Antochshuk, V.; Bhalla, A. S.; Narasimhan, C.; Blaisdell, S.; Shameem, M.; Tessier, P. M. *Mol Pharm* 2012, 9, 744.
- (10) Saluja, A.; Kalonia, D. S. *International Journal of Pharmaceutics* 2008, 358, 1.
- (11) Kanai, S.; Liu, J.; Patapoff, T. W.; Shire, S. J. *J Pharm Sci* 2008, 97, 4219.
- (12) Du, W.; Klibanov, A. M. *Biotechnol Bioeng* 2011, 108, 632.
- (13) Zaccarelli, E. *J Phys: Condens. Matter* 2007, 19, 323101.
- (14) Zarraga, I. E.; Taing, R.; Zarzar, J.; Luoma, J.; Hsiung, J.; Patel, A.; Lim, F. J. *J Pharm Sci* 2013, 102, 2538.
- (15) Baglioni, P.; Fratini, E.; Lonetti, B.; Chen, S. H. *Journal of Physics: Condensed Matter* 2004, 16, S5003.
- (16) Burckbuchler, V.; Mekhloufi, G.; Giteau, A. P.; Grossiord, J. L.; Huille, S.; Agnely, F. *Eur J Pharm Biopharm* 2010, 76, 351.
- (17) Castellanos, M. M.; Pathak, J. A.; Colby, R. H. *Soft Matter* 2014, 10, 122.
- (18) Castellanos, M. M.; Pathak, J. A.; Leach, W.; Bishop, S. M.; Colby, R. H. *Biophys J* 2014, 107, 469.
- (19) Connolly, B. D.; Petry, C.; Yadav, S.; Demeule, B.; Ciaccio, N.; Moore, J. M.; Shire, S. J.; Gokarn, Y. R. *Biophys J* 2012, 103, 69.
- (20) Srinivasan, C.; Weight, A. K.; Bussemer, T.; Klibanov, A. M. *Pharm. Res.* 2013, 30, 1749.
- (21) Johnson, H. R.; Lenhoff, A. M. *Mol Pharm* 2013, 10, 3582.
- (22) Johnston, K. P.; Maynard, J. A.; Truskett, T. M.; Borwankar, A.; Miller, M. A.; Wilson, B.; Dinin, A. K.; Khan, T. A.; Kaczorowski, K. J. *ACS Nano* 2012.
- (23) Borwankar, A. U.; Dinin, A. K.; Laber, J. R.; Twu, A.; Wilson, B. K.; Maynard, J. A.; Truskett, T. M.; Johnston, K. P. *Soft Matter* 2013, 9, 1766.

- (24) Miller, M. A.; Khan, T. A.; Kaczorowski, K. J.; Wilson, B. K.; Dinin, A. K.; Borwankar, A. U.; Rodrigues, M. A.; Truskett, T. M.; Johnston, K. P.; Maynard, J. A. *J Pharm Sci* 2012, 101, 3763.
- (25) Shen, V. K.; Cheung, J. K.; Errington, J. R.; Truskett, T. M. *Journal of biomechanical engineering* 2009, 131, 071002.
- (26) Cheung, J. K.; Truskett, T. M. *Biophys J* 2005, 89, 2372.
- (27) Lee, J. C.; Timasheff, S. N. *Journal of Biological Chemistry* 1981, 256, 7193.
- (28) Kreilgaard, L.; Frokjaer, S.; Flink, J. M.; Randolph, T. W.; Carpenter, J. F. *J Pharm Sci* 1999, 88, 281.
- (29) Li, Y.; Lubchenko, V.; Vekilov, P. G. *Rev Sci Instrum* 2011, 82, 053106.
- (30) Pan, W. C.; Vekilov, P. G.; Lubchenko, V. J. *Phys. Chem. B* 2010, 114, 7620.
- (31) Soraruf, D.; Roosen-Runge, F.; Grimaldo, M.; Zanini, F.; Schweins, R.; Seydel, T.; Zhang, F.; Roth, R.; Oettel, M.; Schreiber, F. *Soft Matter* 2014, 10, 894.
- (32) W, R. *Methods of Enzymatic Analysis*; 2nd ed.; Academic Press Inc., 1974.
- (33) Pertzoff, V. A. *Journal of Biological Chemistry* 1933, 100, 97.
- (34) Windholz, M.; Editor *The Merck Index: An Encyclopedia of Chemicals and Drugs*. 9th Ed; Merck and Co., Publ. Dept., 1976.
- (35) Shukla, D.; Trout, B. L. *J Phys Chem B* 2011, 115, 1243.
- (36) Shukla, D.; Schneider, C. P.; Trout, B. L. *Adv Drug Deliv Rev* 2011, 63, 1074.
- (37) Scherer, T. M. *J Phys Chem B* 2013, 117, 2254.
- (38) Liu, W.; Cellmer, T.; Keerl, D.; Prausnitz, J. M.; Blanch, H. W. *Biotechnol Bioeng* 2005, 90, 482.
- (39) Chi, E. Y.; Krishnan, S.; Kendrick, B. S.; Chang, B. S.; Carpenter, J. F.; Randolph, T. W. *Protein Science* 2003, 12, 903.
- (40) Shukla, D.; Trout, B. L. *The Journal of Physical Chemistry B* 2010, 114, 13426.
- (41) Vagenende, V.; Han, A. X.; Mueller, M.; Trout, B. L. *ACS Chem Biol* 2013, 8, 416.

- (42) Arakawa, T.; Ejima, D.; Tsumoto, K.; Obeyama, N.; Tanaka, Y.; Kita, Y.; Timasheff, S. N. *Biophys Chem* 2007, 127, 1.
- (43) Valente, J. J.; Verma, K. S.; Manning, M. C.; Wilson, W. W.; Henry, C. S. *Biophys J* 2005, 89, 4211.
- (44) Hou, Y.; Cramer, S. M. *J Chromatogr A* 2011, 1218, 7813.
- (45) Holstein, M. A.; Parimal, S.; McCallum, S. A.; Cramer, S. M. *Biotechnol Bioeng* 2012, 109, 176.
- (46) Vondrášek, J.; Mason, P. E.; Heyda, J.; Collins, K. D.; Jungwirth, P. *The Journal of Physical Chemistry B* 2009, 113, 9041.
- (47) Inoue, N.; Takai, E.; Arakawa, T.; Shiraki, K. *Mol Pharm* 2014, 11, 1889.
- (48) Saito, S.; Hasegawa, J.; Kobayashi, N.; Kishi, N.; Uchiyama, S.; Fukui, K. *Pharm. Res.* 2012, 29, 397.
- (49) Hartley, B. S. *Nature* 1964, 201, 1284.
- (50) Groenewold, J.; Kegel, W. K. *J. Phys. Chem. B* 2001, 105, 11702.

Chapter 9: Conclusions and Recommendations

9.1 CONCLUSIONS

9.1.1 Modification of Protein-protein Interactions for Reducing Viscosity

The viscosity of mAb formulations containing high concentrations of arginine along with either glutamic acid or HCl was demonstrated to be 5-6 times lower than that for mAb solutions in buffer with low levels of co-solutes at protein concentrations ranging from 200 to 250 mg/ml. Arginine modifies the protein surface charge distribution through binding to charged sites which will result in modification of both localized and net electrostatic interactions. Additionally arginine also binds to the hydrophobic sites on proteins making them more hydrophilic. Arginine and glutamic acid therefore reduce both hydrophobic and electrostatic interactions for mAbs.¹⁻³ The reduced interactions may be the reason for the lowered viscosity since attractive protein-protein interactions are usually the main reason for elevated viscosity.^{4,5} The co-solutes in addition to binding to sites on proteins can cause osmotic compression of mAbs due to entropy maximization of co-solutes which could potentially stabilize the mAb structure and limit aggregation arising from protein unfolding. Additionally, the co-solutes can give rise to depletion attraction between mAbs which when coupled with the longer ranged electrostatic repulsion can potentially form mAb nanoclusters or locally concentrated regions of mAbs. Introducing depletion attraction by itself seems to have little effect on viscosity since samples with trehalose alone as a co-solute do not have a lower viscosity than the low co-solute controls. The % monomer detected by SEC after dilution remains constant even after storage of the high co-solute formulations for up to 8 weeks in the concentrated state thus providing evidence that the high co-solute concentration has the ability to limit mAb aggregation at high mAb concentrations.

The same strategy of using high co-solute concentration formulations was applied to solubilize α -CGN at concentrations exceeding 200 mg/ml using the same mixture of co-solutes, namely arginine and glutamic acid. The solubilizing effect of arginine and glutamic acid was probably due to their ability to reduce both hydrophobic and electrostatic attractions between proteins which potentially stabilizes them in aqueous media. At least 100 mg/ml total of arginine and glutamic acid was required to ensure the formation of clear dispersions devoid of any turbidity arising from undissolved α -CGN present in the formulation. Similarly the sample pH needs to be above 7 for α -CGN to be dispersed without any turbidity present because at lower pH the fraction of arginine in the co-solute mixture is lower and therefore its concentration may be insufficient for solubilization. Samples with high amounts of arginine and glutamic acid as co-solutes also exhibit low viscosities ranging from 10-15 cP at 200-250 mg/ml α -CGN. The reduction in viscosity is probably a result of the aforementioned reduced interactions although there isn't a good control for comparison since α -CGN is otherwise insoluble at these high concentrations. The addition of trehalose as a co-solute along with arginine and glutamic acid does not affect the inherent viscosity of formulations although the overall solution viscosity is increased as a result of higher solvent viscosity. Also, the addition of arginine and glutamic acid reduces the measured diffusion coefficient of species in the formulation to 16-25% of the monomer diffusion coefficient. Similar to mAb1, this may indicate the presence of larger associated species composed of proteins i.e. nanoclusters in the sample. The addition of arginine and glutamic acid also seems to preserve protein stability as evident from the T_m and enzymatic activity studies.

9.1.2 Characterization of Nanostructure Formation and Dissociation by Orthogonal Techniques

The diffusion coefficient as measured by DLS was seen to decrease significantly in the high co-solute concentration samples compared to the monomer diffusion coefficient measured at low protein concentration. Even at high protein concentrations of 200-250 mg/ml, low co-solute samples did not display any decrease in their diffusion coefficient. Based on this, the high co-solute samples were assumed to contain large nanoclusters comprising of multiple proteins. The size of these nanoclusters was determined from the measured diffusion coefficient by using the Stokes-Einstein equation. This theorized nanocluster size was seen to be tunable by adjusting both protein and co-solute concentrations as supported by a free energy model. The model proposed the formation of nanoclusters through a balance of the short ranged depletion attraction and the long ranged electrostatic repulsion to give a limiting nanocluster size. The model also raised the possibility of simultaneously making nanoclusters while maintaining a low viscosity based on multi-scale interactions with attraction dominant at protein monomer level and repulsion dominant at the intercluster level for lowering viscosity. The formulations with high co-solute concentration could be made by multiple techniques including dissolution of lyophilized protein in addition to centrifugal filtration. The trend of lowered diffusion rates was seen in all samples independent of the method of sample preparation and was again interpreted as the formation of larger structures.

Both the high and low co-solute protein formulations were examined by SAXS and cryo-SEM to validate the formation of nanostructures which was hypothesized based on the DLS data. The high co-solute formulations have significantly higher intensity of scattering at lower q ranges corresponding to bigger sizes which can be seen more clearly in the structure factor plots. Based on these profiles, the high co-solute formulations seem

to contain structures on the ~50 nm size scale. In contrast, the low co-solute formulation had a prominent peak at ~15 nm close to the size of the monomer and no significant features at bigger sizes. The high co-solute formulations also show the characteristic peak seen in the concentrated low co-solute monomer formulations at around 15 nm, although it is shifted to lower scattering vectors and depressed in intensity which indicates modified interactions and structure compared to the monomer. Nanostructures ranging from 50-80 nm, much larger than monomeric protein, were also observed by cryo-SEM in multiple mAb formulations with high co-solute concentrations and different co-solute compositions. As a control, samples with low co-solute concentration in addition to the high co-solute concentration buffer without protein were both imaged and showed no evidence of these larger species in their cryo-SEM micrographs. The measured sizes from cryo-SEM and SAXS are in some agreement with each other for samples with the same composition and with the measured D/D_0 for these samples by DLS.

The formation of these nanostructures in the high co-solute formulations could be responsible for lowering the viscosity of the high excipient samples through modification of the interactions present between the protein monomers in the system. It was hypothesized that the high degree of self-crowding of proteins within the nanoclusters at an unusually high concentration of 700 mg/ml would favor protein folding as was shown theoretically.^{6,7} Experimental analysis with a variety of physical, chemical and biological assays indicated that conformationally stable and active protein monomer was obtained after dilution of the high co-solute formulations. In vivo sub-cutaneous administration of a high co-solute formulation of mAb 1B7 resulted in the same amount of active protein being delivered in the bloodstream as that by intravenous delivery of a dilute mAb solution.

9.1.3 Synthesis of Au Nanoclusters with High NIR Extinction and Controlled Morphology

The growth of a high density of points on a nanocluster core substrate results in the formation of particles with high NIR extinction up to wavelengths of 1100 nm, while maintaining a small diameter of ~ 60 nm. Initially ~ 30 nm Au nanoclusters consisting of ~ 10 nm primary Au nanoparticles were synthesized which then rapidly evolved into more complex geometries. At pH 8.7 and 7.5 in a kinetically controlled regime, the aforementioned points grew on the nanocluster core thereby maintaining the asymmetry and therefore the high NIR extinction. The kinetically controlled regime can avoid relaxation to spheres seen in the more thermodynamically controlled slow growth regime at a higher pH of 9.3. The large number of primary particles per cluster results in a greater number of reactive sites being available for growth of the points, relative to the case of a monolithic core. The high NIR extinction results from the close proximity between primary particles in the initial nanocluster cores, the high density of points on the cores, and the high point length to primary particle diameter aspect ratio. In contrast, much larger points are required for nanoparticles with spherical or monolithic cores (e.g. nanostars) to achieve the same level of NIR extinction usually resulting in much larger particles. This strong NIR extinction obtained for a small particle is of great interest in biomedical imaging including photoacoustic imaging and photothermal therapy.

9.2 RECOMMENDATIONS AND FUTURE RESEARCH

9.2.1 Improvements in the Methods of Nanostructure Size Determination and study of morphology

The size of the nanoclusters has been measured by several different techniques with reasonable agreement obtained between them. However, none of these techniques are capable of determining the fraction of protein contained in nanoclusters versus that present in the monomeric state. Therefore there is an outstanding possibility that a significant fraction of protein may be present in the monomeric state similar to the trend seen for clusters of lysozyme.⁸⁻¹¹ Better modelling of SAXS profiles could be done to extract additional information from the SAXS profile to provide some of this missing information about the nanoclusters. The model could also be extended to improve upon the free energy model proposed in this dissertation which is a fairly rudimentary hard sphere based model. Additionally, more exploration with newer techniques will be required to figure out the fraction of protein that is present in the monomeric state and could be done by: 1. Cross-linking of proteins within the nanocluster, 2. Neutron spin echo (NSE) measurements, and 3. Förster resonance energy transfer (FRET).

There are well established protocols for cross-linking of proteins which is typically used for fixing cells prior to imaging. A dialdehyde can be used to link proteins together via the free amino groups present on surface exposed lysine residues in proteins. The aim of this proposed idea is to covalently link together proteins in a nanocluster to each other by means of the dialdehyde cross-link. Since proteins in a nanocluster are in close proximity to each other, the rate of them linking to each other should be much faster than linking between proteins that are present as free monomers in solution. Based on this, by manipulating the reaction times and rates for the cross-linking reaction, it will be possible to selectively cross-link proteins present in the nanoclusters. After cross-

linking the nanocluster, it would be possible to dilute the formulation without the nanocluster dissociating into monomeric protein like it does in the absence of cross-linking. Retention of the nanoclusters under dilute conditions would lend access to a multitude of techniques for determination of the cluster size and also for measuring the fraction of protein contained in monomer and in nanocluster states in addition to probing the internal structure of the nanoclusters.

NSE measurements can be used to determine the diffusion coefficient of the entities present in a sample which can then be converted to a particle size. Although NSE works on a similar principle as DLS which has been mentioned earlier in this dissertation, NSE (unlike DLS) does not have the same bias towards larger species and therefore its results can be compared with DLS to effectively estimate the fraction of protein present in the nanoclusters versus that present in the monomeric state. The NSE approach has already been used to observe the critical micellization like behavior of mAb oligomers with a majority of mAbs contained in the oligomeric species.¹² Therefore it would be fairly simple to extend the application of this technique to the nanoclusters described in this dissertation.

FRET is a fluorescence based technique which depends on two fluorescent species being within a certain distance of each other for one of them to fluoresce and yield a signal. Therefore it is a very sensitive technique for measurement of the interspecies distances.^{13,14} This technique could be utilized to study the internal structure of nanoclusters by either fluorescently tagging proteins or using a mixture of fluorescent proteins with similar structure and strategically located emission and absorption bands followed by subsequent formation of nanoclusters. Since the fluorescence efficiency in FRET depends on the distance between the two fluorophores, the separation between

proteins in a nanocluster could be measured when FRET is used in conjugation with a supplementary technique to determine the fraction of protein in nanoclusters. Additionally this technique could be used to study the rates of dissociation of the protein nanoclusters both *in vivo* and *in vitro* through observation of both the rate and location of the loss of FRET signal intensity. Therefore through a combination of the above three techniques along with other supplemental techniques and modeling, it should be possible to study the morphology of the protein nanoclusters in terms of their size, fraction of protein contained in them and also their internal structure.

9.2.2 Further Modification of Protein-protein Interactions for Reducing Viscosity

This dissertation uses a mixture of arginine and glutamic acid for modifying the protein-protein interactions in order to lower the viscosity of protein formulations for mAb1 and sheep IgG. There would be great interest in exploring whether the reduction in viscosity is a generic phenomenon and would be also seen for other mAbs. Other mAbs would have different interactions compared to mAb1 and therefore arginine and glutamic acid would have a different effect on the interactions. Another interesting aspect that should be explored is the use of other co-solutes like different amino acids, salts, saccharides, etc. for modifying the protein-protein interactions. This dissertation mentions that the interactions were lowered by the addition of arginine and glutamic acid but does not quantify this change in the interactions. Therefore the quantification of these interactions at dilute protein concentration through measurement of the osmotic second virial coefficient (B_2) or the diffusion interaction parameter (k_d) would be a logical advancement. The measured changes in interactions could then be used as a screening technique for determining the suitability of new co-solutes for viscosity reduction.

9.3 REFERENCES

- (1) Holstein, M. A.; Parimal, S.; McCallum, S. A.; Cramer, S. M. *Biotechnol Bioeng* 2012, 109, 176.
- (2) Hou, Y.; Cramer, S. M. *J Chromatogr A* 2011, 1218, 7813.
- (3) Valente, J. J.; Verma, K. S.; Manning, M. C.; Wilson, W. W.; Henry, C. S. *Biophys J* 2005, 89, 4211.
- (4) Connolly, B. D.; Petry, C.; Yadav, S.; Demeule, B.; Ciaccio, N.; Moore, J. M.; Shire, S. J.; Gokarn, Y. R. *Biophys J* 2012, 103, 69.
- (5) Saito, S.; Hasegawa, J.; Kobayashi, N.; Kishi, N.; Uchiyama, S.; Fukui, K. *Pharm. Res.* 2012, 29, 397.
- (6) Cheung, J. K.; Truskett, T. M. *Biophys J* 2005, 89, 2372.
- (7) Shen, V. K.; Cheung, J. K.; Errington, J. R.; Truskett, T. M. *Journal of biomechanical engineering* 2009, 131, 071002.
- (8) Li, Y.; Lubchenko, V.; Vekilov, P. G. *Rev Sci Instrum* 2011, 82, 053106.
- (9) Pan, W. C.; Vekilov, P. G.; Lubchenko, V. J. *Phys. Chem. B* 2010, 114, 7620.
- (10) Vekilov, P. G. *Ann N Y Acad Sci* 2009, 1161, 377.
- (11) Vekilov, P. G. *Soft Matter* 2010, 6, 5254.
- (12) Yearley, E. J.; Godfrin, P. D.; Perevozchikova, T.; Zhang, H.; Falus, P.; Porcar, L.; Nagao, M.; Curtis, J. E.; Gawande, P.; Taing, R.; Zarraga, I. E.; Wagner, N. J.; Liu, Y. *Biophys J* 2014, 106, 1763.
- (13) Jares-Erijman, E. A.; Jovin, T. M. *Nature biotechnology* 2003, 21, 1387.
- (14) Schuler, B.; Lipman, E. A.; Eaton, W. A. *Nature* 2002, 419, 743.

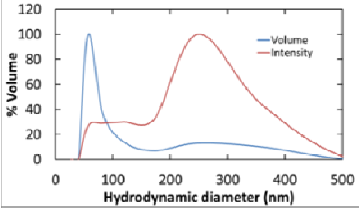
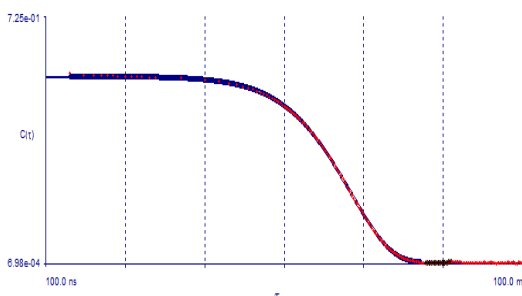
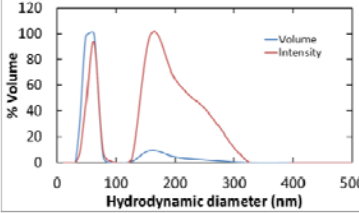
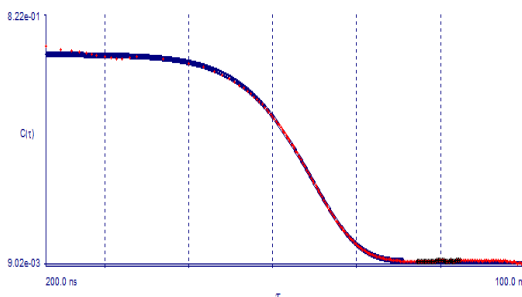
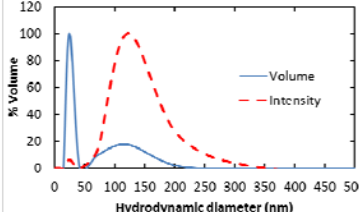
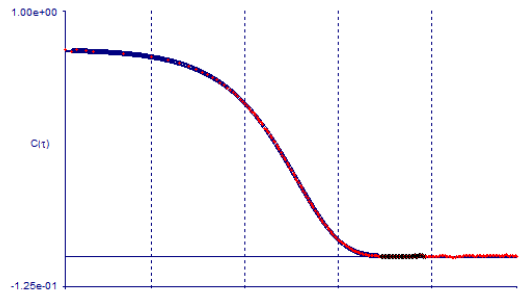
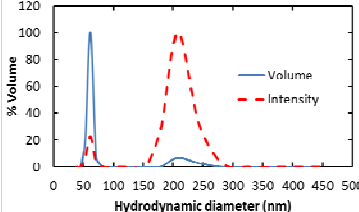
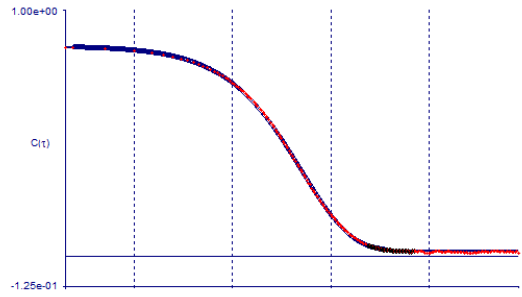
Appendix A: Gold Nanoparticles with High Densities of Small Points on Nanocluster Cores with Strong NIR Extinction

A.1 NOTE ON DLS MEASUREMENTS

DLS is based on measuring the intensity of light scattered where the scattering intensity is biased towards larger particles. In the Rayleigh scattering regime the intensity is proportional to diameter to the sixth power. Therefore even a very small amount of a larger aggregate species would have a large bias on the signal. The intensity distributions for both the particles in the current study and the commercially produced nanourchins were compared as shown in Table A1. Both types of particles showed a peak at a larger size for the intensity distribution, which disappeared upon converting the size to a volume distribution. The conversion to the volume distribution was done through the algorithm built into the software from Brookhaven instruments (Dynamic light scattering software 9kdlsw32 ver. 3.34) which also accounts for contributions from Mie absorption and scattering. The conversion between distributions is given by

$$G'_V(d) = G_I(d)/(d^3P(\theta)) \dots(A1)$$

where G'_V is the size distribution by volume, G_I is the size distribution by intensity, d is the scatterer diameter and $P(\theta)$ is the angular part of the Mie theory scattering coefficient. The real and imaginary refractive indices of pure Au at the laser wavelength of 660 nm where $n = 0.11$ and $k = 3.6$, respectively.¹ It should be noted that the size was not very sensitive to the value used for the refractive indices. All the sizes reported in the current study are the volume average size or the volume distribution determined as described above.

Fig. No. and pH	Diameter by volume (nm)	Volume and intensity distribution	ACF
100 nm nano urchins	101.7		
50 nm nano urchins	133.7		
Fig. 2.2a dotted line (pH 9.3)	25		
Fig. 2.2a dashed line (pH 8.7)	64	 <p>(Table A1 continued on the next page)</p>	

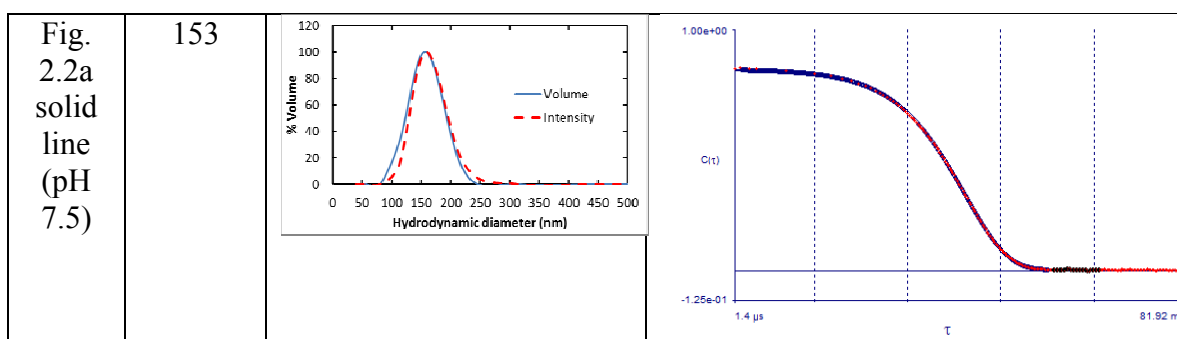


Table A1: Dynamic light scattering ACFs and size distributions for commercial nanourchins contrasted with particles from Chapter 2.

Polymer	pH	Final Gold Concentration (mM)	Hydrodynamic Diameter (nm)	Extinction ratio (800nm/500nm)	Zeta Potential (mV)
Dextran	8.7	0.018	39	1.24	-23.4 ± 1.8

Table A2: Summary of the NIR extinction properties and sizes of nanoclusters synthesized with dextran instead of CMD keeping all other parameters the same.

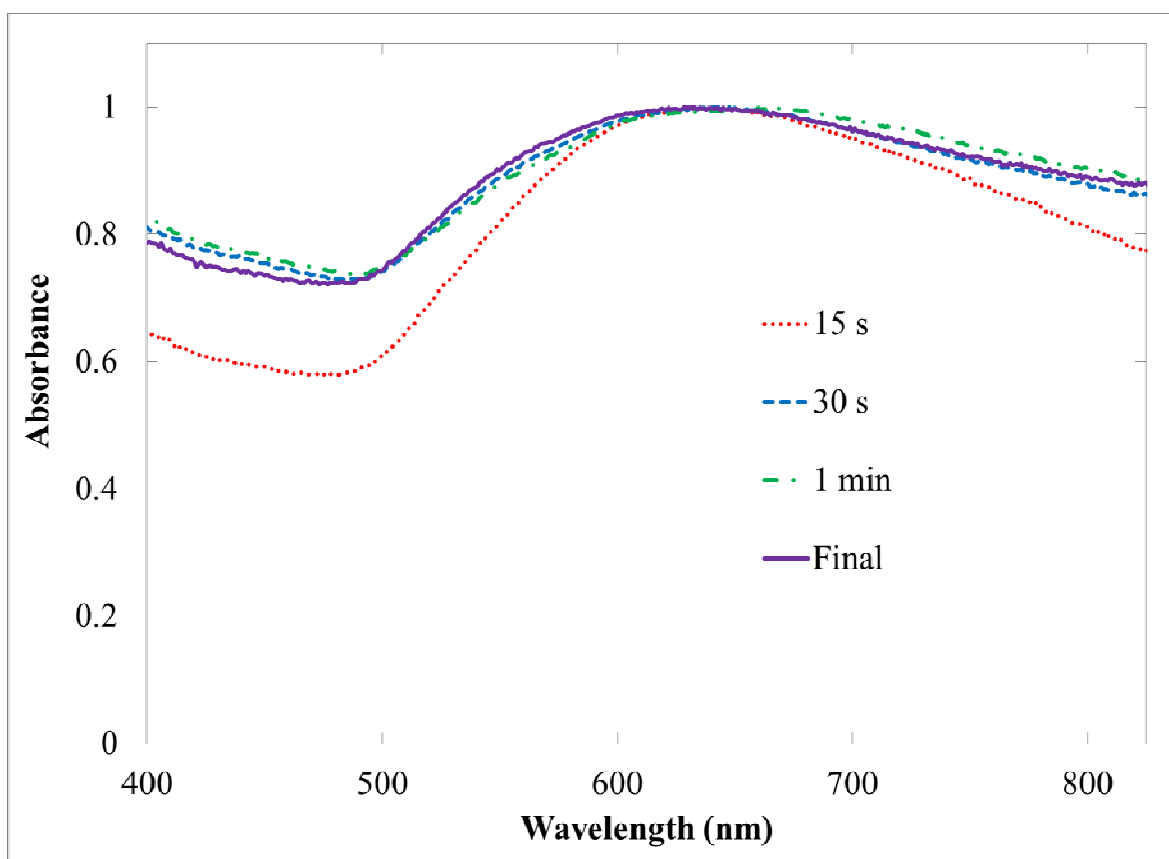
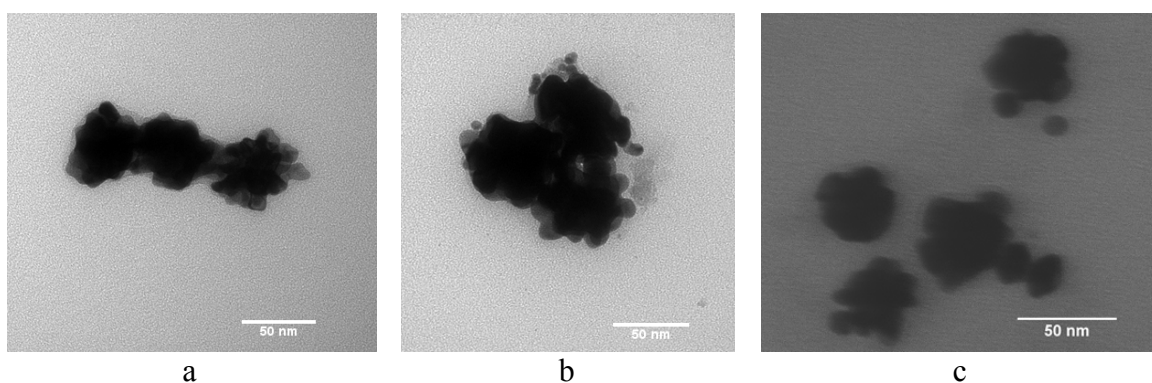


Figure A1: Evolution of Au nanocluster UV-vis extinction with time at 0.018 mM Au precursor and pH 8.7, with the reaction quenched by mercaptoacetic acid at each time point.



(Fig. A2 continued on the next page)

Figure A2: Time evolution of cluster morphology by TEM at 0.018 mM Au precursor and pH 8.7, with the reaction quenched by mercapto acetic acid at: a, 15 s. b, 30 s. c, not quenched.

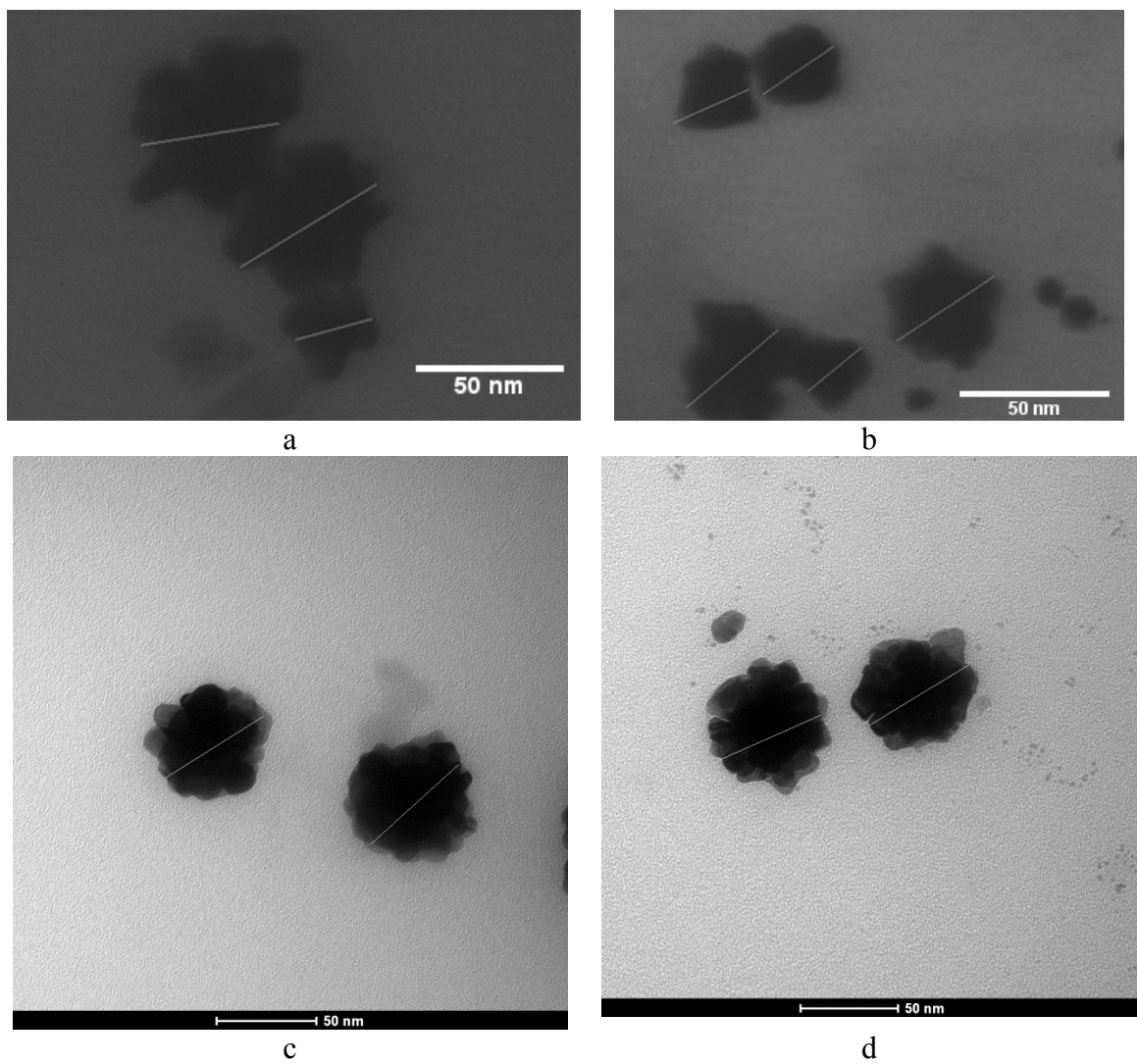


Figure A3: Additional STEM (a and b) TEM images (c and d) of particles synthesized at pH 8.7 at an Au precursor concentration of 0.018 mM.

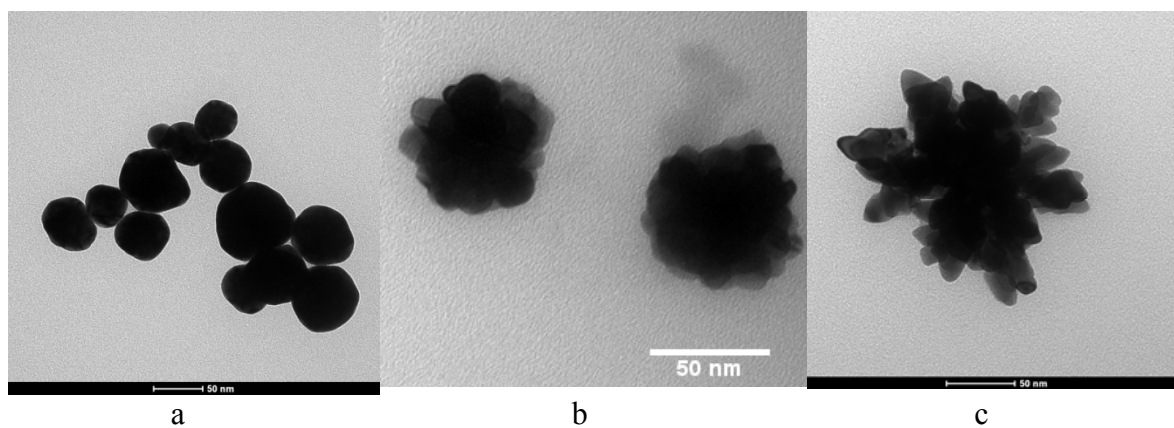


Figure A4: Low resolution TEM of nanoclusters synthesized with dextran as the stabilizing polymer with 0.018 mM Au precursor at a, pH = 9.3. b, pH = 8.7. c, pH = 7.5. Scale bar is 50 nm in all cases.

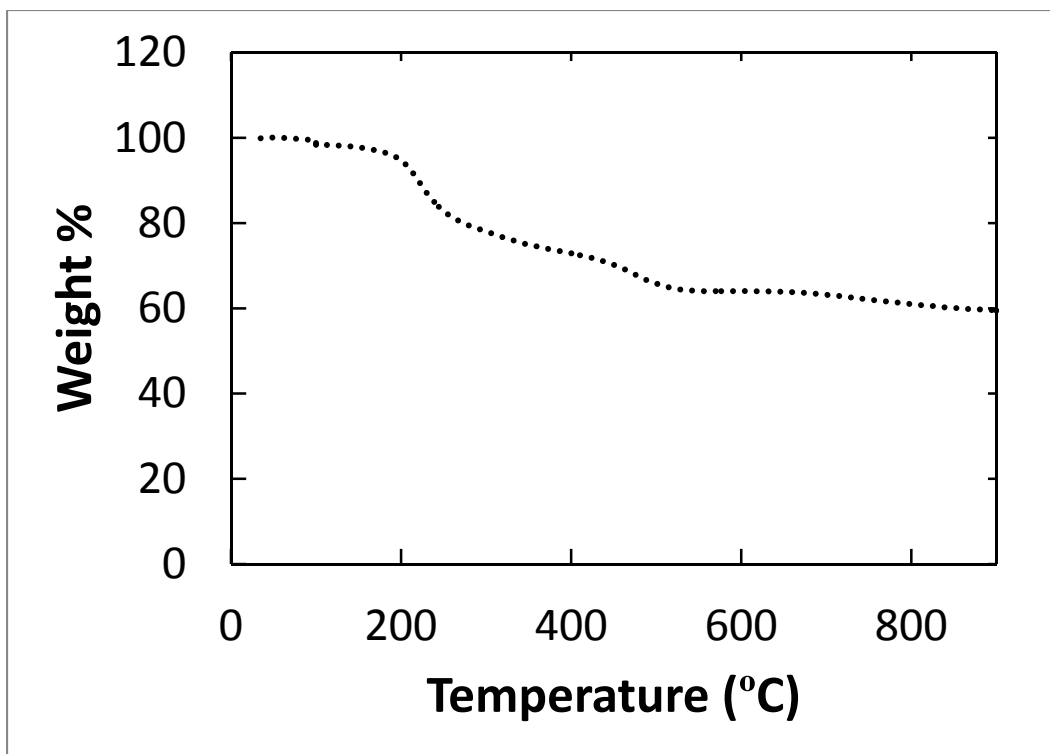


Figure A5: TGA of gold nanoclusters synthesized at 0.018 mM Au³⁺ and a dextran coating at pH 8.7.

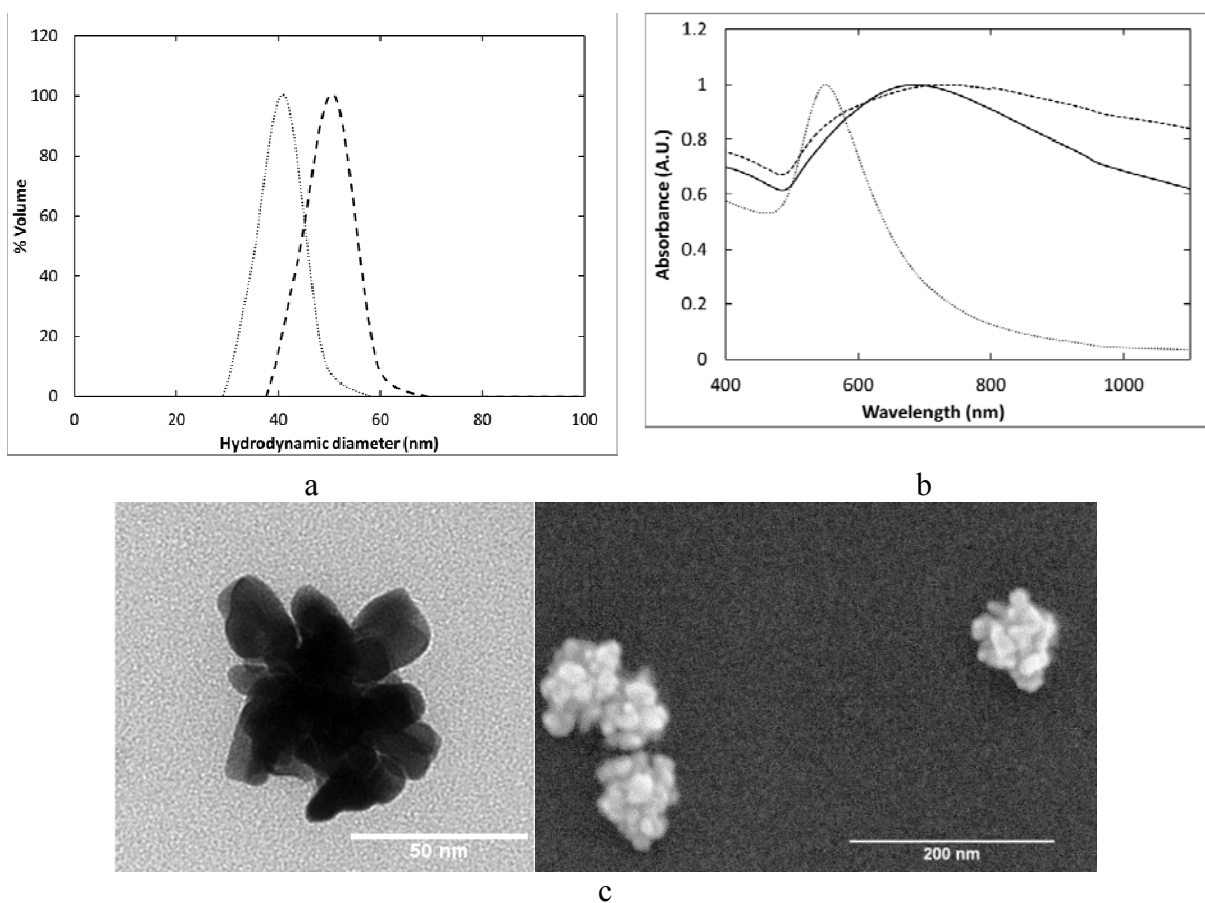


Figure A6: Properties of nanocluster dispersions after 2 iterations of Au at pH = 9.3 (dotted line), pH = 8.7 (dashed line) and pH = 7.5 (solid line) characterized by a. Hydrodynamic diameter by DLS and b. UV- vis spectra. c. Example TEM and SEM images of particles synthesized at pH = 8.7.

A.2 SUPPLEMENTARY REFERENCES

- (1) Raki, A. D.; Djuri?i, A. B.; Elazar, J. M.; Majewski, M. L. *Appl. Opt.* **1998**, 37, 5271.

Appendix B: Concentrated Dispersions of Equilibrium Protein Nanoclusters That Reversibly Dissociate into Active Monomers⁴

B.1 NOTE ABOUT DLS DATA FOR CHAPTER 3

Chapter 3 has DLS data from published work where the fitting protocol was not optimized.¹ In this case, the intensity correlation function was fit by a CONTIN algorithm where the data was fit till the first plateau in the correlation function. The ACFs for the samples contained in this chapter typically have a major second decay. The plateau between the two decays was not very clear and although the fitting was limited to the first plateau as can be seen in Table B4, the placement of the baseline was not very clear. The cluster size obtained by the DLS in this case is very large and may be unreliable because of the lack of confidence in the placement of the baseline. Additionally, only one sample was run in this case with no replication because of the lack of material available. Only the first decay was fit based on the stipulation from the papers from the Vekilov research group that DLS as a technique is only applicable up to correlation times of ~ 1 ms and they typically do not go beyond delays of 20 ms.²⁻⁴ Therefore for longer times interactions between particles would be important and would lead to complications in the correlation function at longer delay times.

The DLS measures the relaxation times for the diffusing entities by means of the autocorrelation in the intensity of scattered light from the sample which is then converted into a diffusion coefficient by using the scattering vector q ($q = \frac{4\pi}{\lambda} \sin(\theta/2)$) using the equation

⁴ Reproduced in large part with permission from: Johnston, K. P.; Maynard, J. A.; Truskett, T. M.; Borwankar, A.; Miller, M. A.; Wilson, B.; Dinin, A. K.; Khan, T. A.; Kaczorowski, K. J. *ACS Nano* **2012**, 6 (2) 1357-1369. Copyright 2012 American Chemical Society

$$D = \frac{1}{\tau q^2} \quad \dots (B1)$$

The diffusion coefficient can then be converted into a size by using the Stokes Einstein equation –

$$R = \frac{k_B T}{6\mu\eta D} \quad \dots (B2)$$

For determining the size by using the Stokes-Einstein equation, the viscosity used was the solvent viscosity. The actual viscosity that the species in solution see may not be the solvent viscosity. There may be free monomer present in the sample which will be a part of the continuum solvent for larger particles which may see a larger viscosity than the solvent viscosity. Therefore there will be uncertainty in the size of the particles reported. These complications in DLS were not known at the time of publication of the work and therefore the appendix is being added to point out the uncertainties in DLS.

B.2 CLUSTER DISSOLUTION TIME

The dissolution time for protein in the nanocluster is of interest for understanding *in vitro* dilution experiments, and more importantly, cluster dissociation upon *in vivo* subcutaneous injection. The dissolution time t_F of a 300 nm cluster was calculated from a shrinking sphere model, assuming a solid sphere of protein⁵:

$$t_F = \frac{\rho}{4D_v(c_{sat} - c_{bulk})} * \frac{1}{2} D_c^2 \quad (B3)$$

where ρ is the density of the protein (1.34 g/ml), D_v is the diffusion coefficient of a single protein in water (4.5×10^{-7} cm²/s, calculated using the Stokes-Einstein equation), c_{sat} is the concentration of a saturated protein solution (assumed to be 50 mg/ml), $c_{bulk} \sim 0$ mg/ml. The dissolution time was found to be 7 ms for a 300 nm diameter cluster. The rapid dissolution to protein monomer is favorable for rapid pharmacokinetics for high bioavailability. It may also be beneficial for minimizing time for which concentrated protein is exposed to fluids where protein denaturation may possibly take place.

B.3 POTENTIAL OF MEAN FORCE BETWEEN TWO PROTEINS IN THE PRESENCE OF THE SURROUNDING MEDIA

The potential of mean force $V(r)$ between two protein particles, whether protein monomers or nanoclusters, in the presence of the other molecules in the media, provides a basis for understanding the relevant multi-scale interactions. It can be modeled as a sum of components, which typically include depletion (dep) interactions, specific short-ranged (ssr) interactions, and van der Waals (vdw) interactions, as well as electrostatic (el) interaction, i.e.,

$$V(r) = V_{dep}(r) + V_{ssr}(r) + V(r)_{vdw} + V_{el}(r) \quad (B4)$$

where r is the separation between particle centers. The depletion attraction⁶⁻⁹ is an effective (osmotic) interaction that particles experience due to the presence of co-solutes (here, trehalose) in solution. It arises because entropy favors microstates where proteins are close to one another; i.e., configurations which make more of the volume available to the smaller co-solutes. The depletion attraction is often described by the Asakura-Oosawa potential^{8,10}

$$\frac{V_{dep}}{k_B T} = -\frac{\phi_E}{2} \left(1 - \frac{r - 2R}{2R_E}\right)^2 \left(2 + \frac{3R}{R_E} + \frac{r - 2R}{2R_E}\right) \quad (B5)$$

where R is the protein particle radius and ϕ_E and R_E represent the volume fraction and radius of the extrinsic co-solute, respectively.¹¹ Since the strength of the depletion attraction is proportional to ϕ_E , it can be tuned experimentally by modifying the co-solute concentration. The range of this attraction scales with R_E (~ 0.5 nm for trehalose), and so it is considerably smaller than R (~ 5.5 nm for the protein monomer).

What we term the specific short-ranged attraction between proteins represents a combination of molecular-scale interactions including hydrogen bonding, hydrophobic interactions between exposed apolar protein patches, and fluctuating charge dipoles.¹²⁻¹⁵ For simplicity, it is often modeled as a square-well potential –

$$V_{ssr}/k_B T = \begin{cases} \infty & r < 2R \\ -V_0/k_B T & 2R \leq r \leq 2R(1 + \Delta) \\ 0 & r > 2R(1 + \Delta) \end{cases} \quad (B6)$$

where $V_0/k_B T$ is the well depth ($V_0/k_B T \sim 2.7$ for a monoclonal antibody¹⁶) and the width ($2R\Delta$) is ~ 1 nm.^{12-15,17} It is reasonable to assume that the range of the specific short-ranged interactions ($2R\Delta$) is constant and thus independent of particle size (R); i.e., $\Delta \sim R^{-1}$.^{12,18,19} Thus, the range of influence of a 1 nm ssr interaction becomes negligible for a 100 nm protein nanocluster relative to a 10 nm protein, which will be shown to play a key role for the low viscosity of the nanocluster dispersions.

The van der Waals attraction between two particles can be expressed in terms of a Hamaker constant between two proteins through water A_{pwp} as²⁰ –

$$\frac{V_{vdw}}{k_B T} = \frac{-A_{pwp}}{6k_B T} \left[\frac{2R^2}{(r-2R)(r+2R)} + \frac{2R^2}{r^2} + \ln \left[\frac{(r-2R)(r+2R)}{r^2} \right] \right] \quad (B7)$$

It is relatively weak compared to the other interactions considered in this study ($A_{pwp}/k_B T$ in water is only ~ 0.04), and hence it is not considered explicitly in our analysis. The electrostatic repulsion between particles is given by²⁰

$$\frac{V_{EL}}{k_B T} = \frac{64\pi R \Gamma_0^2 \eta_\infty}{\kappa^2} \exp(-\kappa[r - 2R]) \quad (B8)$$

where Γ_0 is a function of ψ_0 the particle surface potential²⁰, η_∞ is the bulk ion concentration (50mM), κ is the inverse Debye length ($\kappa^{-1} = 0.7$ nm for the bulk buffer solution). Note that the magnitude of the electrostatic repulsion depends on both the charge and the size of the particles.

B.4 LOW EFFECTIVE DIELECTRIC CONSTANT WITHIN THE CLUSTERS

The concept of equilibrium nanocluster formation assumes long ranged electrostatic forces in the nanocluster, which is favored by a low dielectric constant.²¹ The dielectric constant of water within the nanoclusters will be influenced by confinement between the protein surfaces. Analogously, the heterogeneous environment within each dense protein nanocluster is very different from that of bulk water. As stated in the main text, we have estimated that the ϕ_{int} in the clusters is ~ 0.60 based on the SEM images and SLS measurements on IgG clusters.

$$\phi_{internal} = \left(\frac{D_m}{R_c} \right)^{1/\delta_f} \quad (B9)$$

The dielectric constant in the cluster C according to effective medium theory is given as^{22,23}

$$\frac{\epsilon - \epsilon_2}{3\epsilon} = \phi_1 \frac{\epsilon_1 - \epsilon_2}{\epsilon_1 + 2\epsilon} \quad (B10)$$

where ϵ_1 is the protein dielectric constant (5), ϵ_2 is the dielectric constant of water (80) and ϕ_1 is the volume fraction of protein in the medium. The calculated C is 20 for ϕ_1 as 0.6. This value is similar to the choice of 25 in Table B3.

Assuming uniformly-spaced spherical proteins of $R=5.5\text{nm}$ at $\phi_{int} = 0.6$ implies from simple geometry (if we assume each spherical protein to be contained in a cube and the cubes when put together side to side form the cluster of proteins where $V_{sphere} = 0.6 V_{cube}$) that that water inside the cluster is confined to channels on the order of 1nm or less (see, e.g., Fig. 5 of reference²⁴) between protein surfaces. At this level of confinement, as noted from experiments^{25,26} and model calculations²⁷⁻²⁹ on related systems, the effective dielectric constant of water is reduced to ~ 40 .²⁹ Also only the ions that dissociate from the proteins and few of the extraneous ions tend to be present in these extremely confined spaces.³⁰ This low ion concentration and low C within the clusters will produce less Debye screening as compared to bulk water buffer solutions. This low screening level would further enhance the longer-ranged electrostatic repulsion that influences the cluster size.

B.5 SURFACE POTENTIAL AND ZETA POTENTIAL OF IGG CLUSTERS

The zeta potential for 50 nm clusters of polyclonal sheep IgG, produced from dispersing the same powder as in Fig. B6 with $c = 50$ mg/ml and $c_E = 270$ mg/ml was measured to be 3.9 ± 0.75 mV at a pH of 6.4 near the pI of 6.4. From this value and a Debye length of 2 nm, we estimated about 1-2 effective charges on the surface of each protein from the relation

$$\zeta = \frac{Q}{4\pi\epsilon R_s(1 + \kappa R_s)} \quad (\text{B11})$$

where Q is the surface charge on a particle, R_s the radius for the particle at the shear plane, which was approximated as equal to the radius of the particle (R_c), and κ is the inverse Debye length. Based on this Q , a surface potential of 64 mV was calculated for the IgG nanoclusters

$$\psi_0 = \frac{Q}{4\pi\epsilon R_c} \quad (\text{B12})$$

This surface potential gives a potential barrier of about $15 k_B T$ in the potential of mean force for two protein nanoclusters as shown in Fig. 3.4c which stabilizes the clusters against aggregation. Given the large quantities of protein required to measure ζ , it was not feasible to perform these measurements for 1B7. However, given the similar molecular weights for the two proteins and similar results for n_c and the other properties, we believe the a similar large surface potential would stabilize the 1B7 clusters.

Quantity	Monomer at pI (Fig. 3.4a)	Monomer 3 pH units from pI (Fig. 3.4a)	Cluster (Fig. 3.4c)
Charge per protein	1	25	0.6
Debye Length (κ^{-1})	0.7	0.7	0.7
Γ_0	0.036	0.72	0.76
ϕ_E	0.17	0.17	0.17

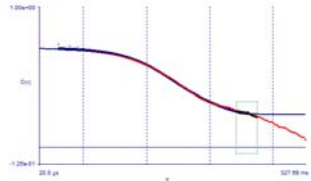
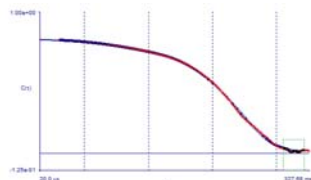
Table B1: Parameters used Figs. 3.4a and 3.4c to determine the potential of mean force.

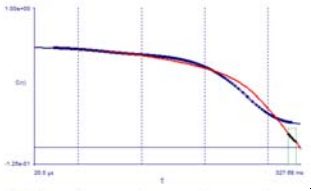
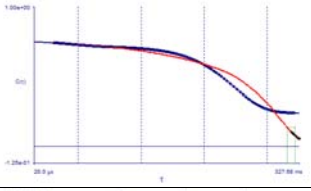
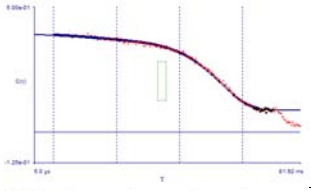
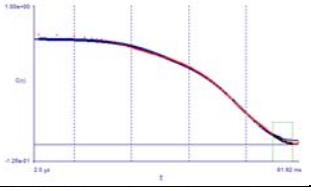
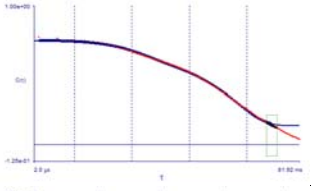
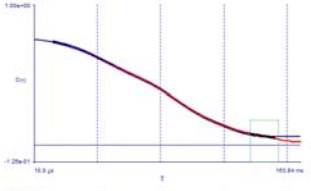
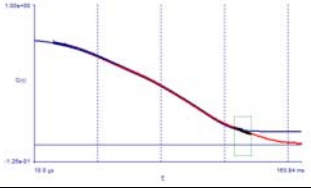
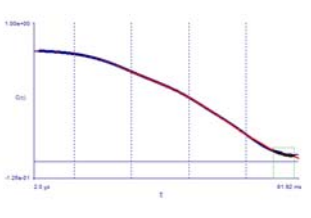
Quantity	Value for 1B7 (Figs. 3.2b and 3.4b)	Value for IgG (Fig. 3.2c)
Fractal dimension (δ_f)	2.6	2.6
Dielectric constant (ϵ_r)	25	15
No. of dissociable sites per unit area of particle surface (σ , nm ⁻²)	0.2	0.2
Distance between opposite charges in an ionic bond (b , nm)	0.1	0.2
Radius of primary particle (R , nm)	5.5	5.5

Table B2: General parameters for calculating cluster diameter contours in Fig. 3.4b.

Quantity	Case 1
Concentration of co-solute (c_E , mg/ml)	220
Attractive energy ($\epsilon/k_B T$)	6.52
Protein volume fraction (ϕ)	0.16
Concentration of protein (c , mg/ml)	220
Charge on a protein monomer (q_0)	0.09
Aggregation number (n_c)	4500
Predicted diameter of the cluster (D_c , nm)	280
Actual diameter of the cluster (D_c , nm)	320

Table B3: Particular parameters for calculating cluster diameters for specific case in Fig. 3.4b.

Protein conc (mg/ml)	Trehalose conc (mg/ml)	Angle	Diameter by volume (by intensity) (nm)	Diameter st dev peak width (nm)	Count rate (kcps)	Correlation function
220	220	160	340.5 (342.4)	-	131	
175 (Table B4 continued on the next page)	175	150	62 (62)	-	123.4	

125	125	150	44.7 (48)	2.4 (3.5)	48.3	
100	100	150	16.2 (18.1)	0.8 (0.6)	47.4	
75	75	150	7.4 (1365)	0.5 (400)	8.9	
70	270	135	365 (2067)	-	312.3	
70	250	135	176 (176)	-	359.5	
70	225	135	96.5 (1587)	20	276.6	
70	200	135	28 (1577)	-	276.9	
70 (Table B4 continued on the next page)	150	135	11.6 (1960.6)	-	273	

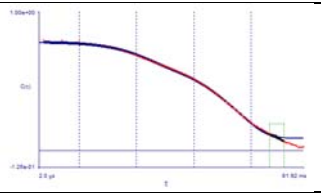
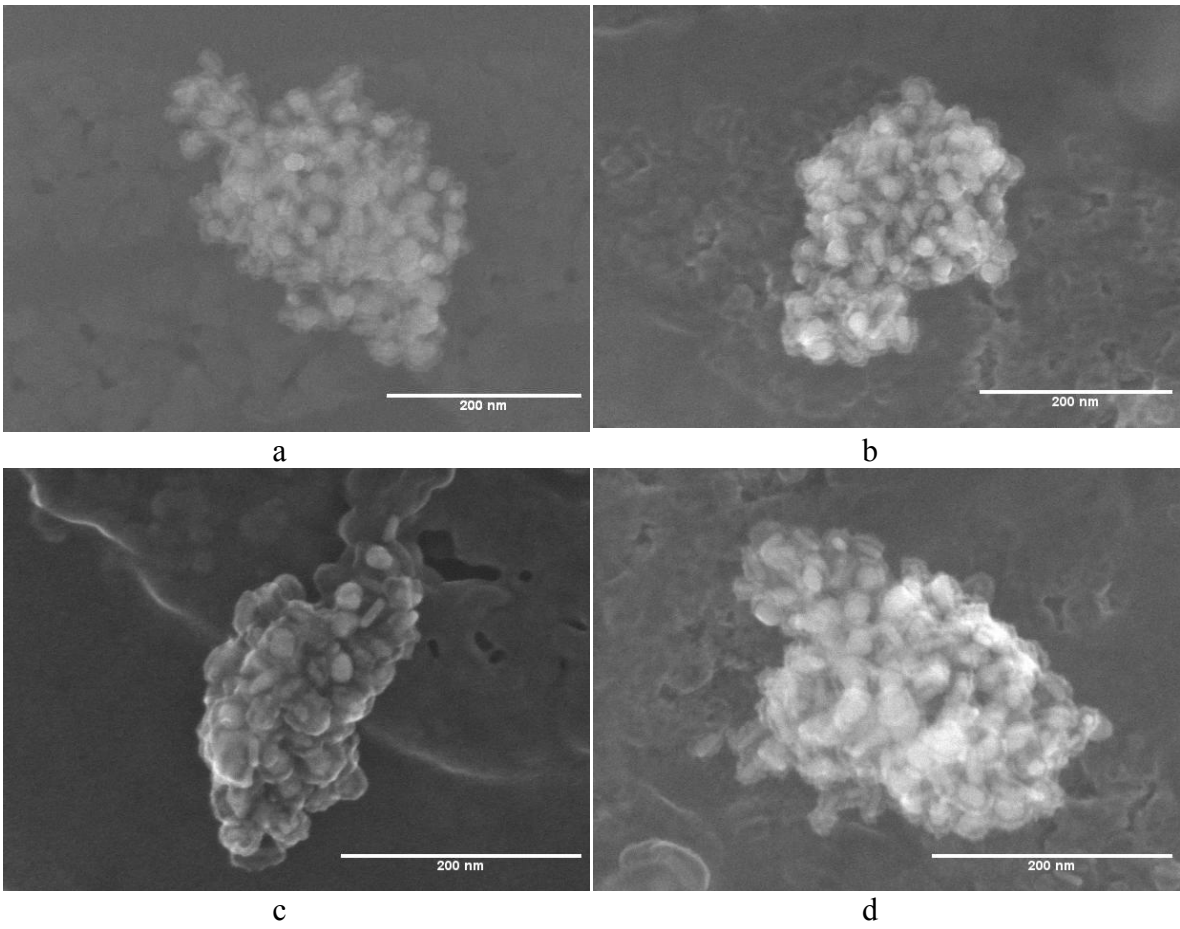
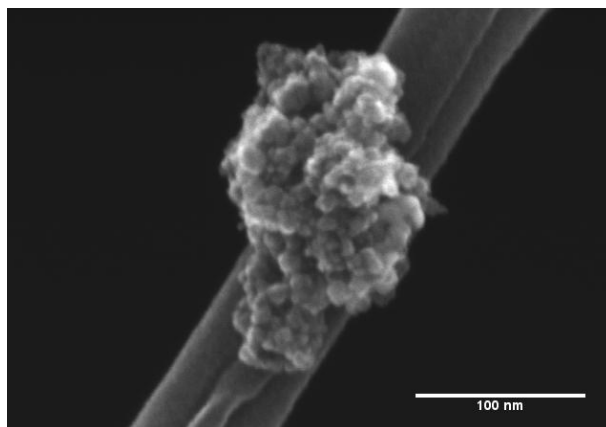
70	270	135	250 (2489)	-	249.4	
----	-----	-----	---------------	---	-------	---

Table B4: Auto correlation functions for all of the samples analyzed by DLS in Chapter 3 with sample composition provided to relate back to the figures and tables in the paper. 200 channels were used for all the measurements.



(Fig. B1 continued on the next page)



e

Figure B1: SEM images of antibody nanoclusters with trehalose as co-solute. a, b, c and d, Reproducibility of multiple SEM images of 1B7 antibody nanoclusters at $c = c_E = 220 \text{ mg/ml}$ (identical conditions as in Fig. 3.1c). The SEM micrographs clearly show good reproducibility in the size of the $\sim 300 \text{ nm}$ clusters in the dispersion for four clusters, consistent with the DLS results in Fig. 3.2a. The images were obtained from regular carbon film copper TEM grids where the nanoclusters were resting on the copper mesh. The individual protein monomers, on the order of 10 nm , appear to have a halo around them. This halo is a layer of trehalose deposited during freezing and lyophilization in sample preparation for SEM. e, Polyclonal IgG nanocluster at $c = c_E = 260 \text{ mg/ml}$. The imaging was done on a lacey carbon TEM grid and the nanocluster is resting on a strand of lacey carbon.

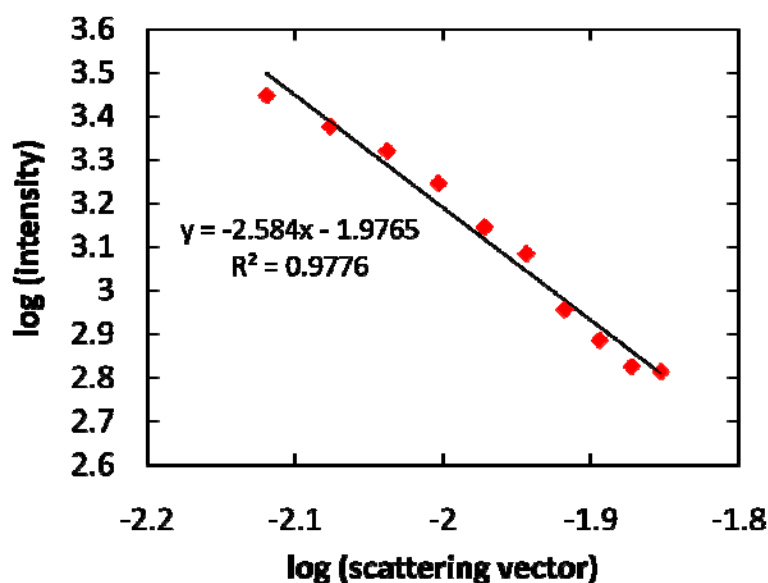


Figure B2: Static light scattering to determine fractal dimension. The 80 nm sheep IgG nanoclusters were formed at $c = 70$ mg/ml IgG and $c_E = 270$ mg/ml trehalose. The intensity which scales as the measured count rate was plotted versus the scattering vector $4\pi\sin(\theta/2)/\lambda$ at various angles from 45° to 90° . The slope of the line fit through the data multiplied by -1, i.e., 2.6 is the fractal dimension.²⁰ In static light scattering, we assume that the structure factor is not a function of the scattering vector and therefore, the intensity is related to the scattering vector through the fractal dimension.

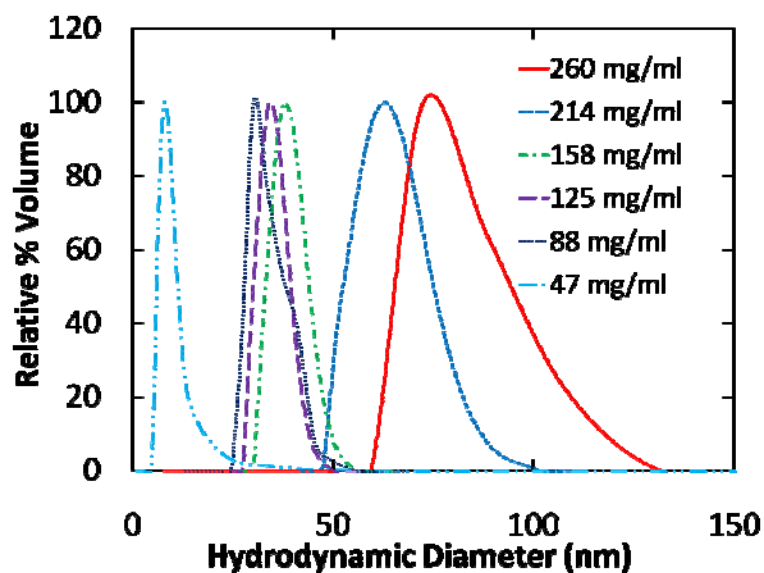


Figure B3: Hydrodynamic diameter by DLS of polyclonal IgG nanoclusters upon dilution in buffer ($c/c_E = 1$). The protein concentrations are shown in the legend. Sequential dilution with phosphate buffer at constant c/c_E yields progressively smaller nanoclusters until monomeric protein with a hydrodynamic diameter of ~ 10 nm is observed at $c = c_E = 47$ mg/ml. The behavior and mechanism for nanocluster dissociation is similar as observed for monoclonal antibody 1B7 in Fig. 3.2a and b.

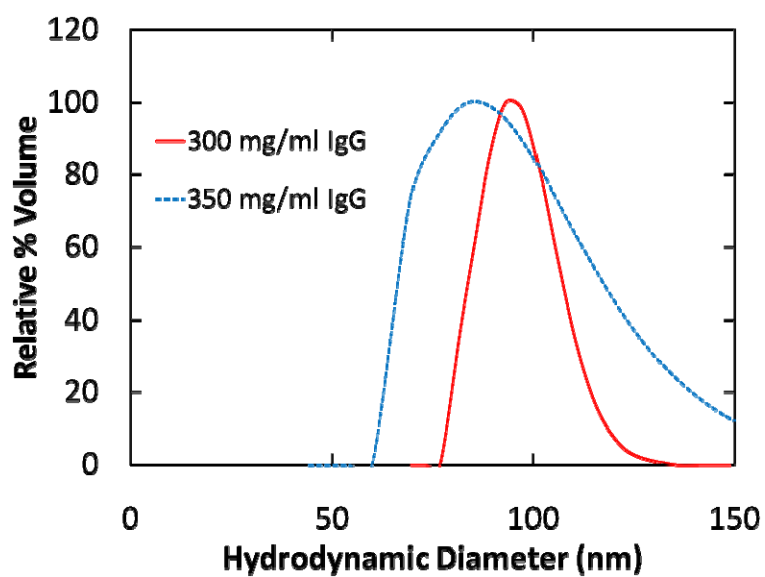


Figure B4: Polyclonal IgG nanocluster size at high concentration. Polyclonal sheep IgG dispersions were formulated with 300 and 350 mg/ml protein with $c/c_E = 1:0.5$ with trehalose and the resulting nanocluster hydrodynamic diameter measured by DLS.

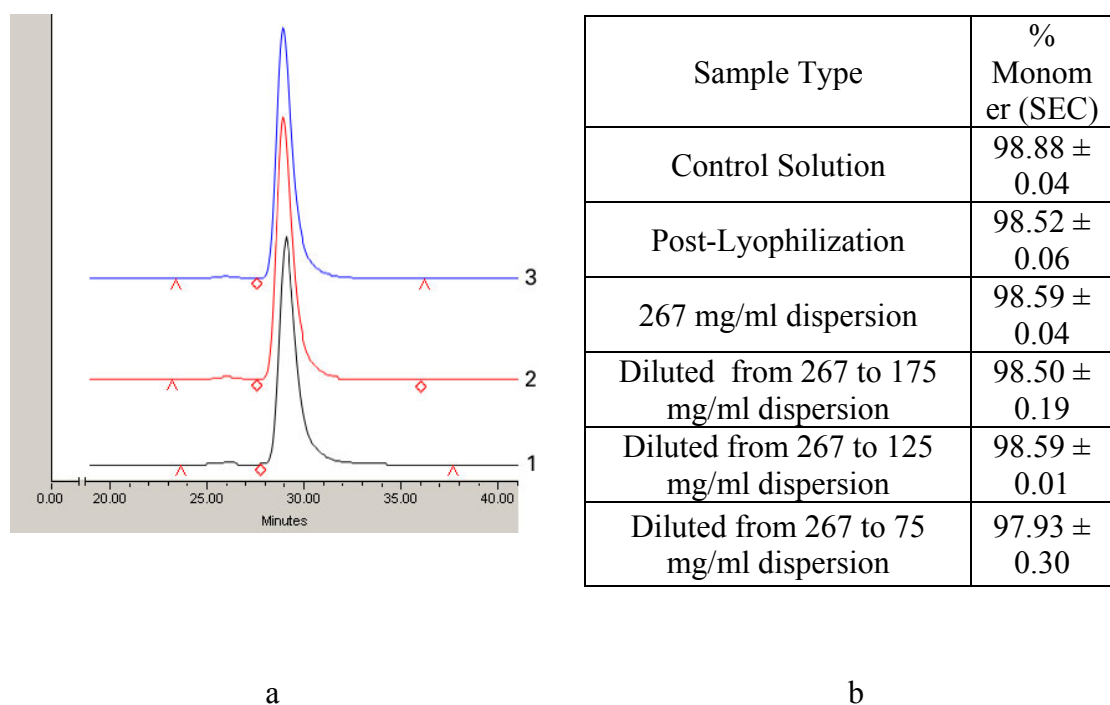


Figure B5: HPLC SEC of monomer concentration after dilution of the dispersion. All samples were diluted to 1 mg/ml in PBS and analyzed with Waters Breeze HPLC with TOSOH Biosciences TSK gel G2000SW and G3000SW_{XL} columns. The mobile phase comprised 100 mM sodium phosphate and 300 mM sodium chloride buffer (pH 7.0), and the eluate was monitored by absorbance at 214 nm. a. Chromatographs are shown for (1) solution control 1B7, (2) lyophilized, reconstituted 1B7, and dispersion formulated with (3) 260 mg/ml 1B7 and 260 mg/ml trehalose. No increase was seen in aggregate concentration throughout formation of the dispersion, dilution of the clusters, and reformation of the clusters with trehalose. b. The % monomer values are given here for a wide range of indicated experiments, shown in Fig. 3.2a and 3.2b. Error indicated is \pm s. d.

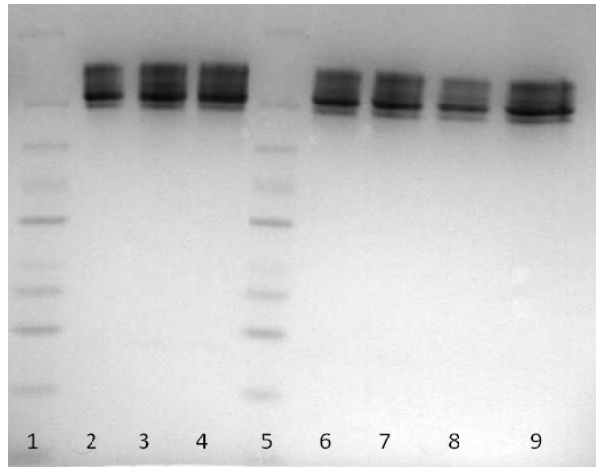


Figure B6: Absence of higher molecular weight aggregates as assessed by non-reducing SDS-PAGE. All dispersions were diluted to 1 mg/ml with PBS prior to analysis. 5 μ g of each sample was combined with non-reducing loading buffer and loaded on to a precast 4–20% SDS-PAGE gel (Bio Rad). Lane (1) molecular weight markers (Spectra BR); (2) solution control 1B7; (3) & (4) 1B7 post-lyophilization; (5) molecular weight markers (Spectra BR); (6) & (7) diluted 260 mg/ml 1B7 dispersion; (8) & (9) 260 mg/ml dispersion diluted to 75 mg/ml that was further diluted. None of the samples showed any change in molecular weight, or formation of any higher molecular weight aggregates.

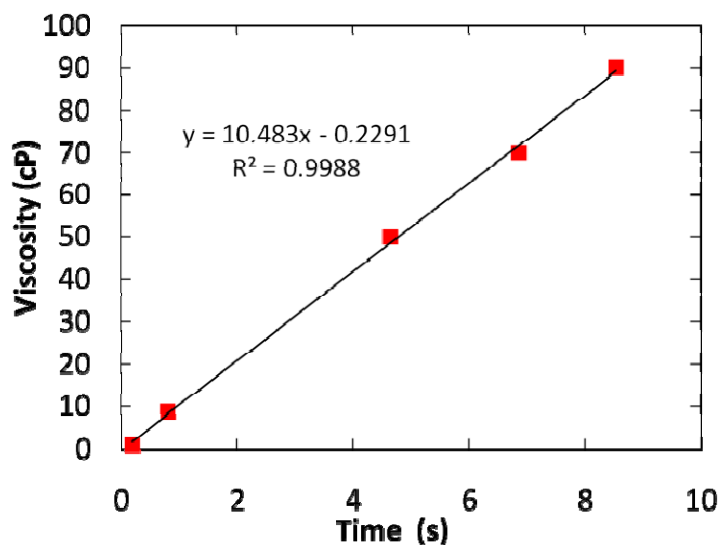


Figure B7: Viscosity calibration curve for measurements with small conical vials. The calibration curve was created using the following solution standards: DI water ($\eta_0 = 1$ cP), benzyl benzoate ($\eta_0 = 8.8$ cP), PEG200 ($\eta_0 = 50$ cP), PEG300 ($\eta_0 = 70$ cP), and PEG400 ($\eta_0 = 90$ cP). The time for the liquid level to be drawn from 0.4" to 0.1" in small conical vial (0.1 mL V-Vial, Wheaton) was measured from a video of the solution (taken with a Kodak EasyShare Z812 IS), converted using ImageJ software to a stack of images with 30 images per second. The time was measured to within 0.05 seconds at least 3 times and averaged, while maintaining the end of the plunger at the 1 ml mark. A maximum volume of 10% of the cavity in the syringe was filled with dispersion to minimize variation in the pressure drop.

B.6 SUPPLEMENTARY REFERENCES

- (1) Johnston, K. P.; Maynard, J. A.; Truskett, T. M.; Borwankar, A.; Miller, M. A.; Wilson, B.; Dinin, A. K.; Khan, T. A.; Kaczorowski, K. J. *ACS Nano* 2012.
- (2) Li, Y.; Lubchenko, V.; Vekilov, P. G. *Rev Sci Instrum* 2011, 82, 053106.
- (3) Vekilov, P. G. *Ann N Y Acad Sci* 2009, 1161, 377.
- (4) Pan, W. C.; Vekilov, P. G.; Lubchenko, V. J. *Phys. Chem. B* 2010, 114, 7620.

- (5) McCabe, W. J.; Smith, J. C.; Harriott, P. Unit Operations of Chemical Engineering. 4th Ed; Macgraw Hill, 1985.
- (6) Zhou, H. X. Proteins: Structure, Function, and Bioinformatics 2008, 72, 1109.
- (7) Zhou, H. X.; Rivas, G.; Minton, A. P. Annual Review of Biophysics 2008, 37, 375.
- (8) Asakura, S.; Oosawa, F. Journal of Polymer Science 1958, 33, 183.
- (9) Minton, A. P. J Pharm Sci 2007, 96, 3466.
- (10) S. Asakura, F. O. J. Chem. Phys. 1954, 22.
- (11) Tuinier, R.; Rieger, J.; De Kruif, C. G. Advances in Colloid and Interface Science 2003, 103, 1.
- (12) Curtis, R. A.; Prausnitz, J. M.; Blanch, H. W. Biotechnol Bioeng 1998, 57, 11.
- (13) Rosenbaum, D. F.; Kulkarni, A. M.; Ramakrishnan, S.; Zukoski, C. F. J Chem Phys 1999, 111, 9882.
- (14) ten Wolde, P. R.; Frenkel, D. Science 1997, 277, 1975.
- (15) Kulkarni, A. M.; Dixit, N. M.; Zukoski, C. F. Farady Discuss. 2003, 123, 37.
- (16) Bajaj, H.; Sharma, V. K.; Kalonia, D. S. Pharm. Res. 2007, 24, 2071.
- (17) Stradner, A.; Sedgwick, H.; Cardinaux, F.; Poon, W. C. K.; Egelhaaf, S. U.; Schurtenberger, P. Nature 2004, 432, 492.
- (18) Kanai, S.; Liu, J.; Patapoff, T. W.; Shire, S. J. J Pharm Sci 2008, 97, 4219.
- (19) Yadav, S.; Liu, J.; Shire, S. J.; Kalonia, D. S. J Pharm Sci 2010, 99, 1152.
- (20) Hiemenz, P. C.; Rajagopalan, R. Principles of Colloid and Surface Chemistry; 3rd ed.; Marcel Dekker, Inc.: New York, 1997.
- (21) Groenewold, J.; Kegel, W. K. Journal of Physical Chemistry B 2001, 105, 11702.
- (22) Reynolds, J. A.; Hough, J. M. Proc. Phys. Soc., London 1957, 70B, 769.
- (23) Bottcher, C. J. F. Recl. Trav. Chim. Pays-Bas Belg. 1945, 64, 47.
- (24) Rintoul, M. D.; Torquato, S. Physical Review E 1998, 58, 532.
- (25) Biswas, R.; Rohman, N.; Pradhan, T.; Buchner, R. The Journal of Physical Chemistry B 2008, 112, 9379.
- (26) Paddison, S. J. Annu. Rev. Mater. Res. 2003, 33, 289.

- (27) Senapati, S.; Chandra, A. *The Journal of Physical Chemistry B* 2001, 105, 5106.
- (28) Wang, M.; Pan, N. *Journal of Applied Physics* 2007, 101, 114102.
- (29) Ahmad, M.; Gu, W.; Geyer, T.; Helms, V. *Nat Commun* 2011, 2, 261.
- (30) Kralchevsky, P. A.; Danov, K. D.; Basheva, E. S. *Current Opinion in Colloid & Interface Science* 2011.

Appendix C: Tunable Equilibrium Nanocluster Dispersions at High Protein Concentrations⁵

C.1 NOTE ON DLS DATA FOR CHAPTER 4

Chapter 4 has DLS data from published work where the fitting protocol was not optimized.¹ In this case, the intensity correlation function was fit by a CONTIN algorithm where the data was fit till the first plateau in the correlation function. The ACFs typically have a slight and sometimes a major second decay as can be seen for all the ACFs in Table C10. The fitting was limited to the plateau at the end of the first decay in the correlation as can be seen in the table. In the case of ACFs in this particular chapter, the ACFs were closer to ideality in terms of the first decay and a plateau followed by a very minor second decay. The baseline placement could be done reliably at the end of the first decay with little ambiguity in terms of its location. The fitting was limited to the first decay based on the stipulation in the papers from the Vekilov research group that DLS as a technique is only applicable up to correlation times of 1ms or less with correlation times of greater than 20 ms never being considered.²⁻⁴ For longer times, interactions between particles would be important and would lead to complications in the correlation function at longer delay times. There may also be complex collective diffusional modes of collective protein molecule or cluster diffusion which contribute to these long tails which will complicate the observed ACFs.

After publication of the paper, the data was analyzed using a different fitting algorithm based on fitting the data with exponential decays. The governing equation used for the fits was –

⁵Reproduced in large part with permission from: Borwankar, A. U.; Dinin, A. K.; Laber, J. R.; Twu, A.; Wilson, B. K.; Maynard, J. A.; Truskett, T. M.; Johnston, K. P. *Soft Matter* **2013**, 9, 1766-1771. Copyright 2012 RSC Publishing.

$$g_2(t) - 1 = A_1 e^{\frac{-t}{\tau_1}} + A_2 e^{\frac{-t}{\tau_2}} \quad \dots (C1)$$

where τ_1 and τ_2 are the relaxation times which correspond to the decay in the correlation function which is represented by $g_2(t) - 1$ and A_1 and A_2 are pre-factors for fitting the amplitude of the curve. The delay times can then be converted into a diffusion coefficient by using the scattering vector q ($q = \frac{4\pi}{\lambda} \sin(\theta/2)$) using the equation

$$D = \frac{1}{\tau q^2} \quad \dots (C2)$$

The diffusion coefficient (D) can then be converted into a size by using the Stokes Einstein equation –

$$R = \frac{k_B T}{6\pi\eta D} \quad \dots (C3)$$

where R is the particle radius, and η is the viscosity of the medium containing the particles. Upon fitting equation (1) to the ACF of samples with a excipient in them utilizing residual minimization, the first relaxation time obtained corresponds to a particles size of 3-4 times the monomer using equations C2 and C3 while setting the viscosity to be the solvent viscosity, as shown in Fig. C11a (28 nm in this case).²⁻⁴ Forcing a fit for this correlation function with a monomeric size yielded a very bad fit as evidenced in Fig. C11b. However when an actual monomer sample for a similar protein was fit in the same manner, the relaxation time resulting was much lower and upon deriving a size using equations C2 and C3 yielded a size corresponding to a monomer sample as shown in Fig. C11c. The fits gave a second relaxation time corresponding to a much larger aggregate peak > 1 micron which was fit using the value of the solution viscosity for η instead of the solvent viscosity.²⁻⁴ In cases where the monomer relaxation

time was forced into the fit for relaxation time for the first decay, the second relaxation time corresponded to a size of 40-50 nm. The fit seemed to be very insensitive to the monomer size and was mainly fitting the larger size with the exponential in the fit with the monomer relaxation time contributing very little as can be seen in Fig C12a-d. The volume fraction of the particles of larger size given by the ratio of A_1/A_2 , is seen to fluctuate wildly with very small changes in the particle size. This leads to the conclusion that the relaxation times returned from the DLS for the samples with excipients in them were higher than those corresponding to monomer size by 3-4 times. The increase could not be accounted for just by the increase in the solvent viscosity as that increase is only about 30%. Free monomer present in the cluster samples should not be responsible for this increase, as it has no effect on the monomer by itself at the same concentration. Therefore, there is some other phenomenon present which is causing these relaxation times to go up.

Also the samples were not sterile filtered because sterile filtration resulted in too much material loss and we did not have enough material to characterize the post sterile filtered material. In general, sterile filtration would serve to remove larger aggregated species from the samples which may interfere with the results from the DLS. In our specific case, we later studied similar systems and found that sterile filtration did not affect the size distribution obtained from DLS and also did not have any effect on the shape of the ACF in most cases. These complications in DLS were not known at the time of publication of the work and therefore the appendix is being added to point out the uncertainties in DLS.

C.2. ELISA

After analysis of the ELISA data with a four-parameter logistic fit, the relative EC50s were found to be 1.38 ± 0.47 for the LD250:100 sample and 1.13 ± 0.84 for the C 220:70 sample, compared with 1.00 ± 0.36 for the unprocessed sample. After verifying the shape of the sigmoidal curve on the Fig. C8, these were determined to be comparable within one standard deviation. Since this is a capture ELISA using polyclonal antibody mixtures to both capture and detect sheep IgG, binding depends upon maintenance of multiple epitopes in the sheep antibody structure. If one epitope on each antibody has altered structure, binding would be reduced; alternatively, if a fraction of all antibodies have multiple compromised epitopes, this would also result in decreased binding and higher EC50 values. We thus conclude that the majority of the antigen binding sites are maintained during the centrifugation and lyophilization steps, keeping the protein stable and intact.

C.3 EQUILIBRIUM MODEL FOR CLUSTER FORMATION

The model we use here is based on an approach originally introduced to qualitatively understand cluster formation of colloids suspended in apolar solvents.^{10, 11} Specifically, we adopt a generalization put forth by Johnston et al.⁵ to study aqueous, protein nanocluster dispersions which accounts for the fractal dimension of the clusters and the possibility of tunable depletion interactions.

The model assumes a hierarchy of multi-scale interactions that drive the formation of clusters shown schematically in Fig. 4.1a. Here, the primary attraction between protein monomers is assumed to be an osmotic depletion force induced by the presence of an extrinsic crowding co-solute (in this case, trehalose). The origin of the

depletion attraction is entropic. Configurations where two proteins are in contact are favored statistically over those in which the proteins are separated in solution because the former excludes trehalose from a smaller overall volume. Since the diameter of trehalose is considerably smaller than that of a protein monomer, the inter-protein depletion interaction is short-ranged. This kind of depletion attraction is commonly described by the Asakura-Oosawa effective pair potential^{6,7}

$$\frac{V_{\text{dep}}}{k_B T} = -\frac{\phi_E}{2} \left(1 - \frac{r - 2R}{2R_E}\right)^2 \left(2 + \frac{3R}{R_E} + \frac{r - 2R}{2R_E}\right) \quad (\text{C4})$$

where r is the center to center distance between two protein molecules, R is the protein molecular radius, ϕ_E is the volume fraction of the extrinsic crowder, and R_E is the crowder radius.⁸ Since the strength of the depletion attraction depends on ϕ_E (as is expected for an osmotic attraction), it can be tuned experimentally by modifying the crowder concentration. Depletion attraction due to poly(ethylene glycol) (PEG) has been demonstrated as being the dominant interaction modulating protein-protein interactions for proteins with weakened electrostatic interactions.⁹⁻¹³ As a result, other short-range attractive interactions arising from hydrogen-bonding, hydrophobic forces, etc., as well as longer-range van der Waals interactions—while also present in the protein system—are assumed to play a secondary role in cluster formation at high crowder concentrations.⁵

Proteins also interact through electrostatic repulsions. In this work, the pH of the solution is adjusted to be near the pI of the protein which minimizes the net charge on the protein molecules.¹⁴ As a result, electrostatic repulsions between two isolated proteins in solution are expected to be weak compared to the short-range attractions, especially under conditions of high crowder concentration (see Fig C7). However, as proteins begin to form a cluster (i.e., each protein acquires multiple contacting neighbors), contributions

from the weak—but longer-range—electrostatic repulsions begin to accumulate. Qualitatively, the balance between attractions and repulsions determines the equilibrium cluster size. For a discussion of why electrostatic screening inside of the protein clusters may be considerably weaker than that between two proteins isolated in aqueous buffer, see Harada et al.¹⁵ and Johnston et al.⁵ The aforementioned balance between short-range attractions and longer-range repulsions is expected to produce interactions between equilibrium-size clusters that are net repulsive, which helps create colloidally-stable nanocluster dispersions that do not readily gel.

In the free energy model for cluster formation, proteins are assumed to assemble into spherical clusters of radius R_c comprising n_c monomers, as shown in Fig. 4.1a. If the strength of the depletion interaction between two neighboring proteins is given by $-\epsilon$ and each protein has C nearest neighbors in the cluster interior, then the effective depletion contribution to the free energy per protein molecule in the cluster interior will be $-\epsilon C/2$. The missing attractive interactions for proteins on the cluster surface are accounted for by adding an effective surface energy term ($4\pi R_c^2 \gamma$), where the surface tension is approximated as $\gamma = \epsilon/4\pi R^2$. Together, the depletion attractions contribute the following to the free energy of cluster formation,

$$F_{att} = -\frac{\epsilon C n_c}{2} + 4\pi R_c^2 \gamma \quad (C5)$$

Assuming that the charges are negligibly screened within the nanocluster (as discussed earlier⁵), their Coulombic self-energy can be approximated as

$$F_{rep} = \frac{3\lambda k_B T n_c^2 q^2}{5R_c} \quad (C6)$$

where λ is the Bjerrum length ($\lambda = e^2/4\pi\epsilon_r\epsilon_0k_BT$), ϵ_r is the relative permittivity of the medium, ϵ_0 is the vacuum permittivity, and q is the charge per protein monomer.

The cluster free energy also depends upon the translational and combinatorial entropy of the counterion dissociation from the proteins in the cluster to the solution. The final free energy per protein of a cluster is given by^{16,17}

$$\frac{f_c}{k_BT} = -\frac{\epsilon C}{2k_BT} + \frac{4\pi R_c^2 \gamma}{k_BT n_c} + \frac{3\lambda n_c q^2}{5R_c} + 2q \left[\ln \left(\frac{q}{q_0} \right) - 1 \right] \quad (C7)$$

where q_0 is the charge that minimizes f_c for weakly charged particles in the limit of low zeta potential.¹⁶

Minimizing with respect to R_c (or n_c) gives the following expression for the equilibrium aggregation number n^*

$$n^* = \frac{10\pi\gamma R^3}{3k_BT\lambda q^2} \quad (C8)$$

As qualitatively discussed above, clusters are predicted to grow with increasing attractions (ϵ) and shrink with increasing charge q (electrostatic repulsion).

To take into account the porosity of the protein nanoclusters, we modify the original model by expressing the cluster radius as

$$R_c = \left(\frac{n_c}{k} \right)^{\frac{1}{\delta_f}} \quad (C9)$$

where δ_f is the fractal dimension (estimated from static light scattering experiments of one protein cluster dispersion to be 2.6 from Johnston et al.⁵) and k is a constant of order 1. For $q = q_0$,^{5,16} the resulting equilibrium aggregation number is given by

$$n^* = k^{\frac{3}{3-2\delta_f}} \left\{ \frac{5(\delta_f - 2)\varepsilon R}{3(\delta_f - 1)k_B T \lambda q_0^2} \right\}^{\frac{\delta_f}{2\delta_f - 3}} \quad (C10)$$

To connect with experimental observables, we can substitute $\varepsilon = -V_{dep}(2R)$ from the depletion potential of eq. C4 into eq. C10. Furthermore, we can use a prediction, $q_0^2 = (1400 * n_d / cb^3) e^{-2-\lambda/b}$, obtained from a simple statistical mechanical site-binding model^{16,17} for the translational and combinatorial entropy of counterion dissociation accounting for the experimentally determined partial molar density of the protein in the solution of 1400 mg/ml. Here, n_d is the number of dissociable sites on a protein surface, and b is the minimum distance between a counterion and a charge on the protein surface. Combining these relations and eq. C3, C9, and C10 with $\phi_E = c_E/1580$ (1580 is the partial molar density of the trehalose in the solution¹⁸) yields the following relation for cluster diameter -

$$D_c = 2R \left\{ \frac{20\pi(\delta_f - 2)R^4 b^3 e^{2+\lambda/b} c_E c}{1400 * 1580 * 9k^2 n_d (\delta_f - 1)\lambda} \left[1 + \frac{3R}{2R_E} \right] \right\}^{\frac{1}{2\delta_f - 3}} \quad (C11)$$

This relation is presented, in simplified form, as eq. (2) of the main text. Importantly, Equation C11 (parameter values provided in Table C6) captures the experimentally observed trends in cluster diameter with changes in extrinsic crowder concentration and protein concentration (Figs. 4.2a-e). This agreement provides further evidence that the dispersed protein clusters are in an equilibrium state.

C.4 TURBIDITY AND ADDITIONAL ELECTRON MICROSCOPY OF THE DISPERSION

The turbidity of the dispersion is quantified in Fig. C1 in the visible range (400-700 nm). Low turbidity is seen in the visible region as quantified by an average turbidity of 0.335 cm^{-1} and absorbance of 0.15 for a path length of 1 cm from 400-700 nm. The dispersion appears transparent to the naked eye, which is highly desirable as a guide during subcutaneous administration of the formulation. The high level of transparency is due to the refractive index of the porous cluster being close to that of the solvent with dissolved trehalose.⁵ Also, the small size of the clusters $< 100 \text{ nm}$ leads to relatively low scattering cross sections. The dispersion has a significant absorbance in the UV region due to the aromatic amino acid residues present in the protein molecules and greater Mie scattering.

C.5 DISPERSIONS WITH CONCENTRATIONS OF 320 MG/ML

In order to demonstrate the robustness of the clustering concept in general and the centrifugal filtration concept in particular, high concentration dispersions of proteins at a concentration of 320 mg/ml were made with the properties given in Table 4.1 and Fig. C4. The dispersions had 70 mg/ml trehalose for providing depletion attraction and stability while still maintaining the isotonicity of the dispersion. The dispersions were syringeable as opposed to solutions which typically gel and aggregate at these concentrations.⁵ The diameter was observed to be 40 nm relative to a value of 37 for the C 220:70 case in Table 4.1. In contrast, the model predicts a larger size increase with protein concentration. The protein was found to be monomeric after dilution by SEC despite the high protein concentrations in the dispersions.

C.6 ROOM TEMPERATURE STORAGE STABILITY

Additionally, the dispersions were observed to be stable for 10 days when stored at room temperature with excellent retention of the size and the % monomeric protein upon dilution as can be seen in Table C4 and Fig. C6. The dispersion also remained clear and there was no phase separation observed during storage, again supporting the concept of nanoclusters at equilibrium.

C.7 EFFECT OF pH ON CLUSTER SIZE

Dispersions were formed at two different pH values of 6.4 (LD 250:100) at the isoelectric point and 6.9 (LD 200:80) to examine the effect of pH on the cluster size. The dispersion properties are contrasted in Table C5. The sizes are seen to be similar at the same protein concentration with the pH having little effect on the dispersion size in this narrow range. The protein charge does not change appreciably within 1 or 2 pH units of the pI leading to the size not changing appreciably as can be seen from equation C10.^{14,19} Also, the sheep IgG being polyclonal has a broader distribution of pIs and hence charge on the protein molecules therefore the charge distribution within the clusters may remain oblivious to pH over a significant range of pH values (2-3 pH units around the pI). These cluster formed at pH 6.9 also dissociated back to monomer upon dilution in buffer.

C.8 CD

Analysis of the circular dichroism spectra demonstrates maintenance of protein secondary structure throughout the centrifugation, lyophilization and dilution processes. Antibodies are composed primarily of beta sheet secondary structure elements and turns, and the data shows only 3% to 5% alpha helices of the total structure. Circular

dichroism provides only an approximation for evaluating secondary structure, but the agreement of the data in Table C7 supports our conclusion based on the ELISA data that antibody structure is maintained throughout the processing steps.

C.9 LONG TERM STORAGE

A C 220:70 dispersion was stored at -40°C for a month and a second dispersion at the same conditions was stored for 2 ½ months. After storage, the dispersions were gently thawed at 4°C and then characterized. The size and viscosity appeared unchanged pre- and post-freezing as is shown in Table C2 and Fig. C4. The constant size provides further evidence the nanoclusters are in an equilibrium state with the size governed by the dispersion composition. The protein is also found to be monomeric by SEC upon dilution with little change in % monomer pre- and post-freezing. The stability after 2 ½ months of storage seems to suggest the potential for long term storage in the frozen state which is a great practical advantage. The stability may result from decreased molecular mobility at low temperatures and the trehalose present in the dispersion acting as a cryoprotectant.^{20,21}

C.10 STERILE FILTRATION OF THE CLUSTERS

A nanocluster dispersion were passed through a 0.22 micron filter membrane with ~220 mg/ml sheep IgG and 70 mg/ml trehalose as shown in Table C9 and Fig. C10. The dispersion properties including concentration of protein, viscosity and nanocluster size were retained after sterile filtration of the dispersion. The viscosity of the dispersion and the nanocluster size (36 nm) were low enough for sterile filtration to be feasible, which

would be desirable for biopharmaceutical processing. Due to the large initial volume needed for filtration, the entire concentration process was carried out in a Millipore Amicon filter (used for buffer exchange as described in the materials and methods section).

Model parameter	Value
Fractal Dimension (δ_f)	2.5
Dielectric constant (ϵ_r)	15
No. of dissociable sites per unit area of colloid surface (σ_s , nm ⁻²)	0.2
Distance between opposite charges in an ionic bond (b , nm)	0.22
Radius of the protein monomer (R , nm)	5.5

Table C1: Model parameters for Sheep IgG. Input variables used in the model proposed by Johnston et al.⁵ and used to generate the plots in Figs. 4.1b, 4.2b, and 4.2e are provided.

c (mg/ml)	D_c (nm)	St Dev in D_c (nm)
220	40	12
190	32	7
170	23	3
150	15	3

Table C2: D_c of C 220:70 nanoclusters and after subsequent sequential dilutions with buffer. The distributions for the D_c are provided in Fig. C3 and the means are in Figs. 4.2b and 4.2e. The starting solution was at a protein concentration of 70 mg/ml and was centrifuged for 35 minutes.

c (mg/ml)	D_c (nm)	St Dev in D_c (nm)
250	51	9
230	42	7
210	32	5
120	17	9
60	13	4

Table C3: D_c of LD 250:100 nanoclusters and after subsequent sequential dilutions with buffer. The distributions for the D_c are provided in Fig. 4.2d.

c (mg/ml)	D_c (nm)	St Dev in D_c (nm)
250	77	8
200	59	8
160	43	9
120	18	1
70	11	2
40	12	2.5

Table C4: D_c of C 250:250 nanoclusters and after subsequent sequential dilutions with buffer. The distributions for the D_c are provided in Fig. C5 and the means are in Fig. 4.2e. The starting solution was at a protein concentration of 50 mg/ml and was centrifuged for 68 minutes.

Time (days)	D_c (nm)	% monomer by SEC
0	49 ± 13	98.6
7	44 ± 5	-
10	47 ± 11	98.5

Table C5: D_c , viscosity and protein % monomer after room temperature storage (C 250:100). The distributions for the D_c s are provided in Fig. C6.

Sample name	c_E (mg/ml)	c (mg/ml)	dispersion pH	D_c (nm)	Std. Dev in D_c (nm)
Dilution of LD 250:100	84	210	6.4	32	5
LD 200:80	80	200	6.9	33	10

Table C6: Effect of pH on D_c . LD 200:80 in pH 6.9 and a dilution of LD 250:100 at pH 6.4 are contrasted to observe the effect of protein charge.

Sample	Helix	Strand	Turn	Unordered
Control	0.04	0.18	0.23	0.33
LD 250:100	0.03	0.17	0.22	0.38
C 220:70	0.02	0.19	0.23	0.34

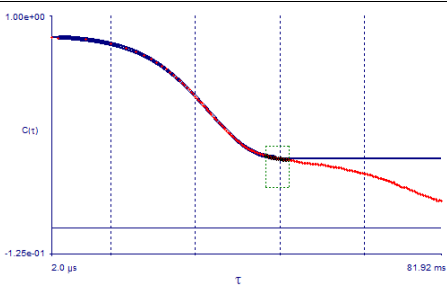
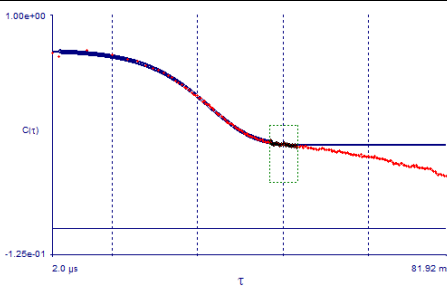
Table C7: Circular Dichroism for protein secondary structure. The fraction of protein in the different secondary structures for both LD and C samples compared to the native protein.

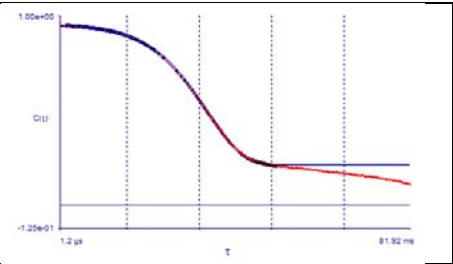
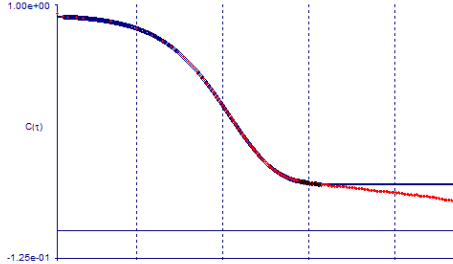
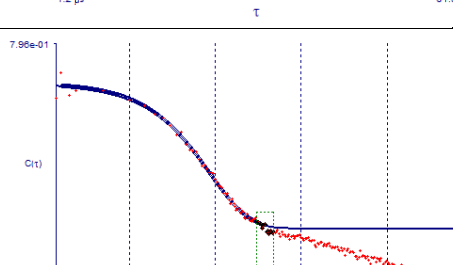
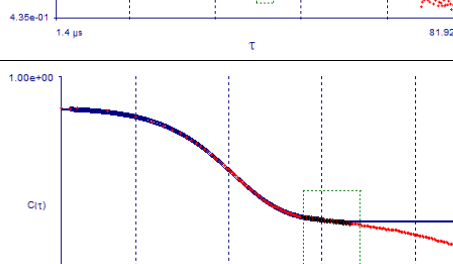
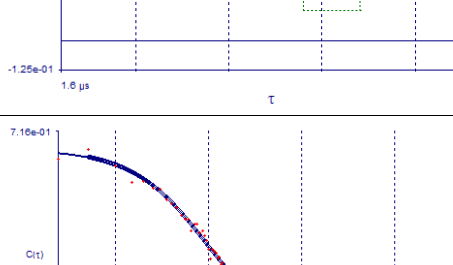
State	Viscosity (cP)	Intrinsic Viscosity	D_c (nm)	Std. Dev. in D_c (nm)	% Monomer by SEC
Pre-freezing	36±9	9	36	9	98.6
Post-freezing (1 month)	35	9	31	10	-
Post-freezing (2 ½ month)	-	-	39	5	99.5

Table C8: D_c , viscosity and protein % monomer before and after freezing and thawing (C 220:70). The distributions for the D_c s are provided in Fig. C9. This was the same dispersion as in Fig. C1.

State of dispersion	c (mg/ml)	Viscosity (cP)	Intrinsic viscosity	D_c (nm)	St. Dev in D_c (nm)	% Monomer by SEC
Pre-filtration	220	36±9	9	33	4.5	99.9
Post-filtration	200	26	10	30	3.31	98.6

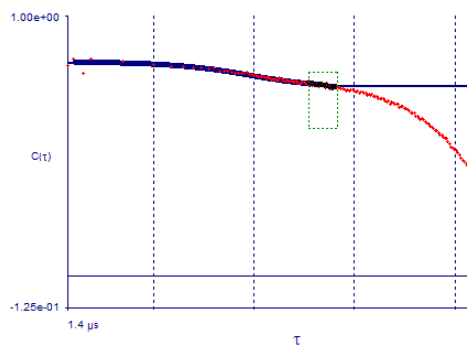
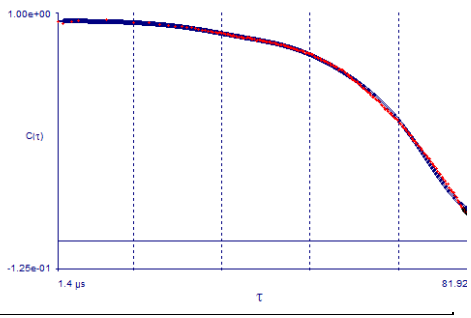
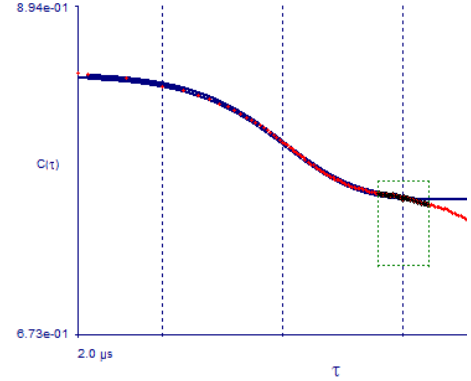
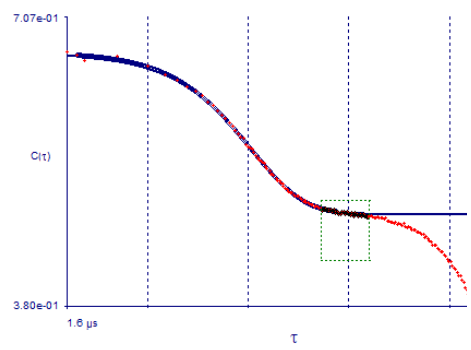
Table C9: D_c and viscosity of a C 220:70 nanocluster dispersion before and after sterile filtration through a 0.22 μm poly(vinylidene difluoride) (PVDF) filter. The distributions for the D_c s are provided in Fig C10. The starting solution at a protein concentration of 48 mg/ml was centrifuged for 27 minutes. After forming the nanoclusters, a portion was saved and a portion was filtered. Both samples were then frozen, stored for a month and thawed, and then analyzed.

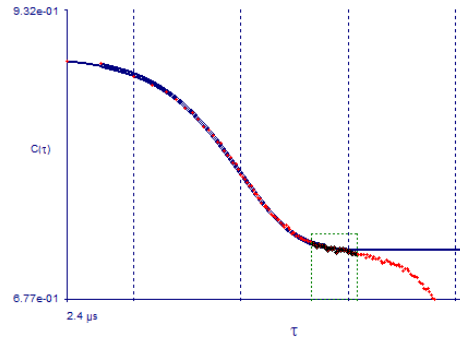
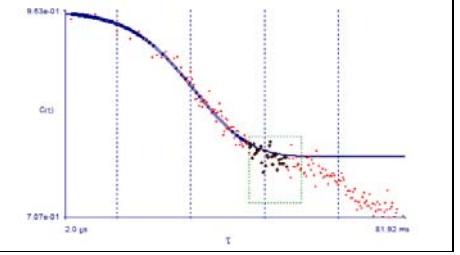
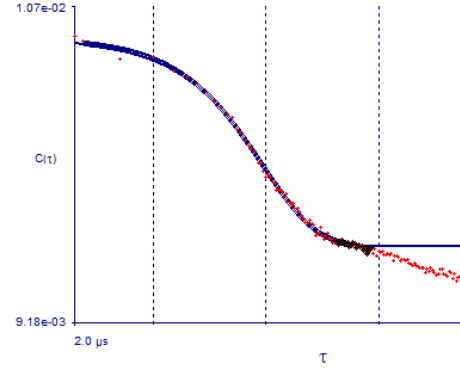
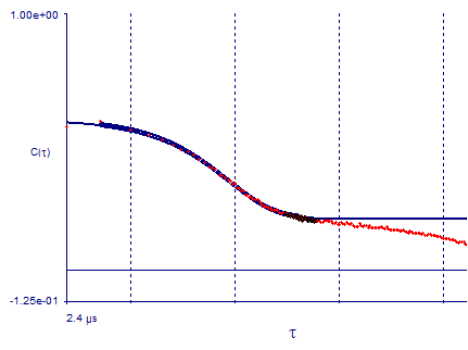
c (mg/ml)	c_E (mg/ml)	Angle	Diameter (nm)	Diameter st dev (nm)	Count rate (kcps)	Correlation function
122	70	150	18.4	4.9	76.4	
176	70	150	29.9 (Table C10 continued on the next page)	18.6	18.875	

201	70	150	35	7.5	27.725	
225	70	150	39.1	9.6	45.35	
226	70	150	41	13.3	19.275	
191	59	150	35	16.7	40.9	
165	51	150	21.8 (Table C10 continued on the next page)	13.8	14.3	

149	46	150	15.9	5.9	199.65	
247	247	150	75.6	9.5	59.575	
197	197	150	55.5	81.5	81.5	
156	156	150	42.3	19.25	19.25	
122	122	150	18.4 (Table C10 continued on the next page)	3.9	213.8	

67	67	150	14.7	1.9	136.4	
40	40	150	10.1	2.9	76.15	
250	100	150	48.6	11.4	88.2	
210	84	135	33.6 (Table C10 continued on the next page)	3.9	81.6	

120	48	135	17.3	4.9	22.6	
60	24	150	14.8	3.8	201.8	
200	100	150	38.4	8	221	
312	70	135	34.2 (Table C10 continued on the next page)	21.9	50.125	

321	70	135	40.5	21.3	61.1	
254	0	150	12.6	5.1	8.8	
220	70	150	35.4	12.1	2650	
220	70	150	39.6 (Table C10 continued on the next page)	9	13	

220	70	150	39.2	5.8	57.2	
220	70	150	39.8	17.5	331	
250	100	135	46.2	5.8	164	
250	100	135	49.3 (Table C10 continued on the next page)	8.4	350	

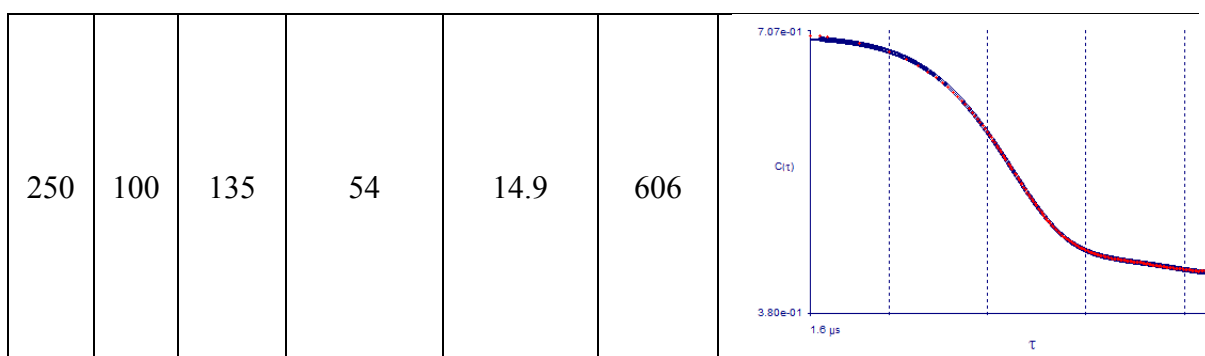


Table C10: Auto correlation functions for all of the samples analyzed by DLS in Chapter 4 with sample composition provided to relate back to the figures and tables in the paper. 200 channels were used for all the measurements.

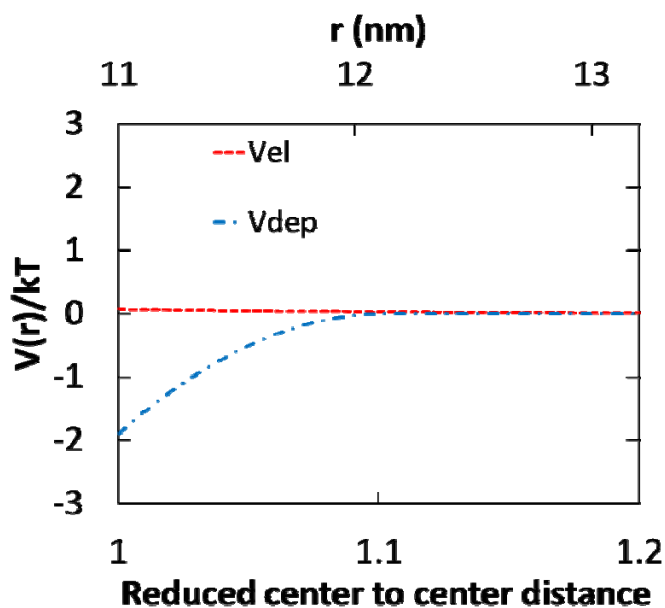


Figure C1: Potential of mean force between two protein monomers at the pI with trehalose concentration 70 mg/ml. V_{dep} is the force due to the depletion attraction from trehalose and V_{el} is the electrostatic repulsion.⁵

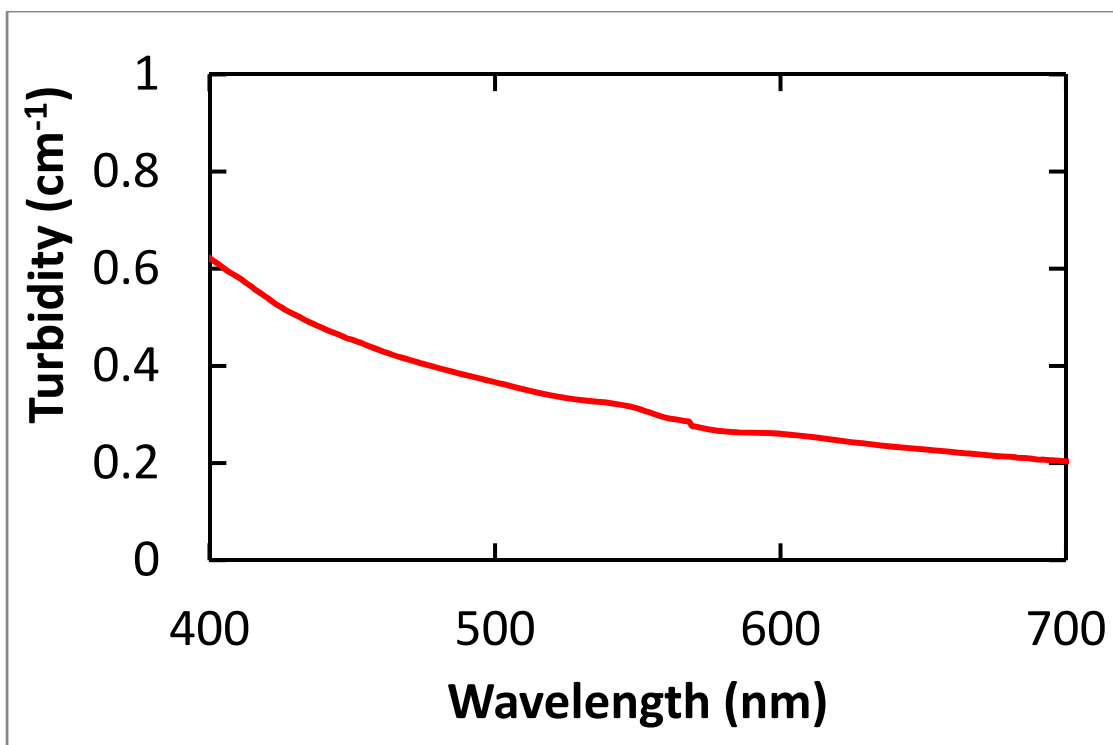


Figure C2: Turbidity of nanocluster dispersion (C 220:70) which appears transparent to the naked eye for a path length of 1 cm.

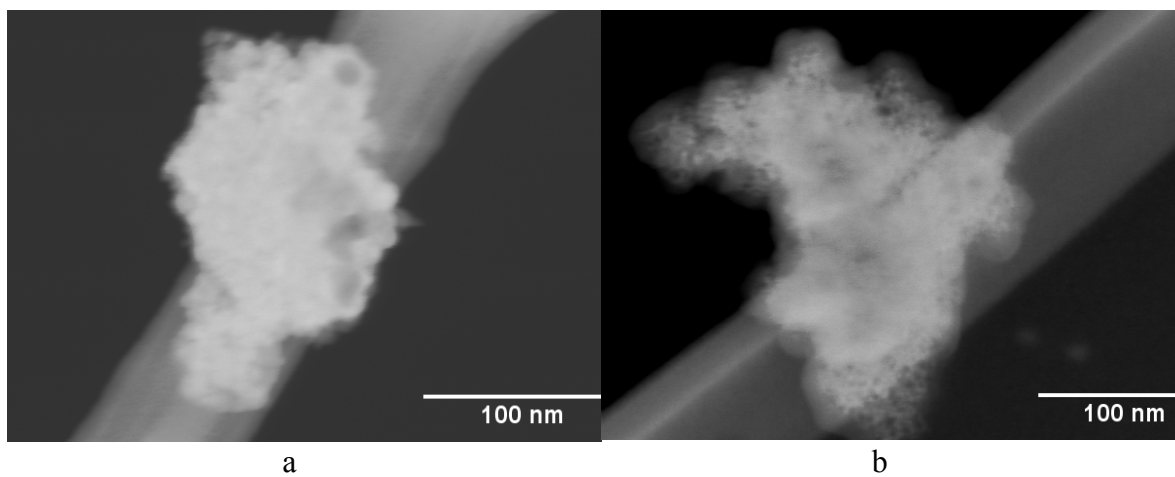


Fig. C3 continued on next page

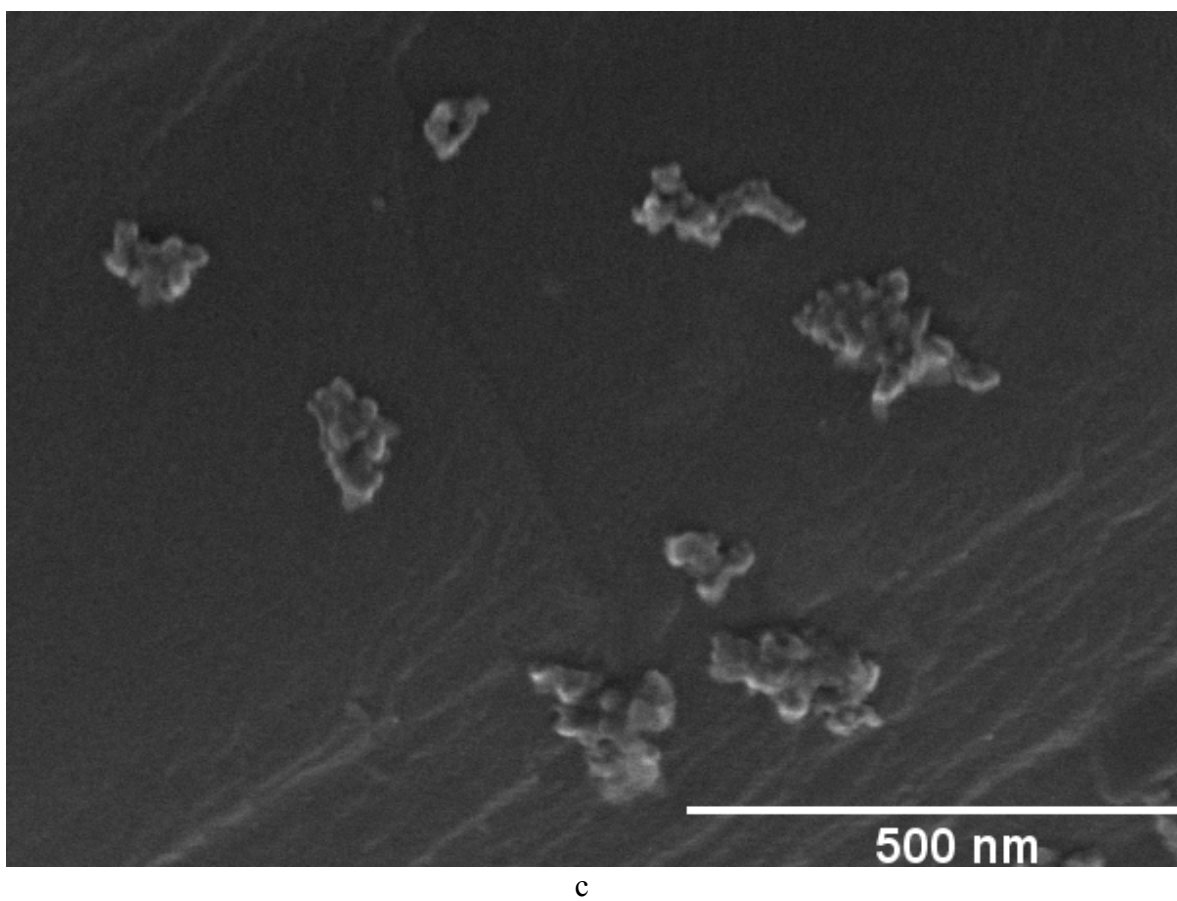


Figure C3: Additional STEM (a and b) and SEM (c) images of protein nanoclusters at $c = 270$ mg/ml and $c_E = 270$ mg/ml.

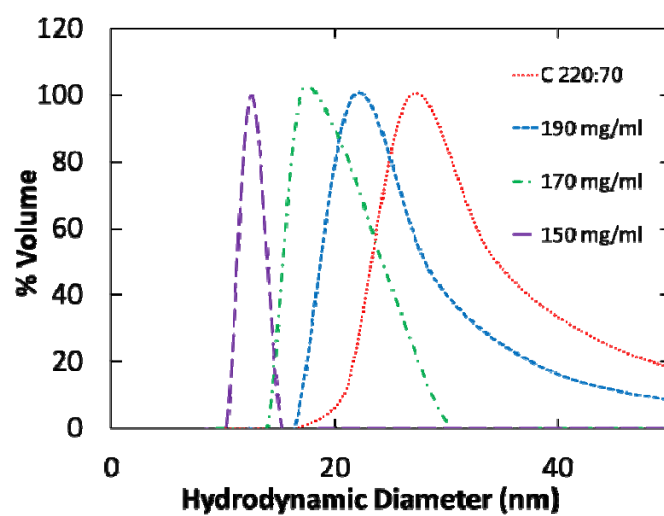


Figure C4: D_c of C 220:70 nanoclusters and after subsequent sequential dilutions with buffer. The legend gives the protein concentration with mean D_c s listed in Table C1 and Figs. 4.2b and 4.2e.

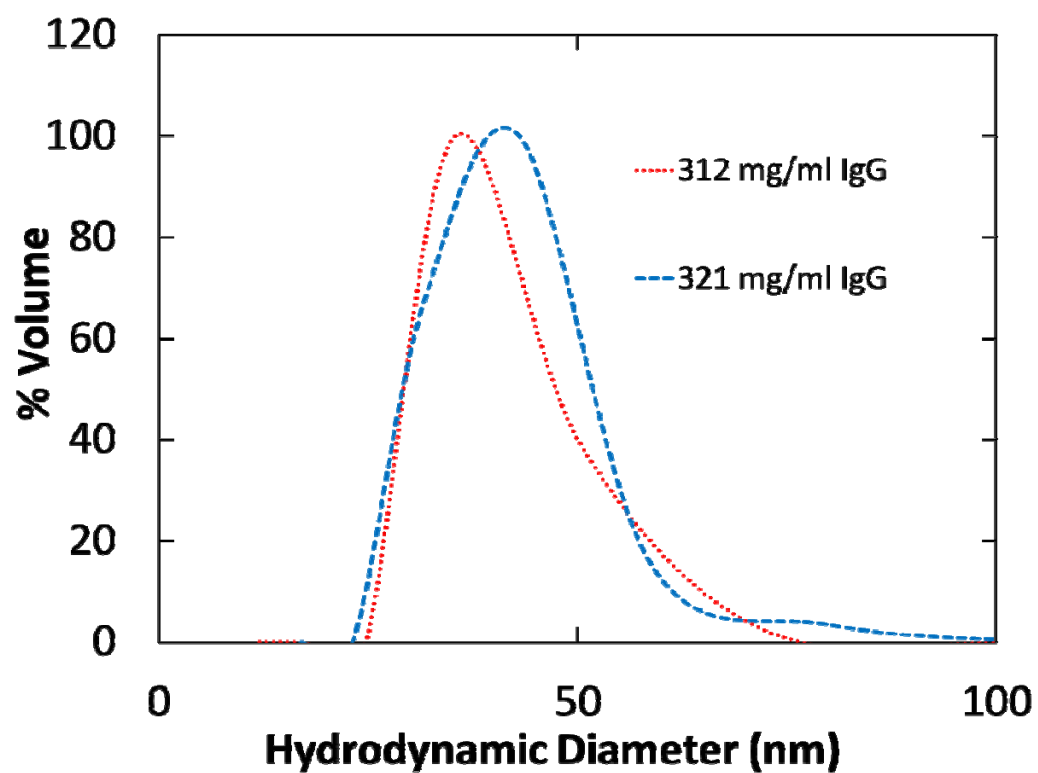


Figure C5: D_c of C 320:70 nanoclusters at an ultra-high protein concentration. The D_c distributions for two different samples are provided with the mean D_c listed in Table 4.1.

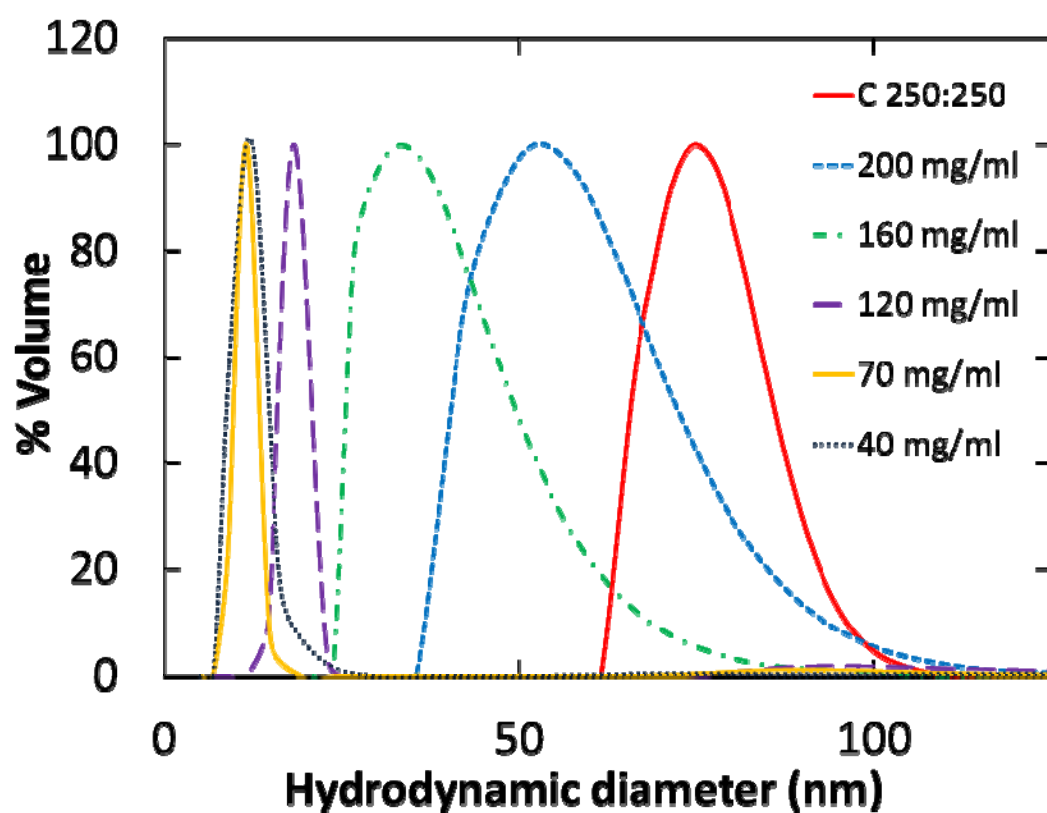


Figure C6: D_c of C 250:250 nanoclusters and after subsequent sequential dilutions with buffer. The legend gives the protein concentration with mean D_c s listed in Table C3 and Fig. 4.2e.

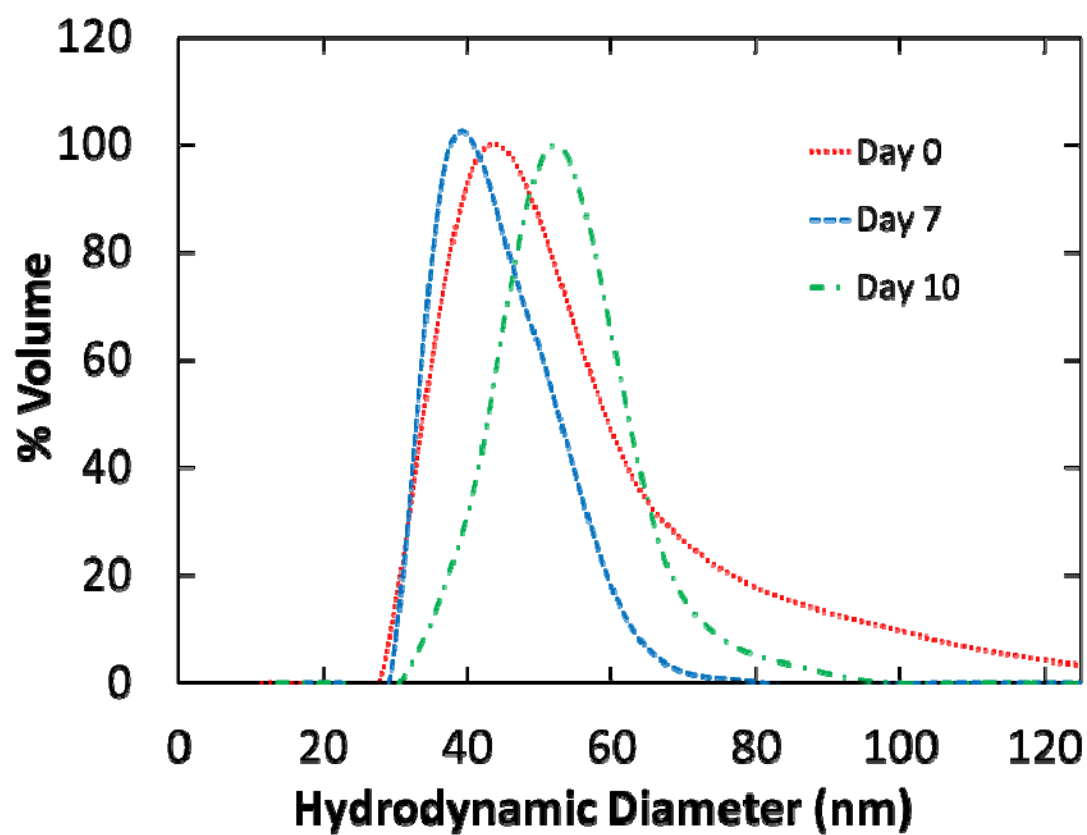


Figure C7: D_c of C 250:100 nanoclusters upon storage of the aqueous dispersion at 23°C for up to 10 days. The mean D_c s are listed in Table C4.

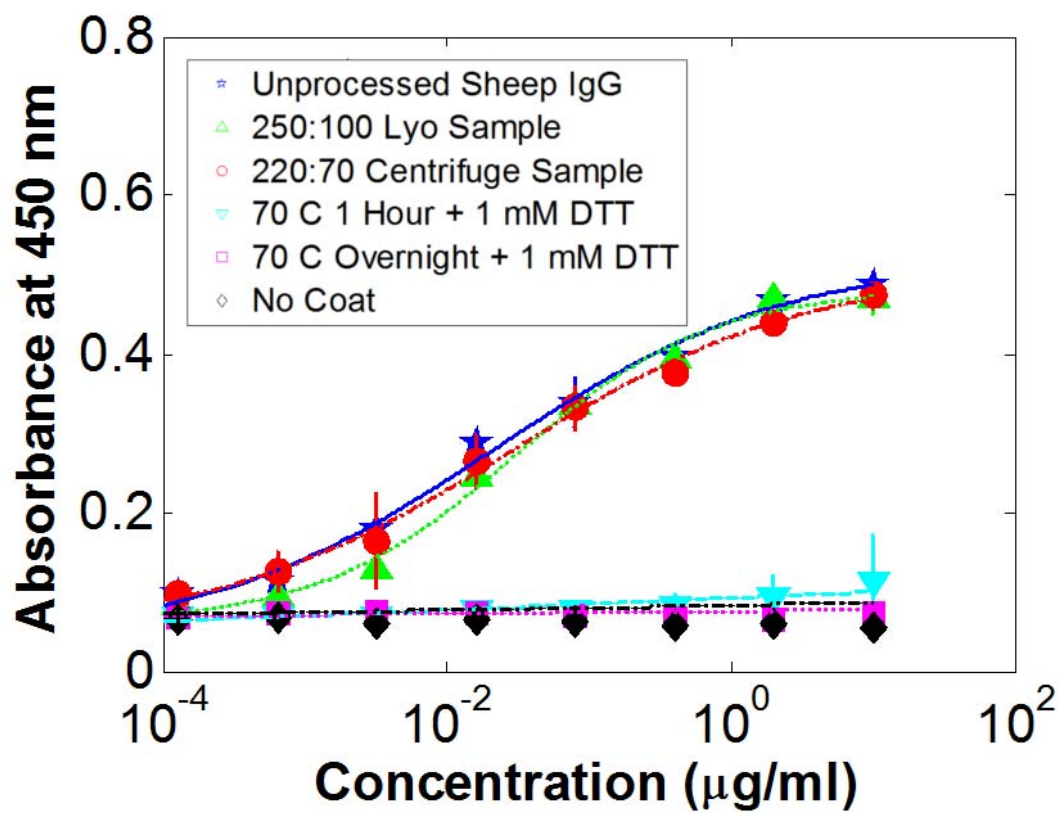


Figure C8: ELISA data for diluted protein samples. The raw data used for calculating the relative EC50 is shown along with the negative controls.

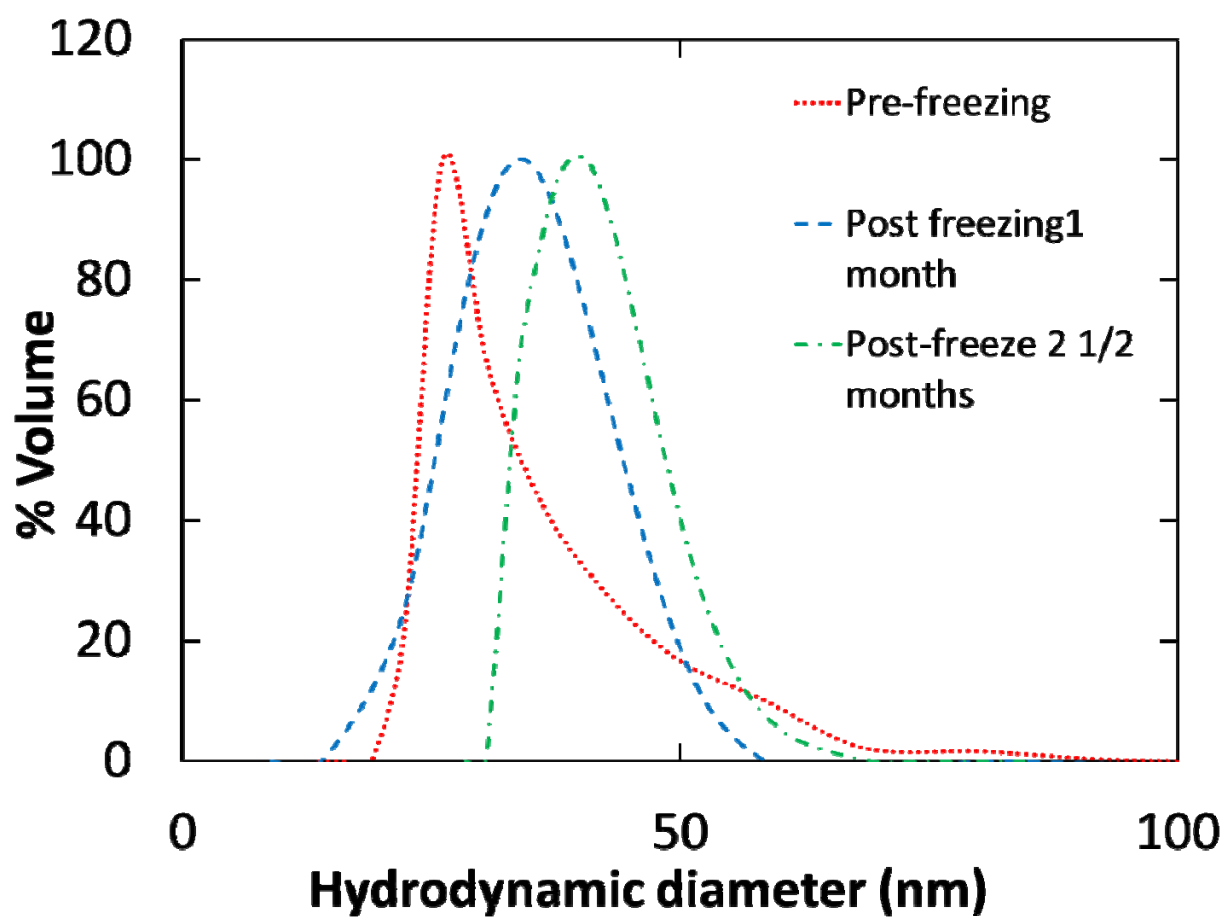


Figure C9: D_c s of C 220:70 nanoclusters before freezing, and after either 1 or 2.5 months of frozen storage at -40°C followed by thawing. The mean D_c s are listed in Table C8.

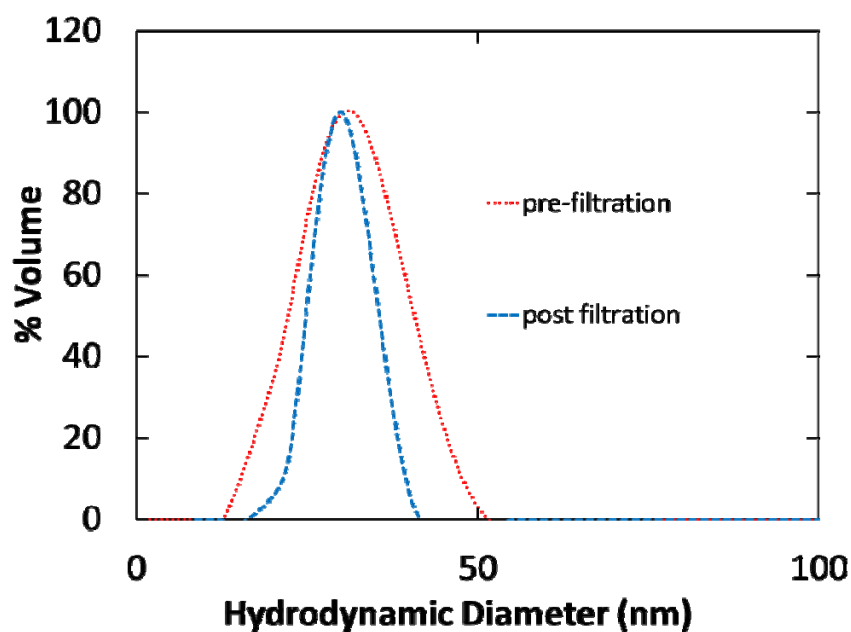


Figure C10: D_c of C 220:70 nanoclusters before and after sterile filtration through a 0.22 μm filter. The mean D_c s are listed in Table C9.

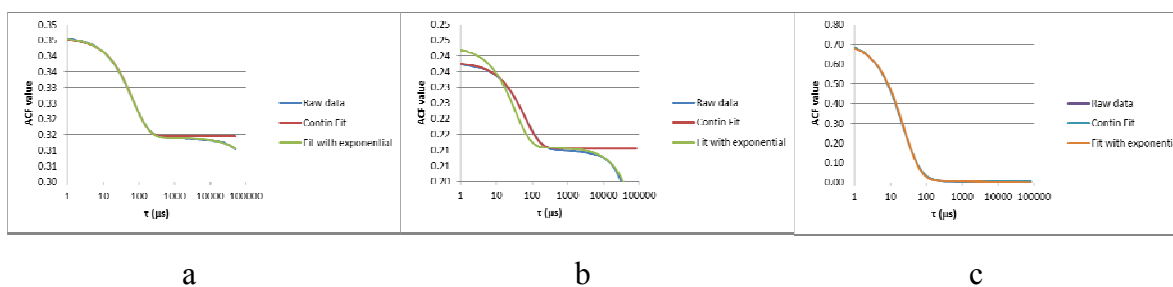


Figure C11: Fits for the ACFs of a. cluster, b. cluster with monomer size, c. In all cases y-axis is the relaxation time in microseconds and the x-axis is the correlation function value.

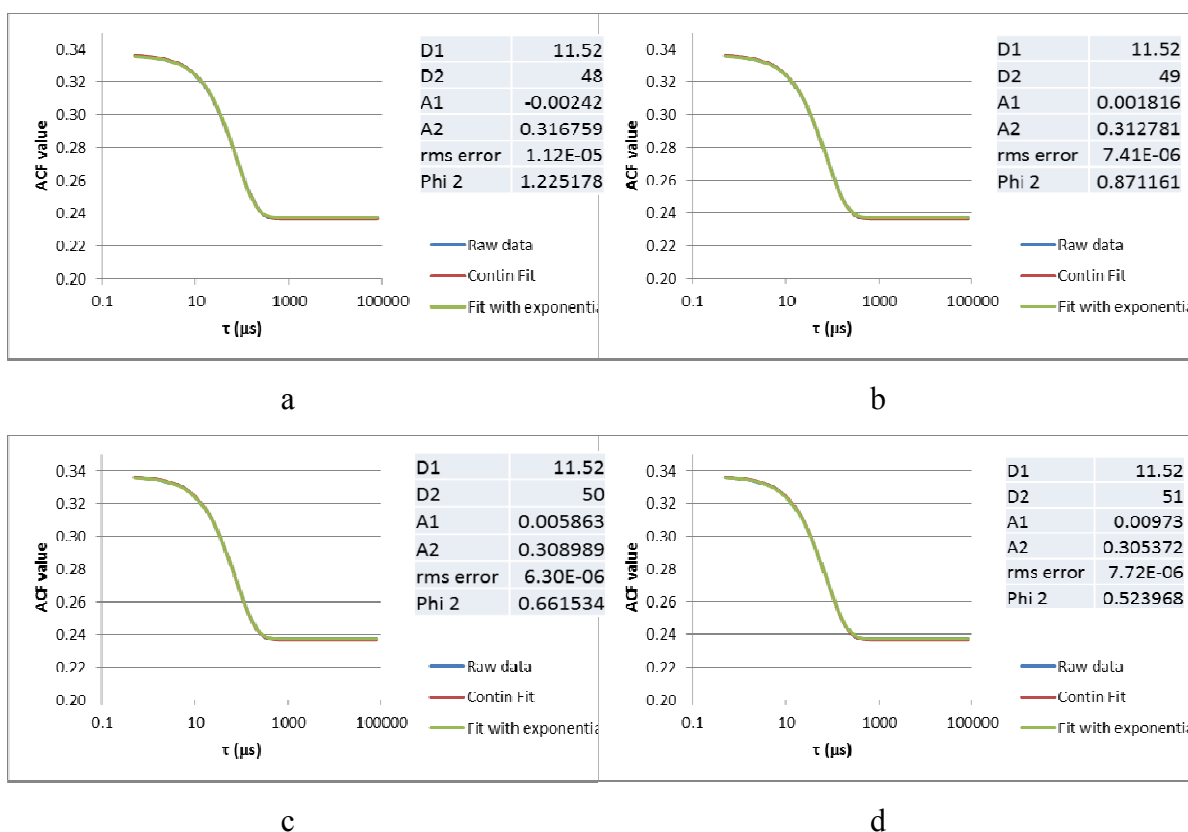


Figure C12: Fits for the ACFs with monomer relaxation time and different second diameters. In all cases Y axis is the relaxation time in microseconds and the x-axis is the correlation function value.

C.11 SUPPLEMENTARY REFERENCES

- (1) Borwankar, A. U.; Dinin, A. K.; Laber, J. R.; Twu, A.; Wilson, B. K.; Maynard, J. A.; Truskett, T. M.; Johnston, K. P. *Soft Matter* 2013, 9, 1766.
- (2) Li, Y.; Lubchenko, V.; Vekilov, P. G. *Rev Sci Instrum* 2011, 82, 053106.
- (3) Vekilov, P. G. *Ann N Y Acad Sci* 2009, 1161, 377.
- (4) Pan, W. C.; Vekilov, P. G.; Lubchenko, V. J. *Phys. Chem. B* 2010, 114, 7620.
- (5) Johnston, K. P.; Maynard, J. A.; Truskett, T. M.; Borwankar, A.; Miller, M. A.; Wilson, B.; Dinin, A. K.; Khan, T. A.; Kaczorowski, K. J. *ACS Nano* 2012.

- (6) Asakura, S.; Oosawa, F. *Journal of Polymer Science* 1958, 33, 183.
- (7) Asakura S.; Oosawa F. *J. Chem. Phys.* 1954, 22.
- (8) Tuinier, R.; Rieger, J.; De Kruif, C. G. *Advances in Colloid and Interface Science* 2003, 103, 1.
- (9) Tessier, P. M.; Lenhoff, A. M. *Current Opinion in Biotechnology* 2003, 14, 512.
- (10) Tessier, P. M.; Johnson, H. R.; Pazhianur, R.; Berger, B. W.; Prentice, J. L.; Bahnson, B. J.; Sandler, S. I.; Lenhoff, A. M. *Proteins-Structure Function and Genetics* 2003, 50, 303.
- (11) Kulkarni, A. M.; Chatterjee, A. P.; Schweizer, K. S.; Zukoski, C. F. *Journal of Chemical Physics* 2000, 113, 9863.
- (12) Rosenbaum, D. F.; Zamora, P. C.; Zukoski, C. F. *Phys Rev Let* 1996, 76, 150.
- (13) Lewus, R. A.; Darcy, P. A.; Lenhoff, A. M.; Sandler, S. I. *Biotechnology progress* 2011, 27, 280.
- (14) Chari, R.; Jerath, K.; Badkar, A. V.; Kalonia, D. S. *Pharm. Res.* 2009, 26, 2607.
- (15) Harada, R.; Sugita, Y.; Feig, M. *J Am Chem Soc* 2012, 134, 4842.
- (16) Groenewold, J.; Kegel, W. K. *J. Phys. Chem. B* 2001, 105, 11702.
- (17) Groenewold, J.; Kegel, W. K. *Journal of Physics-Condensed Matter* 2004, 16, S4877.
- (18) Miller, D. P.; dePablo, J. J.; Corti, H. *Pharm. Res.* 1997, 14, 578.
- (19) Moody, T. P.; Kingsbury, J. S.; Durant, J. A.; Wilson, T. J.; Chase, S. F.; Laue, T. M. *Analytical Biochemistry* 2005, 336, 243.
- (20) Shire, S. J.; Shahrokh, Z.; Liu, J. J. *Pharm. Sci.* 2004, 93, 1390.
- (21) Wang, B.; Tchessalov, S.; Warne, N. W.; Pikal, M. J. *J Pharm Sci* 2009, 98, 3131.

Appendix D: Characterization of structures in protein formulations with high co-solute concentrations by small angle x-ray scattering

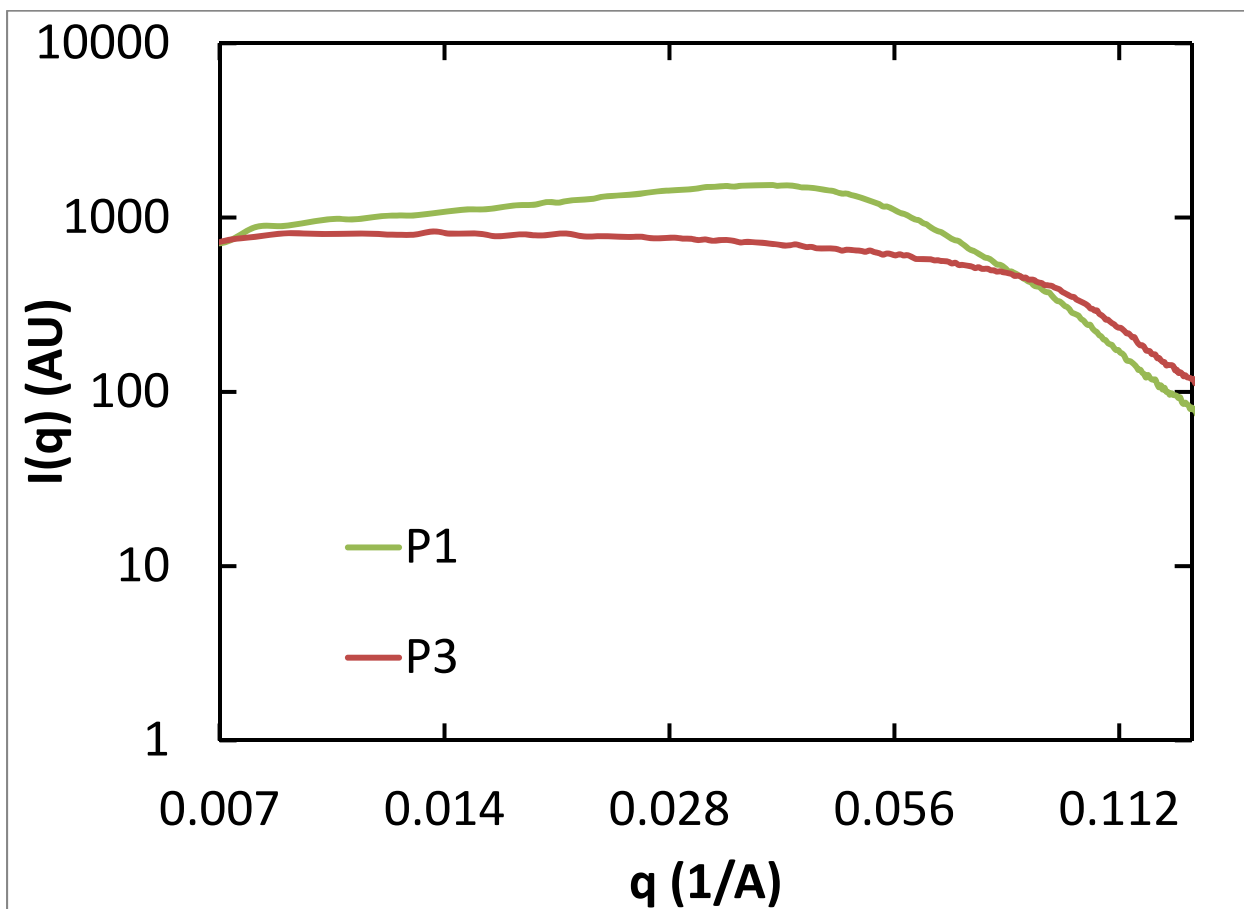


Figure D1: Intensity profile plots for the samples in the current study that were run on the rotating anode instead of the synchrotron.

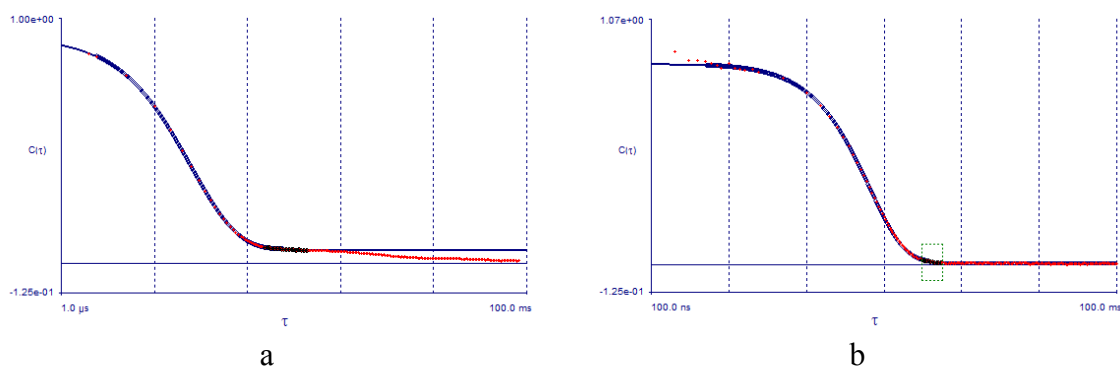


Figure D2: a. ACF for monomer sample from Fig. 5.1. b. ACF for cluster sample from Fig. 5.1.

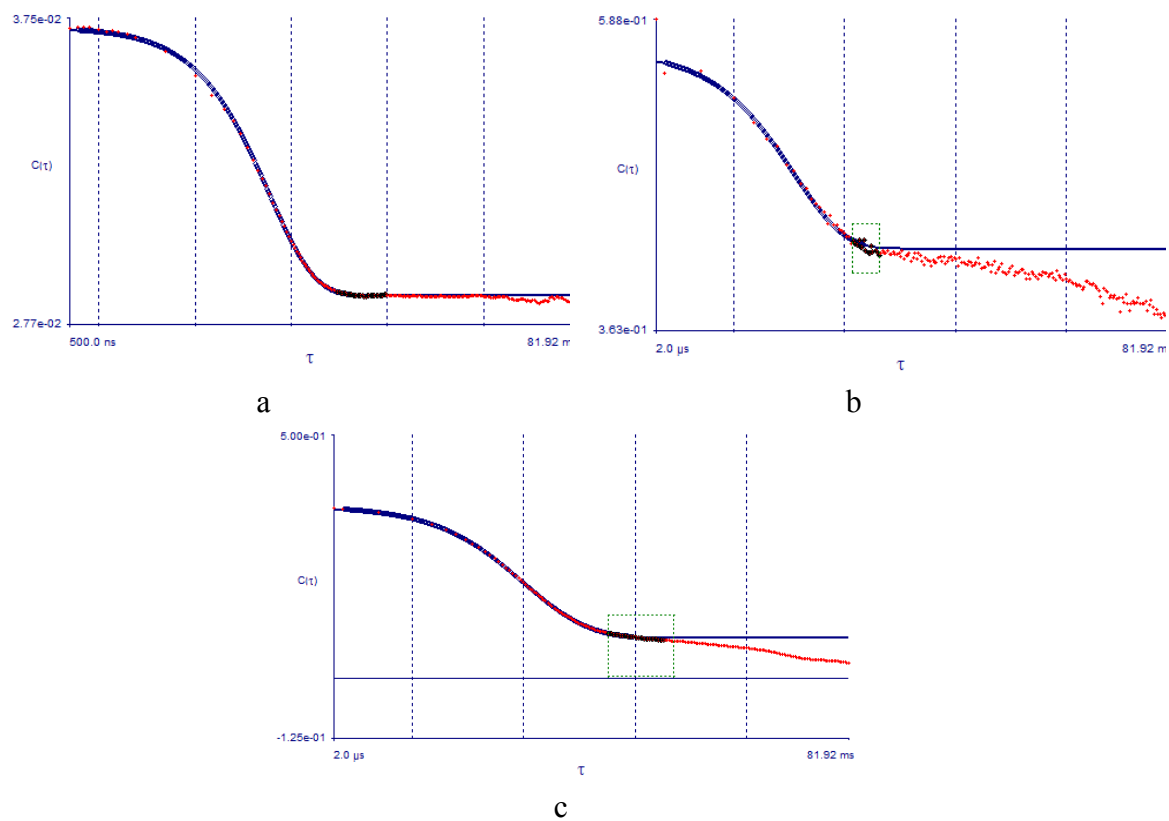


Figure D3: a. ACF for P3, b. ACF for P4 and c. ACF for P5.

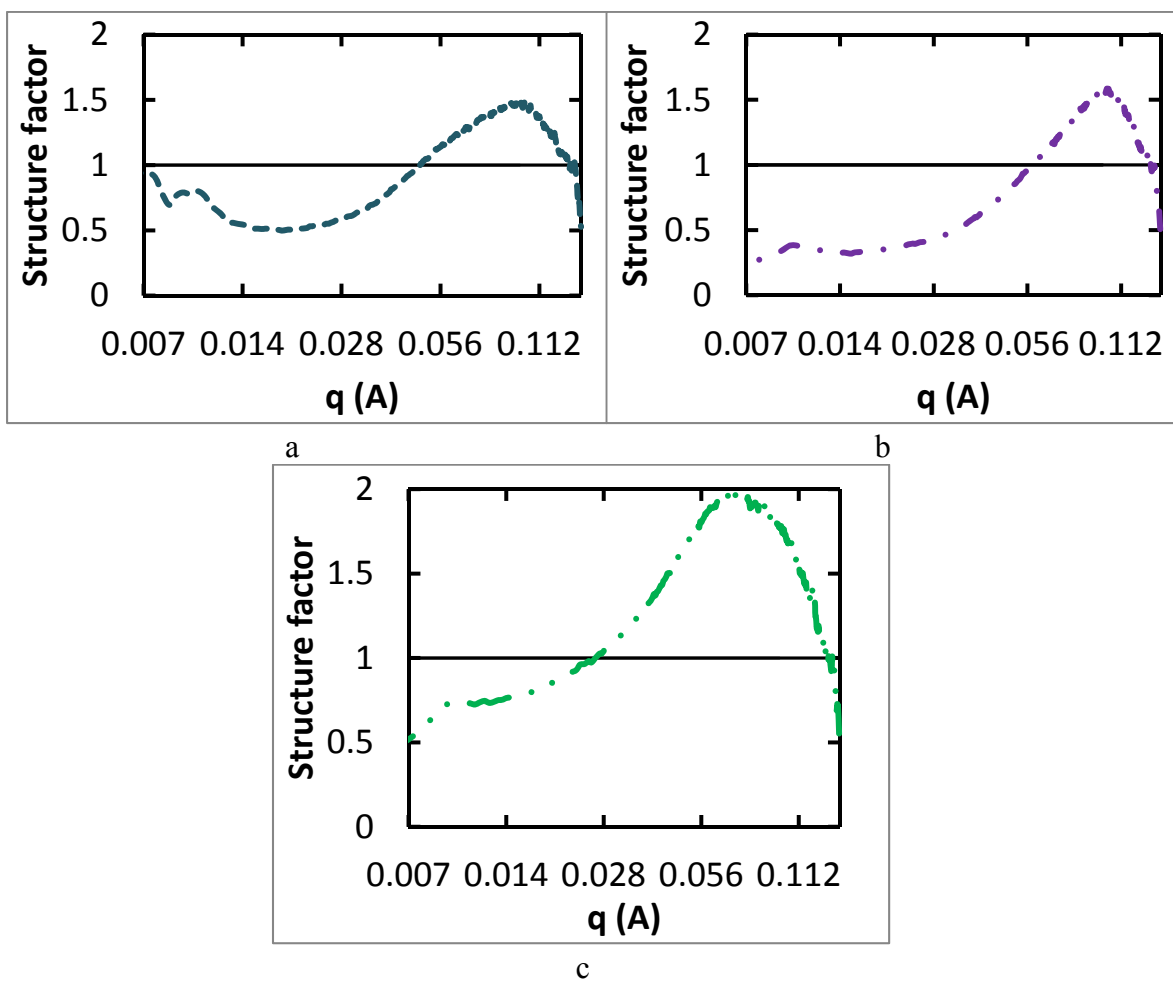


Figure D4: Structure factors of 250 mg/ml cluster samples from Fig. 2. a. P3, b. P4, c. P6.

Appendix E: Cryo-SEM for direct visualization of high concentration protein formulations at high and low co-solute concentration

Sample composition	DLS size (nm)	No of images analyzed	SEM size by hand	St dev (nm)	Comments
241 mg/ml mAb, 40 mg/ml tre, 50 mg/ml his, 17 mg/ml cit, pH 6	35.6 ± 10.4	3	60	12.3	Ok resolution. Sized several other times giving sizes of 70, 100 and 63 nm
241 mg/ml mAb, 40 mg/ml tre, 50 mg/ml his, 17 mg/ml cit pH 6	35.6 ± 10.4	3	70.8	16.1	Not good resolution. Sized several other times giving sizes of 60, 100 and 63 nm
250 mg/ml mAb, 40 mg/ml tre, 50 mg/ml his, 17 mg/ml cit pH 6	29 ± 3.7	3	97.1	20.8	good resolution. Sized several other times giving sizes of 60, 70 and 63 nm
241 mg/ml mAb, 40 mg/ml tre, 50 mg/ml his, 17 mg/ml cit pH 6	31 ± 4.5	3	62.7	12.6	Not good resolution. Sized several other times giving sizes of 60, 70 and 100 nm
250 mg/ml mAb, 40 mg/ml tre, 50 mg/ml his, 17 mg/ml cit pH 6	29 ± 5.1 (Table E1 continued on the next page)	3	115	27	Sample was sublimated prior to imaging. Excellent resolution but may be artifacts as same thing seen for monomer

Table E1: Replicate data for the samples with 240 mg/ml mAb, 40 mg/ml tre, 50 mg/ml his and 17 mg/ml citric acid.

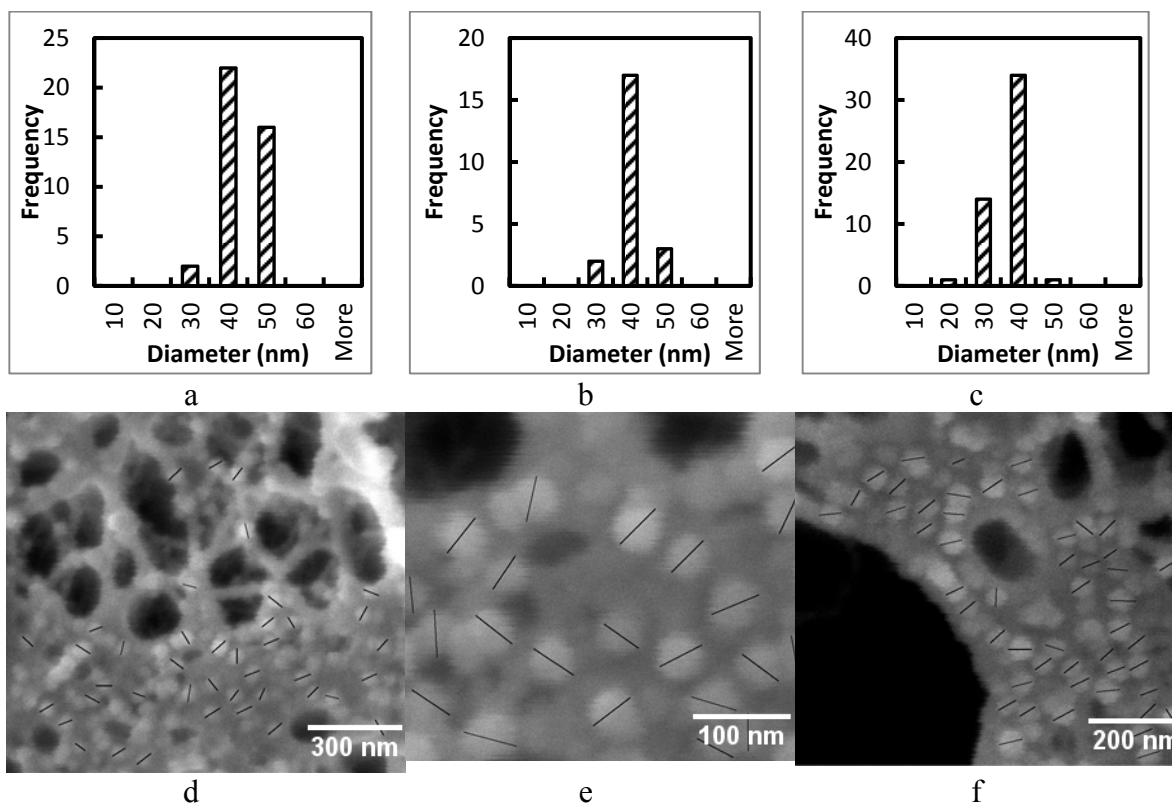


Figure E1: Sized images and histograms for particle sizes from each individual image from Fig. 6.1a-c. a and d are Fig. 6.1a, b and e are Fig. 6.1b and c and f are Fig. 6.1c.

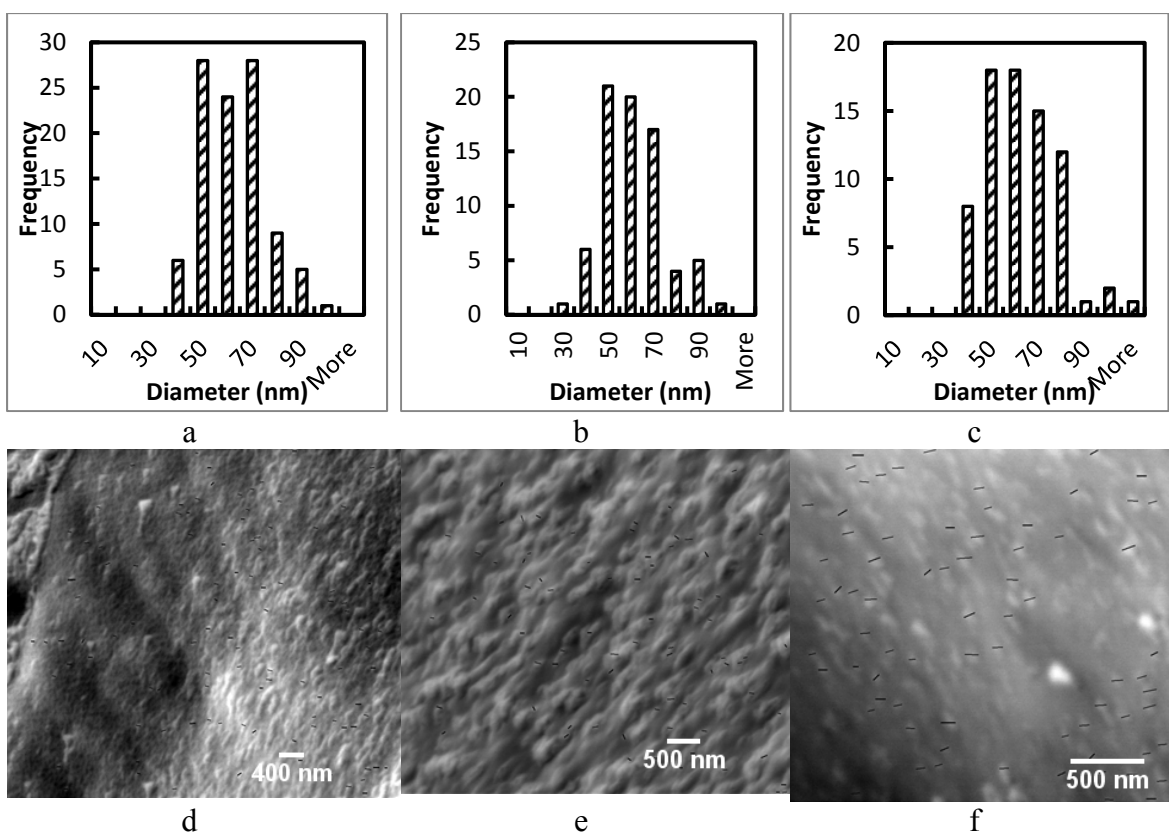


Figure E2: Sized images and histograms for particle sizes from each individual image from Fig. 6.2a-c. a and d are Fig. 6.2a, b and e are Fig. 6.2b and c and f are Fig. 6.2c.

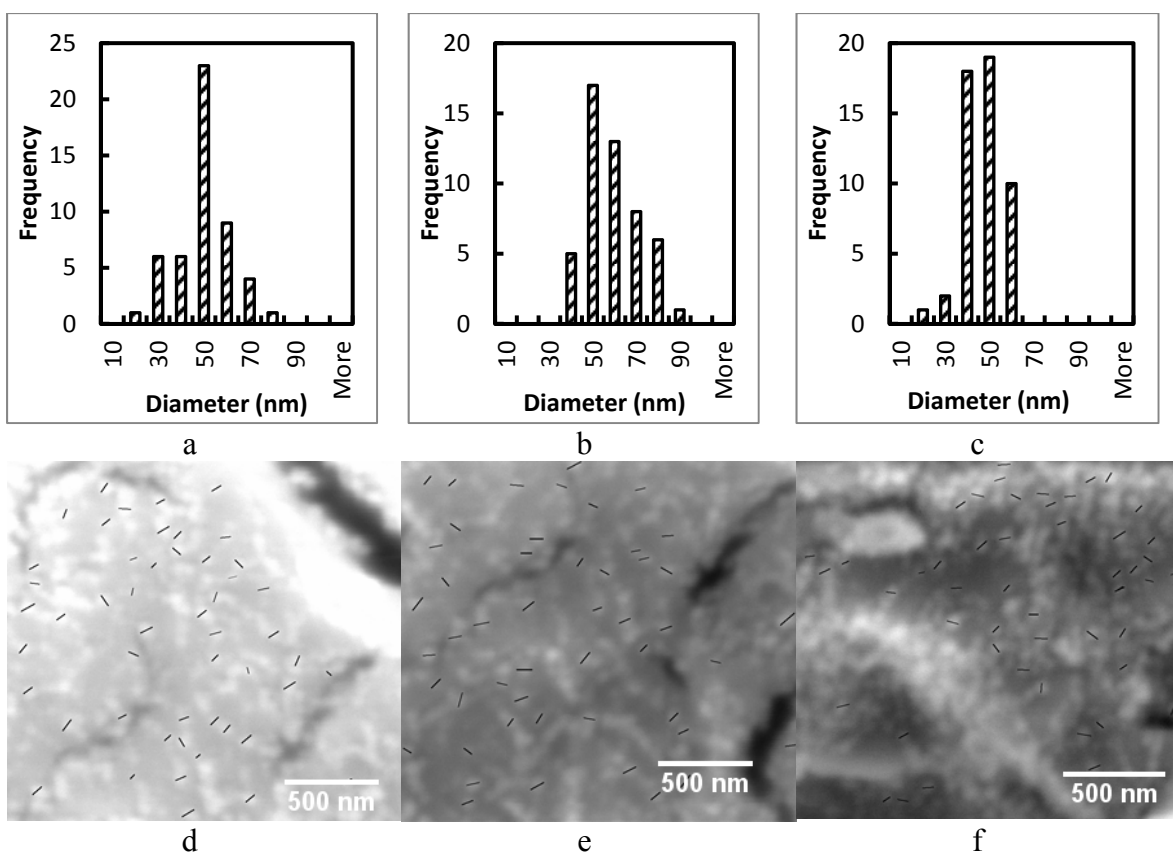


Figure E3: Sized images and histograms for particle sizes from each individual image from Fig. 6.2d-f. a and d are Fig. 6.2d, b and e are Fig. 6.2e and c and f are Fig. 6.2f.

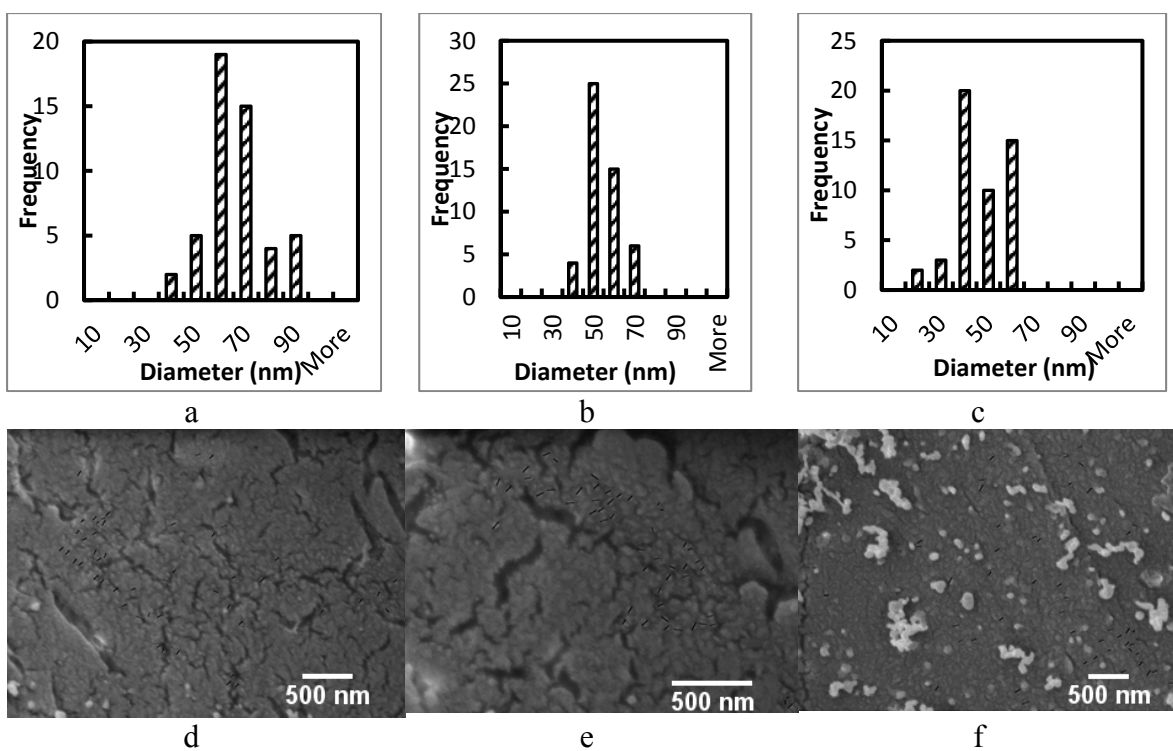
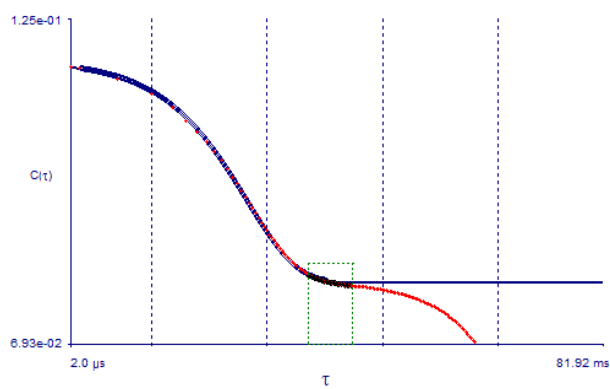
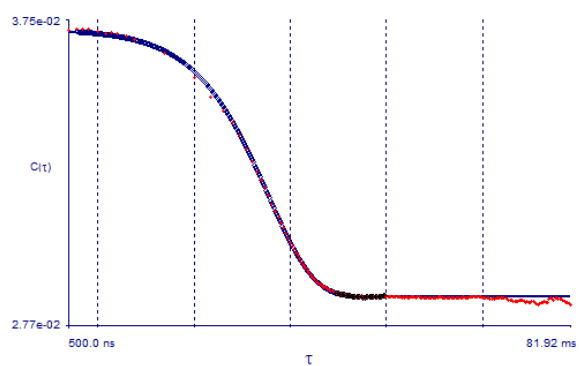


Figure E4: Sized images and histograms for particle sizes from each individual image from Fig. 6.3a-c. a and d are Fig. 6.3a, b and e are Fig. 6.3b and c and f are Fig. 6.3c.

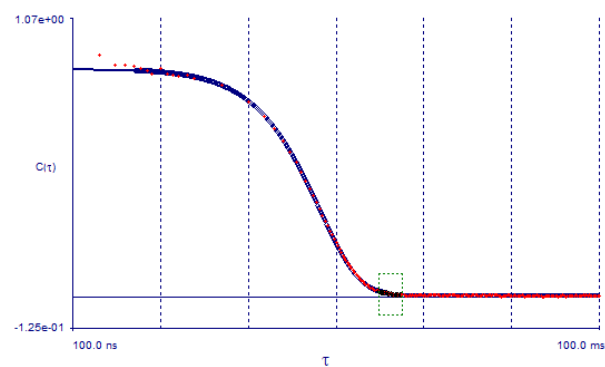


a

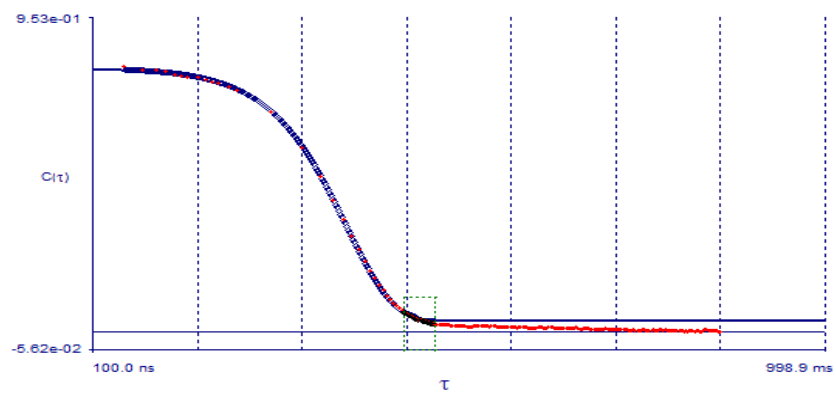
(Fig. E5 continued on the next page)



b



c



d

Figure E5: a. ACF for DLS data from Fig. 6.1. b. ACF for DLS data from Fig. 6.2. c. ACF for DLS data from Fig. 6.3 d. ACF for DLS data from Fig. 6.4.

Appendix F: Reduction of mAb1 viscosity at 250 mg/ml compared to conventional solution formulations by modification of protein-protein interactions

F.1 Co-solute concentration during the filtration process in terms of Donnan equilibrium

At high protein concentrations, the positively charged proteins play an important role in the partitioning of species across the filter membrane. Since the protein molecules are retained on one side of the membrane, there is an excess of positive charge on that side of the membrane as a result of which positively charged his molecules are preferentially pushed through the filter. As a result, the concentration of his in the protein sample decreases as the filtration process proceeds changing the ratio of his ions to his molecules causing the pH of the solution to rise. In the current study, it was observed to rise by 0.2 pH units for the sample in his buffer through the course of the experiment. Theoretically, the Donnan effect is expected to be important an influence co-solute concentrations significantly when the concentrations of positively charged ions and net positive charges on proteins are similar. The mathematical expression for the Donnan effect not being important is given by Bolton et al.,¹ as $0.9 < x < 1.1$ –

$$x = \frac{-I}{2} + \sqrt{\left(\frac{I}{2}\right)^2 + 1}$$

where $I = \frac{zm_p}{m'_{MC}}$ where z is the net charge on the protein molecule, m_p is the protein molality and m'_{mc} is the total permeate side molality of monovalent cations. For 250 mg/ml proteins in 20 mM his, the Donnan ratio, x , is 0.12 indicating that the Donnan

equilibrium will be very important as evident from the pH drift. For a sample with 78 mg/ml arg, the Donnan ratio is 0.96 indicating that the high concentration of positively arg ions in relation to the protein charges swamps out the Donnan effect arising from the protein charges. An arg concentration of above 32 mg/ml is sufficient to yield a value of $x > 0.9$ thus rendering the Donnan effect insignificant for all the data in the current study. Therefore for the high co-solute samples studied here, the final composition and initial composition will be very similar except for the volume exclusion effect from the protein. This is evidenced by the observation of no measured drift in pH for the high co-solute sample throughout the filtration process as arg does not preferentially pass through the filter.

Replicate and pathway	Protein conc (mg/ml)	std dev (mg/ml)	η (cP)	η_{inh} (ml/mg)	D/D_0	% yield	Cfg time (min)
1 concentration	53	2.0	1.8 ± 0.2	-	0.50	N/A	N/A
2 concentration	25	3.0	1.3 ± 0.2	-	0.48	N/A	N/A
1 concentration	103	2.0	1.6 ± 0.1	0.0007	0.44	N/A	N/A
2 concentration	103	0.3	2.5 ± 0.2	0.0050	0.50	N/A	N/A
1 concentration	138	2.4	3.8 ± 0.3	0.0067	0.42	86	25
2 concentration	149	13.6	4.6 ± 0.4	0.0075	0.55	99	30
1 concentration	201	8.8	8.8 ± 0.4	0.0088	0.42	96	35
2 concentration	206	13.7	10.6 ± 0.4	0.0095	0.35	96	35
1 concentration	236	5.7	30.4 ± 6.2	0.0127	0.31	90	40
2 concentration	249	11.5	37.6 ± 0.7	0.0129	0.34	70	40
1 dilution	176	13.8	10.5 ± 0.4	0.0111	-	N/A	N/A
2 dilution	165	4.1	9.7 ± 1.5	0.0113	-	N/A	N/A
1 dilution	87	6.0	2.6 ± 0.1	0.0114	0.65	N/A	N/A
2 dilution	79	3.9	2.0 ± 0.2	0.0090	0.58	N/A	N/A

Table F1: Viscosity and D/D_0 with increasing protein concentration at 78.6 mg/ml arg and 71.4 mg/ml glu at pH 5.5. The inherent viscosity remains more or less constant. D/D_0 seems to decrease with increased protein conc. The data is shown graphically in Fig. 7.1. The centrifugation speed was 5000 rcf. The solvent viscosity in all cases was 1.5.

Replicate and pathway	Protein conc (mg/ml)	std dev (mg/ml)	η (cP)	η_{inh} (ml/mg)	D/D_0	% yield	Cfg time (min)
1 concentration	21	6.0	0.8 ± 0.1	-	0.79	N/A	N/A
2 concentration	69	0.1	1.1 ± 0.1	0.0011	1.10	N/A	N/A
1 concentration	111	6.4	1.2 ± 0.2	0.0018	1.38	N/A	N/A
2 concentration	87	3.5	1.5 ± 0.5	0.0050	1.22	N/A	N/A
1 concentration	147	2.2	9.8 ± 0.6	0.0157	-	88	25
2 concentration	136	2.2	6.0 ± 0.5	0.0133	1.22	67	25
1 concentration	188	2.1	33.2 ± 2.2	0.0165	1.10	75	30
2 concentration	170	0.3	15.2 ± 0.8	0.0137	1.10	58	20
1 concentration	205	5.5	116.4 ± 3.9	0.0233	1.00	76	45
2 concentration	227	4.0	151 ± 11.1	0.0222	1.22	64	40
1 dilution	156	9.2	27.2 ± 0.1	0.0213	-	N/A	N/A
2 dilution	157	2.0	20.1 ± 6.0	0.0192	-	N/A	N/A
1 dilution	77	4.7	1.7 ± 0.4	0.0072	-	N/A	N/A
2 dilution	71	0.1	1.1 ± 0.3	0.0015	-	N/A	N/A

Table F2: Viscosity and cluster size with increasing protein concentration in 20 mM pH 5.5 his buffer. The inherent viscosity increases with protein concentration while the D/D_0 seems to remain constant with increased protein conc. The data is shown graphically in Fig. 7.1. The centrifugation speed was 5000 rcf. The solvent viscosity in all cases was 1.

Protein conc (mg/ml)	std dev (mg/ml)	Arg Conc (mg/ml)	Glu Conc (mg/ml)	Original D/D_0	Effective CONTIN Diameter after dilution (nm)
210	21.4	39.3	35.7	0.48	7.8 ± 1.7
233	18.7	52.4	47.6	0.42	7.5 ± 2.7
245	24.4	52.4	47.6	0.48	7.8 ± 1.8
246	7.1	65.5	59.5	0.28	14.6 ± 4.2
250	1.7	65.5	59.5	0.34	9.0 ± 1.7
281	1.7	78.6	71.4	0.41	9.7 ± 2.1
281	1.5	78.6	71.4	0.38	8.6 ± 1.7

Table F3: DLS sizes for dilution of samples from Table 7.5 which were at pH 5.5.

Protein conc (mg/ml)	std dev (mg/ml)	Arg Conc (mg/ml)	Glu Conc (mg/ml)	η (cP)	η_{inh} (ml/mg)	D/D_0	% yield	Cfg time (min)
224	8.2	39.3	35.7	32 ± 2.0	0.0145	0.52	76	40
210	21.4	39.3	35.7	27 ± 2.3	0.0146	0.48	72	40
240	2.1	52.4	47.6	43 ± 4.4	0.0144	0.33	88	53
233	18.7	52.4	47.6	40 ± 1.7	0.0145	0.42	85	45
246	7.1	65.5	59.5	37 ± 2.6	0.0135	0.28	95	48
250	1.7	65.5	59.5	42 ± 5.3	0.0136	0.34	98	50
246	2.1	78.6	71.4	38 ± 1.6	0.0133	0.31	77	45
281	1.7	78.6	71.4	49 ± 5.3	0.0124	0.41	106	50
281	1.5	78.6	71.4	58 ± 5.2	0.0130	0.38	103	50

Table F4: Viscosity and cluster size with increasing conc of arg/glu. Replicate data for Table 7.5 at a spin speed of 5000 rcf and pH 5.5. Solvent viscosities are given in Table 7.5.

Protein conc (mg/ml)	Arg Conc (mg/ml)	HCl Conc (mg/ml)	pH	η (cP)	η_{inh} (ml/mg)	Yield (%)	Cfg time (min)	Cfg speed (rcf)
238	150		11.4	19 ± 2.6	0.0106	74	30	10000
241	150		11.4	27 ± 6.5	0.0120	71	30	10000
272	150		11.4	66 ± 15.0	0.0139	81	35	10000
280	150		11.4	73 ± 11.7	0.0139	79	40	10000
208	150	15.5	10.1	238 ± 31.8	0.0244	80	60	10000
237	150	29.4	8.0	94 ± 8.2	0.0174	67	40	10000
261	150	29.4	8.0	216 ± 12.7	0.0190	84	80	5000
242	150	30.1	6.4	29 ± 4.1	0.0123	80	30	10000

Table F5: Visc vs pH for formulations with 150 mg/ml arg. Replicate data for Fig. 7.4. Solvent viscosity for all these dispersions was 1.5 cP.

Protein conc (mg/ml)	Arg Conc (mg/ml)	Exc 2	Exc 2 Conc (mg/ml)	pH	η (cP)	η_{inh} (ml/mg)	Yield (%)	Cfg time (min)
245	81.4	glu	68.7	7.1	29 ± 1.5	0.0121	89	35
242	81.4	glu	68.7	7.1	34 ± 10.2	0.0126	79	50
249	81.4	glu	68.7	7.1	33 ± 5.7	0.0124	71	40
279	81.4	glu	68.7	7.1	46 ± 8.8	0.0134	92	45
249	81.4	glu	68.7	7.1	52 ± 9.1	0.0142	73	35
232	81.4	glu	68.7	7.1	31 ± 2.3	0.0130	78	40
244	81.4	glu	68.7	7.1	42 ± 6.8	0.0136	89	45
242	150	HCl	30.1	6.4	29 ± 4.1	0.0123	80	30

Table F6: Glu lowers the viscosity compared to HCl. Same amount of interacting co-solute but glu lowers the osmolality values. The centrifugation speed for all the samples was 10000 rcf.

Protein conc (mg/ml)	std dev (mg/ml)	Arg Conc (mg/ml)	Glu Conc (mg/ml)	η (cP)	η_{inh} (ml/mg)	D/D_0	% yield	Cfg time (min)
269	2.5	78.6	71.4	33 ± 2.6	0.0115	0.26	98	30
228	16.2	0	0	152 ± 19.2	0.0221	0.98	78	30

Table F7: Viscosity and D/D_0 for the samples tested for viscosity versus shear rate in Fig. 7.5. The sample in row 2 was in 20 mM his buffer at pH 5.48.

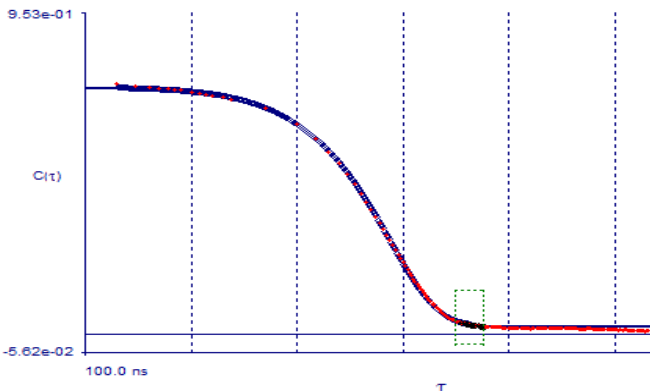
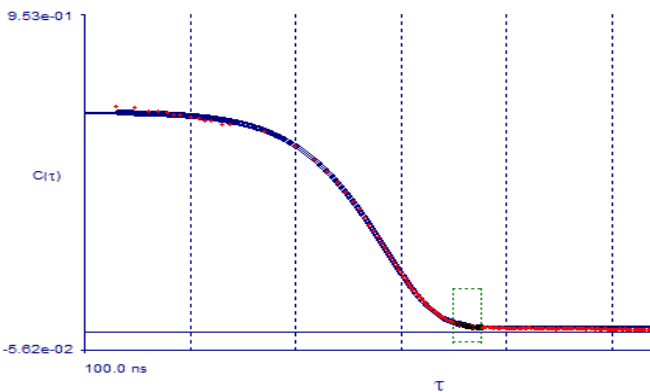
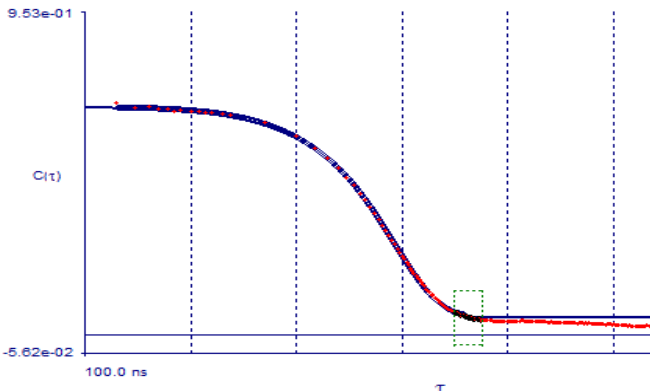
Protein conc (mg/ml)	Arg Conc (mg/ml)	Glu Conc (mg/ml)	Tre Conc (mg/ml)	η (cP)	η_{inh} (ml/mg)	D/D_0	Yield (%)	Cfg time (min)
220	27.5	22.5	25	46 ± 11.9	0.0166	0.21	71	95
223	36.7	30	33.3	35 ± 1.6	0.0145	0.24	65	55
235	73.4	60	66.7	42 ± 1.7	0.0138	0.32	70	75

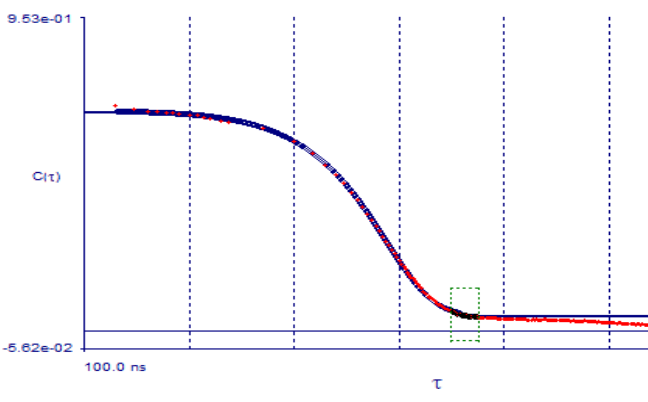
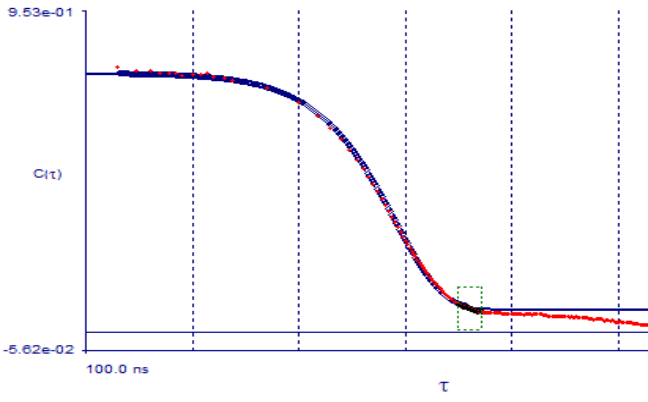
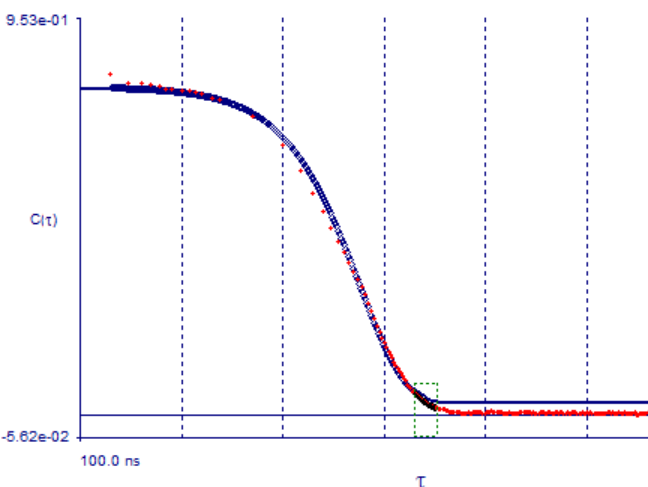
Table F8: Viscosity and cluster size decrease with increasing conc of arg/glu/tre. Replicate data for Table 7.12. Centrifugation speed was 5000 rcf and pH was 7.1.

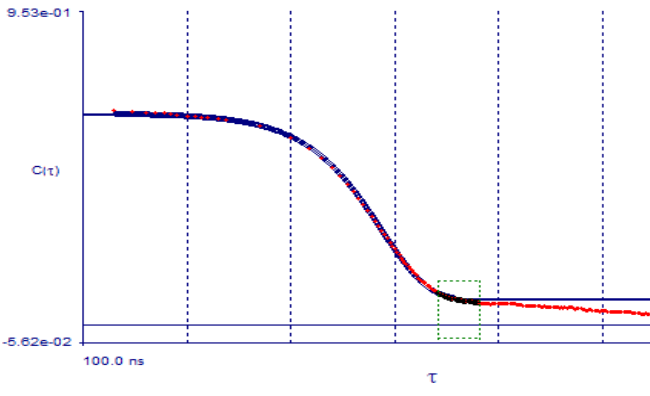
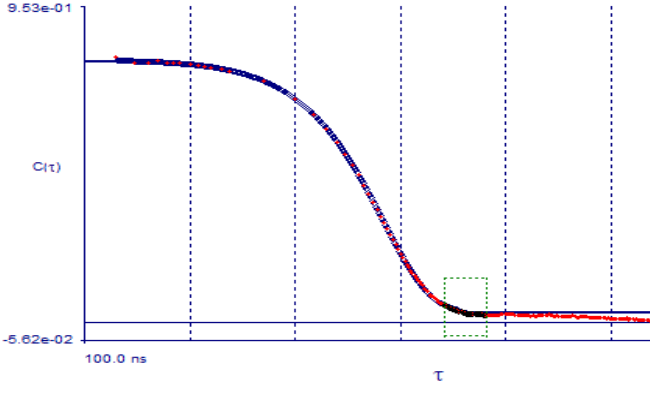
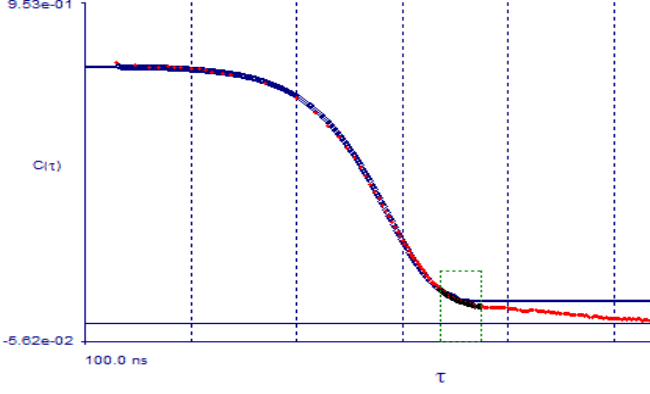
Row no.	An gle	D/D_0	Diameter by volume (by intensity) (nm)	Std. Dev. (nm)	Count rate (kcps)	Comm ents	Correlation function
1	150	1.43	7.7 (31.7)	1.4	59.4	Large second peak present which throws off intensity distribution	
3	150	0.62	17.7 (18.7)	2.2	631.3		
4	150	0.53	20.8 (41.6) (Table F9 continued on the next page)	10.1	958.2	Two peaks present, one at 13-15 nm while second peak is at 40 nm. Results in the disagree	

						ement between n volum e and intensi ty distrib utions	
6	150	0.7 2	15.3 (34)	7.4	800.1		

Table F9: Auto-correlation functions for the DLS data in Table 7.1. All samples were run with 200 channels.

Protein conc.	Angle	D/D_0	Diameter by volume (by intensity) (nm)	Std. Dev. (nm)	Count rate (kcps)	Correlation function
236	90	0.32	32 (39.2)	8	475.7	
249	90	0.34	32 (35.4)	6	439.1	
201	90	0.42	26 (28)	4	289.4 (Table F10 continued on the next page)	

206	90	0.3 5	31 (35.6)	7	441.5	
138	90	0.4 3	26 (29.5)	6	338.8	
149	90	0.5 5	20 (20.8)	2	277.2 (Table F10 continued on the next page)	

103	90	0.4 4	25 (26.4)	3	353.6	
103	90	0.5 0	22 (24)	4	334	
53	90	0.5 1	22 (22.6)	3	447 (Table F10 continued on the next page)	

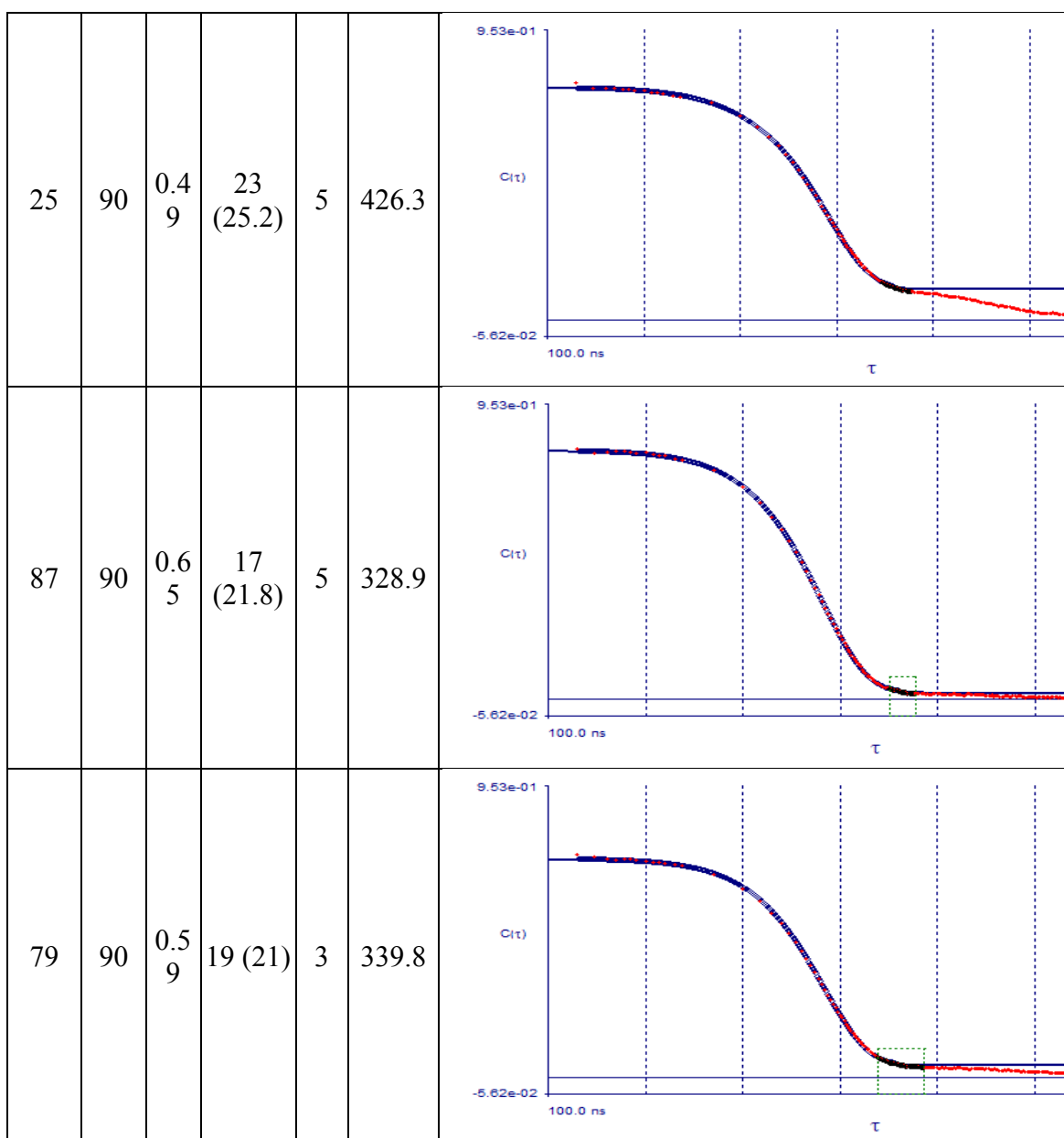


Table F10: Auto-correlation functions for the DLS data for high co-solute (78.6 mg/ml arg and 71.4 mg/ml glu) samples in Fig. 7.1 in the paper. All samples were run with 200 channels.

Protein conc.	Angle	D/D_0	Diameter by volume (by intensity) (nm)	Std. Dev. (nm)	Count rate (kcps)	Correlation function
205	90	1.00	11 (13.1)	2	350.4	
227	90	1.29	9 (9.2)	1	388.3	
188	90	1.15	10 (10.5)	2	480.2 (Table F11 continued on the next page)	

170	90	1.0 8	10 (10.9)	2	258	
136	90	1.2 1	9 (10.8)	2	519.5	
87	90	1.3 3	8 (8.6)	1	426.2 (Table F11 continued on the next page)	

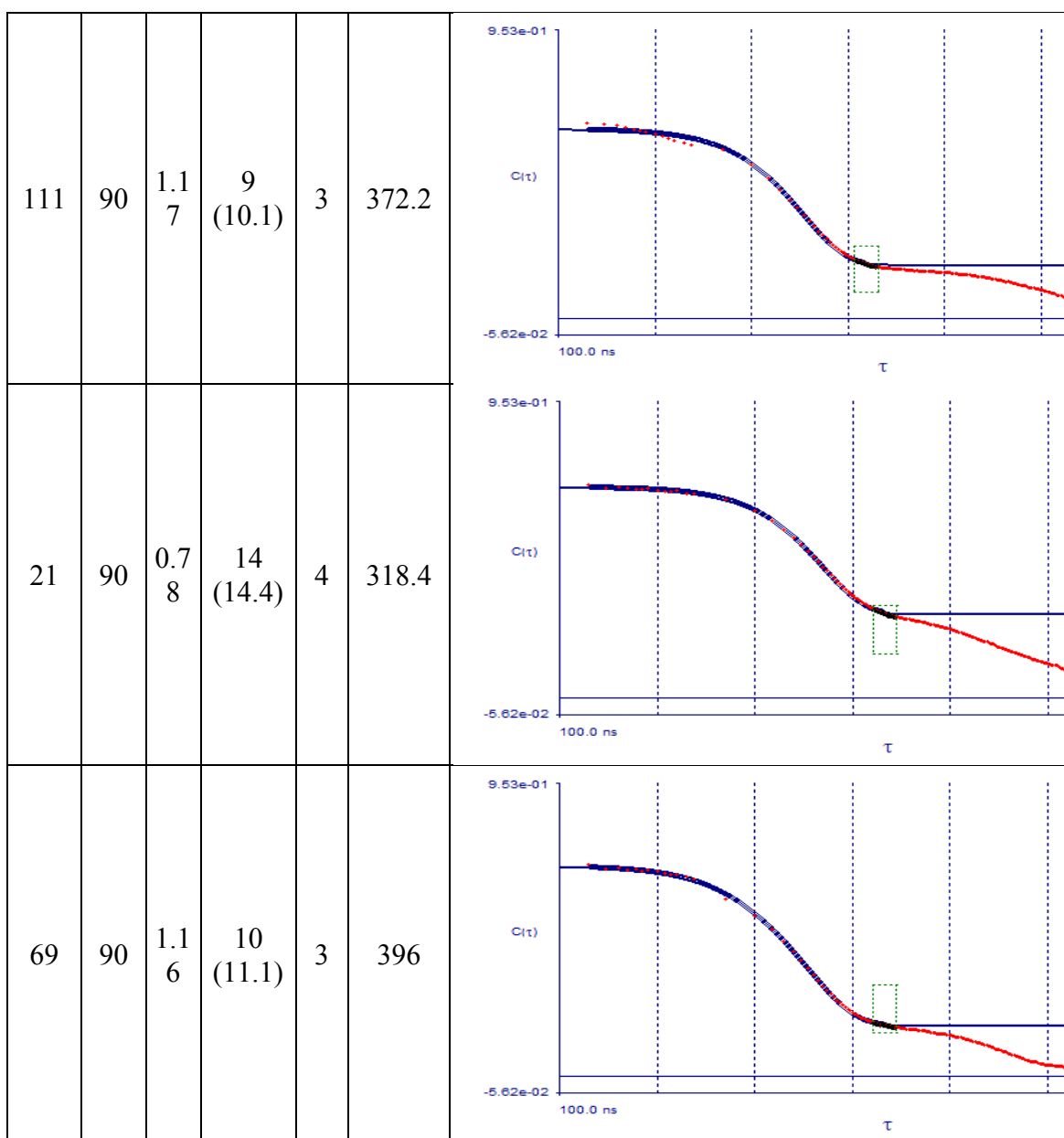
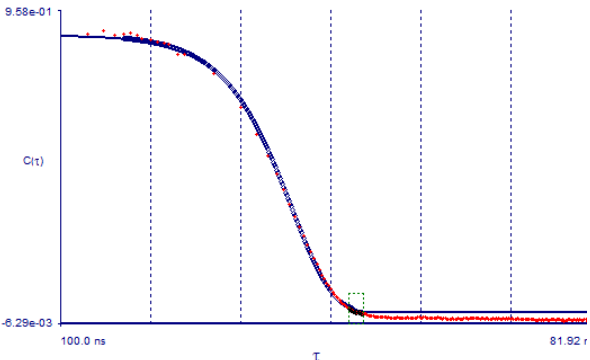
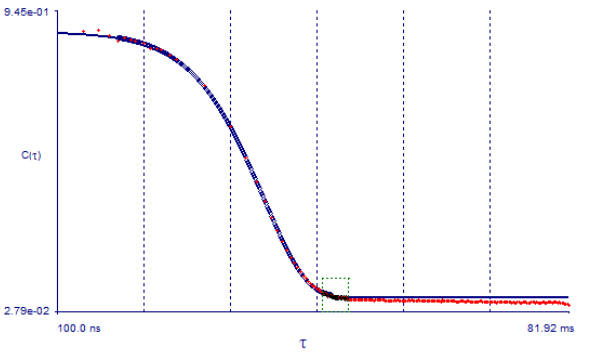
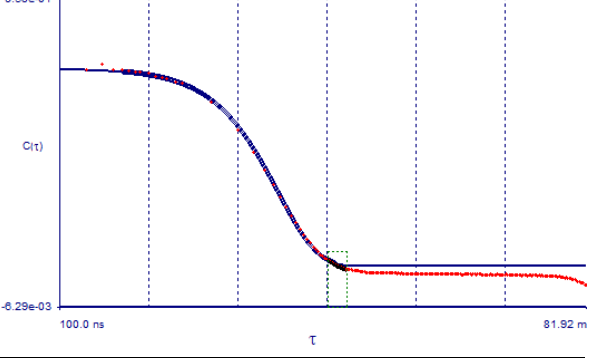
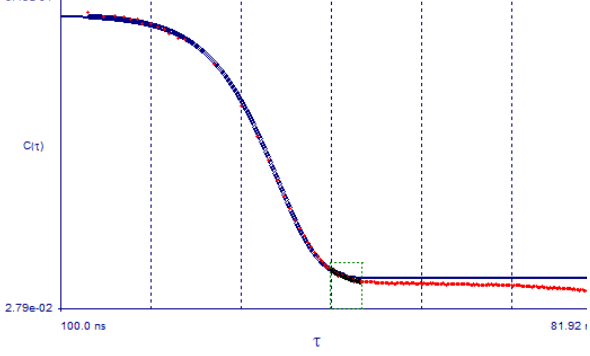


Table F11: Auto-correlation functions for the DLS data for low co-solute (20 mM his pH 5.5) samples in Fig. 7.1 in the paper. All samples were run with 200 channels.

Protein conc.	Angle	D/D_0	Diameter by volume (by intensity) (nm)	Std. Dev. (nm)	Count rate (kcps)	Correlation function
288	150	0.33	33.8 (36.3)	5.4 (5.6)	130.7	
261	150	0.43	25.5 (26.3)	2.6 (2.8)	115.6	
288	150	0.33	33.7 (35.4)	4.3 (4.7)	100.6 (Table F12 continued on the next page)	

269	150	0.35	31.3 (34.8)	5.8 (6.3)	88.9	
260	150	0.58	19.0 (20.0)	2.6 (2.5)	125.3	
241	150	0.67	16.5 (17.2)	1.9 (2.1)	153.9	
283	150	0.72	15.2 (18.0)	3.6 (4.4)	166.4 (Table F12 continued on the next page)	

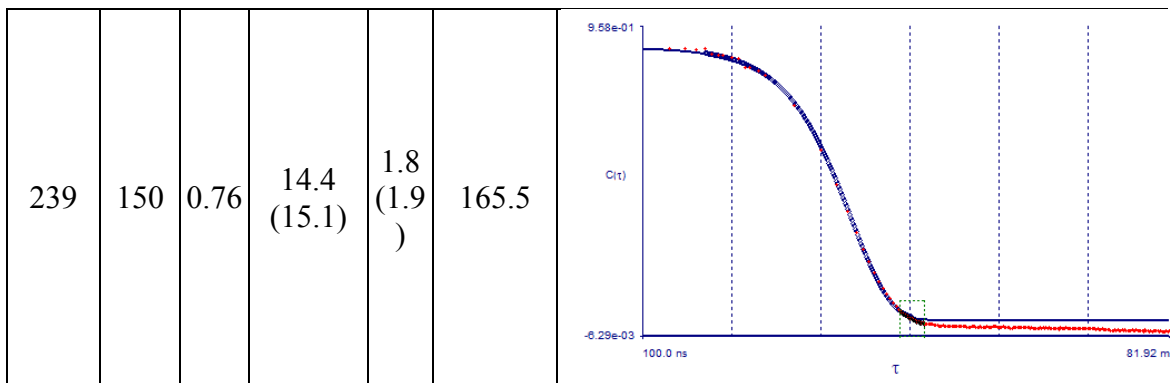
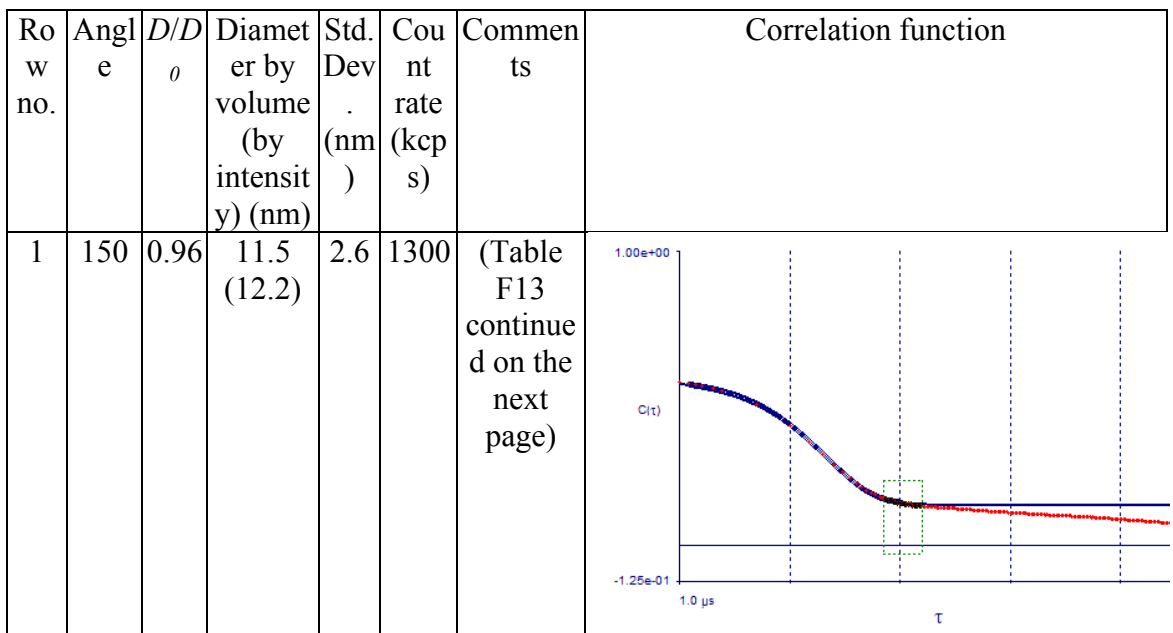


Table F12: Auto-correlation functions for the DLS data for high co-solute (78.6 mg/ml arg and 71.4 mg/ml glu) samples in Table 7.6 in the paper. All samples were run with 200 channels.



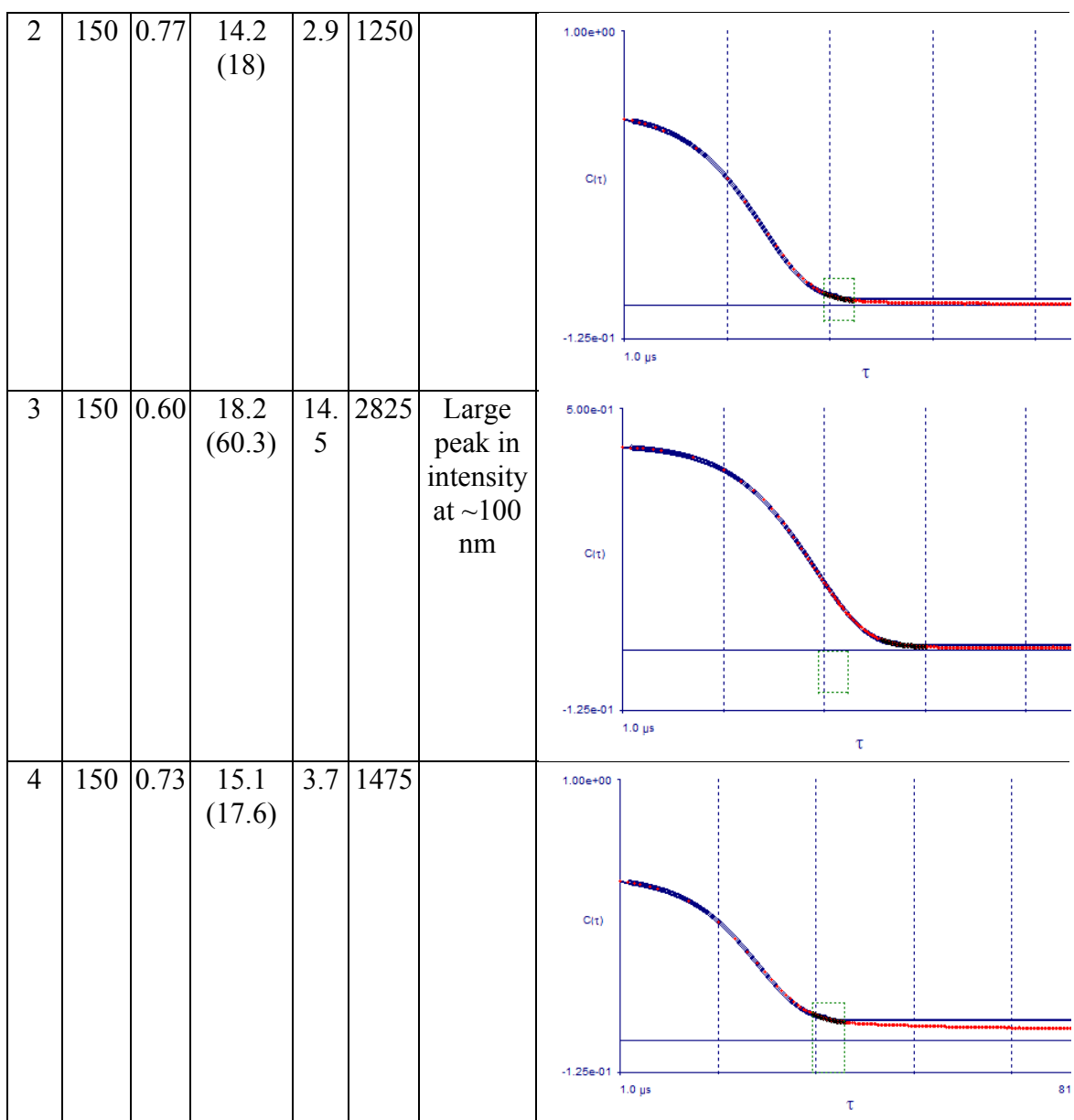


Table F13: Auto-correlation functions for the DLS data in Table 7.7 in the paper. All samples were run with 200 channels.

Row no.	Angle	D/D_0	Diameter by volume (by intensity) (nm)	Std. Dev. (nm)	Count rate (kcps)	Correlation function
2	150	0.25	44.7 (45.5)	3.3	687.8	
3	150	0.34	32.3 (32.8)	2.6	254.6	

Table F14: Auto-correlation functions for the DLS data in Table 7.10 in the paper. All samples were run with 200 channels.

Row no.	Angle	D/D_0	Diameter by volume (by intensity) (nm)	Std. Dev. (nm)	Count rate (kcps)	Correlation function
1	150	0.25	44.1 (60.3)	7.8	182.0	
2	150	0.13	84.6 (97.6)	3.0	408.8	
3	150	0.18	61.1 (78.5)	8.8	101.8	

Table F15: ACFs for the data for DLS of samples from Table 7.12. All samples were run with 200 channels.

Row no.	Angle	D/D_0	Diameter by volume (by intensity) (nm)	Std. Dev. (nm)	Count rate (kcps)	Correlation function
1	90	0.82	13.4 (14.4)	2.0	416.8	
2	90	0.93	11.8 (14.5)	3.0	408.8	

Table F16: ACFs for the data for DLS of dilutions of samples from Fig. 7.1 listed in Table 7.4.

Row no.	Angle	D/D_0	Diameter by volume (by intensity) (nm)	Std. Dev. (nm)	Count rate (kcps)	Correlation function
1	90	0.26	42.8 (46.4)	7.0	341.2	
2 (also row 2 of Table 7.6)	90	0.98	11.2 (11.9)	2.6	345.2	

Table F17: ACFs for the data for DLS of samples from Fig. 7.5 and Table 7.3 listed in Table F7.

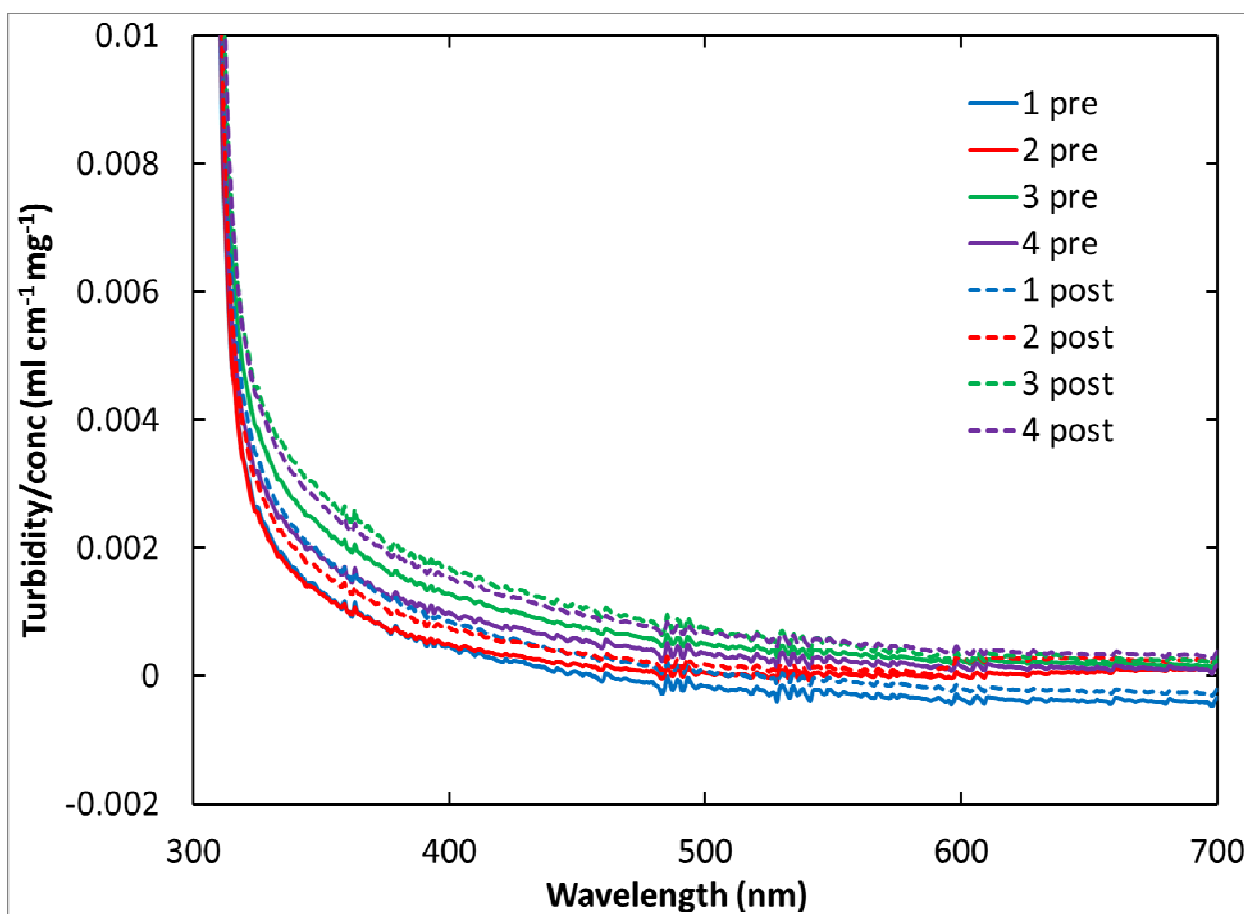
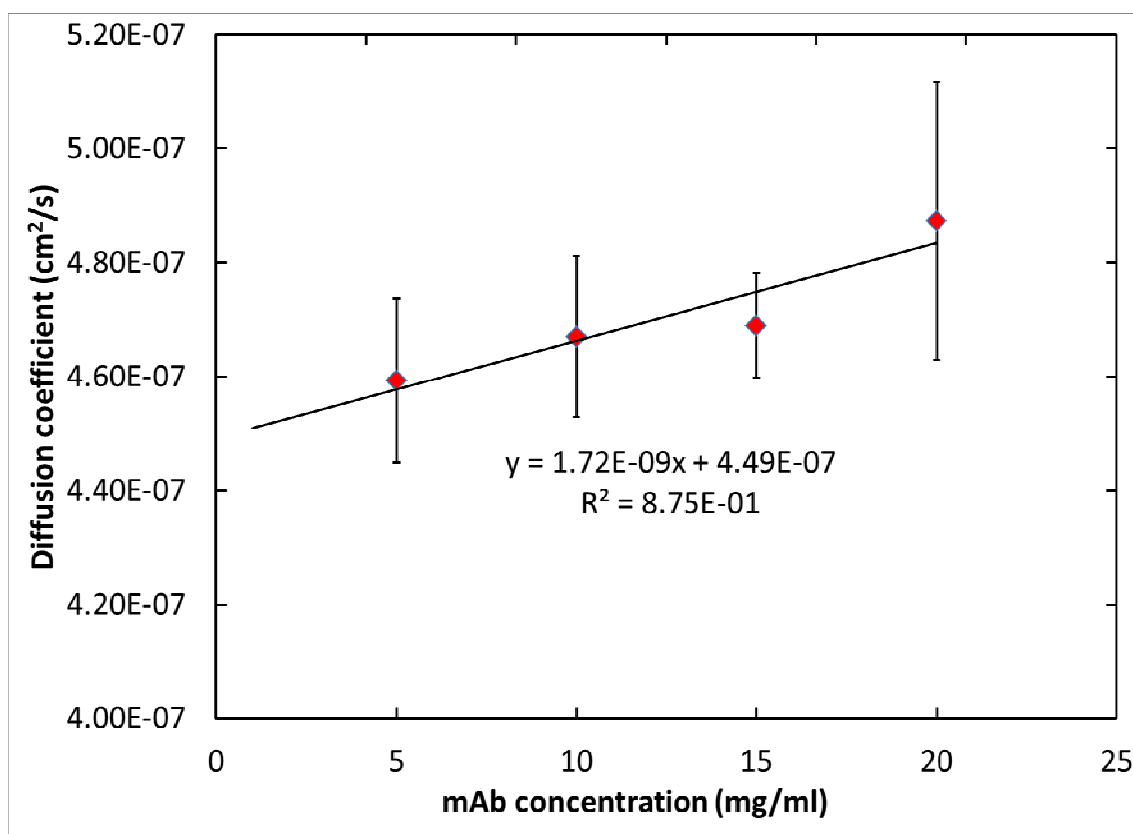


Figure F1: Turbidity divided by concentration for the mAb1 dispersions from Table 7.6 with each pair of rows labelled in order as 1-4.



a

(Fig. F2 continued on the next page)

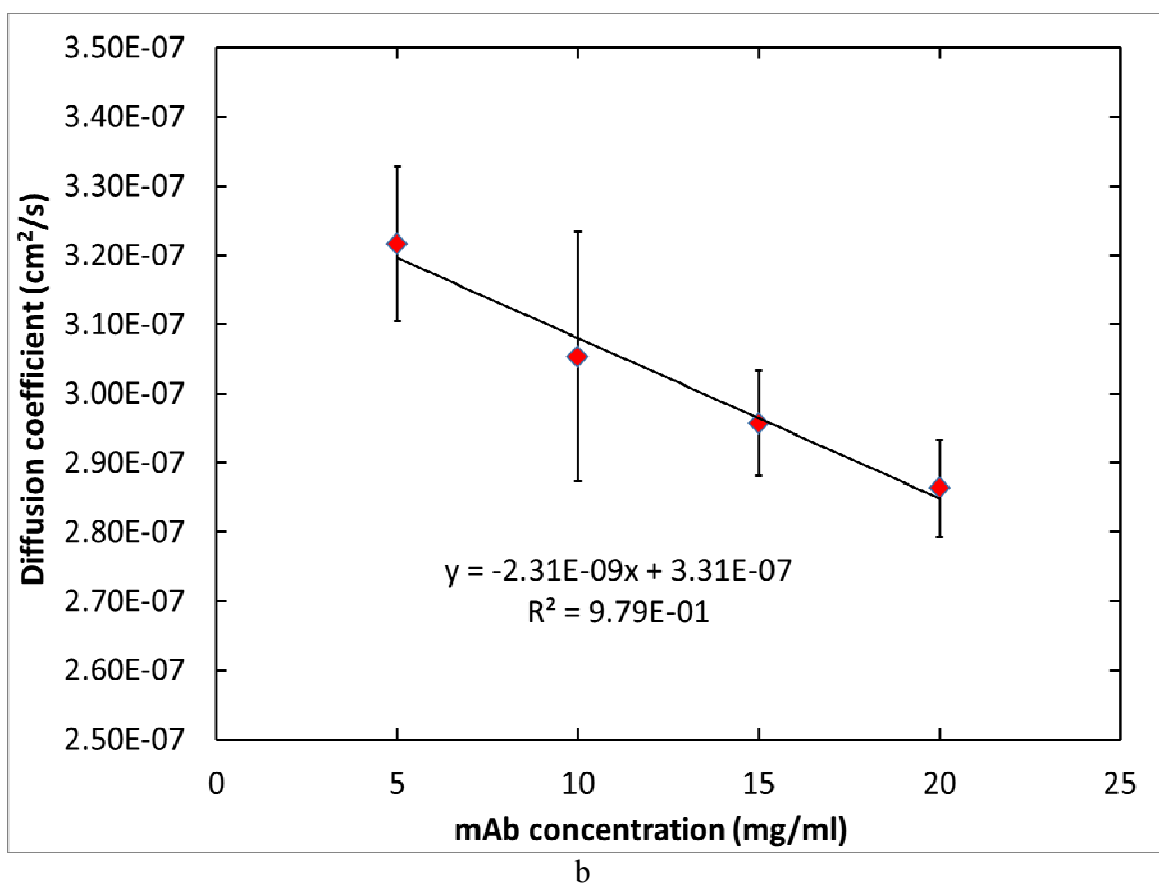


Figure F2: Diffusion coefficient versus concentration data for calculating k_d for a. 30 mM his pH 5.5 and b. 78.6 mg/ml arg and 71.4 mg/ml glu.

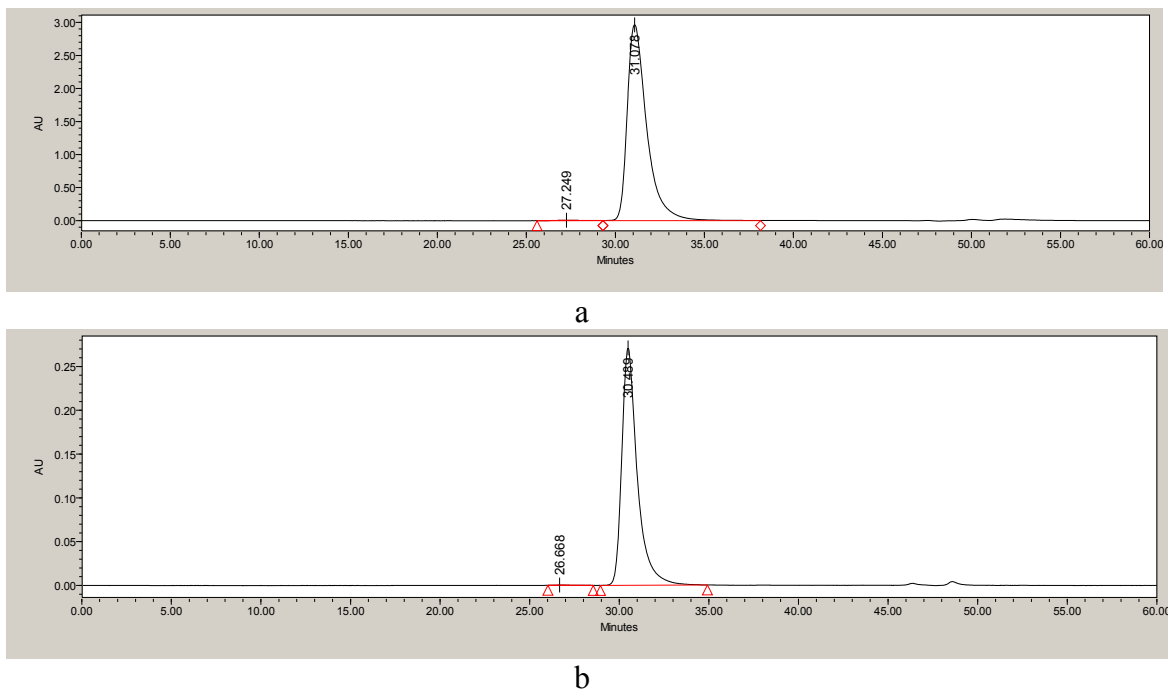


Figure F3: a. Sample SEC trace for the protein pre-processing to show the control data before cluster formation. b. Sample SEC trace for a dispersion that was ~250 mg/ml with 81.4 mg/ml arg and 68.6 mg/ml glu diluted to 1 mg/ml showing very little aggregation.

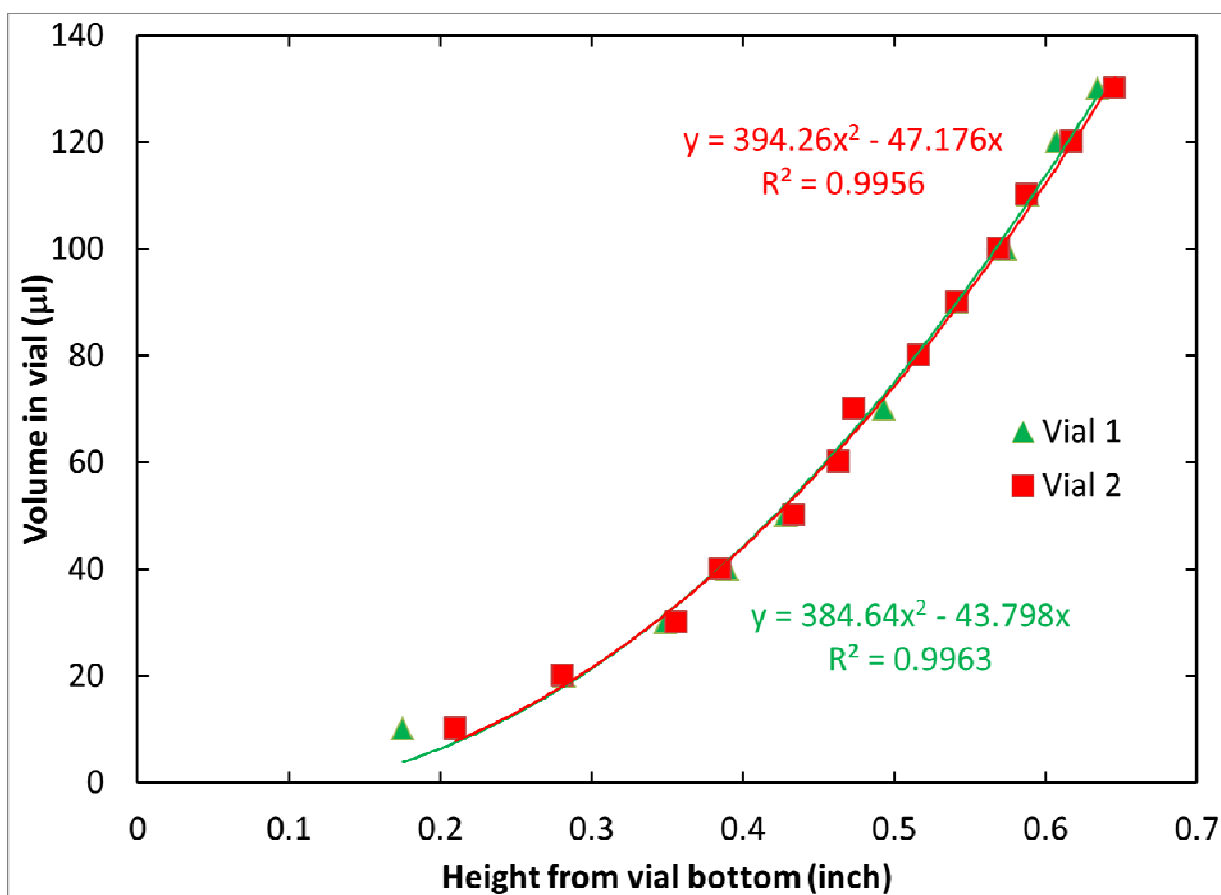


Figure F4: Calibration of vial volume versus height of liquid in vial for two different vials.

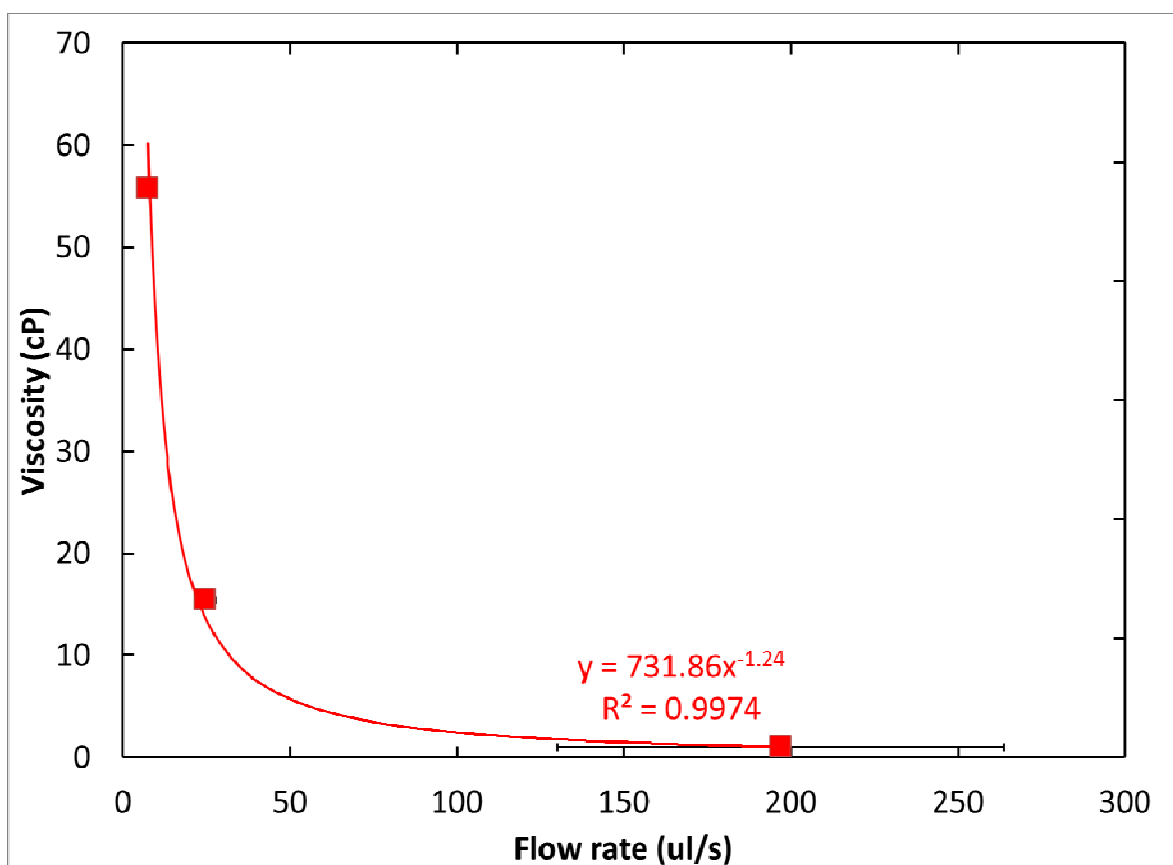
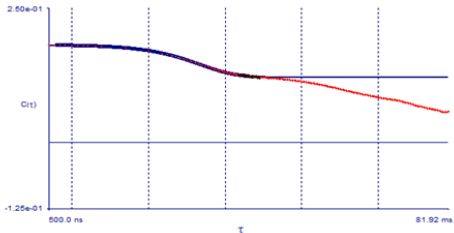
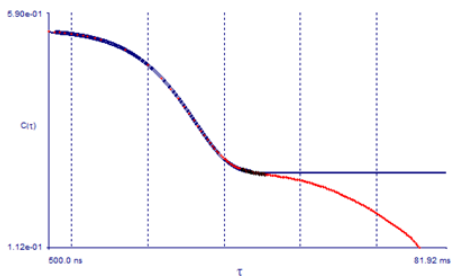
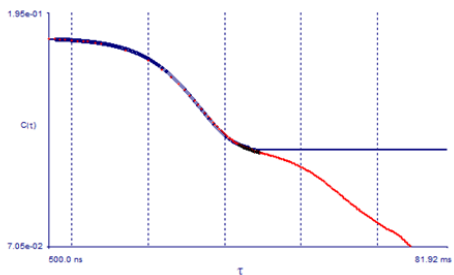
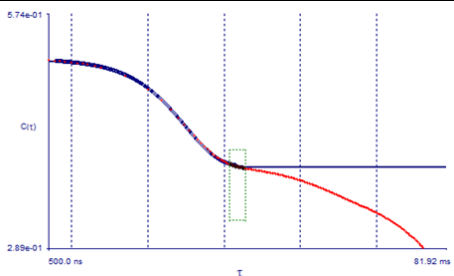


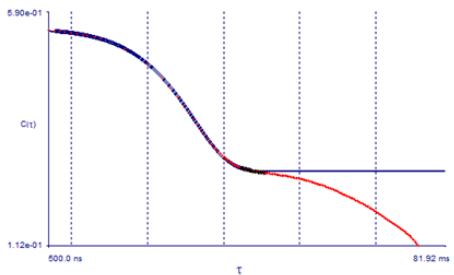
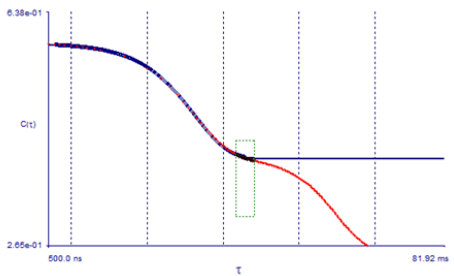
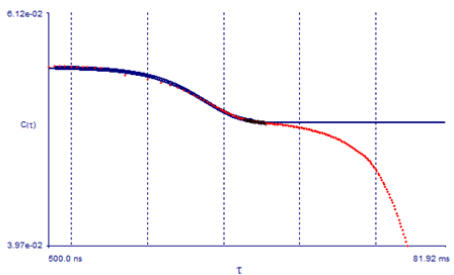
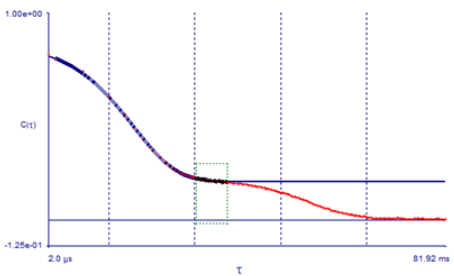
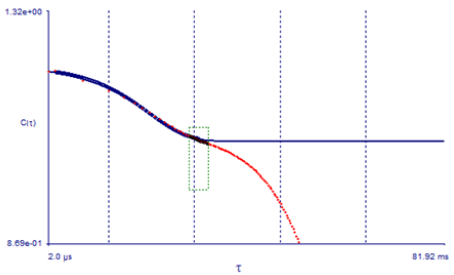
Figure F5: Calibration for viscosity versus flow rate based on water, N10 and N35 standards.

F.2 SUPPLEMENTARY REFERENCES

1. Bolton, G. R.; Boesch, A. W.; Basha, J.; Lacasse, D. P.; Kelley, B. D.; Acharya, H. *Biotechnology progress* 2011, 27, (1), 140-52.

Appendix G: Solubilization of α -Chymotrypsinogen by interaction modification with arginine and glutamic acid

Composition (mg/ml)	Angle	Filt ered	Count Rate (kcps)	CON TIN Vol Diam (nm)	CON TIN Int Diam (nm)	ACF
250 mg/ml α -CGN 100 mg/ml tre 60 mg/ml arg 40 mg/ml glu	173	Yes	2600	16.7	17.1	
250 mg/ml α -CGN 50 mg/ml tre 60 mg/ml arg 40 mg/ml glu	173	Yes	876	15.2	17.6	
250 mg/ml α -CGN 100 mg/ml tre 60 mg/ml arg 40 mg/ml glu	173	Yes	2600	16.7	17.1	
250 mg/ml α -CGN 50 mg/ml tre 60 mg/ml arg 40 mg/ml glu	173	No	1600	11.3	11.9	 (Table G1 continued on the next page)

250 mg/ml α -CGN 100 mg/ml tre 60 mg/ml arg 40 mg/ml glu	173	yes	876	15.2	15.7	
250 mg/ml α -CGN 150 mg/ml tre 60 mg/ml arg 40 mg/ml glu	173	No	828.2	21.6	22.2	
250 mg/ml α -CGN 250 mg/ml tre 60 mg/ml arg 40 mg/ml glu	173	No	6300	18.3	18.7	
6 mg/ml α - CGN	90	Yes	29.3	3.4	7.9	
4 mg/ml α - CGN	90	Yes	110.3	7.4	8.1	

(Table G1 continued on the next page)

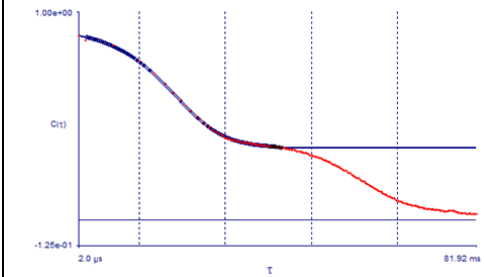
8 mg/ml α -CGN	90	Yes	33.6	4.2	12.6	
-----------------------	----	-----	------	-----	------	--

Table G1: Sample ACFs for α -CGN dispersions.

Bibliography

- (2014). "Herceptin." Retrieved 11/7/2014, 2014, from <http://www.herceptin.com/>.
- (2014). "Orencia." Retrieved 11/7/2014, 2014, from <http://www.orencia.com/index.aspx>.
- (2014). "Therapeutic monoclonal antibodies approved or in review in the European Union or United States." Retrieved 9/27/2014, 2014, from http://www.antibodysociety.org/news/approved_mabs.php.
- Adams, D. J., M. F. Butler, et al. (2009). "A new method for maintaining homogeneity during liquid–hydrogel transitions using low molecular weight hydrogelators." *Soft Matter* 5(9): 1856.
- Adler, D. C., S. W. Huang, et al. (2008). "Photothermal detection of gold nanoparticles using phase-sensitive optical coherence tomography." *Optics Express* 16(7): 4376-4393.
- Ahmad, M., W. Gu, et al. (2011). "Adhesive water networks facilitate binding of protein interfaces." *Nature Communications* 2: 261.
- Ahrer, K., A. Buchacher, et al. (2003). "Analysis of aggregates of human immunoglobulin G using size-exclusion chromatography, static and dynamic light scattering." *Journal of Chromatography A* 1009(1-2): 89-96.
- Allmendinger, A., S. Fischer, et al. (2014). "Rheological characterization and injection forces of concentrated protein formulations: an alternative predictive model for non-Newtonian solutions." *European journal of pharmaceutics and biopharmaceutics : official journal of Arbeitsgemeinschaft fur Pharmazeutische Verfahrenstechnik e.V* 87(2): 318-328.
- Andrews, J. M. and C. J. Roberts (2007). "Non-native aggregation of alpha-chymotrypsinogen occurs through nucleation and growth with competing nucleus sizes and negative activation energies." *Biochemistry* 46(25): 7558-7571.
- Anker, J. N., W. P. Hall, et al. (2008). "Biosensing with plasmonic nanosensors." *Nature Materials* 7(6): 442-453.
- Arakawa, T., D. Ejima, et al. (2007). "Suppression of protein interactions by arginine: a proposed mechanism of the arginine effects." *Biophysical chemistry* 127(1-2): 1-8.
- Arfken, G. B. and H. J. Weber (1995). *Mathematical Methods for Physicists*. San Diego, Academic Press.
- Arruebo, M., R. Fernandez-Pacheco, et al. (2007). "Magnetic nanoparticles for drug delivery." *Nano Today* 2(3): 22-32.

- Asakura, S. and F. Oosawa (1958). "Interaction between Particles Suspended in Solutions of Macromolecules." *Journal of Polymer Science* 33(126): 183-192.
- Asakura S. and Oosawa F. (1954). *J. Chem. Phys.* 22.
- Atwater, H. A. and A. Polman (2010). "Plasmonics for improved photovoltaic devices (vol 9, pg 205, 2010)." *Nature Materials* 9(10): 865-865.
- Bachar, M., A. Mandelbaum, et al. (2012). "Development and characterization of a novel drug nanocarrier for oral delivery, based on self-assembled beta-casein micelles." *Journal of controlled release : official journal of the Controlled Release Society* 160(2): 164-171.
- Baglioni, P., E. Fratini, et al. (2004). "Structural arrest in concentrated cytochrome C solutions: the effect of pH and salts." *Journal of Physics: Condensed Matter* 16(42): S5003-S5022.
- Bajaj, H., V. K. Sharma, et al. (2007). "A high-throughput method for detection of protein self-association and second virial coefficient using size-exclusion chromatography through simultaneous measurement of concentration and scattered light intensity." *Pharm. Res.* 24(11): 2071-2083.
- Baker, M. L., C. F. Hryc, et al. (2013). "Validated near-atomic resolution structure of bacteriophage epsilon15 derived from cryo-EM and modeling." *Proceedings of the National Academy of Sciences of the United States of America* 110(30): 12301-12306.
- Barbosa, S., A. Agrawal, et al. (2010). "Tuning Size and Sensing Properties in Colloidal Gold Nanostars." *Langmuir* 26(18): 14943-14950.
- Beenakker, C. W. J. and P. Mazur (1984). "DIFFUSION OF SPHERES IN A CONCENTRATED SUSPENSION .2." *Physica A* 126(3): 349-370.
- Bellare, J. R., H. T. Davis, et al. (1988). "Controlled environment vitrification system: an improved sample preparation technique." *J Electron Microsc Tech* 10(1): 87-111.
- Bergenholtz, J., W. C. K. Poon, et al. (2003). "Gelation in model colloid-polymer mixtures." *Langmuir* 19(10): 4493-4503.
- Betancourt, T., B. Brown, et al. (2007). "Doxorubicin-loaded PLGA nanoparticles by nanoprecipitation: preparation, characterization and in vitro evaluation." *Nanomedicine* 2(2): 219-232.
- Biswas, R., N. Rohman, et al. (2008). "Intramolecular charge transfer reaction, polarity, and dielectric relaxation in AOT/water/heptane reverse micelles: pool size dependence." *The Journal of Physical Chemistry B* 112(31): 9379-9388.

- Blanco, M. A., T. Perevozchikova, et al. (2014). "Protein-protein interactions in dilute to concentrated solutions: alpha-chymotrypsinogen in acidic conditions." *The journal of physical chemistry. B* 118(22): 5817-5831.
- Boerakker, M. J., N. E. Botterhuis, et al. (2006). "Aggregation behavior of giant amphiphiles prepared by cofactor reconstitution." *Chemistry* 12(23): 6071-6080.
- Bolton, G. R., A. W. Boesch, et al. (2011). "Effect of protein and solution properties on the Donnan effect during the ultrafiltration of proteins." *Biotechnology progress* 27(1): 140-152.
- Borwankar, A. U., A. K. Dinin, et al. (2013). "Tunable equilibrium nanocluster dispersions at high protein concentrations." *Soft Matter* 9(6): 1766-1771.
- Bottcher, C. J. F. (1945). "The dielectric constant of crystalline powders." *Recl. Trav. Chim. Pays-Bas Belg.* 64(Copyright (C) 2011 American Chemical Society (ACS). All Rights Reserved.): 47-51.
- Brust, M., M. Walker, et al. (1994). "Synthesis of thiol-derivatised gold nanoparticles in a two-phase Liquid?Liquid system." *Journal of the Chemical Society, Chemical Communications*(7): 801.
- Burckbuchler, V., G. Mekhloufi, et al. (2010). "Rheological and syringeability properties of highly concentrated human polyclonal immunoglobulin solutions." *European journal of pharmaceutics and biopharmaceutics : official journal of Arbeitsgemeinschaft fur Pharmazeutische Verfahrenstechnik e.V* 76(3): 351-356.
- Cardinaux, F., A. Stradner, et al. (2007). "Modeling equilibrium clusters in lysozyme solutions." *Europhysics Letters (EPL)* 77(4): 48004.
- Cardinaux, F., E. Zaccarelli, et al. (2011). "Cluster-driven dynamical arrest in concentrated lysozyme solutions." *The journal of physical chemistry. B* 115(22): 7227-7237.
- Castellanos, M. M., J. A. Pathak, et al. (2014). "Both protein adsorption and aggregation contribute to shear yielding and viscosity increase in protein solutions." *Soft Matter* 10(1): 122-131.
- Castellanos, M. M., J. A. Pathak, et al. (2014). "Explaining the non-newtonian character of aggregating monoclonal antibody solutions using small-angle neutron scattering." *Biophysical journal* 107(2): 469-476.
- Casu, A., E. Cabrini, et al. (2012). "Controlled Synthesis of Gold Nanostars by Using a Zwitterionic Surfactant." *Chemistry - A European Journal* 18(30): 9381-9390.
- Chakrabarti, R., J.-Y. Delannoy, et al. (2011). "Packing correlations, collective scattering and compressibility of fractal-like aggregates in polymer nanocomposites and suspensions." *Soft Matter* 7(11): 5397-5407.

- Chari, R., K. Jerath, et al. (2009). "Long- and Short-Range Electrostatic Interactions Affect the Rheology of Highly Concentrated Antibody Solutions." *Pharmaceutical Research* 26(12): 2607-2618.
- Chen, J., F. Saeki, et al. (2005). "Gold Nanocages: Bioconjugation and Their Potential Use as Optical Imaging Contrast Agents." *Nano Letters* 5(3): 473-477.
- Cheung, J. K., V. K. Shen, et al. (2007). "Coarse-grained strategy for modeling protein stability in concentrated solutions. III: Directional protein interactions." *Biophysical Journal* 92(12): 4316-4324.
- Cheung, J. K. and T. M. Truskett (2005). "Coarse-Grained Strategy for Modeling Protein Stability in Concentrated Solutions." *Biophysical Journal* 89(4): 2372-2384.
- Cheung, M. S., D. Klimov, et al. (2005). "Molecular Crowding Enhances Native State Stability and Refolding Rates of Globular Proteins." *Proceedings of the National Academy of Sciences of the United States of America* 102(13): 4753-4758.
- Chi, E. Y., S. Krishnan, et al. (2003). "Roles of Conformational Stability and Colloidal Stability in the Aggregation of Recombinant Human Granulocyte Colony-Stimulating Factor." *Protein Science* 12(5): 903-913.
- Connolly, B. D., C. Petry, et al. (2012). "Weak interactions govern the viscosity of concentrated antibody solutions: high-throughput analysis using the diffusion interaction parameter." *Biophysical journal* 103(1): 69-78.
- Crowther, J. R. and Editor (1995). *ELISA: Theory and Practice*. [In: *Methods Mol. Biol.* (Totowa, N. J.), 1995; 42], Humana.
- Curtis, R. A., J. M. Prausnitz, et al. (1998). "Protein-Protein and Protein-Salt Interactions in Aqueous Protein Solutions Containing Concentrated Electrolytes." *Biotechnology and Bioengineering* 57(1): 11-21.
- Dai, W., C. Fu, et al. (2013). "Visualizing virus assembly intermediates inside marine cyanobacteria." *Nature* 502(7473): 707-710.
- Daniel, M. C. and D. Astruc (2004). "Gold nanoparticles: Assembly, supramolecular chemistry, quantum-size-related properties, and applications toward biology, catalysis, and nanotechnology." *Chemical Reviews* 104(1): 293-346.
- Davis-Searles, P. R., A. J. Saunders, et al. (2001). "Interpreting the Effects of Small Uncharged Solutes on Protein-Folding Equilibria." *Annual Review of Biophysics and Biomolecular Structure* 30: 271-306.
- Davis, M. E., Z. Chen, et al. (2008). "Nanoparticle therapeutics: an emerging treatment modality for cancer." *Nature Reviews Drug Discovery* 7(9): 771-782.
- de Kruif, C. G., T. Huppertz, et al. (2012). "Casein micelles and their internal structure." *Advances in colloid and interface science* 171-172: 36-52.

- del Alamo, M., G. Rivas, et al. (2005). "Effect of Macromolecular Crowding Agents on Human Immunodeficiency Virus Type 1 Capsid Protein Assembly In Vitro." *Journal of Virology* 79(22): 14271-14281.
- Desbois, G., J. L. Urai, et al. (2008). "Cryogenic vitrification and 3D serial sectioning using high resolution cryo-FIB SEM technology for brine-filled grain boundaries in halite: first results." *Geofluids* 8(1): 60-72.
- Dhar, A., A. Samiotakis, et al. (2010). "Structure, Function, and Folding of Phosphoglycerate Kinase are Strongly Perturbed by Macromolecular Crowding." *Proceedings of the National Academy of Sciences of the United States of America* 107(41): 17586-17591.
- Dreaden, E. C., A. M. Alkilany, et al. (2012). "The golden age: gold nanoparticles for biomedicine." *Chemical Society Reviews* 41(7): 2740-2779.
- Du, W. and A. M. Klibanov (2011). "Hydrophobic salts markedly diminish viscosity of concentrated protein solutions." *Biotechnology and bioengineering* 108(3): 632-636.
- Durr, N. J., T. Larson, et al. (2007). "Two-photon luminescence imaging of cancer cells using molecularly targeted gold nanorods." *Nano Letters* 7(4): 941-945.
- Falus, P., L. Porcar, et al. (2012). "Distinguishing the monomer to cluster phase transition in concentrated lysozyme solutions by studying the temperature dependence of the short-time dynamics." *Journal of physics. Condensed matter : an Institute of Physics journal* 24(6): 064114.
- Ferry, V. E., J. N. Munday, et al. (2010). "Design considerations for plasmonic photovoltaics." *Advanced Materials* 22(43): 4794-4808.
- Fields, G. B., D. O. V. Alonso, et al. (1992). "Theory for the Aggregation of Proteins and Copolymers." *Journal of Physical Chemistry* 96(10): 3974-3981.
- Forster, F., B. Webb, et al. (2008). "Integration of small-angle X-ray scattering data into structural modeling of proteins and their assemblies." *Journal of molecular biology* 382(4): 1089-1106.
- Frankamp, B. L., A. K. Boal, et al. (2002). "Controlled interparticle spacing through self-assembly of Au nanoparticles and poly(amidoamine) dendrimers." *Journal of the American Chemical Society* 124(51): 15146-15147.
- Garber, E. and S. J. Demarest (2007). "A Broad Range of Fab Stabilities Within a Host of Therapeutic IgGs." *Biochemical and Biophysical Research Communications* 355(3): 751-757.
- Gast, A. P., C. K. Hall, et al. (1983). "Polymer-Induced Phase Separations in Nonaqueous Colloidal Suspensions." *J Colloid Interface Sci* 96(1): 251-267.

- Ge, H., C.-L. Zhao, et al. (2006). "Fracture Behavior of Colloidal Polymer Particles in Fast-Frozen Suspensions Viewed by Cryo-SEM." *Macromolecules* 39(16): 5531-5539.
- Gelamo, E. L., R. Itri, et al. (2004). "Small-angle X-ray scattering and electron paramagnetic resonance study of the interaction of bovine serum albumin with ionic surfactants." *Journal of colloid and interface science* 277(2): 471-482.
- Gindy, M. E. and R. K. Prud'homme (2009). "Multifunctional nanoparticles for imaging, delivery and targeting in cancer therapy." *Expert Opinion on Drug Delivery* 6(8): 865-878.
- Giorgetti, E., S. Trigari, et al. (2012). "Tunable gold nanostars for surface enhanced Raman spectroscopy." *physica status solidi (b)* 249(6): 1188-1192.
- Glaeser, R. M. (2013). "Invited review article: Methods for imaging weak-phase objects in electron microscopy." *The Review of scientific instruments* 84(11): 111101.
- Godfrin, P. D., N. E. Valadez-Perez, et al. (2014). "Generalized phase behavior of cluster formation in colloidal dispersions with competing interactions." *Soft Matter* 10(28): 5061-5071.
- Goia, D. V. and E. Matijevic (1999). "Tailoring the particle size of monodispersed colloidal gold." *Colloids and Surfaces a-Physicochemical and Engineering Aspects* 146(1-3): 139-152.
- González-Pérez, A. and U. Olsson (2008). "Cryo-fracture TEM: direct imaging of viscous samples." *Soft Matter* 4(8): 1625.
- Groenewold, J. and W. K. Kegel (2001). "Anomalous Large Equilibrium Clusters of Colloids." *Journal of Physical Chemistry B* 105(47): 11702-11709.
- Groenewold, J. and W. K. Kegel (2004). "Colloidal Cluster Phases, Gelation and Nuclear Matter." *Journal of Physics-Condensed Matter* 16(42): S4877-S4886.
- Grzelczak, M. and L. M. Liz-Marzán (2013). "Colloidal Nanoplasmonics: From Building Blocks to Sensing Devices." *Langmuir* 29(15): 4652-4663.
- Grzelczak, M., S. A. Mezzasalma, et al. (2012). "Antibonding Plasmon Modes in Colloidal Gold Nanorod Clusters." *Langmuir* 28(24): 8826-8833.
- Grzelczak, M., A. Sánchez-Iglesias, et al. (2012). "Steric Hindrance Induces crosslike Self-Assembly of Gold Nanodumbbells." *Nano Letters* 12(8): 4380-4384.
- Halas, N. J., S. Lal, et al. (2011). "Plasmons in Strongly Coupled Metallic Nanostructures." *Chemical Reviews* 111: 3913-3961.
- Hall, D. and A. P. Minton (2003). "Macromolecular Crowding: Qualitative and Semiquantitative Successes, Quantitative Challenges." *Biochimica et Biophysica Acta (BBA) - Proteins & Proteomics* 1649(2): 127-139.

- Harada, R., Y. Sugita, et al. (2012). "Protein Crowding Affects Hydration Structure and Dynamics." *Journal of the American Chemical Society* 134(10): 4842-4849.
- Harn, N., T. Spitznagel, et al. (2010). *Biophysical Signatures of Monoclonal Antibodies. Current Trends in Monoclonal Antibody Development and Manufacturing.* S. J. Shire. New York, Springer: 229-246.
- Hartl, F. U. and M. Hayer-Hartl (2002). "Protein Folding - Molecular Chaperones in the Cytosol: from Nascent Chain to Folded Protein." *Science* 295(5561): 1852-1858.
- Hartley, B. S. (1964). "Amino-Acid Sequence of Bovine Chymotrypsinogen-A." *Nature* 201(4926): 1284-1287.
- He, F., C. E. Woods, et al. (2011). "Effect of sugar molecules on the viscosity of high concentration monoclonal antibody solutions." *Pharmaceutical Research* 28(7): 1552-1560.
- Hiemenz, P. C. and R. Rajagopalan (1997). *Principles of Colloid and Surface Chemistry.* New York, Marcel Dekker, Inc.
- Hirsch, L. R., R. J. Stafford, et al. (2003). "Nanoshell-mediated near-infrared thermal therapy of tumors under magnetic resonance guidance." *Proc. Nat. Acad. Sci.* 100(23): 13549-13554.
- Holstein, M. A., S. Parimal, et al. (2012). "Mobile phase modifier effects in multimodal cation exchange chromatography." *Biotechnology and bioengineering* 109(1): 176-186.
- Horn, F. M., W. Richtering, et al. (2000). "Hydrodynamic and Colloidal Interactions in Concentrated Charge-Stabilized Polymer Dispersions." *Journal of colloid and interface science* 225(1): 166-178.
- Hou, Y. and S. M. Cramer (2011). "Evaluation of selectivity in multimodal anion exchange systems: a priori prediction of protein retention and examination of mobile phase modifier effects." *Journal of chromatography. A* 1218(43): 7813-7820.
- Huang, X., I. H. El-Sayed, et al. (2006). "Cancer Cell Imaging and Photothermal Therapy in the Near-Infrared Region by Using Gold Nanorods." *Journal of the American Chemical Society* 128(6): 2115-2120.
- Hura, G. L., A. L. Menon, et al. (2009). "Robust, high-throughput solution structural analyses by small angle X-ray scattering (SAXS)." *Nature Methods* 6(8): 606-U683.
- Ilett, S., A. Orrock, et al. (1995). "Phase behavior of a model colloid-polymer mixture." *Physical Review E* 51(2): 1344-1352.

- Inoue, N., E. Takai, et al. (2014). "Specific decrease in solution viscosity of antibodies by arginine for therapeutic formulations." *Molecular pharmaceutics* 11(6): 1889-1896.
- Issman, L. and Y. Talmon (2012). "Cryo-SEM specimen preparation under controlled temperature and concentration conditions." *Journal of microscopy* 246(1): 60-69.
- Jana, N. R., L. Gearheart, et al. (2001). "Evidence for seed-mediated nucleation in the chemical reduction of gold salts to gold nanoparticles." *Chemistry of Materials* 13(7): 2313-2322.
- Jares-Erijman, E. A. and T. M. Jovin (2003). "FRET imaging." *Nature biotechnology* 21(11): 1387-1395.
- Ji, X., X. Song, et al. (2007). "Size control of gold nanocrystals in citrate reduction: The third role of citrate." *Journal of the American Chemical Society* 129(45): 13939-13948.
- Jiang, T. and J. Wu (2009). "Cluster formation and bulk phase behavior of colloidal dispersions." *Physical Review E* 80(2).
- Johnson, H. R. and A. M. Lenhoff (2013). "Characterization and suitability of therapeutic antibody dense phases for subcutaneous delivery." *Molecular pharmaceutics* 10(10): 3582-3591.
- Johnston, K. P., J. A. Maynard, et al. (2012). "Concentrated Dispersions of Equilibrium Protein Nanoclusters That Reversibly Dissociate into Active Monomers." *Acs Nano*.
- Jungjohann, K. L., S. Bliznakov, et al. (2013). "In situ liquid cell electron microscopy of the solution growth of Au-Pd core-shell nanostructures." *Nano Letters* 13(6): 2964-2970.
- Kanai, S., J. Liu, et al. (2008). "Reversible self-association of a concentrated monoclonal antibody solution mediated by Fab-Fab interaction that impacts solution viscosity." *J Pharm Sci* 97(10): 4219-4227.
- Kedia, A. and P. S. Kumar (2013). "Controlled reshaping and plasmon tuning mechanism of gold nanostars." *Journal of Materials Chemistry C* 1(30): 4540.
- Kendrick, B. S., J. F. Carpenter, et al. (1998). "A Transient Expansion of the Native State Precedes Aggregation of Recombinant Human Interferon- γ ." *PNAS* 95: 14142-14146.
- Khlebtsov, N. G., L. A. Dykman, et al. (2000). "Light Absorption by the Clusters of Colloidal Gold and Silver Particles Formed During Slow and Fast Aggregation." *Colloid Journal* 62(6): 765-779.

- Kim do, Y., T. Yu, et al. (2011). "Synthesis of gold nano-hexapods with controllable arm lengths and their tunable optical properties." *Angewandte Chemie* 50(28): 6328-6331.
- Koifman, N., M. Schnabel-Lubovsky, et al. (2013). "Nanostructure formation in the lecithin/isooctane/water system." *The journal of physical chemistry. B* 117(32): 9558-9567.
- Kooi, M. E., V. C. Cappendijk, et al. (2003). "Accumulation of ultrasmall superparamagnetic particles of iron oxide in human atherosclerotic plaques can be detected by in vivo magnetic resonance imaging." *Circulation* 107(19): 2453-2458.
- Kowalczyk, P., A. Ciach, et al. (2011). "Equilibrium clusters in concentrated lysozyme protein solutions." *Journal of colloid and interface science* 363(2): 579-584.
- Kralchevsky, P. A., K. D. Danov, et al. (2011). "Hydration force due to the reduced screening of the electrostatic repulsion in few-nanometer-thick films." *Current Opinion in Colloid & Interface Science*.
- Kreilgaard, L., S. Frokjaer, et al. (1999). "Effects of additives on the stability of *Humicola lanuginosa* lipase during freeze-drying and storage in the dried solid." *Journal of Pharmaceutical Sciences* 88(3): 281-290.
- Krishnan, S., E. Y. Chi, et al. (2002). "Aggregation of Granulocyte Colony Stimulating Factor under Physiological Conditions: Characterization and Thermodynamic Inhibition." *Biochemistry* 41: 6422-6431.
- Kroetsch, A. M., E. Sahin, et al. (2012). "Relating particle formation to salt- and pH-dependent phase separation of non-native aggregates of alpha-chymotrypsinogen A." *Journal of pharmaceutical sciences* 101(10): 3651-3660.
- Kulkarni, A. M., A. P. Chatterjee, et al. (2000). "Effects of polyethylene glycol on protein interactions." *Journal of Chemical Physics* 113(21): 9863-9873.
- Kulkarni, A. M., N. M. Dixit, et al. (2003). "Ergodic and non-ergodic phase transitions in globular protein suspensions." *Faraday Discussions* 123: 37-50.
- Kulkarni, A. M., N. M. Dixit, et al. (2003). "Ergodic and non-ergodic phase transitions in globular protein suspensions." *Farady Discuss.* 123: 37-50.
- Kumar, V., V. K. Sharma, et al. (2009). "In Situ Precipitation and Vacuum Drying of Interferon Alpha-2a: Development of a Single-Step Process for Obtaining Dry, Stable Protein Formulation." *International Journal of Pharmaceutics* 366(1-2): 88-98.
- Kuo, C. H. and M. H. Huang (2005). "Synthesis of branched gold nanocrystals by a seeding growth approach." *Langmuir* 21(5): 2012-2016.

- Langille, M. R., M. L. Personick, et al. (2011). "Bottom-Up Synthesis of Gold Octahedra with Tailorable Hollow Features." *Journal of the American Chemical Society* 133(27): 10414-10417.
- Langille, M. R., M. L. Personick, et al. (2012). "Defining rules for the shape evolution of gold nanoparticles." *Journal of the American Chemical Society* 134(35): 14542-14554.
- Langille, M. R., J. Zhang, et al. (2012). "Stepwise evolution of spherical seeds into 20-fold twinned icosahedra." *Science* 337(6097): 954-957.
- Lavinder, J. J., S. B. Hari, et al. (2009). "High-Throughput Thermal Scanning: a General, Rapid Dye-Binding Thermal Shift Screen for Protein Engineering." *Journal of the American Chemical Society* 131(11): 3794-3795.
- Lee, J. C. and S. N. Timasheff (1981). "The Stabilization of Proteins by Sucrose." *Journal of Biological Chemistry* 256(14): 7193-7201.
- Lekkerkerker, H. N. W. and R. Tuinier (2011). *Colloids and the Depletion Interaction*. New York, Springer.
- Lewus, R. A., P. A. Darcy, et al. (2011). "Interactions and phase behavior of a monoclonal antibody." *Biotechnology progress* 27(1): 280-289.
- Li, L., S. Kumar, et al. (2014). "Concentration Dependent Viscosity of Monoclonal Antibody Solutions: Explaining Experimental Behavior in Terms of Molecular Properties." *Pharmaceutical Research*.
- Li, Y., V. Lubchenko, et al. (2011). "The use of dynamic light scattering and brownian microscopy to characterize protein aggregation." *The Review of scientific instruments* 82(5): 053106.
- Lilyestrom, W. G., S. Yadav, et al. (2013). "Monoclonal antibody self-association, cluster formation, and rheology at high concentrations." *The journal of physical chemistry. B* 117(21): 6373-6384.
- Litman, G. W., J. P. Rast, et al. (1993). "Phylogenetic diversification of immunoglobulin genes and the antibody repertoire." *Mol Biol Evol* 10(1): 60-72.
- Liu, J., M. D. H. Nguyen, et al. (2005). "Reversible self-association increases the viscosity of a concentrated monoclonal antibody in aqueous solution." *Journal of Pharmaceutical Sciences* 94(9): 1928-1940.
- Liu, W., T. Cellmer, et al. (2005). "Interactions of lysozyme in guanidinium chloride solutions from static and dynamic light-scattering measurements." *Biotechnology and bioengineering* 90(4): 482-490.
- Liu, Y., L. Porcar, et al. (2011). "Lysozyme Protein Solution with an Intermediate Range Order Structure." *The Journal of Physical Chemistry B* 115(22): 7238-7247.

- Liu, Y., L. Porcar, et al. (2011). "Lysozyme protein solution with an intermediate range order structure." *The journal of physical chemistry. B* 115(22): 7238-7247.
- Loo, C., A. Lowery, et al. (2005). "Immunotargeted nanoshells for integrated cancer imaging and therapy." *Nano Letters* 5(4): 709-711.
- Lu, L. H., K. Ai, et al. (2008). "Environmentally friendly synthesis of highly monodisperse biocompatible gold nanoparticles with urchin-like shape." *Langmuir* 24(3): 1058-1063.
- Lu, P. J., J. C. Conrad, et al. (2006). "Fluids of Clusters in Attractive Colloids." *Physical Review Letters* 96(2).
- Lu, P. J., E. Zaccarelli, et al. (2008). "Gelation of Particles with Short-Range Attraction." *Nature* 453(7194): 499-503.
- Lu, Z., C. Gao, et al. (2011). "Direct assembly of hydrophobic nanoparticles to multifunctional structures." *Nano letters* 11(8): 3404-3412.
- Lu, Z., M. Ye, et al. (2010). "Self-Assembled TiO₂ Nanocrystal Clusters for Selective Enrichment of Intact Phosphorylated Proteins." *Angewandte Chemie International Edition* 49(10): 1862-1866.
- Luk'yanchuk, B., N. I. Zheludev, et al. (2010). "The Fano resonance in plasmonic nanostructures and metamaterials." *Nature Materials* 9(9): 707-715.
- Ma, L. L., A. U. Borwankar, et al. (2013). "Growth of textured thin Au coatings on iron oxide nanoparticles with near infrared absorbance." *Nanotechnology* 24(2).
- Ma, L. L., M. D. Feldman, et al. (2009). "Small Multifunctional Nanoclusters (Nanoroses) for Targeted Cellular Imaging and Therapy." *Acs Nano* 3(9): 2686-2696.
- Ma, Y., N. Li, et al. (2005). "One-step synthesis of amino-dextran-protected gold and silver nanoparticles and its application in biosensors." *Analytical and Bioanalytical Chemistry* 382(4): 1044-1048.
- McCabe, W. J., J. C. Smith, et al. (1985). *Unit Operations of Chemical Engineering*. 4th Ed, Macgraw Hill.
- Miklos, A. E., C. Kluwe, et al. (2012). "Structure-based design of supercharged, highly thermoresistant antibodies." *Chem Biol* 19(4): 449-455.
- Miller, D. P., J. J. dePablo, et al. (1997). "Thermophysical properties of trehalose and its concentrated aqueous solutions." *Pharmaceutical Research* 14(5): 578-590.
- Miller, M. A., J. D. Engstrom, et al. (2010). "Low Viscosity Highly Concentrated Injectable Nonaqueous Suspensions of Lysozyme Microparticles." *Langmuir* 26(2): 1067-1074.

- Miller, M. A., T. A. Khan, et al. (2012). "Antibody nanoparticle dispersions formed with mixtures of crowding molecules retain activity and In Vivo bioavailability." *Journal of Pharmaceutical Sciences* 101(10): 3763-3778.
- Minati, L., F. Benetti, et al. (2014). "One-step synthesis of star-shaped gold nanoparticles." *Colloids and Surfaces A: Physicochemical and Engineering Aspects* 441: 623-628.
- Minton, A. P. (1999). "Adsorption of Globular Proteins on Locally Planar Surfaces. II. Models for the Effect of Multiple Adsorbate Conformations on Adsorption Equilibria and Kinetics." *Biophysical Journal* 76(1): 176-187.
- Minton, A. P. (2007). "The effective hard particle model provides a simple, robust, and broadly applicable description of nonideal behavior in concentrated solutions of bovine serum albumin and other nonassociating proteins." *Journal of Pharmaceutical Sciences* 96(12): 3466-3469.
- Moody, T. P., J. S. Kingsbury, et al. (2005). "Valence and anion binding of bovine ribonuclease A between pH 6 and 8." *Analytical Biochemistry* 336(2): 243-252.
- Moren, A. K., O. Regev, et al. (2000). "A Cryo-TEM Study of Protein-Surfactant Gels and Solutions." *Journal of colloid and interface science* 222(2): 170-178.
- Mosbaek, C. R., P. V. Konarev, et al. (2012). "High concentration formulation studies of an IgG2 antibody using small angle X-ray scattering." *Pharmaceutical Research* 29(8): 2225-2235.
- Mueller, M., M. Tebbe, et al. (2012). "Large-area organization of pNIPAM-coated nanostars as SERS platforms for polycyclic aromatic hydrocarbons sensing in gas phase." *Langmuir : the ACS journal of surfaces and colloids* 28(24): 9168-9173.
- Murphy, K. (2012). *Immunobiology*. New York, Garland Science.
- Murthy, A. K., R. J. Stover, et al. (2013). "Equilibrium Gold Nanoclusters Quenched with Biodegradable Polymers." *Acs Nano* 7(1): 239-251.
- Murthy, A. K., R. J. Stover, et al. (2013). "Charged gold nanoparticles with essentially zero serum protein adsorption in undiluted fetal bovine serum." *Journal of the American Chemical Society* 135(21): 7799-7802.
- Mutch, K. J., J. S. van Duijneveldt, et al. (2007). "Colloid-Polymer Mixtures in the Protein Limit." *Soft Matter* 3(2): 155.
- Nehl, C. L., H. W. Liao, et al. (2006). "Optical properties of star-shaped gold nanoparticles." *Nano Letters* 6(4): 683-688.
- Nhung, T. T., Y. Bu, et al. (2013). "Facile synthesis of chitosan-mediated gold nanoflowers as surface-enhanced Raman scattering (SERS) substrates." *Journal of Crystal Growth* 373: 132-137.

- Nijssse, J., P. Walther, et al. (2004). "Cold-induced imbibition damage of lettuce embryos: a study using cryo-scanning electron microscopy." *Seed Science Research* 14(2): 117-126.
- Oconnor, T., P. Debenedetti, et al. (2007). "Stability of Proteins in the Presence of Carbohydrates; Experiments and Modeling Using Scaled Particle Theory." *Biophysical Chemistry* 127(1-2): 51-63.
- Paddison, S. J. (2003). "Proton conduction mechanisms at low degrees of hydration in sulfonic acid-based polymer electrolyte membrane." *Annu. Rev. Mater. Res.* 33: 289-319.
- Pallavicini, P., A. Donà, et al. (2013). "Triton X-100 for three-plasmon gold nanostars with two photothermally active NIR (near IR) and SWIR (short-wavelength IR) channels." *Chemical Communications* 49(56): 6265.
- Pan, W. C., P. G. Vekilov, et al. (2010). "Origin of Anomalous Mesoscopic Phases in Protein Solutions." *Journal of Physical Chemistry B* 114(22): 7620-7630.
- Pathak, J. A., R. R. Sologuren, et al. (2013). "Do clustering monoclonal antibody solutions really have a concentration dependence of viscosity?" *Biophysical journal* 104(4): 913-923.
- Pazos-Perez, N., F. J. Garcia de Abajo, et al. (2012). "From nano to micro: synthesis and optical properties of homogeneous spheroidal gold particles and their superlattices." *Langmuir : the ACS journal of surfaces and colloids* 28(24): 8909-8914.
- Pazos-Perez, N., C. S. Wagner, et al. (2012). "Organized plasmonic clusters with high coordination number and extraordinary enhancement in surface-enhanced Raman scattering (SERS)." *Angewandte Chemie* 51(51): 12688-12693.
- Perchiacca, J. M., M. Bhattacharya, et al. (2011). "Mutational analysis of domain antibodies reveals aggregation hotspots within and near the complementarity determining regions." *Proteins* 79(9): 2637-2647.
- Pertzoff, V. A. (1933). "THE SOLUBILITY OF GLUTAMIC ACID IN WATER AND CERTAIN ORGANIC SOLVENTS." *Journal of Biological Chemistry* 100(1): 97-104.
- Pielak, G. J. and A. C. Miklos (2010). "Crowding and Function Reunite." *Proceedings of the National Academy of Sciences* 107(41): 17457-17458.
- Pilz, I., G. Puchwein, et al. (1970). "Small Angle X-Ray Scattering of a Homogeneous GammaG1 Immunoglobulin." *Biochemistry* 9(2): 211-219.
- Ping, G., G. Yang, et al. (2006). "Depletion Force from Macromolecular Crowding Enhances Mechanical Stability of Protein Molecules." *Polymer* 47(7): 2564-2570.

- Pissuwan, D., S. M. Valenzuela, et al. (2007). "Targeted destruction of murine macrophage cells with bioconjugated gold nanorods." *Journal of Nanoparticle Research* 9(6): 1109-1124.
- Porcar, L., P. Falus, et al. (2010). "Formation of the Dynamic Clusters in Concentrated Lysozyme Protein Solutions." *J. Phys. Chem. Lett.* 1: 126-129.
- Qiu, L., T. A. Larson, et al. (2007). "Single gold nanorod detection using confocal light absorption and scattering spectroscopy." *Ieee Journal of Selected Topics in Quantum Electronics* 13(6): 1730-1738.
- Raki, A. D., A. B. Djuri?i, et al. (1998). "Optical properties of metallic films for vertical-cavity optoelectronic devices." *Applied Optics* 37(22): 5271-5283.
- Ramakrishnan, S., M. Fuchs, et al. (2002). "Entropy driven phase transitions in colloid-polymer suspensions: Tests of depletion theories." *The Journal of Chemical Physics* 116(5): 2201.
- Reynolds, J. A. and J. M. Hough (1957). "Formulas for dielectric constant of mixtures." *Proc. Phys. Soc., London* 70B(Copyright (C) 2011 American Chemical Society (ACS). All Rights Reserved.): 769-775.
- Rintoul, M. D. and S. Torquato (1998). "Hard-sphere statistics along the metastable amorphous branch." *Physical Review E* 58(1): 532.
- Roberts, C. J. and M. A. Blanco (2014). "Role of Anisotropic Interactions for Proteins and Patchy Nano-particles." *The journal of physical chemistry. B.*
- Roosen-Runge, F., M. Hennig, et al. (2011). "Protein self-diffusion in crowded solutions." *Proceedings of the National Academy of Sciences* 108(29): 11815-11820.
- Rosenbaum, D. F., A. M. Kulkarni, et al. (1999). "Protein interactions and phase behavior: Sensitivity to the form of the pair potential." *J Chem Phys* 111(21): 9882-9890.
- Rosenbaum, D. F., P. C. Zamora, et al. (1996). "Phase Behavior of Small Attractive Colloidal Particles." *Phys Rev Let* 76(1): 150-153.
- Rosenberg, E., S. Hepbildikler, et al. (2009). "Ultrafiltration concentration of monoclonal antibody solutions: Development of an optimized method minimizing aggregation." *Journal of Membrane Science* 342(1-2): 50-59.
- Ross, P. D. and A. P. Minton (1977). "Hard quasispherical model for the viscosity of hemoglobin solutions." *Biochemical and biophysical research communications* 76(4): 971-976.
- Rozycki, B., Y. C. Kim, et al. (2011). "SAXS ensemble refinement of ESCRT-III CHMP3 conformational transitions." *Structure* 19(1): 109-116.

- S. Asakura, F. O. (1954). *J. Chem. Phys.* 22.
- Saito, S., J. Hasegawa, et al. (2012). "Behavior of monoclonal antibodies: relation between the second virial coefficient ($B(2)$) at low concentrations and aggregation propensity and viscosity at high concentrations." *Pharmaceutical Research* 29(2): 397-410.
- Saluja, A. and D. S. Kalonia (2008). "Nature and consequences of protein-protein interactions in high protein concentration solutions." *International Journal of Pharmaceutics* 358(1-2): 1-15.
- Scherer, T. M. (2013). "Cosolute Effects on the Chemical Potential and Interactions of an IgG1 Monoclonal Antibody at High Concentrations." *The journal of physical chemistry. B* 117(8): 2254-2266.
- Scherer, T. M., J. Liu, et al. (2010). "Intermolecular Interactions of IgG1 Monoclonal Antibodies at High Concentrations Characterized by Light Scattering." *J Phys Chem B* 114: 12948-12957.
- Schipper, M. L., G. Iyer, et al. (2009). "Particle Size, Surface Coating, and PEGylation Influence the Biodistribution of Quantum Dots in Living Mice." *Small* 5(1): 126-134.
- Schneider, C. A., W. S. Rasband, et al. (2012). "NIH Image to ImageJ: 25 years of image analysis." *Nat Meth* 9(7): 671-675.
- Schneider, C. P. and B. L. Trout (2009). "Investigation of cosolute-protein preferential interaction coefficients: new insight into the mechanism by which arginine inhibits aggregation." *The journal of physical chemistry. B* 113(7): 2050-2058.
- Schuler, B., E. A. Lipman, et al. (2002). "Probing the free-energy surface for protein folding with single-molecule fluorescence spectroscopy." *Nature* 419(6908): 743-747.
- Sedgwick, H., S. U. Egelhaaf, et al. (2004). "Clusters and Gels in Systems of Sticky Particles." *Journal of Physics: Condensed Matter* 16(42): S4913-S4922.
- Senapati, D., A. K. Singh, et al. (2010). "Real time monitoring of the shape evolution of branched gold nanostructure." *Chemical Physics Letters* 487(1-3): 88-91.
- Senapati, S. and A. Chandra (2001). "Dielectric constant of water confined in a nanocavity." *The Journal of Physical Chemistry B* 105(22): 5106-5109.
- Senthil Kumar, P., I. Pastoriza-Santos, et al. (2008). "High-yield synthesis and optical response of gold nanostars." *Nanotechnology* 19(1): 015606.
- Senthil Kumar, P., I. Pastoriza-Santos, et al. (2008). "High-yield synthesis and optical response of gold nanostars." *Nanotechnology* 19(1): 015606.

- Sharma, A. and J. Y. Walz (1996). "Direct Measurement of the Depletion Interaction in a Charged Colloidal Dispersion." *Journal of the Chemical Society, Faraday Transactions* 92(24): 4997.
- Sharma, V., A. Jaishankar, et al. (2011). "Rheology of globular proteins: apparent yield stress, high shear rate viscosity and interfacial viscoelasticity of bovine serum albumin solutions." *Soft Matter* 7(11): 5150.
- Shen, V. K., J. K. Cheung, et al. (2006). "Coarse-Grained Strategy for Modeling Protein Stability in Concentrated Solutions II: Phase Behavior." *Biophysical Journal* 90: 1949-1960.
- Shen, V. K., J. K. Cheung, et al. (2009). "Insights into crowding effects on protein stability from a coarse-grained model." *Journal of biomechanical engineering* 131(7): 071002-071002.
- Shire, S. J., Z. Shahrokh, et al. (2004). "Challenges in the Development of High Protein Concentration Formulations." *J. Pharm. Sci.* 93(6): 1390-1402.
- Shukla, A., E. Mylonas, et al. (2008). "Absence of equilibrium cluster phase in concentrated lysozyme solutions." *Proceedings of the National Academy of Sciences of the United States of America* 105(13): 5075-5080.
- Shukla, D., C. P. Schneider, et al. (2011). "Molecular level insight into intra-solvent interaction effects on protein stability and aggregation." *Advanced drug delivery reviews* 63(13): 1074-1085.
- Shukla, D. and B. L. Trout (2010). "Interaction of Arginine with Proteins and the Mechanism by Which It Inhibits Aggregation." *The Journal of Physical Chemistry B* 114(42): 13426-13438.
- Shukla, D. and B. L. Trout (2011). "Preferential interaction coefficients of proteins in aqueous arginine solutions and their molecular origins." *The journal of physical chemistry. B* 115(5): 1243-1253.
- Skrabalak, S. E., J. Chen, et al. (2007). "Gold nanocages for biomedical applications." *Advanced Materials* 19(20): 3177-3184.
- Soraruf, D., F. Roosen-Runge, et al. (2014). "Protein cluster formation in aqueous solution in the presence of multivalent metal ions--a light scattering study." *Soft Matter* 10(6): 894-902.
- Spinozzi, F., E. Maccioni, et al. (2003). "Synchrotron SAXS studies on the structural stability of *Carcinus aestuarii* hemocyanin in solution." *Biophysical journal* 85(4): 2661-2672.
- Srinivasan, C., A. K. Weight, et al. (2013). "Non-aqueous suspensions of antibodies are much less viscous than equally concentrated aqueous solutions." *Pharmaceutical Research* 30(7): 1749-1757.

- Stagg, L., S.-Q. Zhang, et al. (2007). "Molecular crowding enhances native structure and stability of alpha/beta protein flavodoxin." *Proceedings of the National Academy of Sciences of the United States of America* 104(48): 18976-18981.
- Stewart, M. E., C. R. Anderton, et al. (2008). "Nanostructured plasmonic sensors." *Chemical Reviews* 108(2): 494-521.
- Stradner, A., H. Sedgwick, et al. (2004). "Equilibrium Cluster Formation in Concentrated Protein Solutions and Colloids." *Nature* 432(7016): 492-495.
- Su, Q., X. Ma, et al. (2011). "A Reproducible SERS Substrate Based on Electrostatically Assisted APTES-Functionalized Surface-Assembly of Gold Nanostars." *ACS Applied Materials & Interfaces* 3(6): 1873-1879.
- Sule, S. V., J. K. Cheung, et al. (2012). "Solution pH that minimizes self-association of three monoclonal antibodies is strongly dependent on ionic strength." *Molecular pharmaceutics* 9(4): 744-751.
- Sutherland, J. N., C. Chang, et al. (2011). "Antibodies Recognizing Protective Pertussis Toxin Epitopes are Preferentially Elicited by Natural Infection Versus Acellular Immunization." *Clinical and Vaccine Immunology* 18(6): 954-962.
- Sutherland, J. N. and J. A. Maynard (2009). "Characterization of a Key Neutralizing Epitope on Pertussis Toxin Recognized by Monoclonal Antibody 1B7." *Biochemistry* 48: 11982-11993.
- Tabrizi, M. A., C. M. L. Tseng, et al. (2006). "Elimination Mechanisms of Therapeutic Monoclonal Antibodies." *Drug Discovery Today* 11(1-2): 81-88.
- Tam, J. M., A. K. Murthy, et al. (2010). "Kinetic Assembly of Near-IR-Active Gold Nanoclusters Using Weakly Adsorbing Polymers to Control the Size." *Langmuir* 26(11): 8988-8999.
- Tam, J. M., J. O. Tam, et al. (2010). "Controlled Assembly of Biodegradable Plasmonic Nanoclusters for Near-Infrared Imaging and Therapeutic Applications." *Acs Nano* 4(4): 2178-2184.
- ten Wolde, P. R. and D. Frenkel (1997). "Enhancement of Protein Crystal Nucleation by Critical Density Fluctuations." *Science* 277: 1975-1978.
- Tessier, P. M., H. R. Johnson, et al. (2003). "Predictive crystallization of ribonuclease A via rapid screening of osmotic second virial coefficients." *Proteins-Structure Function and Genetics* 50(2): 303-311.
- Tessier, P. M. and A. M. Lenhoff (2003). "Measurements of protein self-association as a guide to crystallization." *Current Opinion in Biotechnology* 14(5): 512-516.

- Tong, H., L. Zhang, et al. (2013). "Peptide-conjugation induced conformational changes in human IgG1 observed by optimized negative-staining and individual-particle electron tomography." *Scientific reports* 3: 1089.
- Torquato, S., T. M. Truskett, et al. (2000). "Is Random Close Packing of Spheres Well Defined?" *Physical Review Letters* 84(10): 2064-2067.
- Trevino, S. R., J. M. Scholtz, et al. (2008). "Measuring and increasing protein solubility." *Journal of pharmaceutical sciences* 97(10): 4155-4166.
- Trigari, S., A. Rindi, et al. (2011). "Synthesis and modelling of gold nanostars with tunable morphology and extinction spectrum." *Journal of Materials Chemistry* 21(18): 6531-6540.
- Tuinier, R., J. Rieger, et al. (2003). "Depletion-Induced Phase Separation in Colloid-Polymer Mixtures." *Advances in Colloid and Interface Science* 103: 1-31.
- Tuinier, R., G. A. Vliegenthart, et al. (2000). "Depletion Interaction Between Spheres Immersed in a Solution of Ideal Polymer Chains." *Journal of Chemical Physics* 113(23): 10768-10775.
- Uchida, T., M. Nagayama, et al. (2009). "Trehalose Solution Viscosity at Low Temperatures Measured by Dynamic Light Scattering Method: Trehalose Depresses Molecular Transportation for Ice Crystal Growth." *Journal of Crystal Growth* 311(23-24): 4747-4752.
- Vagenende, V., A. X. Han, et al. (2013). "Protein-associated cation clusters in aqueous arginine solutions and their effects on protein stability and size." *ACS chemical biology* 8(2): 416-422.
- Valente, J. J., K. S. Verma, et al. (2005). "Second virial coefficient studies of cosolvent-induced protein self-interaction." *Biophysical Journal* 89(6): 4211-4218.
- Van de Broek, B., F. Frederix, et al. (2011). "Shape-controlled synthesis of NIR absorbing branched gold nanoparticles and morphology stabilization with alkanethiols." *Nanotechnology* 22(1).
- Vekilov, P. G. (2009). "Metastable mesoscopic phases in concentrated protein solutions." *Annals of the New York Academy of Sciences* 1161: 377-386.
- Vekilov, P. G. (2010). "Phase transitions of folded proteins." *Soft Matter* 6(21): 5254.
- Vondrášek, J., P. E. Mason, et al. (2009). "The Molecular Origin of Like-Charge Arginine–Arginine Pairing in Water." *The Journal of Physical Chemistry B* 113(27): 9041-9045.
- Vrij, A. (1976). "Polymer at Interfaces and Interactions in Colloidal Dispersions." *Pure and Applied Chemistry* 48(4): 471-483.
- W, R. (1974). *Methods of Enzymatic Analysis*, Academic Press Inc.

- Wallace, B. A., R. W. Janes, et al. (2009). Modern Techniques for Circular Dichroism and Synchrotron Radiation Circular Dichroism Spectroscopy. [In: Adv. Biomed. Spectrosc., 2009; 1], IOS Press.
- Walther, P. and M. Muller (1999). "Biological ultrastructure as revealed by high resolution cryo-SEM of block faces after cryo-sectioning." *Journal of microscopy* 196(Pt 3): 279-287.
- Wang, B., S. Tchessalov, et al. (2009). "Impact of sucrose level on storage stability of proteins in freeze-dried solids: I. correlation of protein-sugar interaction with native structure preservation." *Journal of Pharmaceutical Sciences* 98(9): 3131-3144.
- Wang, M. and N. Pan (2007). "Numerical analyses of effective dielectric constant of multiphase microporous media." *Journal of Applied Physics* 101(11): 114102.
- Wang, Z. D., J. Q. Zhang, et al. (2010). "DNA-Mediated Control of Metal Nanoparticle Shape: One-Pot Synthesis and Cellular Uptake of Highly Stable and Functional Gold Nanoflowers." *Nano Letters* 10(5): 1886-1891.
- Watzky, M. A. and R. G. Finke (1997). "Transition Metal Nanocluster Formation Kinetic and Mechanistic Studies. A New Mechanism When Hydrogen Is the Reductant: Slow, Continuous Nucleation and Fast Autocatalytic Surface Growth." *Journal of the American Chemical Society* 119(43): 10382-10400.
- Weiss, W. F. t., T. K. Hodgdon, et al. (2007). "Nonnative protein polymers: structure, morphology, and relation to nucleation and growth." *Biophysical journal* 93(12): 4392-4403.
- Weissleder, R. (2001). "A clearer vision for in vivo imaging." *Nature Biotechnology* 19(4): 316-317.
- Whitmore, L. and B. A. Wallace (2008). "Protein secondary structure analyses from circular dichroism spectroscopy: Methods and reference databases." *Biopolymers* 89(5): 392-400.
- Wilcoxon, J. P., J. E. Martin, et al. (1989). "AGGREGATION IN COLLOIDAL GOLD." *Physical Review A* 39(5): 2675-2688.
- Win, K. Y. and S. S. Feng (2005). "Effects of particle size and surface coating on cellular uptake of polymeric nanoparticles for oral delivery of anticancer drugs." *Biomaterials* 26(15): 2713-2722.
- Windholz, M. and Editor (1976). *The Merck Index: An Encyclopedia of Chemicals and Drugs*. 9th Ed, Merck and Co., Publ. Dept.
- Xia, Y., T. D. Nguyen, et al. (2011). "Self-assembly of self-limiting monodisperse supraparticles from polydisperse nanoparticles." *Nat Nano* 6(9): 580-587.

- Xia, Y. S., T. D. Nguyen, et al. (2011). "Self-assembly of self-limiting monodisperse supraparticles from polydisperse nanoparticles." *Nature Nanotechnology* 6(9): 580-587.
- Xie, J., J. Y. Lee, et al. (2007). "Seedless, Surfactantless, High-Yield Synthesis of Branched Gold Nanocrystals in HEPES Buffer Solution." *Chem Mater* 19(11): 2823-2830.
- Xie, J., Q. Zhang, et al. (2008). "The Synthesis of SERS-Active Gold Nanoflower Tags for In Vivo Applications." *Acs Nano* 2(12): 2473-2480.
- Yadav, S., J. Liu, et al. (2010). "Specific Interactions in High Concentration Antibody Solutions Resulting in High Viscosity." *J Pharm Sci* 99(3): 1152-1168.
- Yadav, S., S. J. Shire, et al. (2011). "Viscosity analysis of high concentration bovine serum albumin aqueous solutions." *Pharmaceutical Research* 28(8): 1973-1983.
- Yadav, S., S. J. Shire, et al. (2012). "Viscosity behavior of high-concentration monoclonal antibody solutions: correlation with interaction parameter and electroviscous effects." *Journal of pharmaceutical sciences* 101(3): 998-1011.
- Yearley, E. J., P. D. Godfrin, et al. (2014). "Observation of small cluster formation in concentrated monoclonal antibody solutions and its implications to solution viscosity." *Biophysical journal* 106(8): 1763-1770.
- Yi, S., L. Sun, et al. (2013). "One-step synthesis of dendritic gold nanoflowers with high surface-enhanced Raman scattering (SERS) properties." *RSC Advances* 3(26): 10139.
- Young, T. M. and C. J. Roberts (2009). "Structure and Thermodynamics of Colloidal Protein Cluster Formation: Comparison of Square-Well and Simple Dipolar Models." *The Journal of Chemical Physics* 131(12): 125104.
- Yuan, H., W. Ma, et al. (2007). "Shape and SPR Evolution of Thorny Gold Nanoparticles Promoted by Silver Ions." *Chemistry of Materials* 19(7): 1592-1600.
- Zaccarelli, E. (2007). "Colloidal Gels: Equilibrium and Non-Equilibrium Routes." *J Phys: Condens. Matter* 19: 323101.
- Zarraga, I. E., R. Taing, et al. (2013). "High shear rheology and anisotropy in concentrated solutions of monoclonal antibodies." *Journal of pharmaceutical sciences* 102(8): 2538-2549.
- Zhang, F., F. Roosen-Runge, et al. (2012). "Hydration and interactions in protein solutions containing concentrated electrolytes studied by small-angle scattering." *Physical chemistry chemical physics : PCCP* 14(7): 2483-2493.
- Zhang, J., K. Sasaki, et al. (2007). "Stabilization of platinum oxygen-reduction electrocatalysts using gold clusters." *Science* 315(5809): 220-222.

- Zhang, L. and G. Ren (2012). "High-Resolution Single-Molecule Structure Revealed by Electron Microscopy and Individual Particle Electron Tomography." *Journal of Physical Chemistry & Biophysics* 02(02).
- Zhang, L., H. Tong, et al. (2013). "Optimized negative-staining electron microscopy for lipoprotein studies." *Biochimica et biophysica acta* 1830(1): 2150-2159.
- Zhao, L. L., X. H. Ji, et al. (2009). "Formation and Stability of Gold Nanoflowers by the Seeding Approach: The Effect of Intraparticle Ripening." *Journal of Physical Chemistry C* 113(38): 16645-16651.
- Zhao, Y., L. Xu, et al. (2013). "Alternating Plasmonic Nanoparticle Heterochains Made by Polymerase Chain Reaction and Their Optical Properties." *The Journal of Physical Chemistry Letters* 4(4): 641-647.
- Zhou, H.-X., G. Rivas, et al. (2008). "Macromolecular Crowding and Confinement: Biochemical, Biophysical, and Potential Physiological Consequences*." *Annual Review of Biophysics* 37(1): 375-397.
- Zhou, H. X. (2008). "Effect of mixed macromolecular crowding agents on protein folding." *Proteins: Structure, Function, and Bioinformatics* 72(4): 1109-1113.
- Zhou, H. X., G. Rivas, et al. (2008). "Macromolecular Crowding and Confinement: Biochemical, Biophysical, and Potential Physiological Consequences." *Annual Review of Biophysics* 37(1): 375-397.
- Zhu, J., K. T. Yong, et al. (2010). "Additive controlled synthesis of gold nanorods (GNRs) for two-photon luminescence imaging of cancer cells." *Nanotechnology* 21(28).
- Zou, X. Q., E. B. Ying, et al. (2006). "Seed-mediated synthesis of branched gold nanoparticles with the assistance of citrate and their surface-enhanced Raman scattering properties." *Nanotechnology* 17(18): 4758-4764.

Vita

Ameya Umesh Borwankar was born in Thane, Maharashtra, India. After graduating from A.K. Joshi English Medium School (Thane, Maharashtra, India) in April 2003, he attended V.G. Vaze junior college where he graduated with a high school diploma in April 2005. After this, he enrolled in the University Institute of Chemical Technology (UICT) (Mumbai, Maharashtra, India), where he obtained a Bachelor of Chemical Engineering degree from the Chemical Engineering Department in May 2009. During his undergraduate tenure, he conducted research over the summers on the surface tension behavior of sodium oleate surfactant as a function of its dimerization under the guidance of Dr. Savita Ladage. After graduation from UICT, he enrolled in the graduate program in the Chemical Engineering Department at the University of Texas at Austin in August 2009. He performed graduate work under the guidance of Prof. Keith P. Johnston and Prof. Thomas M. Truskett, and obtained a Doctor of Philosophy in Chemical Engineering in December 2014.

E-mail address: ameyaborwankar@gmail.com

This dissertation was typed by the author.